======== **ELECTRONIC AND OPTICAL PROPERTIES** ========
OF SEMICONDUCTORS

Optical Properties of ZnGeP$_2$ in the UV Spectral Region

Yu. M. Basalaev^, A. B. Gordienko, and A. S. Poplavnoĭ

Kemerovo State University, Kemerovo, 650043 Russia
^e-mail: ymbas@kemsu.ru
Submitted December 20, 2004; accepted for publication December 27, 2004

Abstract—In the context of the density functional theory and pseudopotential approach, the electronic structure of ZnGeP$_2$ crystal is calculated on the basis of localized orbitals. The calculated behavior of the imaginary part of the permittivity ε_2 in the UV spectral region is in good agreement with the experimental data. Analysis of direct interband transitions allows the origin of singularities in the behavior of ε_2 to be established. © *2005 Pleiades Publishing, Inc.*

Interest in the application of chalcopyrite-structured II–IV–V$_2$ crystals (the D_{2d}^{12} space group) as materials for nonlinear optics is motivated by their birefringence. ZnGeP$_2$ single crystals have gained acceptance, among other applications, in the laser industry, where they are used in mid-IR lasers as converters of radiation from one spectral region to another.

Recently [1], the pseudodielectric functions of optically uniaxial ZnGeP$_2$ crystal have been reported. These functions were determined by spectroscopic ellipsometry for the two orthogonal directions (along the lattice vectors a and c) $\langle\varepsilon_a\rangle = \langle\varepsilon_{a1}\rangle + i\langle\varepsilon_{a2}\rangle$ and $\langle\varepsilon_c\rangle = \langle\varepsilon_{c1}\rangle + i\langle\varepsilon_{c2}\rangle$ in the energy range 1.5 to 6.0 eV. The authors of [1] interpreted their data on the basis of theoretical calculations [2] performed in 1974. In [2], three

characteristic peaks at the energies $E_1 = 3$ eV, $E_c = 3.6$ eV, and $E_2 = 4.8$ eV were found for ZnGeP$_2$. The origin and notation of these peaks were discussed on the basis of the spectra of III–V compounds, which are the binary analogues of ZnGeP$_2$.

We calculated the electronic structure of ZnGeP$_2$ in the local approximation of density functional theory [3–6] with the aid of nonempiric norm-preserving pseudopotentials [7–9]. The solutions to Kohn–Sham's equations were represented on the basis of pseudo-atomic orbitals (PAOs) [10]. The PAO basis involved only s orbitals for Zn atoms and spd orbitals for Ge and P atoms. For the case of the 8-atom chalcopyrite lattice cell, this basis had 56 functions (dimensions). The advantage of the basis of localized orbitals over that of plane waves or over a mixed basis [11, 12] is its rela-
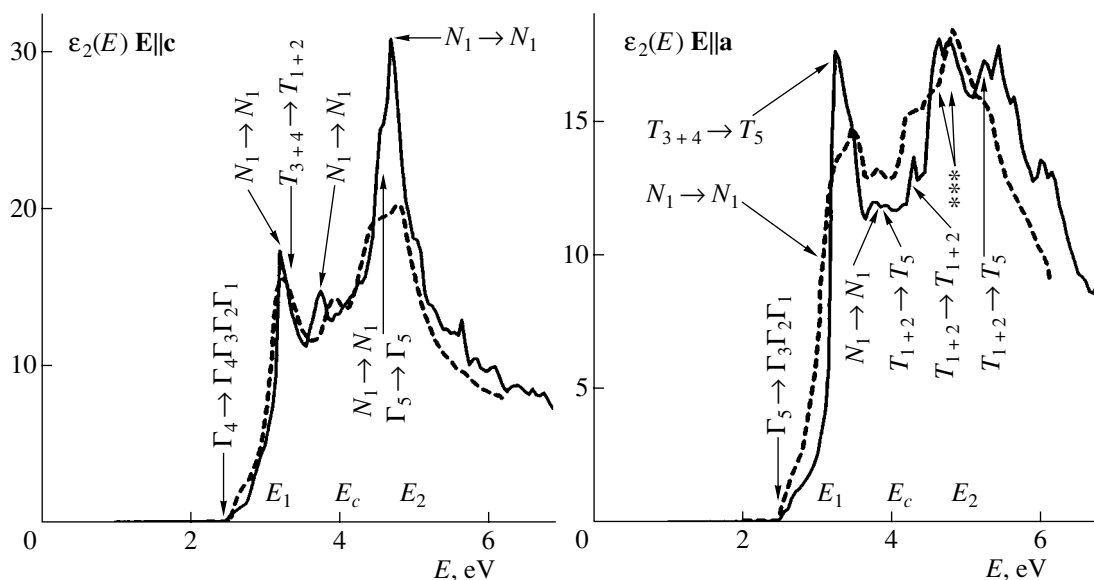
Function $\varepsilon_2(\mathbf{E})$ for ZnGeP$_2$, (solid line) calculated and (dashed line) determined experimentally. The transitions responsible for the basic spectral singularities are indicated. (Symbol *** denotes the transitions listed in Table 2.)

Table 1. Singularities of the function $\varepsilon_2(E)$ for the ZnGeP$_2$ compound in the range up to 6 eV at $\mathbf{E} \parallel \mathbf{c}$

Characteristics, eV		Transitions from the valence band to the conduction band, eV
experiment [1]	our calculation	
2.35 (edge)	2.35 (edge)	2.20*, 2.23*, 2.28 – $\Gamma_4(16) \longrightarrow \Gamma_3(17), \Gamma_2(18), \Gamma_1(19)$
2.88 (peak)	3.10 (peak)	2.63 – $N_1(15, 16) \longrightarrow N_1(17, 18)$; 2.99 – $N_1(13, 14) \longrightarrow N_1(17, 18)$
3.12 (shoulder)	3.15 (shoulder)	3.45 – $T_{3+4}(15, 16) \longrightarrow T_{1+2}(19, 20)$
3.68 (peak)	3.65 (peak)	3.76 – $N_1(11, 12) \longrightarrow N_1(17, 18)$
4.19 (shoulder)	4.20 (shoulder)	4.32 – $N_1(15, 16) \longrightarrow N_1(19, 20)$; 4.38 – $\Gamma_5(14, 15) \longrightarrow \Gamma_5(20, 21)$
4.61 (peak)	4.60 (peak)	4.68 – $N_1(13, 14) \longrightarrow N_1(19, 20)$

Note: The symbol * indicates forbidden transitions.

Table 2. Singularities of the function $\varepsilon_2(E)$ for the ZnGeP$_2$ compound in the range up to 6 eV at $\mathbf{E} \parallel \mathbf{a}$

Characteristics, eV		Transitions from the valence to the conduction band, eV
experiment [1]	our calculation	
2.45 (edge)	2.45 (edge)	2.21, 2.24, 2.29 – $\Gamma_5(14, 15) \longrightarrow \Gamma_3(17), \Gamma_2(18), \Gamma_1(19)$
3.00 (shoulder)	3.00 (shoulder)	2.99 – $N_1(13, 14) \longrightarrow N_1(17, 18)$
3.39 (peak)	3.35 (peak)	3.10 – $T_{3+4}(15, 16) \longrightarrow T_5(17, 18)$
3.58 (peak)	3.85 (peak)	3.76 – $N_1(11, 12) \longrightarrow N_1(17, 18)$; 3.79 – $T_{1+2}(13, 14) \longrightarrow T_5(17, 18)$
4.07 (shoulder)	4.05 (shoulder)	4.14* – $T_{1+2}(13, 14) \longrightarrow T_{1+2}(19, 20)$
4.38 (shoulder)	4.40 (peak)	4.32 – $N_1(15, 16) \longrightarrow N_1(19, 20)$; 4.38 – $\Gamma_4(16) \longrightarrow \Gamma_5(20, 21)$; 4.36* – $T_5(11, 12) \longrightarrow T_5(17, 18)$
4.67 (peak)	4.75 (peak)	4.44, 4.47, 4.53 – $\Gamma_5(12, 13) \longrightarrow \Gamma_3(17), \Gamma_2(18), \Gamma_1(19)$; 4.58 – $\Gamma_5(14, 15) \longrightarrow \Gamma_4(22)$; 4.68 – $N_1(13, 14) \longrightarrow N_1(19, 20)$; 4.52 – $T_{3+4}(15, 16) \longrightarrow T_5(21, 22)$; 4.71 – $T_5(11, 12) \longrightarrow T_{1+2}(19, 20)$
5.12 (shoulder)	4.90 (shoulder)	5.22 – $T_{1+2}(13, 14) \longrightarrow T_5(21, 22)$

Note: The symbol * indicates forbidden transitions.

tively low dimensionality. This circumstance means that it can be applied not only to computationally more complex systems [13] but also used to obtain results that are highly competitive in their accuracy with those derived using the basis of plane waves [10–18]. In the calculations presented below, the matrix elements of the Hamiltonian and the overlap integrals were calculated by expanding the basis Bloch functions into a Fourier series in plane waves [11, 12], with the total number of plane waves ranging from 1600 to 1700. Such a number of plane waves yields convergence on an order between 10^{-2} and 10^{-3} au in the total energy. The lattice parameters required for the calculations, $a = 5.465$ Å and $c = 10.711$ Å, and the shifts of anions in ZnGeP$_2$, $u = 0.017$ Å, were taken from [19].

The results of calculations of $\varepsilon_2(E)$ for ZnGeP$_2$ are shown in the figure for the longitudinal ($\mathbf{E} \parallel \mathbf{c}$) and transverse ($\mathbf{E} \parallel \mathbf{a}$) orientations of the electric field $\mathbf{E}$ with respect to the tetragonal axis of the crystal. In the figure, the pseudodielectric function $\varepsilon_2(E)$ experimentally obtained in [1] is shown by the dashed line. As is obvious from the figure, the theory is in good qualitative agreement with the experimental data. The experi-

mentally identified singularities in $\varepsilon_2(E)$ can be interpreted in terms of direct interband transitions from the valence band to the conduction band. It is known that the most probable points of the Brillouin zone at which electronic transitions from the valence to the conduction band can occur in II–IV–V$_2$ crystals are the Γ, T, and N points (see, e.g., [20, 21]). The notation in the figure is related to transitions from the valence band to the conduction band. The interpretation of the singularities of the function $\varepsilon_2(E)$ observed experimentally, as well as those calculated in terms of direct interband transitions for the ZnGeP$_2$ crystal in the cases of $\mathbf{E} \parallel \mathbf{c}$ and $\mathbf{E} \parallel \mathbf{a}$, is illustrated in more detail in Tables 1 and 2. The numbers in parentheses near the related energy levels denote the number of branches in the Brillouin zone. It should be noted that, for II–IV–V$_2$ compounds, the valence band consists of 16 branches, which means that indices of 17 and above refer to the conduction band. Comparing the singularities in the dielectric function $\varepsilon_2(E)$, we can see that, for the $\mathbf{E} \parallel \mathbf{c}$ polarization, the edge of the function is formed by transitions in the center of the Brillouin zone of chalcopyrite from the top of the valence band $\Gamma_4(16)$ to the three lower energy levels

of the conduction band, namely, $\Gamma_3(17)$, $\Gamma_2(18)$, and $\Gamma_1(19)$. According to the calculation, all of the three peaks observed experimentally at **E** ∥ **c** have their origin in transitions occurring at the point *N*. The shoulder in the energy region at about 3.12 eV is due to the onset of transitions at the point *T*. At the same time, the shoulder at 4.19 eV is of a mixed nature: transitions in the center of the Brillouin zone and at the point *N* are responsible for this singularity.

For the **E** ∥ **a** polarization, similarly to the case of **E** ∥ **c**, the edge of the dielectric function is formed by optical transitions in the center of the Brillouin zone ($\Gamma_5(14, 15) \longrightarrow \Gamma_3(17)$, $\Gamma_2(18)$, and $\Gamma_1(19)$). However, these transitions occur from a doublet level separated from the top of the valence band due to crystalline splitting. The shoulder at 3.00 eV corresponds to transitions from the second doublet level of the valence band to the lowest level of the conduction band at the point *N*. The peak at 3.39 eV and the shoulders at 4.07 and 5.12 eV correspond to transitions at the point *T*. As can be seen from Table 2, the peaks at the energies 3.58, 4.38, and 4.67 eV are of a more complicated nature and involve a series of transitions at the points Γ, *T*, and *N*.

The results presented above show that the relatively nontrivial polarization spectra of structurally and compositionally complex crystals can be interpreted in the context of one-electron theory in terms of direct interband transitions. The quantitative differences between the theory and the experimental data arise from the known limitations of the density functional approach when applied to electron states of the conduction band and do not exceed the discrepancies typical for this approach.

REFERENCES

1. V. Blickle, K. Flock, N. Dietz, and D. E. Aspnes, Appl. Phys. Lett. **81**, 628 (2002).

2. C. V. de Alvarez, M. L. Cohen, L. Ley, *et al.*, Phys. Rev. B **10**, 596 (1974).

3. P. Hohenberg and W. Kohn, Phys. Rev. **136**, B864 (1964).

4. W. Kohn and S. J. Sham, Phys. Rev. **140**, A1138 (1965).

5. A. Ceperly and B. Alder, Phys. Rev. Lett. **45**, 566 (1980).

6. J. P. Perdew and A. Zunger, Phys. Rev. B **23**, 5048 (1981).

7. G. B. Bachelet and M. Schlüter, Phys. Rev. B **25**, 2103 (1982).

8. G. B. Bachelet, D. R. Hamann, and M. Schlüter, Phys. Rev. B **26**, 4199 (1982).

9. C. Hartwigsen, S. Goedecker, and J. Hutter, Phys. Rev. B **58**, 3641 (1998).

10. R. W. Jansen and O. F. Sankey, Phys. Rev. B **36**, 6520 (1987).

11. A. B. Gordienko and A. S. Poplavnoĭ, Izv. Vyssh. Uchebn. Zaved. Fiz., No. 1, 1 (1997).

12. A. B. Gordienko and A. S. Poplavnoĭ, Phys. Status Solidi B **202**, 941 (1997).

13. A. Zunger and M. L. Cohen, Phys. Rev. B **19**, 568 (1979).

14. S. G. Louie, K.-M. Ho, and M. L. Cohen, Phys. Rev. B **19**, 1774 (1979).

15. A. B. Gordienko and A. S. Poplavnoĭ, Phys. Status Solidi B **208**, 407 (1998).

16. A. B. Gordienko and A. S. Poplavnoĭ, Izv. Vyssh. Uchebn. Zaved. Fiz., No. 4, 126 (1998).

17. A. B. Gordienko and A. S. Poplavnoĭ, Izv. Vyssh. Uchebn. Zaved. Fiz., No. 3, 96 (2004).

18. A. B. Gordienko and A. S. Poplavnoĭ, Izv. Vyssh. Uchebn. Zaved. Fiz., No. 4, 44 (2001).

19. A. A. Vaĭpolin, Fiz. Tverd. Tela (Leningrad) **15**, 1430 (1973) [Sov. Phys. Solid State **15**, 965 (1973)].

20. A. S. Poplavnoĭ, Yu. I. Polygalov, and V. A. Chaldyshev, Izv. Vyssh. Uchebn. Zaved. Fiz., No. 6, 95 (1970).

21. Yu. I. Polygalov, Yu. M. Basalaev, M. L. Zolotarev, and A. S. Poplavnoĭ, Izv. Vyssh. Uchebn. Zaved., Fiz., No. 4, 125 (1988).

Translated by É. Smorgonskaya

Instability of Drift Waves in Two-Component Solid-State Plasma

A. A. Bulgakov and O. V. Shramkova^

Institute of Radiophysics and Electronics, National Academy of Sciences of Ukraine, Kharkov, 61085 Ukraine
^e-mail: O.Shramkova@mail.ru
Submitted July 27, 2004; accepted for publication December 27, 2004

Abstract—The instabilities of longitudinal waves in infinite semiconductor plasma containing charge carriers of two types are considered under the assumption that the thermal velocity of electrons slightly exceeds that of holes. The main result of this study is that instability can occur in intrinsic semiconductors if the electron drift velocity is lower than the thermal velocity. Drift wave instabilities are studied in intrinsic semiconductors and semiconductors with identical plasma frequencies of electrons and holes. The influence of dissipation on the instability of these waves is also considered. © 2005 Pleiades Publishing, Inc.

1. INTRODUCTION

In modern microwave engineering, bands of short millimeter and submillimeter waves are the most poorly understood. In these regions, tube-based devices can no longer be used, and solid-state structures efficiently operate as solid-state lasers only at shorter wavelengths, i.e., in the infrared and visible regions. At the same time, short millimeter and submillimeter waves are of significant interest for modern communication, medical research, and studies of the physical properties of materials [1, 2]. Therefore, the search for materials and physical effects to be applied in the development active devices in the millimeter and submillimeter ranges is obviously an important problem.

One conventional approach is the study of the possibility of developing solid-state devices demonstrating a prolonged interaction between an electromagnetic traveling wave and carriers drifting in dc fields in semiconductor plasma. Surveys of this problem are published from time to time, one example being the excellent review paper [3]. Paper [1] is also of considerable interest. In particular, this paper describes an experiment in which instability was observed in the millimeter range during the interaction of carriers drifting in a semiconductor layer with a periodic structure such as a dielectric waveguide with a periodic wall of complex shape. In our opinion, however, the mechanism of this instability is not completely clear. Finally, review [4] shows that study of the possibility of inducing instabilities in short-wavelength ranges and developing solid-state oscillators and amplifiers using these instabilities is of great interest to many researchers.

To date, great progress has been achieved in the technology of solid-state semiconductor periodic structures such as superlattices. These structures are new artificial materials whose properties can significantly differ from those of natural crystals. If the layer thicknesses are about 1–3 μm, then, in the millimeter and terahertz ranges, such structures represent a continuous semiconductor medium. By selecting semiconductors with different types of conductivity in their superlattice layers, one can obtain a material in which plasma frequencies, drift velocities, etc., for different carriers are of the same order of magnitude. At the same time, instabilities in semiconductors and plasma have been studied taking into account the significant difference in the parameters of the electron and hole components. The objective of this study was to examine the possibility of obtaining instability in electron–hole plasma consisting of a homogeneous semiconductor with a drift velocity smaller than the thermal velocity of carriers. In order to simplify the formulas, we do not consider the transition from a layered periodic structure to a homogeneous medium; these problems were considered in [5, 6].

The papers [7–11] of the late 1950s to early 1960s dealt with the instabilities induced by the carrier drift in plasma generated under external electric fields. In [12], these instabilities were considered in the kinetic and hydrodynamic approximations.

It has previously been shown that two-component plasma becomes unstable if the electron drift velocity with respect to ions is fairly high. The conditions for the instability onset were studied in [7–9] for plasma formed by electrons and ions with equal temperatures. It was shown that plasma becomes unstable if the electron drift velocity $v_{0e} \geq 1.32 v_{Te}$. When the electron temperature is much higher than the ion temperature, the drift velocity at which instability occurs decreases $v_{0e} \leq (m_e/m_p)^{1/2} v_{Te}$ [10].

The interaction of drift waves with plasma waves in semiconductors was considered in [11], where the two-stream instability caused by carrier drift in an external electric field was studied in the kinetic approximation. Dispersion relations were obtained for two modes of collective oscillations: a high-frequency optical mode,

$$\omega^2 = (\omega_{0e}^2 + \omega_{0p}^2)/\varepsilon_0,$$

in which electrons and holes move out of phase, and a low-frequency acoustic plasma mode

$$\omega = \frac{m_e}{m_p} k v_{Te},$$

in which electrons and holes move in phase. In these formulas, the following notation is used: $\omega_{0e,p}$ are the Langmuir frequencies of electrons and holes, $m_{e,p}$ are their masses, v_{Te} is the thermal velocity of electrons, k is the wave number, and ε_0 is the lattice component of the permittivity. These solutions were derived in the following approximations:

$$\frac{\omega_{0p}}{\omega_{0e}} \ll 1, \quad \frac{\omega_{0p}}{\omega_{0e}}\frac{v_{Te}}{v_{Tp}} \gg 1.$$

It follows from these inequalities that the thermal velocity of electrons should significantly exceed the hole velocity. At the same time, for many semiconductors, the electron thermal velocity only slightly exceeds the hole velocity; i.e., the second inequality is violated. This factor is taken into account in this study. We consider the interaction of plasma oscillations of electrons and holes (see [13]),

$$\begin{aligned}
\omega^2 &= \omega_{0e}^2/\varepsilon_0 + k^2 v_{Te}^2, \\
\omega^2 &= \omega_{0p}^2/\varepsilon_0 + k^2 v_{Tp}^2,
\end{aligned} \tag{1}$$

in the presence of carrier drift. It will be shown below that a specific feature of these waves is that they have regions of negative phase velocity, where the resonant interaction of the hole and electron drift waves with negative phase velocities is possible.

Significant attention was paid to the instability of spatially separated electron–hole streams in the studies of Romanov *et al.* [14–18]. The analysis was carried out in the quasi-hydrodynamic approximation and took into account the thermal velocity and collision frequency of carriers. The main aim of those studies was to find out if it was possible to decrease the drift velocity at which the instability occurs. The studies were carried out in a wide range of drifting carrier parameters, and the results were compared to the data presented in [11].

The existence of two carrier streams significantly complicates the problem; accordingly, we use the hydrodynamic approximation. It is known that the hydrodynamic equations are valid for the frequencies $\omega \gg \nu$ (collisionless plasma [19]) and $\omega \ll \nu$ only if the collective dynamics of the particles is studied and effects such as Landau damping are disregarded. The effect of thermal motion of the carriers can also be taken into account in the hydrodynamic approximation. As was shown in [20], the error of the hydrodynamic description (compared to the kinetic approach) does not exceed 10%, even at $\nu\lambda/2\pi v_T \geq 3$ (λ is the wavelength). Using the plasma frequencies $\omega_p = (4\pi e^2 n_0/m\varepsilon_0)^{1/2} \approx 10^{11}$–$10^{13}$ s^{-1}, effective masses $m \approx 10^{-28}$–10^{-29} g, and collision frequencies $\nu \approx 5 \times 10^{10}$–$10^{13}$ s^{-1} (at temperatures from 4.2 to 300 K) [21], which are typical of semiconductors, we obtain the thermal velocities $v_T \approx 10^7$–10^8 cm/s, Debye length $R_D = v_T/\omega_p \approx 10^{-4}$ cm, and carrier free paths $l = v_T/\nu \approx 10^{-4}$–$10^{-5}$ cm. Thus, our approach is valid for the frequencies $\omega \approx 10^{10}$–5×10^{13} s^{-1}. It should also be taken into account that, compared to the kinetic approximation, in the hydrodynamic approximation, a numerical coefficient slightly exceeding unity appears at the term $k^2 v_T^2$ in relation (1).

2. BASIC EQUATIONS

Let us consider an infinite two-component solid-state plasma formed by electrons and holes. Let us assume that an external dc electric field causes electron drift with the velocity v_{0e} and hole drift with the velocity $-v_{0p}$. We direct the $0x$ axis along electron drift direction. The electromagnetic processes in such a structure are described by Maxwell's equations, as well as constitutive equations for electrons and holes,

$$\begin{cases}
\dfrac{\partial \mathbf{v}_e}{\partial t} + (\mathbf{v}_{0e}\text{grad})\mathbf{v}_e = -\dfrac{e}{m_e}\mathbf{E} - \dfrac{\mathbf{v}_{Te}^2}{n_{0e}}\text{grad}\,n_e - \nu_e\mathbf{v}_e, \\[2mm]
\dfrac{\partial n_e}{\partial t} + \text{div}(n_{0e}\mathbf{v}_e + n_e\mathbf{v}_{0e}) = 0, \\[2mm]
\dfrac{\partial \mathbf{v}_p}{\partial t} - (\mathbf{v}_{0p}\text{grad})\mathbf{v}_p = \dfrac{e}{m_p}\mathbf{E} - \dfrac{\mathbf{v}_{Tp}^2}{n_{0p}}\text{grad}\,n_p - \nu_p\mathbf{v}_p, \\[2mm]
\dfrac{\partial n_p}{\partial t} + \text{div}(n_{0p}\mathbf{v}_p - n_p\mathbf{v}_{0p}) = 0,
\end{cases} \tag{2}$$

where n_{0e} and n_{0p} are the equilibrium electron and hole concentrations; ν_e and ν_p are collision frequencies; v_{Te} and v_{Tp} are thermal velocities; and n_e, n_p, v_e and v_p are the variable concentrations and velocities of carriers.

In order to determine the components of the permittivity tensor, we use the following relation for the electric displacement:

$$\begin{aligned}
\mathbf{D} &= \varepsilon_0\mathbf{E} \\
&+ i\frac{4\pi}{\omega}(-en_{0e}\mathbf{v}_e - en_e\mathbf{v}_{0e} + en_{0p}\mathbf{v}_p - en_p\mathbf{v}_{0p}).
\end{aligned} \tag{3}$$

Here, the time and coordinate dependence is assumed to be of the form $\exp(-i\omega t + ikx)$.

In the chosen coordinate system, Maxwell's equations are separated into the equations for the two polarization types. We study the polarization involving the nonzero components E_x, E_z, and H_y. Substituting the above expression for a plane wave into Maxwell's equation, we derive the dispersion relation. Let us consider longitudinal waves propagating along the $0x$ axis

disregarding any delay ($\omega/c \longrightarrow 0$). Then, we obtain the dispersion relation for longitudinal waves $\varepsilon = 0$; i.e.,

$$\varepsilon_0 - \frac{\omega_{0e}^2}{(\omega - kv_{0e} + i\nu_e)(\omega - kv_{0e}) - k^2 v_{Te}^2}$$

$$- \frac{\omega_{0p}^2}{(\omega + kv_{0p} + i\nu_e)(\omega + kv_{0p}) - k^2 v_{Tp}^2} = 0. \tag{4}$$

We note that the solutions to this equation were studied by Mikhaĭlovskiĭ [12] for various relations between the electron and hole concentrations and disregarding thermal velocities and collision frequencies.

3. INSTABILITIES IN INTRINSIC SEMICONDUCTORS

First of all, let us consider a case where $\nu_e = 0$, $\nu_p = 0$, and the semiconductor is intrinsic, i.e., the electron and hole concentrations are equal, $n_{0e} = n_{0p}$. Let us use a coordinate system linked to moving electrons, $\Omega = \omega - kv_{0e}$. Then, the drift oscillations are described by the dispersion relation

$$(\Omega^2 - \omega_{0e}^2/\varepsilon_0 - k^2 v_{Te}^2)$$

$$\times [(\Omega + kv_0)^2 - \omega_{0p}^2/\varepsilon_0 - k^2 v_{Tp}^2] = \alpha \omega_{0e}^4/\varepsilon_0^2, \tag{5}$$

where $v_0 = v_{0e} + v_{0p}$ and $\alpha = \omega_{0p}^2/\omega_{0e}^2 = m_e/m_p \ll 1$. In this case, we have a fourth-order equation with respect to the frequency Ω, whose solutions are given by

$$\omega_{1,2} = kv_{0e} \pm \sqrt{\omega_{0e}^2/\varepsilon_0 + k^2 v_{Te}^2} + O(\alpha), \tag{6a}$$

$$\omega_{3,4} = -kv_{0p} \pm \sqrt{\omega_{0p}^2/\varepsilon_0 + k^2 v_{Tp}^2} + O(\alpha). \tag{6b}$$

Waves $\omega_{1,2}$ are fast and slow electron drift waves, and $\omega_{3,4}$ are slow and fast hole drift waves. It should be taken into account that the waves are usually separated into fast and slow types at $k > 0$. If the wave vector can be positive and negative, such separation is conditional. In Fig. 1, the dashed lines correspond to the solutions ω_1, ω_3, and ω_4 at $\alpha \longrightarrow 0$. In this and all further figures, numbers 1–4 correspond to the curves for waves ω_{1-4}, respectively. The feature of these solutions is that, at negative wave numbers, the phase velocity of the electron drift wave becomes negative and that of the hole drift waves, positive. With regard to the limitations on the parameters imposed by the hydrodynamic approximation, it follows from formula (6a) that the frequency of slow electron drift wave ω_2 is negative (not shown in Fig. 1).

In order to explain this result, let us first consider a case where $v_{0e} = 0$ and $\omega_{\pm} = \pm\sqrt{\omega_{0e}^2/\varepsilon_0 + k^2 v_{Te}^2}$ [15]. The plots for $\omega_{\pm}$ are shown in Fig. 2. The thin curves correspond to waves propagating in the positive direction of the coordinate axis, while the dashed lines cor-
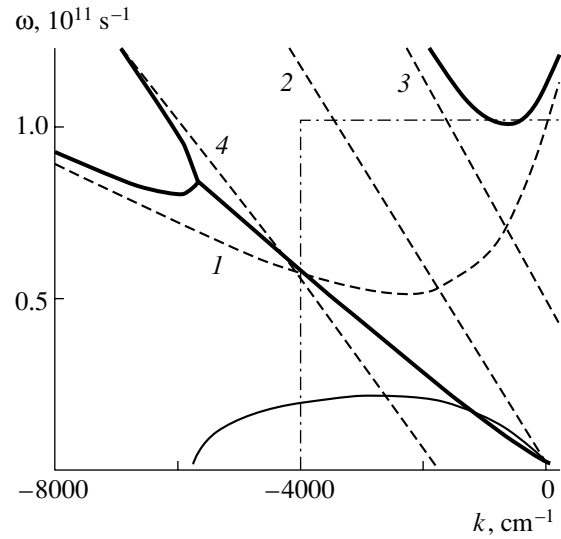

Fig. 1. Dispersion curves for electron and hole drift waves in an intrinsic semiconductor: $v_{0e} = 6 \times 10^7$ cm/s, $v_{Te} = 7 \times 10^7$ cm/s, $v_{0p} = 3 \times 10^7$ cm/s, $v_{Tp} = 1 \times 10^7$ cm/s, $\varepsilon_0 = 17.8$, $\omega_{0e} = 4.2 \times 10^{11}$ s^{-1}, and $\omega_{0p} = 2.1 \times 10^{11}$ s^{-1}. Dashed curves 1, 3, and 4 are the dependences corresponding to waves ω_1, ω_3, and ω_4 at $\alpha \longrightarrow 0$.
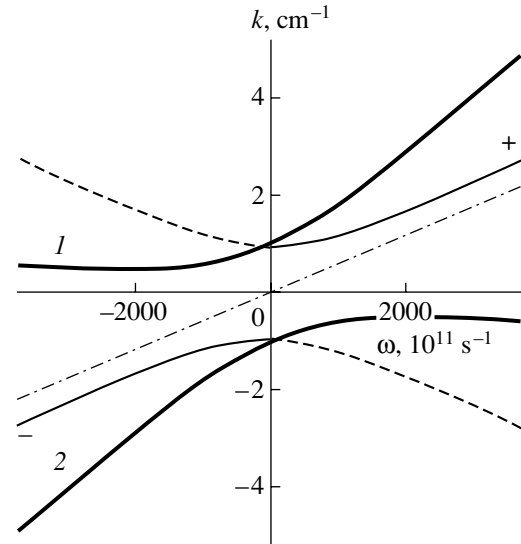

Fig. 2. Dispersion curves for electron and hole waves in the absence of drift (curves +, −) and at $v_{0e,p} \neq 0$.

respond to waves with negative phase velocities. We can see that the dispersion relations for waves with positive and negative phase velocities are transformed into each other and that the curves for waves propagating in one direction exhibit a discontinuity at $k = 0$. The dash–dotted line corresponds to the relation $\omega_a = kv_{0e}$. By summing these curves, we obtain the curves for $\omega_{1,2}$ (bold lines). We note that all the curves are symmetric with respect to the origin; therefore, hereafter, we consider only waves with positive frequencies. In the case
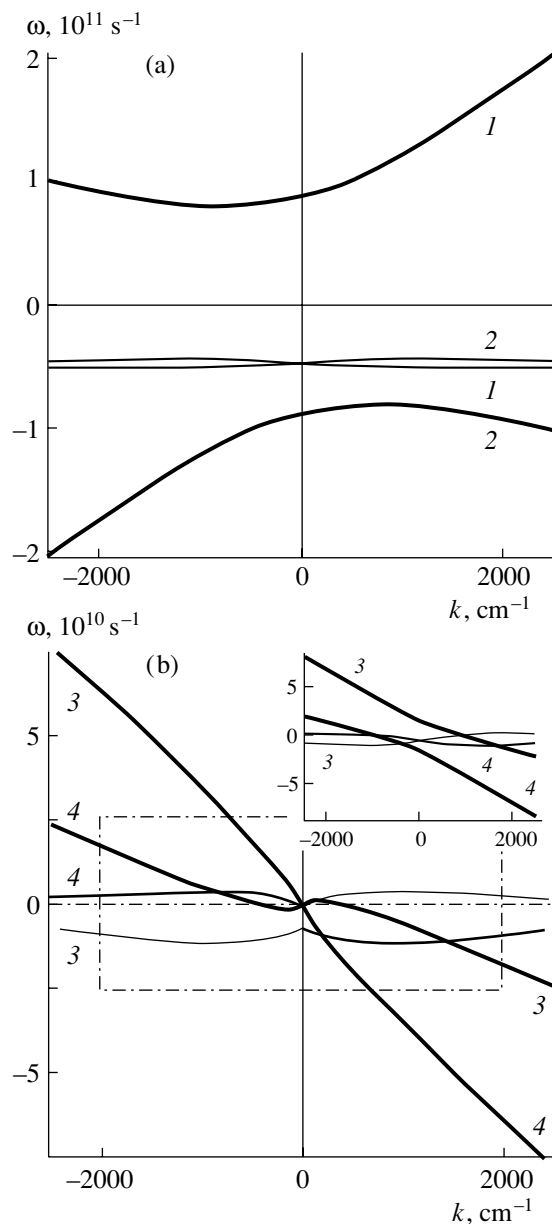
Fig. 3. Dispersion curves for drift waves in the presence of spatial damping: (a) ω_1 and ω_2; (b) $-\omega_3$ and ω_4; $v_{0e} = 2 \times 10^7$ cm/s, $v_{Te} = 5 \times 10^7$ cm/s, $v_{0p} = 2 \times 10^7$ cm/s, $v_{Tp} = 0.7 \times 10^7$ cm/s, $\omega_{0e} = 4.2 \times 10^{11}$ s^{-1}, $\omega_{0p} = 1.1 \times 10^{11}$ s^{-1}, $\varepsilon_0 = 17.8$, $\nu_e = 1 \times 10^{11}$ s^{-1}, and $\nu_p = 0$.

where $v_{0p} = 0$ and $\omega_{\pm} = \pm\sqrt{\omega_{0p}^2/\varepsilon_0 + k^2 v_{Tp}^2}$, the dependences $\omega_{3,4}(k)$ are similar.

We now return to Fig. 1. The dispersion relation for fast wave ω_1 exhibits a characteristic bend in the range of negative k and can intersect curves ω_3 and ω_4. It should be noted that, if we take into account the thermal velocity, we find that this wave propagates along the negative direction of the Ox axis. If we take into account

the small parameter α, then we obtain the repulsion of the curves at the crossing points. The solid curves in Fig. 1 are the dispersion curves obtained when α is taken into account. Physically, the crossing points correspond to resonance interaction between drift waves of various types. Near these points, the dispersion curves are changed and a resonance region is formed. In Fig. 1, this region corresponds to $k \approx -5800$ to 0 cm^{-1}. We note that, in contrast to the known cases of slow drift wave instability, the thermal velocities change the type of interaction, with the result that the interaction between a fast electron wave with negative phase velocity and a slow drift wave results in instability. There are two interaction points: between waves ω_1 and ω_3 and between waves ω_1 and ω_4. Resonance-type instability occurs when $\omega_1 = \omega_4$ and

$$k_{res} = -\frac{\omega_{0e} + \omega_{0p}}{\sqrt{\varepsilon_0}\,v_0}\left(1 + \frac{\omega_{0e} + \omega_{0p}}{v_0^2}\left(\frac{v_{Te}^2}{2\omega_{0e}} + \frac{v_{Tp}^2}{2\omega_{0p}}\right)\right). \quad (7)$$

In this case, the correction to the frequency is given by

$$\frac{\Delta\omega}{\omega} = i\frac{\omega_{0e}}{2}\sqrt{\frac{\alpha}{\varepsilon_0}}$$
$$\times [(\omega_{0e}^2/\varepsilon_0 + k_{res}^2 v_{Te}^2)(\omega_{0p}^2/\varepsilon_0 + k_{res}^2 v_{Tp}^2)]^{-1/4}. \quad (8)$$

This instability was further studied numerically. Figure 1 shows the dispersion curves for $\alpha = 0.25$. The bold and thin lines correspond to the dependences $\text{Re}\,\omega(k)$ and $\text{Im}\,\omega(k)$, respectively. The domain of applicability of the hydrodynamic approximation is denoted by the dash–dotted line. We note that the range of instability widens as α increases and that the increment of growth increases. The maximum range corresponds to k_{res}, and the increment is given by Eq. (8). Simulation shows that the instability range increases with the electron plasma frequency, and the domain of applicability of the hydrodynamic approximation increases as well. We note that instability of this type exists if

$$(v_{0e} + v_{0p})^2 > \frac{1}{2}\left(v_{Te}^2 + v_{Tp}^2\frac{\omega_{0e}}{\omega_{0p}}\right).$$

4. DISSIPATIVE PROCESSES

Let us consider the effect of collisions in the semiconductor. To this end, we rewrite Eq. (4) as

$$[\Omega(\Omega + i\nu_e) - k^2 v_{Te}^2 - \omega_{0e}^2/\varepsilon_0]$$
$$\times [(\Omega + k v_0)(\Omega + k v_0 + i\nu_p) - k^2 v_{Tp}^2 - \omega_{0p}^2/\varepsilon_0] \quad (9)$$
$$= \alpha\omega_{0e}^4/\varepsilon_0^2,$$

where $\Omega = \omega - k v_{0e}$, $v_0 = v_{0e} + v_{0p}$, and $\alpha = \omega_{0p}^2/\omega_{0e}^2$.

The solutions to this equation for the electron and hole drift waves are given by

$$\omega_{1,2} = \omega_{1,2}^{(0)} \pm \alpha \frac{\omega_{0e}^4}{2\varepsilon_0^2 A}$$

$$\times \frac{1}{(\omega_{1,2}^{(0)} + kv_{0p})(\omega_{1,2}^{(0)} + kv_{0p} + i\nu_p) - k^2 v_{Tp}^2 - \omega_{0p}^2/\varepsilon_0},$$

(10)

$$\omega_{3,4} = \omega_{3,4}^{(0)} \pm \alpha \frac{\omega_{0e}^4}{2\varepsilon_0^2 B}$$

$$\times \frac{1}{(\omega_{3,4}^{(0)} - kv_{0e})(\omega_{3,4}^{(0)} - kv_{0e} + i\nu_e) - k^2 v_{Te}^2 - \omega_{0e}^2/\varepsilon_0},$$

$$A = \frac{\sqrt{4(\omega_{0e}^2/\varepsilon_0 + k_x^2 v_{Te}^2) - \nu_e^2}}{2},$$

$$B = \frac{\sqrt{4(\omega_{0p}^2/\varepsilon_0 + k_x^2 v_{Tp}^2) - \nu_p^2}}{2},$$

where $\omega_{1,2,3,4}^{(0)}$ are the roots of Eq. (9) at $\alpha \longrightarrow 0$:

$$\omega_{1,2}^{(0)} = kv_{0e} - \frac{i\nu_e}{2} \pm A,$$

$$\omega_{3,4}^{(0)} = -kv_{0p} - \frac{i\nu_p}{2} \pm B.$$

(11)

In formulas (10), the signs "+" and "−" refer to waves $\omega_{1,3}$ and $\omega_{2,4}$, respectively.

Electron waves $\omega_{1,2}^{(0)}$ are damped with the decrement $\nu_e/2$, and the hole wave decrement $\omega_{3,4}^{(0)}$ of decay is $\nu_p/2$, since the radicands in A and B are always positive. We note that the influence of electron and hole collisions on dispersion curves $\omega_{1,2,3,4}^{(0)}$ is insignificant.

Let us consider the interaction of drift waves with each other (Fig. 3). The imaginary part of the frequency from Eq. (10) for small α is written as

$$\mathrm{Im}\,\omega_{1,2} = -\frac{\nu_e}{2} \pm \alpha \frac{1}{2} \frac{\omega_{0e}^4}{\varepsilon_0^2 A} \frac{(\nu_e - \nu_p)(kv_0 \pm A)}{\left((kv_0 \pm A)^2 - k^2 v_{Tp}^2 - \omega_{0p}^2/\varepsilon_0\right)^2 + (\nu_e - \nu_p)^2(kv_0 \pm A)^2},$$

(12)

$$\mathrm{Im}\,\omega_{3,4} = -\frac{\nu_p}{2} \pm \alpha \frac{1}{2} \frac{\omega_{0e}^4}{\varepsilon_0^2 B} \frac{(\nu_p - \nu_e)(-kv_0 \pm B)}{\left((-kv_0 \pm B)^2 - k^2 v_{Te}^2 - \omega_{0e}^2/\varepsilon_0\right)^2 + (\nu_p - \nu_e)^2(-kv_0 \pm B)^2}.$$

(13)

The second terms on the right-hand sides in formulas (12) and (13) are approximately equal to $\alpha\nu_e$. Therefore, waves ω_1 and ω_2 decay in the entire frequency range, as is also shown by calculation using an exact formula (Fig. 3). Waves ω_3 and ω_4 can grow if the relation

$$1 > \frac{\omega_{0p}^2}{\omega_{0e}^2} > \frac{\nu_p}{\nu_e}$$

(14)

is satisfied. Furthermore, it can be seen from Eq. (13) that the necessary condition for the existence of instability is the following relation between the drift velocity and parameters of the problem:

$$v_0 > k^{-1}\sqrt{\omega_{0p}^2/\varepsilon_0 + k^2 v_{Tp}^2 - \nu_p^2/4}.$$

(15)

These conclusions are confirmed by exact calculation. Figure 3 shows the dispersion relations for ω_1 and ω_2 (Fig. 3a), in addition to ω_3 and ω_4 (Fig. 3b), calculated using formula (12). The bold and thin lines are the dependences $\mathrm{Re}\,\omega(k)$ and $\mathrm{Im}\,\omega(k)$, respectively, and the dash–dotted lines are the boundaries for the range of applicability of the hydrodynamic relations (Fig. 3b). At the chosen values of the parameters, waves ω_1 and ω_2 decay with a decrement of $\sim -\nu_e/2$. The wave ω_3 at $k > 0$ grows, and the phase velocity of the hole drift wave is positive at small k and negative at large k. At

$k < 0$, the wave decays. The curve for wave ω_4 is symmetric to ω_3 with respect to the origin; i.e., this wave is amplified at $k < 0$. The inset in Fig. 3b shows the results of the calculation using approximate formula (13). We can see that, near the origin, these results are slightly different.

5. CONCLUSIONS

We considered the instabilities of semiconductor electron–hole plasma under the assumption that the Langmuir frequencies and thermal velocities of carriers are slightly different. This assumption is a distinctive feature of this study as opposed to those carried out in the early 1960s. In this approximation, electron and hole drift waves, which differ only by the parameters associated with electron and hole mobilities and masses, can propagate in plasma. It is clear that the propagation directions of electron and hole drift waves are opposite to each other.

We showed that efficient interaction of various drift waves is possible in the range of negative phase velocities. Inequalities for the electron and hole drift velocities at which instabilities occur were derived. Simulation showed that there exists a resonance frequency range that increases as the ratio of the Langmuir frequencies for electrons and holes tends to unity.

When the Langmuir frequencies and thermal velocities are exactly equal, it is shown that the instabilities are aperiodic. If the thermal velocity is taken into account, the increment decreases, and the condition for instability contains the sum of the electron and hole drift velocities. Dissipative processes give rise to nonresonance instability of the hole waves. This instability can occur at both positive and negative phase velocities. In this case, the electron drift waves are damped.

Finally, we mention the two most significant results obtained in this study. We showed that a resonance interaction occurs between electron and hole drift waves (1); therewith, both waves should have negative phase velocities. The interaction appears if the condition

$$(v_{0e} + v_{0p})^2 > \frac{1}{2}\left(v_{Te}^2 + v_{Tp}^2 \frac{\omega_{0e}}{\omega_{0p}}\right)$$

is satisfied or if the electron and hole concentrations are equal:

$$(v_{0e} + v_{0p})^2 > \frac{v_{Te}^2}{2}\left(1 + \sqrt{\frac{m_e}{m_p}}\right).$$

Assuming that $v_{0p} = v_{0e}(1 - \alpha)$, where $\alpha < 1$, we obtain

$$v_{0e}^2 > \frac{v_{Te}^2}{8}\left(1 + \sqrt{\frac{m_e}{m_p}} + \alpha\right).$$

It follows from this inequality that, for instability to occur, the electron drift velocity must be lower than their thermal velocity by a factor of 2 or greater.

When studying cases in which the electron and hole Langmuir frequencies are equal and the dissipative processes are taken into account, we found that, for the instability to occur, the carrier velocity should exceed the thermal velocity, which is impossible in semiconductors.

In order to observe the effects under study, semiconductors with a high mobility of about 5×10^5 cm^2/(V s) are required, e.g., InSb at liquid-nitrogen temperature or PbTe at liquid-helium temperature. For thin-layer materials, GaAs-based layered structures can apparently be used.

ACKNOWLEDGMENTS

REFERENCES

1. V. E. Lyubchenko, Radiotekhnika **1** (1), 87 (2000).

2. C. Sirtori, Nature **417**, 132 (2002).

3. Ya. K. Trokhimenko and V. N. Dmitruk, Izv. Vyssh. Uchebn. Zaved. Radiofiz. **14**, 1395 (1971).

4. A. A. Belyanin, D. Deppe, V. V. Kocharovskiĭ, *et al.*, Usp. Fiz. Nauk **173**, 1015 (2003) [Phys. Usp. **46**, 986 (2003)].

5. Ya. B. Faĭnberg and N. A. Khizhnyak, Zh. Tekh. Fiz. **25**, 711 (1955).

6. S. M. Rytov, Zh. Éksp. Teor. Fiz. **29**, 605 (1955) [Sov. Phys. JETP **2**, 466 (1956)].

7. O. Buneman, Phys. Rev. Lett. **1**, 8 (1958).

8. O. Buneman, Phys. Rev. **115**, 503 (1959).

9. J. D. Jackson, J. Nucl. Energy, Part C **1**, 171 (1960).

10. I. Berstein, E. A. Frieman, R. M. Kulsrud, and M. N. Rosenbluth, Phys. Fluids **3**, 136 (1960).

11. D. Pines and J. R. Schriffer, Phys. Rev. **124**, 1387 (1961).

12. A. B. Mikhaĭlovskiĭ, *Theory of Plasma Instabilities*, Vol. 1: *Instabilities of a Homogeneous Plasma*, 2nd ed. (Atomizdat, Moscow, 1975; Consultants Bureau, New York, 1974).

13. L. Tonks and I. Lengmuir, Phys. Rev. **33**, 195 (1929).

14. V. F. Dryakhlushin and Yu. A. Romanov, Zh. Éksp. Teor. Fiz. **58**, 348 (1970) [Sov. Phys. JETP **31**, 187 (1970)].

15. E. P. Bogdanov, L. K. Orlov, and Yu. A. Romanov, Izv. Vyssh. Uchebn. Zaved. Radiofiz. **14**, 228 (1971).

16. E. P. Bogdanov, L. K. Orlov, and Yu. A. Romanov, Izv. Vyssh. Uchebn. Zaved. Radiofiz. **14**, 801 (1971).

17. E. P. Bogdanov, L. K. Orlov, and Yu. A. Romanov, Izv. Vyssh. Uchebn. Zaved. Radiofiz. **15**, 521 (1972).

18. E. P. Bogdanov and Yu. A. Romanov, Izv. Vyssh. Uchebn. Zaved. Radiofiz. **17**, 1446 (1974).

19. V. P. Silin and A. A. Rukhadze, *Electromagnetic Properties of Plasma and Plasma-like Media* (Atomizdat, Moscow, 1961) [in Russian].

20. E. P. Bogdanov, Yu. A. Romanov, and V. M. Troshin, Zh. Tekh. Fiz. **45**, 32 (1975) [Sov. Phys. Tech. Phys. **20**, 19 (1975)].

21. M. C. Steele and B. Vural, *Wave Interactions in Solid State Plasmas* (McGraw-Hill, New York, 1969; Atomizdat, Moscow, 1973).

Translated by A. Kazantsev

Electron Traps in Thin Layers of Low-Temperature-Grown Gallium Arsenide with As–Sb Nanoclusters

P. N. Brunkov*^, A. A. Gutkin*, V. V. Chaldyshev*, N. N. Bert*, S. G. Konnikov*,
V. V. Preobrazhenskiĭ**, M. A. Putyato**, and B. R. Semyagin**

*Ioffe Physicotechnical Institute, Russian Academy of Sciences, Politekhnicheskaya ul. 26, St. Petersburg, 194021 Russia
^e-mail: brunkov@mail.ioffe.ru
**Institute of Semiconductor Physics, Siberian Division, Russian Academy of Sciences,
pr. Akademika Lavrent'eva 13, Novosibirsk, 630090 Russia
Submitted January 1, 2004; accepted for publication January 1, 2005

Abstract—Electron traps in low-temperature-grown ~40-nm-thick GaAs layers containing nanometer As–Sb clusters have been studied using deep-level transient spectroscopy. Measurements at various bias voltages and small-amplitude filling pulses have allowed the identification of two groups ($T1$ and $T2$) of traps with substantially different thermal electron emission rates. It is shown that the density of traps $T2$ (with an activation energy of 0.56 ± 0.04 eV and electron capture cross section of 2×10^{-13}–10^{-12} cm^2) is ~2×10^{12} cm^{-2}, while the density of traps $T1$ (0.44 ± 0.02 eV and 2×10^{-14}–10^{-13} cm^2, respectively) is ten times lower. It is assumed that, according to the existence of the two cluster groups observed in the layers under study, traps $T2$ are associated with clusters 4–7 nm in diameter and traps $T1$, with clusters up to ~20 nm in diameter. © 2005 Pleiades Publishing, Inc.

1. INTRODUCTION

Doping of gallium arsenide grown by low-temperature molecular-beam epitaxy (LT GaAs) can be used to control the spatial distribution of clusters in this material [1–5]. The "two-dimensional" (2D) cluster layers generally obtained in this case contain, in addition to excess As atoms, a significant number of dopant atoms (Si, In, Sb). This circumstance can affect the properties of the layers and their electron traps. However, the parameters of these traps have barely been studied. In the only study [6] dealing with this problem, carried out using 2D layers of As–Sb clusters in LT GaAs, traps with an activation energy of thermal electron emission close to 0.5 eV and a density of ~2×10^{12} cm^{-2} were detected.

This paper continues the investigation initiated in [6]. We comprehensively study thermal electron emission from traps in a thin LT-GaAs layer using deep-level transient spectroscopy (DLTS).

The application of various reverse biases to a structure with a Schottky barrier whose space charge region contains a 2D layer of As–Sb clusters has made it possible to identify trap groups with significantly different thermal emission rates of electrons and to estimate their parameters. The results were confirmed and complemented by measurements of the current–voltage (I–V) and capacitance–voltage (C–V) characteristics.

The samples under study and the measuring system were described in [6].

2. STUDY OF ELECTRON EMISSION RATES FROM DEEP TRAPS

When there is a sufficiently large reverse bias on the Schottky barrier ($U_b \leq -3$ V), if the voltage on it remains above ~-1 V during the filling pulse, the DLTS spectrum contains two well resolved peaks, which indicates the recharging of two different deep-level centers (Fig. 1a). However, under these measurement conditions, after the filling pulse is turned off, the space charge layer of the Schottky barrier penetrates into the heavily doped substrate due to the large negative charge accumulated at these centers, which distorts the capacitance relaxation curves and the DLTS spectrum [7]. Therefore, to construct Arrhenius plots characterizing the deep levels, we measured DLTS spectra at different U_b but kept the amplitude of the filling pulse small and constant (1 V). The variation in the capacitance of the structure showed that, under these conditions, the space charge region did not reach the substrate during DLTS, thus providing a normal shape of the temporal capacitance relaxation corresponding to displacements of the space charge layer boundary in a uniformly doped region. In this case, only a minor fraction of the entire set of deep centers, whose energy levels lie near the quasi-Fermi level in the 2D cluster layer, is filled and depleted. The DLTS spectrum generally exhibited a single peak corresponding to almost monoenergetic levels (Fig. 1b, curves *1*, *3*). A change in the reverse bias resulted in a shift of the peak of the DLTS spectrum (Fig. 1b), since the quasi-Fermi level position is changed with respect to the spectrum of energy states in the cluster layer [6].
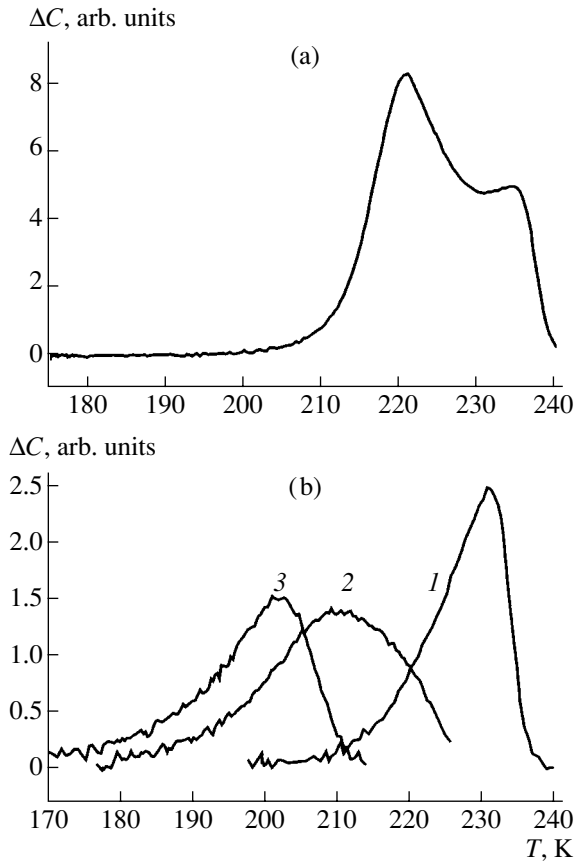
Fig. 1. DLTS spectra of the structures under study with the emission-rate window $e_n = 1.55$ ms^{-1} at various bias voltages: (a) $U_b = -4$ V and $U_p = 4$ V; (b) (*1*) $U_b = -4$ V and $U_p = 1$ V, (*2*) $U_b = -2$ V and $U_p = 0.8$ V, and (*3*) $U_b = -2.5$ V and $U_p = 1$ V.

The Arrhenius plots constructed on the basis of the DLTS spectra at various bias voltages are shown in Fig. 2. At $U_b \leq -3$ V, the deep-center parameters, as in [6], were determined from the high-temperature segments of the curves shown in Fig. 2, since the low-temperature segments were distorted due to the temperature dependence of the level-filling factor [6].

We see in Fig. 2 that the electron traps detected in the structure can be classified into two groups. One group, denoted as $T1$, consists of centers that manifest themselves at low reverse-bias voltages (–1.8 to –2.7 V). The activation energy E_{T1} of these centers is 0.44 ± 0.02 eV, and the electron capture cross sections σ_{T1} (calculated under the assumption that the coefficient related to the degeneracy of the level under study is unity) lie in the range 2×10^{-14}–10^{-13} cm^2. In this case, the electron emission rate from the probed fraction of these centers decreases as the reverse bias increases in the measured temperature range (190–240 K). Since an increase in the reverse bias causes an increase in the activation energy of the probed fraction of deep centers, such a decrease is at least in part associated with the
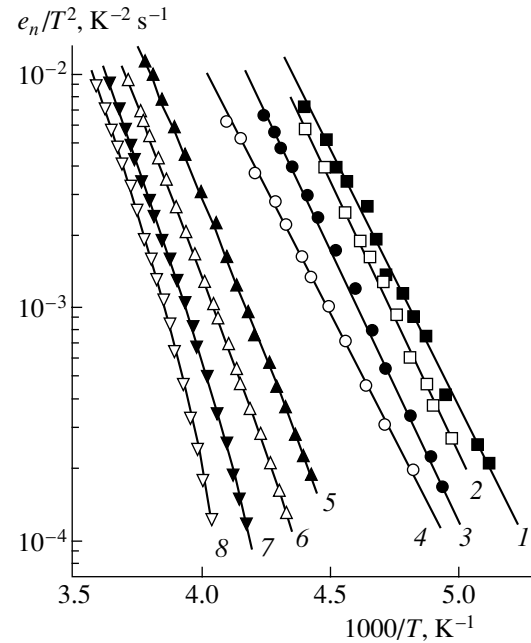

Fig. 2. Arrhenius plots for the electron traps detected at $U_p = 1$ V and at various bias voltages applied to the structure. $U_b =$ (*1*) –2, (*2*) –2.3, (*3*) –2.5, (*4*) –2.7, (*5*) –3.1, (*6*) –5, (*7*) –8, and (*8*) –13 V.

increase occurring in the above-mentioned E_{T1} range. The second group of traps, denoted as $T2$, consists of centers detected at $U_b \leq -3.1$ V (Fig. 2). Thermal electron emission from these centers is characterized by the following parameters: $E_{T2} = 0.56 \pm 0.04$ eV and $\sigma_{T2} = 2 \times 10^{-13}$–$5 \times 10^{-12}$ cm^2.

In the intermediate range of reverse biases ($U_b \approx -2.8$ to –2.9 V), the peak in the DLTS spectrum is appreciably broadened (Fig. 1b, curve *2*), since the recharging of both observed groups of centers, whose peaks are not resolved in the DLTS spectrum, contributes to a change in capacitance.

3. STUDY OF THE *I–V* AND *C–V* CHARACTERISTICS OF THE STRUCTURE

First, we note that the current through the structure is limited by the high-resistivity of the LT-GaAs layer and linearly increases with the forward bias on the Schottky barrier if the barrier is sufficiently wide (Fig. 3a). The dependence of the structure conductivity in this segment of the *I–V* characteristic on the inverse temperature (Fig. 3b) is described by an activation energy of 0.42 eV, which is almost equal to that of thermal electron emission from the $T1$ levels. This fact indicates that the Fermi level in the LT-GaAs layer is controlled by the $T1$ centers, whose electron-capture cross section varies slightly with temperature.
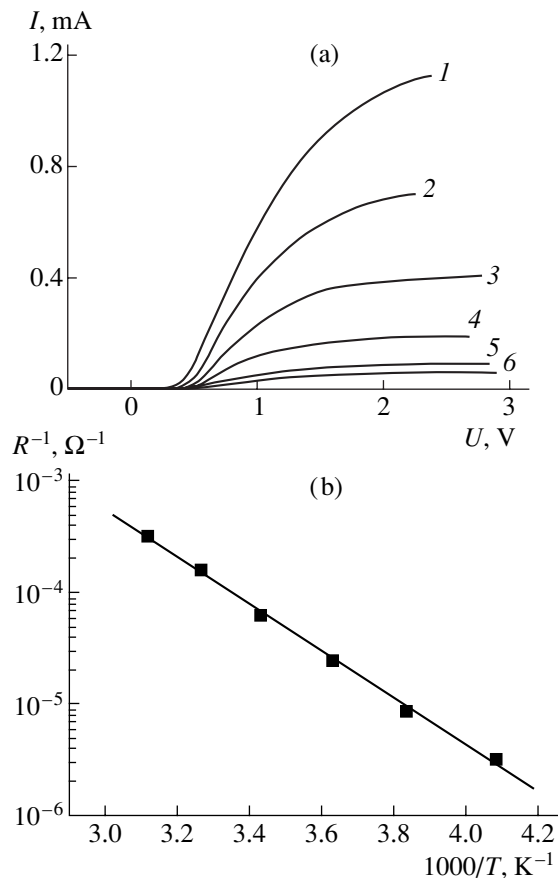
Fig. 3. (a) Current–voltage characteristics of the structure at various temperatures: $T = (1)$ 306, (2) 291, (3) 275, (4) 261, (5) 245, and (6) 230 K; (b) the temperature dependence of the conductivity of the structure at a bias exceeding 2 V.

Fig. 4. Capacitance–voltage characteristics of the structure at various temperatures: $T = (1)$ 190, (2) 210, (3) 230, (4) 250, and (5) 270 K.

The dependence of the high-frequency capacitance of the structures (at 1 MHz) on the reverse bias, measured at various temperatures, is shown in Fig. 4. As in [6], the bias voltage was varied from $U_b = 0$ in steps of 15 mV, and the time of sample exposure at each bias was 2.5 s. A small decrease in the capacitance C with temperature in the regions of the initial decrease in C and the C quasi-independence is associated with a change in the built-in contact potential of the barriers, as well as with a decrease in the contribution of high-frequency electron exchange between the GaAs conduction band and relatively shallow electronic states (these states exist both in LT GaAs and the neighboring low-resistivity n-type GaAs) to the structure capacitance. The main changes in the C–V characteristic as the temperature is lowered consist in the narrowing of the region of quasi-constant capacitance (Fig. 4) due to a decrease in the number of states that have time to excite trapped electrons to the GaAs conduction band as the reverse bias increases.

Since no peaks corresponding to the $T2$ levels were observed in the DLTS spectra at $U_b \geq -2.7$ V (Figs. 1b, 2),
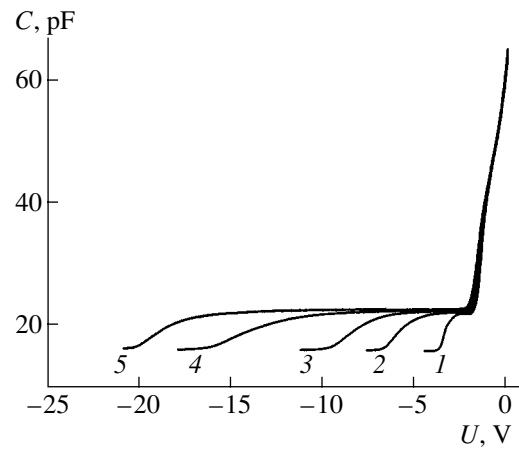
the quasi-Fermi level in the LT-GaAs layer at such bias voltages lies above the $T2$ levels in a steady state. Therefore, the region of quasi-constant capacitance observed at 190 K (Fig. 4), whose upper boundary lies at $U_b \approx -2.7$ V, is controlled only by electron emission from the $T1$ traps. The data presented in Fig. 2 show that the thermal electron emission rate from the $T1$ traps at $T = 190$ K is no lower than 2 s^{-1}. Hence, almost all the $T1$ traps that have captured electrons at $U_b = 0$ have time to excite them to the conduction band during the measurement of the C–V characteristic. At the same time, the extrapolation of Arrhenius curves for the fastest centers of the $T2$ group (Fig. 2) to the low-temperature region shows that the electron emission rate for these traps lies in the range 0.03–0.05 s^{-1} at $T = 190$ K. This result means that, even if the quasi-Fermi level is close to the $T2$ levels, these centers have no time to efficiently maintain the quasi-constancy of the capacitance at $T = 190$ K at the experimental bias variation rates. At the same time, all the $T2$ centers have rather high electron emission rates at $T = 270$ K and the region of quasi-constant capacitance extends down to $U_b \approx -18$ V (Fig. 4). Since the emitted charge is equal to the product of the capacitance and the voltage difference ΔU_b corresponding to the width of this region, the data shown in Fig. 4 allow us to estimate the density of electrons trapped by the $T1$ and $T2$ centers in equilibrium at zero bias. Since the sample area was 1.1×10^{-3} cm^2, such an estimation yields $n_{T1} \approx 10^{11}$ cm^{-2} ($\Delta U_b \approx 1$ V) and $n_{T2} \approx 2 \times 10^{12}$ cm^{-2} ($\Delta U_b \approx 18 - 3 = 15$ V).

Since the Fermi level in the LT-GaAs layer lies in the region of the $T1$ energy levels (as was shown in this section), the total concentration of $T1$ traps is slightly higher than n_{T1}, while the total concentration of $T2$ traps is n_{T2}.

4. CONCLUSIONS

We have shown that there are two groups of centers with significantly different thermal electron emission rates in thin LT-GaAs layers containing As–Sb clusters. We may assume that this circumstance is caused by the fact that the material under study contains two groups of As–Sb clusters of different sizes, namely, clusters 4–7 nm in diameter and very large clusters up to 22 nm in diameter [6]. The electron emission rates for the $T2$ centers are close to those for $Q2$ centers, which we previously associated with As clusters 6–8 nm in diameter [7]. Therefore, under the assumption that incorporation of a significant number of Sb atoms into the clusters only slightly changes the parameters of the traps associated with these clusters, we may assume that the $T2$ traps are related to clusters 4–7 nm in diameter. Then, the $T1$ traps can be associated with the large As–Sb clusters. However, an accurate identification of the origin of the detected traps requires further study.

ACKNOWLEDGMENTS

REFERENCES

1. M. R. Melloch, N. Otsuka, K. Mahalingam, *et al.*, Appl. Phys. Lett. **61**, 177 (1992).

2. T. M. Cheng, C. Y. Chang, and J. H. Huang, J. Appl. Phys. **76**, 5697 (1994).

3. N. N. Bert, V. V. Chaldyshev, D. N. Lubyshev, *et al.*, Fiz. Tekh. Poluprovodn. (St. Petersburg) **29**, 2242 (1995) [Semiconductors **29**, 1170 (1995)].

4. N. N. Bert, B. B. Chaldyshev, A. E. Kunitsyn, *et al.*, Appl. Phys. Lett. **70**, 3146 (1997).

5. V. V. Chaldyshev, Mater. Sci. Eng. B **88**, 195 (2002).

6. P. N. Brunkov, A. A. Gutkin, Yu. G. Musikhin, *et al.*, Fiz. Tekh. Poluprovodn. (St. Petersburg) **39**, 41 (2005) [Semiconductors **39**, 33 (2005)].

7. P. N. Brunkov, A. A. Gutkin, A. K. Moiseenko, *et al.*, Fiz. Tekh. Poluprovodn. (St. Petersburg) **38**, 401 (2004) [Semiconductors **38**, 387 (2004)].

Translated by A. Kazantsev

ELECTRONIC AND OPTICAL PROPERTIES
OF SEMICONDUCTORS

Study of the Properties of $Hg_{1-x-y-z}Cd_xMn_yZn_zTe$ as a New Infrared Optoelectronic Material

I. N. Gorbatyuk*, S. E. Ostapov*^, S. G. Dremlyuzhenko*, R. A. Zaplitnyĭ*,
I. M. Fodchuk*, V. V. Zhikharevich*, V. G. Deĭbuk*, N. A. Popenko**,
I. V. Ivanchenko**, A. A. Zhigalov**, and S. Yu. Karelin**

*Fed'kovich State University, ul. Kotsyubinskogo 2, Chernovtsy, 58012 Ukraine
^e-mail: sergey.ostapov@gmail.com
**Usikov Institute for Radiophysics and Electronics, National Academy of Sciences of Ukraine, Kharkov, 61085 Ukraine
Submitted December 7, 2004; accepted for publication January 13, 2005

Abstract—The physical parameters of a new five-component HgCdMnZnTe semiconductor alloy are studied. It is shown that this material is quite competitive with HgCdTe, i.e., the basic material for photoelectronics in infrared ranges of 3–5 and 8–14 μm. © 2005 Pleiades Publishing, Inc.

1. INTRODUCTION

Currently, due to its unique properties, the basic optoelectronic material for the infrared range is $Hg_{1-x}Cd_xTe$ (MCT) [1, 2]. The wide band-gap range (0–1.6 eV) of this alloy and the minimum lattice mismatch between CdTe and $Hg_{0.8}Cd_{0.2}Te$ allow efficient growth of epitaxial structures based on these materials, and the high carrier mobility makes it possible to develop fast-response devices [3]. A major disadvantage of MCT is the weak chemical bond Hg–Te, which gives rise to a large number of mercury vacancies and mercury diffusion to the surface. This process results not only in degradation of the material bulk parameters but also in problems in maintaining stability of the surface and interface properties in the structures.

In [2], a hundredfold decrease in the carrier lifetime, as well as conductivity-type inversion of MCT crystals, was observed after five years of storage. In our opinion, these changes are caused by mercury vacancy formation and a subsequent diffusion of Hg atoms to the crystal surface, where they evaporate. These conclusions were confirmed in [4]. Direct measurements of the surface concentration of MCT components upon heating to 470 K [5] demonstrated a decrease in the surface mercury concentration with temperature. In this case, concentrations of the other MCT components remained unchanged.

At the same time, an alternative mechanism of changes in the MCT parameters during storage was suggested in [6]. It was assumed that the carrier lifetime in MCT directly depends on local gradients of the component concentrations (i.e., on the inclusion concentration) and the mercury concentration gradients in an initial material [6]. Material "aging" is directly related to structural defects: grain and low-angle boundaries, dislocations, etc. This conclusion was also confirmed by

our studies of thin MCT layers (15–20 μm thick) exposed to a temperature of 80°C over six months.

The described MCT disadvantages can mostly be eliminated using modern technology; however, this greatly increases the cost of the produced materials. Thus, it remains urgent to search for ways to improve MCT crystal stability and homogeneity or to synthesize analogues with more perfect and stable lattices.

This goal can be achieved by introducing elements with ion radii smaller than that of MCT into the alloy, which should stabilize the Hg–Te crystal bond. Particularly favored as such isovalent elements are Mn and Zn, whose ion radii (1.39 and 1.3 Å) are much smaller than that of cadmium (1.56 Å) [7, 8]. An increase in the Hg–Te bonding energy in the presence of manganese was theoretically predicted in [9]. In [10–12], it was shown that Mn has a beneficial effect not only on the crystal structure quality but also on the alloy surface properties. Annealing of $Hg_{1-x}Zn_xTe$ (MZT) crystals in mercury vapor was studied in [13], In that case, the results suggested that zinc decreases the mercury diffusivity more than ten times in comparison with MCT without Zn.

Taking into account the above-mentioned findings, we believe that a five-component $Hg_{1-x-y-z}Cd_xMn_yZn_zTe$ (MCMZT) alloy with an insignificant manganese and zinc content should advantageously differ from MCT by demonstrating (i) higher temporal and thermal stability, (ii) higher structural quality, and (iii) better surface and interface properties.

2. CRYSTAL GROWTH AND X-RAY DIFFRACTION STUDIES

MCMZT crystals were grown using a modified form of the floating-zone melting method from preliminarily synthesized homogeneous polycrystalline ingots 15–

Fig. 1. X-ray topographic image of an MCMZT crystal in a (422) reflection. The magnification was ×16.
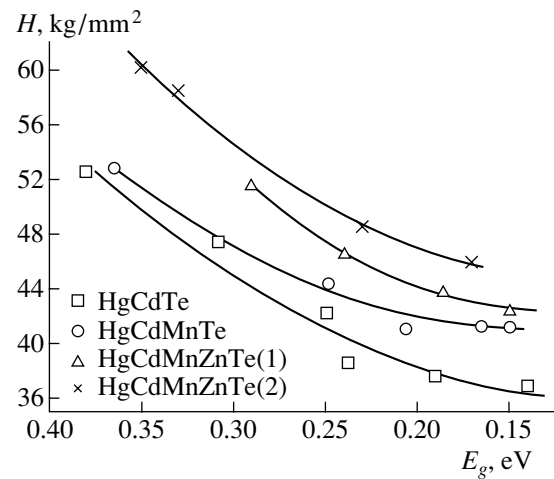

Fig. 2. Microhardness of MCT, MCM", and MCMZT crystals with various manganese contents. HgCdMnZnTe(1) and HgCdMnZnTe(2) are the first and second MCMZT ingots, with 2% and 4% of Mn, respectively.

18 cm long and 15–20 nm in diameter. We used initial Cd, Te, Zn, and Hg components with a purity of no lower than 99.9999 wt % and a Mn component of 99.998 wt % purity that was additionally purified by double vacuum distillation. The modification of the conventional vertical floating-zone melting consisted in ingot growth at an angle of 30°–60° to the horizontal and intense mixing of the melt due to axial rotation. Two MCMZT ingots with various manganese contents were grown. The initial contents of the components were $x = 0.14$ and 0.1, $y = 0.02$ and 0.04, and $z = 0.01$ and 0.01 for the first and second ingots, respectively.

As a rule, the distributions of the components and, hence, the band gap along the ingot length were non-uniform; therefore, samples cut from various areas of the ingots were studied.

Samples for studying the optical, electrical, and mechanical properties were cut from 500- to 600-μm-thick wafers obtained by cutting an ingot normally to the growth direction. The damaged layer formed during cutting and grinding was removed by polishing using ASM2/1 and ASM1/0 diamond pastes. The surface was subjected to a finishing chemomechanical polishing.

According to X-ray diffraction studies using the Berg–Barret and Laue methods, the MCMZT crystals are of a large-block type, with block sizes of 0.9–4.5 mm and misorientations between them of 25″–300″ (see Fig. 1). It should be noted that the block size increases with the number of components in semiconductor alloys such as MCT from 0.2–0.6 mm for $Hg_{1-x}Cd_xTe$ to 0.5–1.5 mm for $Hg_{1-x-y}Cd_xMn_yTe$ and 0.9–4.5 mm for $Hg_{1-x-y-z}Cd_xMn_yZn_zTe$.

Thus, an increase in the block size for MCMZT by a factor of 7–8 in comparison with MCT indicates improvement of the crystal structure of the proposed five-component alloy. In order to confirm this conclusion, the microhardness of these alloys was studied.

3. MICROHARDNESS STUDY

Microhardness was studied in MCT, MCM", and MCMZT samples whose surfaces were oriented close to the {110} plane. Measurements were carried out by the conventional Vickers technique using a PMT-3 device at a load of 35 g, which corresponded to the microhardness "plateau." The loading time was 5 s. The microhardness was averaged over 10–12 measurements.

In this case, the most accurate results are obtained by comparing the microhardness of crystals of various compositions but with approximately equal band gaps at room temperature (Fig. 2). The data obtained for MCT agree well with the previously obtained results [14]. The microhardness of all the crystals under study was found to increase with the band gap, which corresponds to an increase in the Cd, Mn, and Zn content.

For MCT, the microhardness varied from 36.8 kg/mm² at the band gap $E_g = 0.14$ eV (which corresponds to the composition $x \approx 0.19$) to 52.7 kg/mm² at $E_g = 0.38$ eV ($x \approx 0.37$) (Fig. 2).

The MCMT microhardness varied from 41.2 kg/mm² at $E_g = 0.15$ eV to 52.9 kg/mm² (at $E_g = 0.365$ eV), and the MCMZT microhardness varied from 42.3 kg/mm² ($E_g = 0.15$ eV) to 53.7 kg/mm² ($x = 0.29$ eV) for the first ingot, containing 2% Mn (in the initial mixture), and from 45.8 kg/mm² ($E_g = 0.17$ eV) to 60.1 kg/mm² ($E_g = 0.35$ eV) for the second ingot, which had 4% Mn. We can see that the crystal microhardness increases by ~12% as

manganese is added to the alloy at $E_g = 0.15$ eV and by ~3% at $E_g = 0.35$ eV for MCMT. This result is also confirmed by an increase of ≲8% in the microhardness of the second MCMZT ingot in comparison with the first ingot.

These results obviously suggest that the lattice of mercury-containing materials such as MCT is strengthened due to small amounts of both Zn and Mn.

4. BAND GAP DETERMINATION

The band gap of the MCMZT crystals was determined by optical absorption curves at room temperature, since almost all the crystals were optically transparent after growth. The transmittance varied from several percent to 60%. The fundamental absorption edge lay in the wavelength range 4–8 μm, which corresponds to a band gap from 0.15 to 0.3 eV. Typical absorption curves are shown in Fig. 3.

We can see that samples taken from the first ingot (2% Mn) feature a band gap from ~0.16 to 0.3 eV and a rather smooth fundamental absorption edge. Samples cut from the second ingot (4% Mn) (not shown in Fig. 3) are characterized by a band gap from 0.2 to 0.34 eV and, on average, have a wider band gap than the first ingot. However, the absorption edge of the narrow-gap samples from this ingot has an insufficient steepness for reliable determination of the band gap.

The band gap of the obtained MCMZT samples was also determined from the temperature dependence of the Hall coefficient in the intrinsic conductivity region (in the case of samples with a pronounced intrinsic conductivity region).

A summary of the results of E_g determination at room temperature is given in Table 1.

We can see that the band gaps determined using the two methods are almost identical for samples 1a-1, 1a-15, 1b-2 and correlate for the nearby samples (2a-3 and 2a-4). As we recede from the ingot origin (the samples are arranged in Table 1 exactly in this way), the band gap decreases, which corresponds to the normal distribution of components in the ingot from its origin to its end.

5. GALVANOMETRIC MEASUREMENTS

The Hall coefficient, conductivity, and mobility of carriers were determined by the dc Van der Pauw method in the temperature range 4.2–300 K using the setup described in [15].

Three samples from the first ingot (1b-2, 1a-1, and 1a-15) and two samples from the second ingot (2a-1 and 2a-6) were chosen for further analysis. On the one hand, the properties of these particular samples are closest to $Hg_{0.8}Cd_{0.2}Te$ and $Hg_{0.7}Cd_{0.3}Te$; on the other hand, their temperature dependences of the Hall coefficient and mobility allow determination of the impurity concentration and activation energy (Fig. 4).
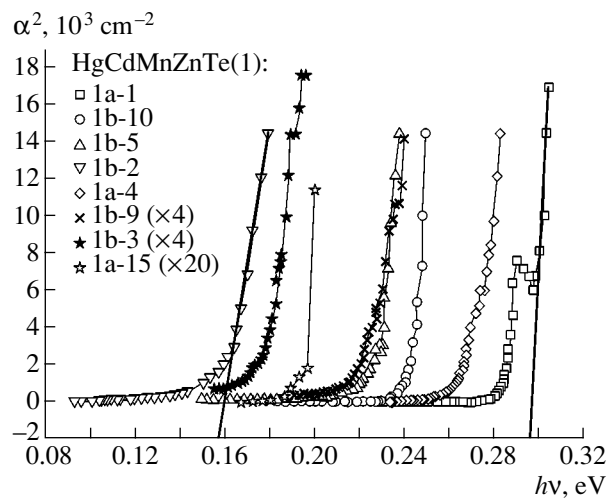

Fig. 3. Curves showing the optical absorption of MCMZT samples from the first ingot ($T = 300$ K). The symbols correspond to data on various samples from the HgCdMnZnTe(1) ingot.

The results of the study show that the conductivity of the majority of the samples increases as the temperature is elevated from 4.2 to 300 K (Fig. 4b). For the chosen samples from the first ingot, a rather wide range of intrinsic conductivity is observed at $T > 150$ K. At the same time, sample 2a-6 from the second ingot exhibits an almost constant conductivity in the range 50–300 K. In our opinion, this offers an indication of a significant concentration of impurities and their low activation energy.

The carrier mobility in the chosen samples varied from 10 to 3×10^4 cm²/(V s) (Fig. 4c) depending on their band gap, which indicates that the narrow- and wide-gap crystals have different properties. It should be

Table 1. Band gap of the MCMZT samples

Sample	E_g, eV (optical measurements)	E_g, eV (galvanomagnetic measurements)
1a-1	0.297	0.3
1a-4	0.275	–
1a-15	0.194	0.188
1b-10	0.244	–
1b-9	0.235	–
1b-5	0.224	–
1b-2	0.157	0.151
1b-3	0.175	–
2a-3	0.335	–
2a-4	–	0.322
2a-6	0.244	–
2a-7	0.23	–
2b-1	0.2	–

$|R_H|$, cm^3/C

(a)

10^5

10^4

10^3

10^2

10

1

0   50   100   150   200   250   300

T, K

- ■ 1a-1
- × 1a-15
- ▲ 1b-2
- ◆ 2a-1
- □ 2a-6

σ, (Ω cm)$^{-1}$

(b)

10

1

10^{-1}

10^{-2}

10^{-3}

0   50   100   150   200   250   300

T, K

- ■ 1a-1
- × 1a-15
- ▲ 1b-2
- ◆ 2a-1
- □ 2a-6

$|\mu|$, cm^2/(V s)

(c)

10^4

10^3

10^2

10

0   50   100   150   200   250   300   350

T, K

- ■ 1a-1
- × 1a-15
- ▲ 1b-2
- ◆ 2a-1
- □ 2a-6
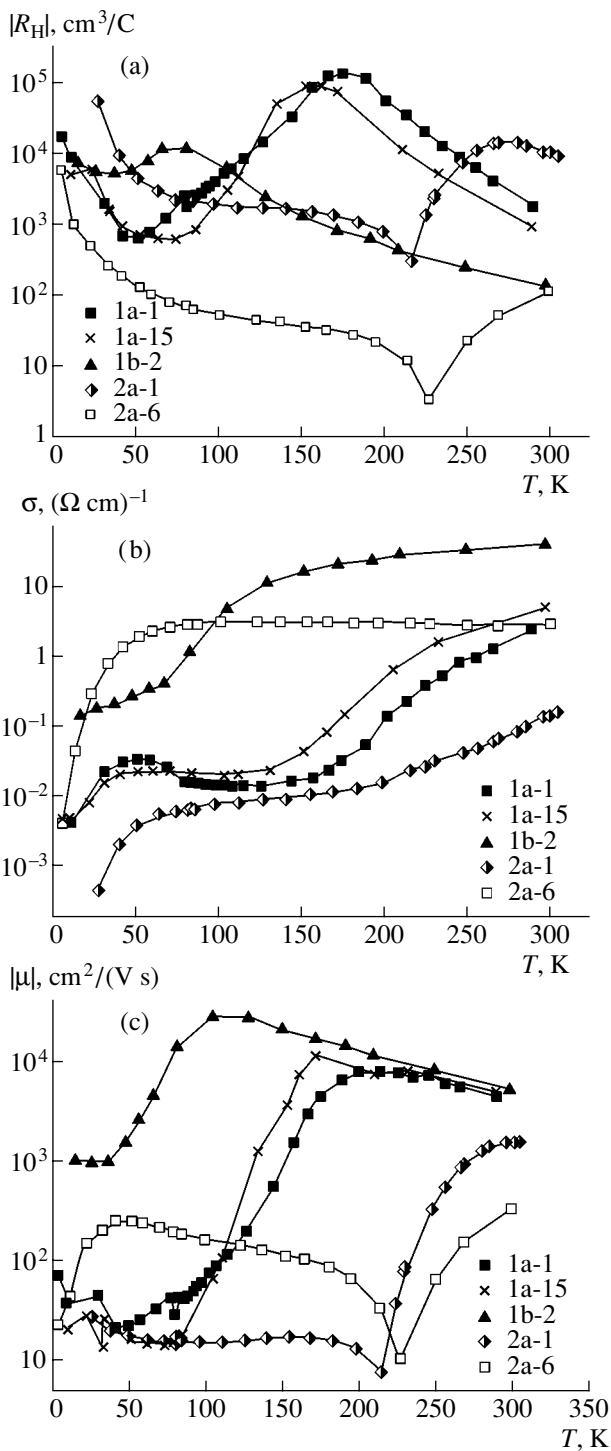
Fig. 4. Temperature dependences of the (a) Hall coefficient, (b) conductivity, and (c) Hall mobility of MCMZT samples from the two ingots.

noted that the highest mobility observed among all the samples under study was 8.4×10^5 cm/(V s) at $T = 78$ K in one of the samples from the first ingot.

In the high-temperature region, carrier mobilities in the samples from the first ingot, as well as the slope of

the temperature dependences, were almost identical, which is caused by identical mechanisms of carrier scattering at $T > 200$ K (Fig. 4c). At the same time, the room-temperature carrier mobility in samples from the second ingot was much lower than that in samples from the first ingot. This difference can be explained by the fact that the manganese content in the second ingot was two times larger, which resulted in an increase in the material band gap and, hence, a decrease in the intrinsic concentration of carriers and their mobility.

6. IMPURITY CONCENTRATION AND ACTIVATION ENERGY

Since we are concerned with two types of temperature dependences of the Hall coefficient for the chosen samples, i.e., a minimum in the low-temperature region (samples from the first ingot) and a sign reversal of the Hall coefficient in the high-temperature region (samples from the second ingot), two methods were used to determine the impurity concentration.

The first method was based on a model involving a single discrete acceptor level near the valence-band top and a single donor level near the conduction-band bottom. This method was used to determine the parameters of the samples from the second ingot, which were p-type at low temperatures [16]. Here, it was assumed that a donor impurity is always ionized. Then, the temperature dependence of the hole concentration at low temperatures is given by

$$\frac{p(p + N_D)}{(N_A - N_D) - p} = \frac{N_V}{g}\exp(-E_A/k_0 T), \qquad (1)$$

where N_V is the effective density of states in the valence band; g is the factor of acceptor level degeneracy; E_A is the impurity activation energy; and N_D and N_A are the donor and acceptor concentrations, respectively. In the case of a compensated material, Eq. (1) is simplified to the form

$$p = \frac{(N_A - N_D)N_V}{N_D}\frac{1}{g}\exp(-E_A/k_0 T). \qquad (2)$$

The effective mass of heavy holes in the calculation was taken as $m_{hh} = 0.55 m_0$ [17], and the level degeneracy factor g was set to four [16]. Then, the dependence $R_H T^{3/2}$ (or R_H) on the inverse temperature was plotted, and N_D, N_A, and E_A were determined in the low temperature region by the method of best fit with respect to the theory and experimental data.

In order to determine N_D and N_A for samples from the first ingot, a second method, based on estimation of the impurity concentration from the temperature dependence of the carrier mobility in the region of dominant scattering by ionized impurities, was used. To determine the temperature range in which scattering by ionized impurities is the prevalent mechanism, the temperature dependences of the carrier mobility were numeri-

Table 2. Impurity content and activation energy in the MCMZT samples

Sample	Hall coefficient*		Mobility**		Impurity activation energy E_A, meV
	N_D, cm^{-3}	N_A, cm^{-3}	N_D, cm^{-3}	N_A, cm^{-3}	
2a-1	1.7×10^{17}	2×10^{17}	1.9×10^{17}	2×10^{17}	9
2a-6	8.5×10^{16}	1.4×10^{17}	–	–	0.1
1a-1	–	–	1.9×10^{16}	1.92×10^{16}	–
1a-15	–	–	1.5×10^{16}	1.6×10^{16}	–
1b-2	–	–	3×10^{15}	10^{16}	–

  * Data obtained by studying the temperature dependence of the Hall coefficient in the temperature range 5–40 K.

 ** Data obtained by calculating the temperature dependence of mobility.

cally simulated for scattering by optical phonons and ionized impurities.

In order to calculate the mobility for carrier scattering by ionized impurities, the Brooks–Herring formula [16] was used:

$$\mu_i = \frac{2^{7/2}\kappa^2(4\pi\varepsilon_0)^2(k_0T)^{3/2}}{\pi^{3/2}N_ie^3(m_{hh}^*)^{1/2}\ln y}. \qquad (3)$$

Here, $\ln y = \ln(1 + b) - b/(1 + b)$; in nondegenerate semiconductors,

$$b = \frac{6\kappa(4\pi\varepsilon_0)m_{hh}^*(k_0T)^2}{\pi n\hbar^2 e^2};$$

in the case of degeneracy,

$$b = \frac{2\kappa(4\pi\varepsilon_0)k_0T}{e^2}\left(\frac{\pi}{3n}\right)^{1/3}.$$

Here, κ is the crystal permittivity, N_i is the concentration of ionized impurities, and n is the free-carrier concentration.

In order to calculate the mobility for carrier scattering by polar optical phonons, a relaxation time formula [18] was used:

$$\tau_{op} = \frac{\hbar\chi^*}{2e^2k_0TF_{op}}\frac{\partial\varepsilon}{\partial k}, \qquad (4)$$

where

$$\chi^* = \frac{\chi_s\chi_\infty}{\chi_s - \chi_\infty}.$$

Here, χ_s and χ_∞ are the static and high-frequency permittivities, respectively; ε is the energy; κ is the carrier quasi-momentum; and F_{op} is a function accounting for the nonparabolicity of the material band structure.

The mobility was simulated by using donor and acceptor concentrations as adjustable parameters. The impurity concentrations estimated by both methods are listed in Table 2. The temperature dependences of the Hall coefficient and mobility of sample 2a-1 allowed determination of the impurity concentration by both methods, which yielded almost identical results.

It follows from an analysis of the data that the first ingot was "purer" than the second one: $(0.3–1.92) \times 10^{16}$ as opposed to $(0.85–2) \times 10^{17}$ cm^{-3}. It is clear that the narrower (on average) band gap and lower impurity concentration in the first ingot result in rather high mobilities, as indicated above.

For sample 2a-1, at the point of the Hall coefficient inversion, we estimated the ratio of electron and hole mobilities. The value obtained (~117) is consistent with the conventional value for this type of material (~100), which also indicates the similarity between the properties of MCMZT and MCT [19].

7. CONCLUSION

The structural, mechanical, and galvanomagnetic properties of single crystals of the new semiconductor alloy $Hg_{1-x-y-z}Cd_xMn_yZn_zTe$, grown using a modified floating-zone melting, were studied for the first time.

It was shown that a minor admixture of zinc and manganese (up to 5–7%) in the alloy causes an increase in single-crystal block sizes, as well as an increase in the crystal microhardness, which indicates strengthening of the lattice of mercury-containing materials such as MCT.

The donor and acceptor concentration in the samples studied was estimated as $(0.3–20) \times 10^{16}$ cm^{-3}, and the activation energy of the acceptor level was estimated as 0.1–9 meV.

The band gap of the samples was determined as 0.15–0.335 eV. The values of E_g determined from the fundamental absorption curves correlate well with the values obtained from galvanomagnetic measurements.

These results allow us to conclude that the studied alloy has the potential to become an alternative material for producing infrared detectors sensitive in spectral ranges of 3–5 and 8–14 μm.

REFERENCES

1. R. Dornhaus and G. Nimtz, Springer Tracts Mod. Phys. **98**, 119 (1983).
2. G. Nimtz, B. Schlicht, and R. Dornhaus, Appl. Phys. Lett. **34**, 490 (1979).
3. H. R. Vydynath, J. Electrochem. Soc. **128**, 2609 (1981).
4. R. F. C. Farrow, G. R. Jones, G. M. Williams, *et al.*, J. Phys. D: Appl. Phys. **12**, L117 (1979).
5. H. M. Nitz, O. Ganschow, U. Kaiser, *et al.*, Surf. Sci. **104**, 365 (1981).
6. W. F. H. Mickletwaite and R. F. Redden, Appl. Phys. Lett. **36**, 379 (1980).
7. I. S. Virt, N. N. Grigor'ev, A. V. Lyubchenko, *et al.*, Poverkhnost: Fiz. Khim. Mekh. **4**, 60 (1988).
8. I. I. Izhnin, Proc. SPIE **3890**, 519 (1998).
9. A. Wall, C. Captile, and A. Franciosi, J. Vac. Sci. Technol. A **4**, 818 (1986).
10. O. A. Bodnaruk, I. N. Gorbatyuk, V. I. Kalenik, *et al.*, Neorg. Mater. **38**, 335 (1992).
11. O. G. Lanskaya, V. I. Kalenik, E. P. Lilenko, *et al.*, in *Proceedings of II All-Union Workshop on Impurities and Defects in Narrow-Gap Semiconductors* (Pavlodar, 1989), Chap. 1, p. 332.
12. P. M. Bridenbaugh, Mater. Lett. **3**, 287 (1985).
13. R. Grangler, A. Lasbley, S. Rolland, *et al.*, J. Cryst. Growth **88**, 682 (1988).
14. S. Cole, A. F. W. Willonghby, and M. J. Brown, J. Cryst. Growth **59**, 370 (1982).
15. A. Zhigalov and S. Karelin, Vestn. L'vov. Univ. **36**, 199 (2003).
16. W. Scott, F. Stelzer, and J. Hager, J. Appl. Phys. **47**, 1408 (1976).
17. I. N. Gorbatyuk, A. V. Markov, S. É. Ostapov, and I. M. Rarenko, Fiz. Tekh. Poluprovodn. (St. Petersburg) **38**, 1414 (2004) [Semiconductors **38**, 1369 (2004)].
18. S. M. Komirenko, Semicond. Sci. Technol. **9**, 19 (1994).
19. I. M. Nesmelova, *Optical Properties of Narrow-Gap Semiconductors* (Nauka, Novosibirsk, 1992) [in Russian].

Translated by A. Kazantsev

ELECTRONIC AND OPTICAL PROPERTIES OF SEMICONDUCTORS

Transport Coefficients of n-Bi$_2$Te$_{2.7}$Se$_{0.3}$ in a Two-Band Model of the Electron Spectrum

P. P. Konstantinov*, L. V. Prokof'eva*^, M. I. Fedorov*, D. A. Pshenaĭ-Severin*,
Yu. I. Ravich**, V. V. Kompaniets***, and V. A. Chistyakov***

*Ioffe Physicotechnical Institute, Russian Academy of Sciences, St. Petersburg, 194021 Russia
^e-mail: l.prokofieva@mail.ioffe.ru
**St. Petersburg State Polytechnical University, St. Petersburg, 195251 Russia
***Kryotherm Joint Stock Company, St. Petersburg, 197348 Russia
Submitted December 17, 2004; accepted for publication January 24, 2005

Abstract—The Hall factor and thermoelectric properties of an n-Bi$_2$Te$_{2.7}$Se$_{0.3}$ solid solution with the room-temperature Seebeck coefficient $|S|$ = 212 µV/K have been studied in the temperature range 77–350 K. The observed temperature dependences demonstrate a number of specific features, which were earlier found in samples with a lower electron density N. The effect of these specific features on the thermoelectric figure of merit Z appears to be more favorable for the sample under study: this sample is most efficient in the temperature range 120–340 K, and the average value of ZT is 0.71. It is found that a rise in the density N enhances the factor responsible for the effective mass decreasing as the temperature increases. This effect appears when the analysis is carried out in terms of a single-band parabolic model with N = const(T). This finding suggests that the most probable reason for the unusual behavior of these properties is the complex structure of the electron spectrum. Temperature dependences obtained from calculations of the transport coefficients show good agreement with the experimental data for two samples of the mentioned composition with different electron densities. The calculations have been performed in terms of a two-band model and an acoustic scattering mechanism and take into account the anisotropy and nonparabolicity of the light-electron spectrum. © 2005 Pleiades Publishing, Inc.

In a previous paper [1], we discussed the difference between the thermoelectric properties of lightly doped n-Bi$_2$Te$_{1-x}$Se$_x$ and PbTe$_{1-x}$Se$_x$ solid solutions, where the thermoelectric figure of merit Z reaches its maximum at temperatures T below room temperature. It was shown that the standard model considering a single-band electron spectrum and acoustic scattering mechanism, which is applicable for the second type of these solid solutions, does not provide a satisfactory description of temperature behavior of the transport coefficients and thermoelectric figure of merit for solid solutions based on Bi$_2$Te$_3$. For example, the application of this model yields a nonmonotonic temperature dependence of the effective mass in a Bi$_2$Te$_{2.7}$Se$_{0.3}$ solid solution; no explanation is found for the weaker temperature variation of the Seebeck coefficient when the Se content increases. The problems arising when describing the properties of these materials at T = 77–300 K in terms of this model were reported much earlier [2]. However, attempts to explain the observed discrepancies were limited to the introduction of a scattering parameter r_{eff}, which was found to be dependent on T, the Se content x, and the electron density N in terms of a model of a single-band parabolic spectrum [3]. This approach does not allow the physical factors that govern the transport of electrons in the materials under study to be included in the consideration. In order to explain the observed specific features, several ideas were suggested in [1], including possible variations in the scattering mechanism as well as in the electron spectrum. The importance of the last factor follows from the fact that the Hall factor decreases as the temperature increases, which has been observed in a solid solution with x = 0.3 in [1] and, earlier [2, 4]. If the possibility of an electron density increase with temperature is taken into account, the effective mass increases steadily with temperature, in agreement with the data for a Bi$_2$Te$_{2.88}$Se$_{0.12}$ solid solution. This observation indicates the nonparabolicity of the conduction band in the materials under study. Among possible sources of the electron density increase discussed in [1], a random profile of the conduction band bottom, which leads to the existence of a mobility threshold in samples of inhomogeneous composition, and the formation of defect levels near the band bottom are typical of lightly doped materials, whose properties were studied in [1]. A third possible source, the involvement of a heavy conduction band in transport phenomena, is more important for more heavily doped samples, where the contribution of heavy electrons is stronger due to their higher density. This circumstance constituted the reason for our further efforts to develop a theoretical model offering an adequate description of the specific features found in the thermoelectric properties of the materials under study.
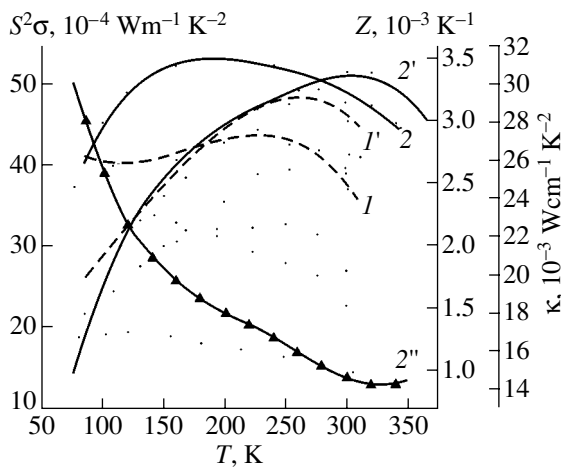
Fig. 1. Temperature dependences of (*1*, *2*) the power factor $S^2\sigma$, (*1'*, *2'*) the thermoelectric figure of merit Z, and (*2''*) the thermal conductivity κ for two samples of a $Bi_2Te_{2.7}Se_{0.3}$ solid solution with different doping levels. (*1*, *1'*), sample no. 1, (*2*, *2'*, *2''*), sample no. 2. The Seebeck coefficient $|S|$ at 300 K for sample nos. 1 and 2 was 285 [1] and 212 μV/K, respectively.

Now, we present experimental data on the temperature dependences of the Seebeck coefficient S, the electrical and thermal conductivity σ and κ, and the Hall factor in a chlorine-doped $Bi_2Te_{2.7}Se_{0.3}$ solid solution (the doping level was chosen so as to obtain the highest thermoelectric figure of merit Z at room temperature). The thermoelectric parameters were measured in the temperature range 77–350 K; the current and temperature gradient were parallel to the cleavage planes. The Hall effect was measured at temperatures up to 450 K in a magnetic field perpendicular (ρ_{123}) or parallel (ρ_{231}) to the cleavage plane. Analysis of the experimental data showed that the specific features observed earlier in samples of a solid solution with a lower electron density [1] are also inherent in the sample under study. Specifically, the features in question are a decrease in Hall factor as the temperature increases; a small variation in the Seebeck coefficient and, especially, the electrical conductivity within the mentioned temperature range, which results in a nonmonotonic temperature dependence and a high magnitude of the power factor; and, finally, a shift of the thermoelectric figure of merit maximum to the range where the effect of intrinsic carriers is significant. Owing to these specific features, which are the most quantitatively favorable in the case in question, the given sample demonstrates the highest thermoelectric figure of merit Z in the temperature range 120–340 K, with the average $(ZT)_{av} = 0.71$. This result is confirmed by the temperature dependences of some of the characteristics of the sample, which are shown in Fig. 1. The power factor $S^2\sigma$ and the figure of merit Z are presented in comparison with data for a more lightly doped solid solution with a room-temperature Seebeck coefficient $S = -285$ μV/K [1]. The last of

the above-mentioned specific features is illustrated by the thermal conductivity curve: the peak of Z lies in the temperature range where the bipolar contribution to the total thermal conductivity of the sample is significant.

An estimation of the temperature dependence of the effective mass in the range 85–240 K, performed in a similar way to that in [1], in terms of a parabolic model with a temperature-independent electron density yields a weak steady decrease in m^* under the law $m^* \propto T^{-0.06}$ as the temperature increases. This result means that the anomalous behavior of the effective mass, which appears at the temperatures 85–120 K in lightly doped samples, extends over the whole temperature range in the sample with a higher electron density. Thus, the role of the factor leading to the decrease in m^* as temperature increases is enhanced not only by an increase in the Se content [1, 5] but also by an increase in the electron density. If the increase in the electron density with temperature is taken into account in the analysis of the Hall-effect data, we obtain a weak increase in the effective mass under the law $m^* \propto T^{0.035}$ as the temperature increases.

On the basis of these estimates, we can assume that the most probable source of the specific features observed in the transport properties of $Bi_2(TeSe)_3$ solid solutions is the complex structure of the electron spectrum. The necessity of applying the concept of a complex conduction band structure in Bi_2Te_3 and $Bi_2(TeSe)_3$ solid solutions to explain their low-temperature ($T \approx 4.2$ K) characteristics was shown in [6, 7]. Therefore, it seemed reasonable to calculate the transport coefficients at 85–300 K for two samples of a $Bi_2Te_{2.7}Se_{0.3}$ solid solution with different doping levels, taking into account the second conduction band with a heavier electron mass.

An anisotropy of the energy spectrum and scattering is inherent in $Bi_2Te_{3-x}Se_x$ solid solutions. The anisotropy of the relaxation time is small when acoustic scattering dominates, as is the case in the temperature range under study. The anisotropy of the energy spectrum exerts influence on the contributions of each band to the transport coefficients; however, accurate calculation of these contributions is possible only if the anisotropy of the dispersion law for both bands is known. In our calculations, we used the Drabble–Wolfe model for describing the dispersion law in the light conduction band (C_1 band) [8]. Due to the lack of published data for the heavier electron band (C_2 band), an isotropic parabolic dispersion law with a density-of-states effective mass of $3m_0$ was used [6]. The calculations showed that, to achieve good agreement between the calculated and experimental temperature dependences of the Hall factor, it is necessary to take into account the nonparabolicity of the dispersion law in the C_1 band [1, 6]. In our calculations, the nonparabolicity was described by

Fitting parameters for the calculations taking into account (first row) and disregarding (second row) the nonparabolicity of the dispersion law in the light-electron band

ε_1, 10^{-4} eV K^{-1}	$\dfrac{(m_{01}^*)^{(1)}}{m_0}$	$\dfrac{(m_{01}^*)^{(2)}}{m_0}$	$s^{(1)}$	$s^{(2)}$	$N^{(1)}$, cm^{-3}	$N^{(2)}$, cm^{-3}	b	p_a
1.74	0.35	0.40	0.123	0.042	1.26×10^{19}	4.73×10^{19}	7.52	0.19
1.88	0.39	0.39	0	0	0.97×10^{19}	4.48×10^{19}	5.92	0.14

a power dependence of the density-of-states effective mass on the temperature in the form

$$m_1^* = m_{01}^*\left(\frac{T}{T_0}\right)^s. \tag{1}$$

Here, we set $T_0 = 85$ K, and m_{01}^* and s were fitting parameters dependent on the electron density.

For the solid solution under study with $x = 0.3$, the energy spacing $\Delta\varepsilon$ between the minima of the two conduction bands is zero at liquid-helium temperature [7]. It then increases linearly with temperature, with the coefficient ε_1, which was also considered to be a fitting parameter; therefore, $\Delta\varepsilon = \varepsilon_1 T$.

As was mentioned above, the relaxation time for scattering on acoustic phonons can be regarded as isotropic and can be represented as

$$\tau_i = \tau_{0i}\left(\frac{\varepsilon}{k_0 T}\right)^{-1/2}, \tag{2}$$

where k_0 is the Boltzmann constant, ε is the energy calculated from the bottom of the respective band, and the index $i = 1, 2$ indicates the bands (1 denotes the light-electron band and 2, the heavy-electron band). Then, the electrical conductivity in the C_1 band can be represented, in the approximation of an anisotropic, but parabolic, dispersion law, as [8]

$$\sigma_1 = \frac{p_a + 1}{2}\sigma_{01}F_1(\mu^*). \tag{3}$$

Here, μ^* is the chemical potential in $k_0 T$ units;

$$F_\nu(\mu^*) = \int_0^\infty -(\partial f_0(\varepsilon)/\partial\varepsilon)x^\nu dx$$

are the Fermi integrals; and the factor σ_{01} equals

$$\sigma_{01} = \frac{e^2(2m_1^* k_0 T)^{3/2}\tau_{01}}{3\pi^2\hbar^3 m_{12}^*}, \tag{4}$$

where m_{1k}^* is the effective mass in the direction of the kth principal axis of the ellipsoid and the anisotropy parameter is

$$p_a = \cos^2\theta(m_{12}^*/m_{11}^*) + \sin^2\theta(m_{12}^*/m_{13}^*),$$

where θ is the angle between the axis of the ellipsoid, which corresponds to the index $k = 1$, and the twofold axis. Relation (3) can also be used when calculating the conductivity for the nonparabolic dispersion law, assuming that the nonparabolicity in the C_1 band neither distorts the shape of the ellipsoid nor changes the angle θ but gives rise only to the temperature dependence of the effective mass m_{1k}^*, similarly to (1), with the same exponent s. In this case, the parameter p_a is temperature-independent.

Using (3) and (4) and taking into account the contribution of the two bands, we obtain the following expression for the conductivity:

$$\sigma = \sigma_{01}\left(\frac{p_a+1}{2}F_1(\mu^*) + b\frac{m_1^*}{m_2^*}F_1(\mu^* - \Delta\varepsilon^*)\right). \tag{5}$$

Here, $\Delta\varepsilon^*$ is the energy spacing between the minima of the two bands in $k_0 T$ units, and the temperature-independent parameter b is defined by the ratio between the deformation potential constants in the two bands and takes the form

$$b = \frac{\tau_{02}(m_2^*)^{3/2}m_{12}^*}{\tau_{01}(m_1^*)^{3/2}m_1^*}. \tag{6}$$

Similarly, for the Seebeck coefficient and the Hall factor we obtain

$$S = \frac{k_0}{eA}\left\{\frac{p_a+1}{2}[F_2(\mu^*) - \mu^* F_1(\mu^*)] \right.$$

$$\left. + b\frac{m_1^*}{m_2^*}[F_2(\mu^* - \Delta\varepsilon^*) - (\mu^* - \Delta\varepsilon^*)F_1(\mu^* - \Delta\varepsilon^*)]\right\}, \tag{7}$$

$$\rho_{123} = \frac{1}{ecn_{01}A^2}$$

$$\times\left[p_a F_{1/2}(\mu^*) + b^2\left(\frac{m_1^*}{m_2^*}\right)^{7/2}F_{1/2}(\mu^* - \Delta\varepsilon^*)\right], \tag{8}$$
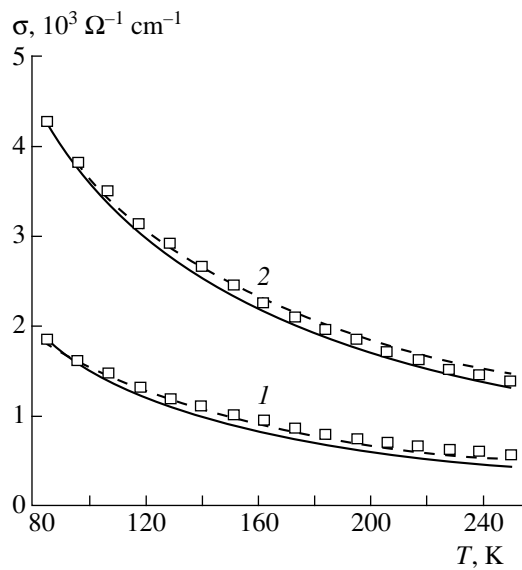
σ, 10^3 Ω^{-1} cm^{-1}

Fig. 2. Temperature dependences of the electrical conductivity σ for samples (*1*) no. 1 and (*2*) no. 2. The solid lines show the calculation taking into account the nonparabolicity of the dispersion law in the light-electron band, the dashed lines indicate that the nonparabolicity has been disregarded, and the squares represent the experimental data.
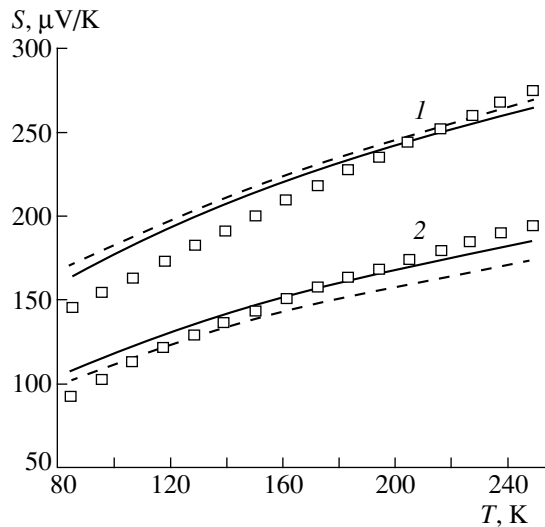
S, μV/K

Fig. 3. Temperature dependence of the Seebeck coefficient S. The notation is the same as in Fig. 2.

where

$$A = \frac{p_a + 1}{2} F_1(\mu^*) + b \frac{m_1^*}{m_2^*} F_1(\mu^* - \Delta\varepsilon^*),$$

$$n_{01} = \frac{(2 m_1^* k_0 T)^{3/2}}{3 \pi^2 \hbar^3}. \tag{9}$$

Using the obtained relations, the model parameters were found via the least-squares procedure. In the calculation, the chemical potential was determined using

the neutrality equation under the assumption that the total density of electrons is constant in the temperature range under study. For two samples with different carrier densities $N^{(1),(2)}$, the following fitting parameters were chosen: $(m_{01}^*)^{(1),(2)}$, $s^{(1),(2)}$, $N^{(1),(2)}$, b, p_a, and ε_1; the last three parameters were considered to be the same for the two samples with different electron densities, whereas the effective masses $(m_0^*)^{(1),(2)}$ and the exponents in their temperature dependences $s^{(1),(2)}$ differed in the two samples. Several variants of calculation were tested, with the anisotropy and nonparabolicity of C_1 band either taken or not taken into account and C_2 band disregarded. The best fit parameters for the two variants of the calculation, i.e., with or without consideration of the nonparabolicity of the light-electron band, are listed in the table. Figures 2–4 show the experimental temperature dependences of the conductivity and the Seebeck and Hall coefficients as well as those simulated in the two models. As can be seen, the two-band model with the nonparabolic C_1 band sufficiently describes the temperature dependences of the transport coefficients for both samples. The root-mean-square error does not exceed 10% for the electrical conductivity, 5% for the Seebeck coefficient, and 2% for the Hall coefficient. The values of the fitting parameters seem quite reasonable. In particular, the calculated density-of-states effective masses increase with temperature, as occurs in pure Bi_2Te_3. As was expected, the effective mass is smaller in the more lightly doped sample, and the obtained density-of-states effective mass at 85 K agrees with the value obtained on the bottom of the band in Bi_2Te_3 at 4.2 K (~$0.27m_0$) [6]. The calculated ratio between the light- and heavy-electron mobilities also lies within a reasonable range, varying between 9 and 15 depending on the electron density and temperature.

The two-band model also presents a qualitative explanation for the decrease in the Hall factor as the temperature increases, which is observed in both samples. Figure 5 shows, along with the temperature-related variation in the chemical potential and light-electron effective mass in the samples, the relative position of the C bands' minima, ε_{C_1} and ε_{C_2}. It can be seen that the energy spacing between the subbands increases, with a temperature coefficient of 1.74×10^{-4} eV/K, which leads to carrier redistribution between the bands. As a result, the carrier density in the lower band C_1, which makes the major contribution to the Hall factor due to its high electrical conductivity, increases, and its contribution to the total conductivity of the sample increases as the temperature increases.

When the calculation is performed in terms of the parabolic model for the C_1 band, the fitting parameters are close to those mentioned above, with less than a 10% difference (see table). For the second sample, which demonstrated weaker temperature dependence of the effective mass, all the calculated data agree with
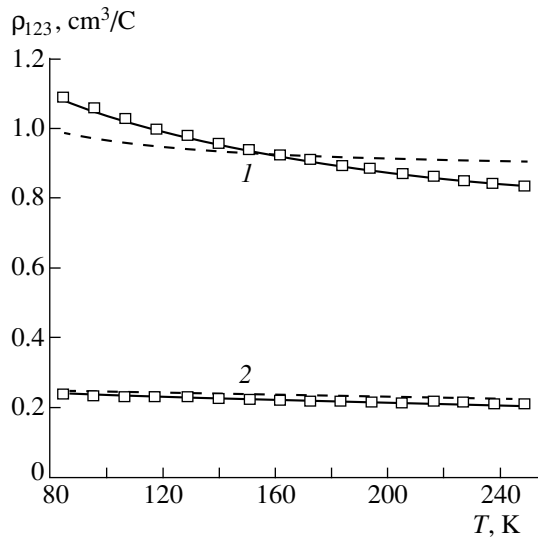
Fig. 4. Temperature dependence of the Hall factor ρ_{123}. The notation is the same as in Fig. 2.
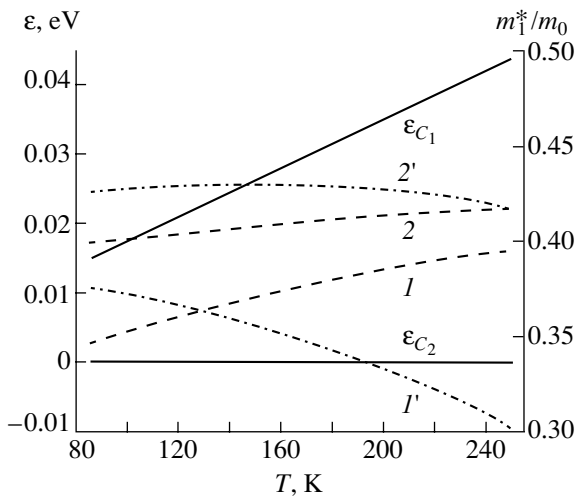

Fig. 5. Temperature dependences for sample nos. 1 and 2: dashed lines *1* and *2* show the light-electron effective mass, dot-dashed lines *1'* and *2'* show the chemical potential, and the solid lines show the positions of the conduction band minima (ε_{C_1} and ε_{C_2}).

the experiment. A significant difference between the calculated and experimental data is observed for the lightly doped sample (Fig. 4). The calculation yields a Hall factor decrease as the temperature increases, but this decrease is too small to fit the experimental data.

In terms of the nonparabolic model, the increase in the light-electron effective mass as the temperature increases results in stronger temperature enhancement of the electron density in the C_1 band. This circumstance leads to better agreement between the calculated and experimental temperature dependences of the Hall factor.

Thus, the best fit for both samples was obtained by taking into account the contributions of the two conduction bands to the transport coefficients. Consideration of the nonparabolicity of the light-electron band appeared to be essential for an adequate description of the temperature dependence of the Hall factor in the lightly doped sample.

REFERENCES

1. P. P. Konstantinov, L. V. Prokof'eva, Yu. I. Ravich, *et al.*, Fiz. Tekh. Poluprovodn. (St. Petersburg) **38**, 811 (2004) [Semiconductors **38**, 778 (2004)].
2. V. A. Kutasov and L. N. Luk'yanova, Fiz. Tverd. Tela (Leningrad) **20**, 3065 (1978) [Sov. Phys. Solid State **20**, 1767 (1978)]; Fiz. Tverd. Tela (Leningrad) **24**, 402 (1982) [Sov. Phys. Solid State **24**, 228 (1982)].
3. V. A. Kutasov and L. N. Luk'yanova, Fiz. Tverd. Tela (Leningrad) **26**, 2501 (1984) [Sov. Phys. Solid State **26**, 1515 (1984)].
4. V. A. Kutasov, L. N. Luk'yanova, P. P. Konstantinov, and G. T. Alekseeva, Fiz. Tverd. Tela (St. Petersburg) **39**, 483 (1997) [Phys. Solid State **39**, 419 (1997)].
5. B. M. Gol'tsman, G. N. Ikonnikova, V. A. Kutasov, and Yu. I. Ravich, Fiz. Tverd. Tela (Leningrad) **27**, 542 (1985) [Sov. Phys. Solid State **27**, 334 (1985)].
6. H. Köhler, Phys. Status Solidi B **73**, 95 (1976).
7. H. Köhler, W. Haigis, and A. von Middendorff, Phys. Status Solidi B **78**, 637 (1976).
8. B. M. Gol'tsman, V. A. Kudinov, and I. A. Smirnov, *Semiconducting Thermoelectric Materials Based on Bi$_2$Te$_3$* (Nauka, Moscow, 1972) [in Russian].

Translated by D. Mashovets

SEMICONDUCTOR STRUCTURES, INTERFACES, AND SURFACES

The Formation of Nanodimensional Structures on the Surface of *p*-CdTe Crystals Exposed to a Single Radiation Pulse from a Ruby Laser

A. Baĭdullaeva^, A. I. Vlasenko, L. F. Cuzan, O. S. Litvin, and P. E. Mozol'

Lashkarev Institute of Semiconductor Physics, National Academy of Sciences of Ukraine, Kiev, 03028 Ukraine
^e-mail: baidulla@yahoo.com
Submitted November 10, 2004; accepted for publication December 7, 2004

Abstract—The formation of nanodimensional structures on the surface of *p*-CdTe crystals has been studied as a function of the radiation-power density of a laser under a single irradiation dose. The best conditions for laser irradiation of the crystals are found. Under these conditions, a homogeneous structure with a period of 100 nm is formed. The lateral size of the structure is ~(19–20) nm, and the average height is ~(3.40–9.38) nm. It is found that periodicity manifests itself clearly in one crystallography direction. © *2005 Pleiades Publishing, Inc.*

1. INTRODUCTION

Currently, study of the formation of nanodimensional structures on crystal surfaces under laser irradiation is one of the most interesting and promising lines of research in semiconductor technology. The dimensions and distribution density of the elements of these structures depend, in a complex manner, on local thermal effects, the power density or irradiation dose, the concentration of defects generated under laser irradiation, the physical nature of the material, and other factors.

We have previously studied the formation of nanostructures on the surface of *p*-CdTe crystals in relation to the radiation dose under a fixed intensity of laser radiation [1, 2]. We showed that an accumulation effect plays the main role in this process. Consequently, it is important to set the energy density of a single pulse of laser radiation so as to cause the formation of ordered nanodimensional structures on the surface of CdTe crystals. The solution to this problem would make it possible to further develop modern optoelectronic engineering. In optoelectronics, CdTe crystals are used as a material in the fabrication of room-temperature fast-response modulators of the intensity of luminous fluxes and as a substrate material for CdHgTe layers. Therefore, the fabrication of ordered structures on the surface of CdTe crystals may possibly help to solve problems related to the growth of nanodimensional CdHgTe layers.

The purpose of this study was to determine the lowest intensity of a single radiation pulse from a ruby laser at which uniformly distributed nanodimensional elements start to form on the surface of *p*-CdTe crystals.

2. EXPERIMENTAL

We studied undoped lamellar dislocation-free *p*-CdTe (111) crystals, which were obtained by synthesis from vapors of the initial elements [3]. The samples were ~100 µm thick.

The crystals were irradiated at room temperature with a single radiation pulse from a multimode ruby laser operating in the Q-switched mode at a pulse duration $\tau = 2 \times 10^{-8}$ s. The laser radiation was focused into a spot ~1 µm in diameter. In order to obtain uniform laser radiation, we used an additional quartz diffuser. The laser radiation intensity (I) was measured using neutral gray filters. During the intensity measurement, the illuminated spot was moved to a previously unirradiated area of the sample surface.

The crystal surface morphology prior to and after irradiation was studied using a NanoScope IIIa atomic force microscope (AFM) (Digital Instruments) in a periodic contact mode (Tapping Mode™).

3. RESULTS

Figure 1 shows AFM images of a 1×1 µm^2 area of the surface of the *p*-CdTe crystals in relation to the laser-radiation power density. The arithmetical mean value of the surface roughness for an initial (unirradiated) sample was ~0.075 nm (Fig. 1a). In the region of the crystals irradiated under the laser radiation power density $I_1 = 4$ MW/cm^2, an island Te film emerged on the sample surface (Fig. 1b). This film was washed off in a 1 N KOH solution in methanol [1, 2]. The arithmetical mean surface roughness of the samples increased to ~0.171 nm. In this case, we observed the onset of formation of a profiled structure with lateral sizes of ~(23–46.87) nm and an average height of ~1.30 nm. In the region of the crystals irradiated under the laser-radiation power density $I_2 = 8$ MW/cm^2, the arithmetical mean surface roughness was ~0.760 nm (Fig. 1c). A profiled structure with lateral sizes of ~(27–132) nm
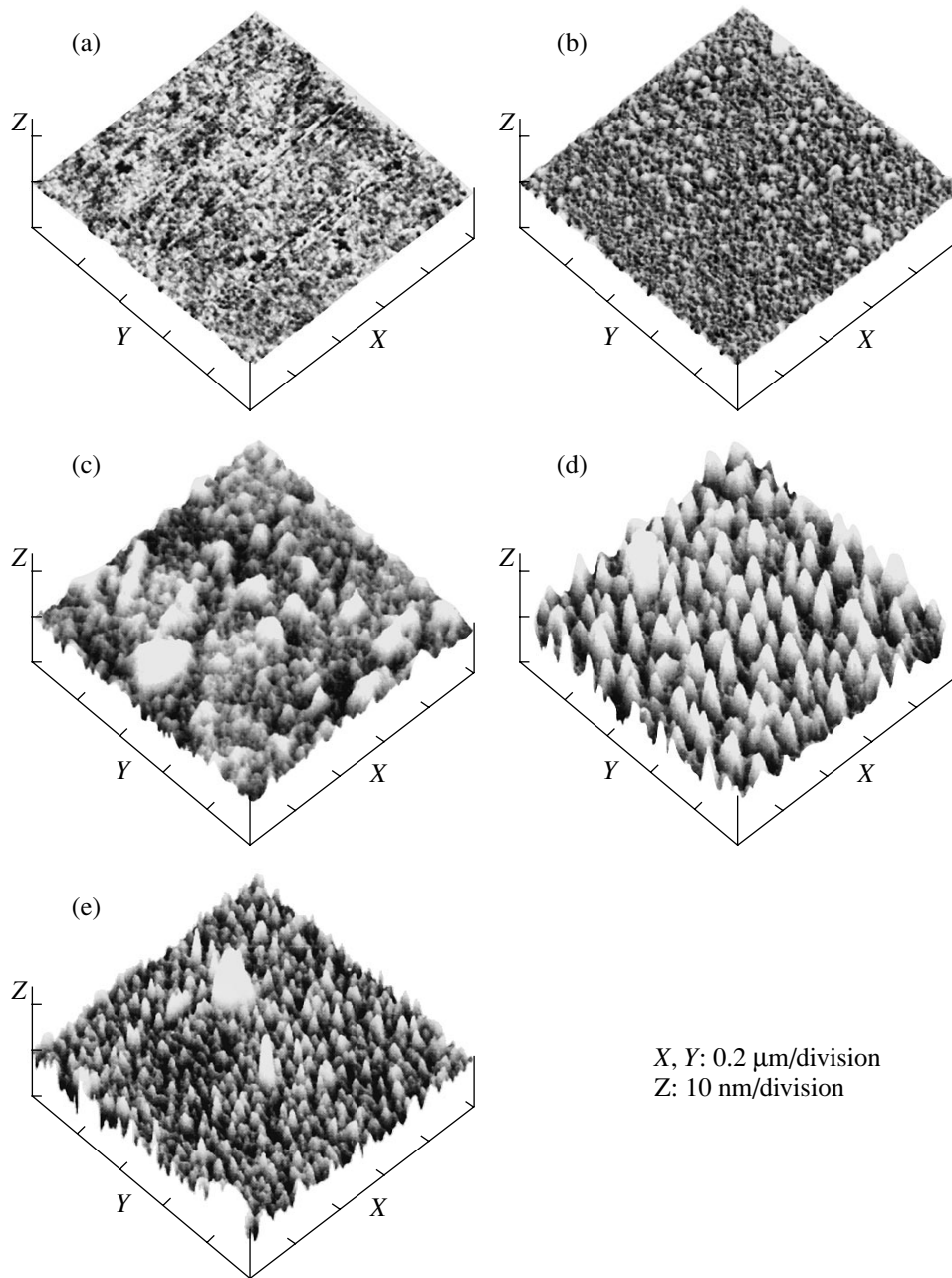
Fig. 1. AFM images of the surface of the p-CdTe crystal (a) prior to and (b–e) after the irradiation with a single laser-radiation pulse at a power density I = (b) 4, (c) 8, (d) 12, and (e) 16 MW/cm^2.

and an average height of ~(1.84–4.32) nm was randomly distributed over the crystal surface. Clearly formed structural elements uniformly distributed in density and with lateral sizes of ~(19–20) nm and an average height of ~(3.40–9.38) nm were observed in the region subjected to laser irradiation at a laser-radiation power density I_3 = 12 MW/cm^2 (Fig. 1d). The nanoclusters were dome-shaped and their density was 1.8×10^{10} cm^{-2}. The arithmetical mean surface roughness was 1.583 nm after such a treatment. In this case, we observed ordering of the nanostructural elements along

certain crystallographic directions in conjunction with the formation of a periodic surface profile. As the irradiation intensity increased to I_4 = 16 MW/cm^2, the density of the nanostructures increased. The lateral sizes of the clusters were ~(19–23) nm, and their height was ~(2.0–5.7) nm (Fig. 1e). The arithmetical mean surface roughness was ~0.870 nm.

Figure 2 shows an AFM image of a surface area 5 × 5 μm^2 in size and the Fourier transform of this image for the irradiated p-CdTe crystal. The Fourier transform

Z range: 94.9 nm

(a)

Z range: 99.7 µm

(b)
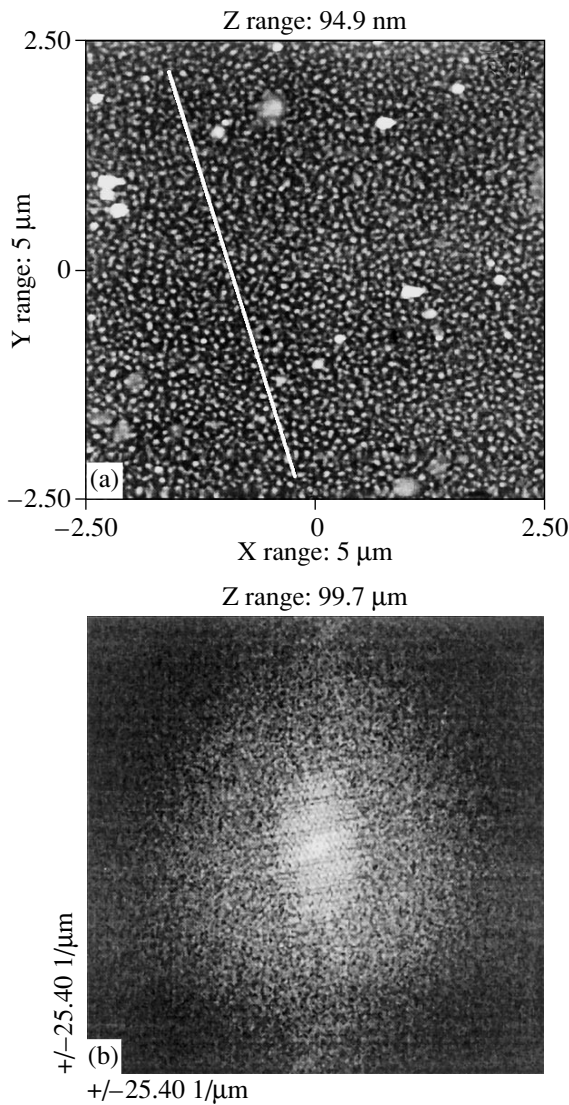
Fig. 2. (a) AFM image and (b) the Fourier transform of this image of the surface of the *p*-CdTe crystal after the irradiation with a single laser-radiation pulse at $I_3 = 12$ MW/cm^2.

shows that the nanoclusters form a homogeneous structure with a period of 100 nm on the crystal surface only in the region exposed to laser irradiation at a laser-radiation power density $I_3 = 12$ MW/cm^2 (Fig. 2b). In this case, the periodicity of the nanostructures preferentially manifests itself in one crystallographic direction (the inclined line in Fig. 2a).

The AFM study showed that the surface morphology, namely the cluster size and distribution, remained the same after the sample was kept in air for several days.

4. DISCUSSION

Nanodimensional clusterization (cluster diameter of 20 nm and height of 3 nm) has been observed on the surface of a CdTe layer grown by atomic epitaxy [4].

Marsal *et al.* [4] attributed the formation of these nanoclusters to the appearance of TeO$_2$ due to oxidation after storage in air. However, our results were not in agreement. First, the sizes and density of the structural elements were unchanged after being kept in air. Second, the structure shown in Fig. 1d was not observed on the surface of the CdTe crystals with Te film, even after several days of storage in air. Note that Te oxidizes in 3–4 days [5]. Our measurements of the Raman spectra show that the bands related to TeO$_2$ and CdTeO$_3$ are absent in the frequency region 500–800 cm^{-1} [2]. Taking into account these data and, also, the fact that a more volatile component (specifically, Cd) evaporates from the surface of CdTe crystals under irradiation, we can assume that our nanodimensional structures consist of a nonstoichiometric Cd$_{1-y}$Te$_y$ alloy formed under laser irradiation. We earlier showed that a thin layer of nonstoichiometric Cd$_{1-y}$Te$_y$ alloy was formed within the surface layer of a CdTe crystal under irradiation with radiation pulses from a ruby laser [6]. The formation of such a composition is caused by the fact that Cd atoms are preferentially removed from the surface layers of the CdTe crystal under irradiation with nanosecond laser pulses. Thus, the surface layer is depleted of Cd, and a polycrystalline Te film is formed on the crystal surface. A thin (12–15 nm) layer of the nonstoichiometric Cd$_{1-y}$Te$_y$ alloy is formed under the Te film. Note that irradiation of the CdTe crystal at a radiation-power density $I_3 = 12$ MW/cm^2 removes the Te film, which is apparently associated with dissolution of this film in the liquid CdTe phase.

Along with evaporation of the components of the crystal, the defect structure of the surface region of the crystal varies under the effect of nanosecond irradiation of the CdTe crystals [1, 2, 6]. A change in the defect structure depends heavily on the laser-radiation power density. As the laser-radiation power density increases, the concentration of defects (mainly, V_{Cd} and V_{Te}) increases in the crystal. This concentration is an externally controllable parameter [7, 8]. Estimation of the concentration of generated defects under laser irradiation of the CdTe crystals using a known formula [8] yields the value ~10^{19} cm^{-3}, which corresponds to the first critical concentration giving rise to screening of the elastic interaction of point defects. In this case, nanometer-sized defect clusters form via a second-order phase transition [7].

5. CONCLUSIONS

Thus, irradiation of *p*-CdTe crystals with a single nanosecond laser pulse substantially modifies their surface structure. Analysis of the experimental data allowed us to establish the optimal value of laser-radiation intensity at which periodic nanostructures with the smallest lateral sizes and a period of 100 nm are formed on the surface of the CdTe crystals.

REFERENCES

1. A. Baĭdullaeva, M. B. Bulakh, A. I. Vlasenko, *et al.*, Fiz. Tekh. Poluprovodn. (St. Petersburg) **38**, 26 (2004) [Semiconductors **38**, 23 (2004)].

2. V. V. Artamonov, A. Baĭdullaeva, A. I. Vlasenko, *et al.*, Fiz. Tverd. Tela (St. Petersburg) **46**, 1489 (2004) [Phys. Solid State **46**, 1533 (2004)].

3. B. M. Bulakh and S. M. Krasikova, Izv. Akad. Nauk SSSR, Neorg. Mater. **9**, 1112 (1973).

4. L. Marsal, H. Mariette, Y. Samson, *et al.*, Appl. Phys. Lett. **73**, 2974 (1998).

5. A. K. Gutakovskiĭ, V. M. Eliseev, R. I. Lyubinskaya, *et al.*, Poverkhnost, No. 9, 80 (1988).

6. V. N. Babentsov, A. Baĭdullaeva, A. I. Vlasenko, *et al.*, Fiz. Tekh. Poluprovodn. (St. Petersburg) **27**, 1618 (1993) [Semiconductors **27**, 894 (1993)].

7. V. I. Emel'yanov, Fiz. Tverd. Tela (St. Petersburg) **43**, 637 (2001) [Phys. Solid State **43**, 663 (2001)].

8. B. L. Volodin and B. I. Emel'yanov, Izv. Akad. Nauk SSSR, Ser. Fiz. **55**, 1274 (1991).

Translated by N. Korovin

SEMICONDUCTOR STRUCTURES, INTERFACES, AND SURFACES

Effect of a Submonolayer Metal Film on Band Bending in a Semiconductor Substrate

S. Yu. Davydov[1, 2^] and A. V. Pavlyk[2]

[1]Ioffe Physicotechnical Institute, Russian Academy of Sciences, St. Petersburg, 194021 Russia
[2]St. Petersburg State Electrotechnical University (LETI), St. Petersburg, 197376 Russia
^e-mail: sergei.davydov@mail.ioffe.ru
Submitted December 6, 2004; accepted for publication December 17, 2004

Abstract—Within the framework of the problem of band bending, the correlation between the bending induced by the adsorption of a submonolayer metal film at the surface of a semiconductor and the change in the work function of the system is established. The data on the adsorption of metals at *n*- and *p*-type GaAs and SiC substrates are analyzed. © 2005 Pleiades Publishing, Inc.

The problem of formation of a Schottky barrier at a metal–semiconductor interface has a long history, but no commonly accepted unambiguous solution has yet been found [1, 2]. In recent times, two models have been widely used, namely, the unified defect model [3] and the model of metal-induced states in the semiconductor band gap [4]. The defect model accounts, in particular, for pinning of the Fermi level and, as a consequence, for only small differences in the Schottky barrier height Φ_b for different metal components in contact with a certain semiconductor (see, e.g., [5–8]). In contrast, the model of metal-induced states can describe substantial variations in Φ_b when considering different metal components (see, for example, [9–13]). The predictions of both models have been confirmed experimentally.

The initial stages of the formation of Schottky barriers are of particular interest. If the metal film thickness is less than one or two monolayers, the film cannot be characterized by the work function ϕ_m of the metal bulk. Therefore, the Schottky rule

$$\Phi_b^n = \phi_m - \chi \quad \text{and} \quad \Phi_b^p = E_g - \Phi_b^n \tag{1}$$

cannot be used to define the barrier height Φ_b [2]. Here, the superscripts in the barrier height Φ_b denote the conductivity type of the substrate, ϕ_m is the work function of the metal, E_g is the band gap, and χ is the electron affinity of the semiconductor. In this case, we should consider band bending near the surface of the semiconductor V_s rather than the Schottky barrier.

As was shown in [14], the charge density Q_s at the surface of a semiconductor that contains completely ionized dopants in the bulk is related to V_s via the expression

$$Q_s = 2en_iL_{\mathrm{D}}R^{\pm}, \tag{2}$$
$$(R^{\pm})^2 = \gamma(e^{\pm\psi} - 1) + \gamma^{-1}(e^{\mp\psi} - 1) \pm \psi(\gamma^{-1} - \gamma).$$

Here, $\psi = V_s/k_{\mathrm{B}}T$, where the surface potential is $V_s > 0$; $\gamma = n/n_i = n_i/p$, where n_i, n, and p are the concentrations of intrinsic carriers, electrons, and holes, respectively; e is the elementary charge; k_{B} is the Boltzmann constant, and T is the temperature. The signs + and – in Eq. (2) correspond to upward (on adsorption at an *n*-type substrate) or downward (on adsorption at a *p*-type substrate) band bending (with respect to the direction into the bulk of the substrate). The parameter L_{D} is the Debye length for an intrinsic semiconductor:

$$L_{\mathrm{D}} = (\varepsilon_0 k_{\mathrm{B}}T/8\pi e^2 n_i)^{1/2}. \tag{3}$$

Here, ε_0 is the static permittivity.

In the problem of adsorption considered here, the surface charge density Q_s is formed by adatoms. In fact,

$$Q_s = e\Theta|Z|N_{\mathrm{ML}}, \tag{4}$$

where $\Theta = N/N_{\mathrm{ML}}$, N is the concentration of adatoms, N_{ML} is the concentration of adatoms in a monolayer, and Z is the charge of a single adatom. We take into account that the adsorption-induced variation in the work function $\Delta\phi$ is defined by the relation (see, e.g., [15])

$$\Delta\phi(\Theta) = -\Phi\Theta Z, \quad \Phi = 4\pi e^2 N_{\mathrm{ML}}\lambda, \tag{5}$$

where 2λ is the width of an electric double layer formed by the charged adatoms and their electrical images in the substrate. Then, the surface charge density Q_s can be expressed as

$$Q_s = |\Delta\phi|/4\pi e\lambda. \tag{6}$$

Equations (2)–(6) establish the relationship between semiconductor band bending and variation in the work function of the adsorption system. Unfortunately, we are aware of only two papers [16, 17] in which measurements of the work function in parallel with band bending as dependences of the degree of surface coverage were reported. In [16], the adsorption of alkali metals by n- and p-type GaAs was studied. In [17], a Cs/TiO$_2$ system was considered. In [18], the quantity $\Delta\phi(\Theta)$ was not measured. However, the authors of [18] considered the band bending resulting from adsorption of alkali metals (Na, K, Rb, and Cs) by n- and p-type GaAs (110) substrates at $T = 85$ K. In that case, no chemical reactions took place at the interface. It was shown, among other things, that the band bending $V_s^{n, p}$ was noticeably different in magnitude for n- and p-type substrates at $\Theta \ll 1$ but tended to the same value as Θ increased. We will discuss these results below.

We consider n- and p-type semiconductors, assuming that $\gamma_n = n/n_i \gg 1$, $\gamma_p = n_i/p \ll 1$, $\Psi_{n, p} = V_s^{n, p}/k_BT \gg 1$, and $\gamma_p^2 \exp\Psi_s^p \gg \Psi_s^p$. We use formulas (2) and (6) to obtain

$$V_s^{n, p}(\Theta) = 2k_BT\ln\left[\gamma_{n, p}^{\pm 1/2}\frac{|\Delta\phi^{n, p}|}{\Phi}\frac{N_{ML}}{2n_iL_D}\right], \qquad (7)$$

where the signs + and – refer to n and p types, respectively. However, if $\gamma_p^2 \exp\Psi_s^p \ll \Psi_s^p$, then

$$V_s^p = 2k_BT\ln\left[\gamma_p^{1/2}\frac{|\Delta\phi^p|}{\Phi}\frac{N_{ML}}{2n_iL_D}\right]. \qquad (8)$$

Let us make some estimations. The quantity $N_{ML} \approx 5 \times 10^{14}$ cm^{-2}. At $T = 85$ K, we have $E_g = 1.48$ eV [18], $m_{dn}/m = 0.068$, $m_{dp}/m = 0.5$ [14], and the product $n_iL_D \approx 3 \times 10^{-11}$ cm^{-2}. At $T = 300$ K, we have $E_g = 1.43$ eV and $n_iL_D \approx 4 \times 10^5$ cm^{-2}. The ratio $|\Delta\phi_{ML}|/\Phi$ ranges from 0.15 to 0.18 [19]. Hence, the arguments of the logarithms in (7) and (8) exceed unity for any reasonable values of γ_n and γ_p. (Of course, the case of $\Delta\phi^{n, p} = 0$, which corresponds to $V_s^{n, p} = 0$, is disregarded.)

According to [18], the inequality $V_s^n > V_s^p$ is satisfied over the entire range of degrees of coverage. This result immediately follows from a comparison of expressions (7) and (8) for n- and p-type substrates, respectively. Since the concentrations of Si donors and Zn acceptors are $N_d = 2.8 \times 10^{18}$ cm^{-3} and $N_a = 1 \times 10^{18}$ cm^{-3}, the inequality $V_s^n > V_s^p$ is satisfied for the case described by expression (7) as well. Note that, in accordance with expressions (2) and (6), we assume $V_s^{n, p} = 0$ if $\Theta = 0$

and $V_s^{n, p} = (V_s^{n, p})_{max}$ if $\Theta = 1$. In contrast, the authors of [18] take the value of $\tilde{V}_s^{n, p}$ at $\Theta = 0$ as the maximal band bend. It can easily be verified that $\tilde{V}_s^{n, p}(\Theta) = (V_s^{n, p})_{max} - V_s^{n, p}(\Theta)$.

As Θ increases, the surface potentials V_s^n and V_s^p grow, since $|\Delta\phi^{n, p}|$ increases. At $\Theta \longrightarrow 1$, the work function of the adsorption system, $\phi = \phi_s + \Delta\phi$, where ϕ_s is the work function of the semiconductor substrate, tends to the work function of the metal bulk ϕ_m and attains this value as soon as the second monolayer is formed. In this case, the values of V_s^n and V_s^p should approach each other and become nearly equal if $\gamma_n \approx \gamma_p^{-1}$. This was exactly the result observed in [18] under an increasing degree of coverage (see Fig. 4 in [18]). For two or three monolayers, it was found that $V_s^n \approx V_s^p$ and $V_s^n + V_s^p = E_g$.

Similar conclusions can be drawn by analyzing the detailed data available on contacts of various metals with p- and n-type 6H-SiC crystal [12, 20]. This data showed that, for carefully prepared contacts, the Schottky relation $\Phi_b^n + \Phi_b^p = E_g$ is satisfied to a high accuracy. Since $\Phi_b^n = V_s^n + \phi^n - E_C$ and $\Phi_b^p = V_s^p - \phi^p + E_V$, we have $\phi^p - \phi^n = V_s^p + V_s^n$. Assuming that $\phi^p \approx E_V$ and $\phi^n \approx E_C$, we obtain $V_s^p + V_s^n \approx E_g$.

Thus, a model of the states induced by adatoms allowed us to relate band bending to changes in the work function and in the height of a Schottky barrier.

REFERENCES

1. W. Mönch, Rep. Prog. Phys. **53**, 221 (1990).
2. T. Bechshtedt and R. Enderlein, *Semiconductor Surfaces and Interfaces. Their Atomic and Electronic Structures* (Akademie, Berlin, 1988; Mir, Moscow, 1990).
3. W. E. Spicer, W. Chye, P. R. Skeath, *et al.*, J. Vac. Sci. Technol. **16**, 1422 (1979).
4. V. Heine, Phys. Rev. **138**, A1689 (1965).
5. R. Ludeke, G. Jezequel, and A. Taleb-Ibrahimi, Phys. Rev. Lett. **61**, 601 (1988).
6. R. Ludeke, Phys. Rev. B **40**, 1947 (1989).
7. S. Yu. Davydov, A. A. Lebedev, O. V. Posrednik, and Yu. M. Tairov, Fiz. Tekh. Poluprovodn. (St. Petersburg) **35**, 1437 (2001) [Semiconductors **35**, 1375 (2001)].
8. S. Yu. Davydov, A. A. Lebedev, O. V. Posrednik, and Yu. M. Tairov, Fiz. Tekh. Poluprovodn. (St. Petersburg) **36**, 690 (2002) [Semiconductors **36**, 652 (2002)].
9. S. Yu. Davydov and Yu. M. Tikhonov, Fiz. Tverd. Tela (St. Petersburg) **37**, 2749 (1995) [Phys. Solid State **37**, 1514 (1995)].

10. V. van Elsbergen, T. U. Kampen, and W. Mönch, J. Appl. Phys. **79**, 316 (1996).

11. W. Mönch, Appl. Surf. Sci. **92**, 367 (1996).

12. J. R. Waldrop, J. Appl. Phys. **75**, 4548 (1994).

13. M. M. Anikin, A. N. Andreev, A. A. Lebedev, *et al.*, Fiz. Tekh. Poluprovodn. (Leningrad) **25**, 328 (1991) [Sov. Phys. Semicond. **25**, 198 (1991)].

14. V. L. Bonch-Bruevich, I. P. Zvyagin, I. V. Karpenko, and O. G. Mironov, *A Collection of Problems in the Physics of Semiconductors* (Nauka, Moscow, 1968) [in Russian].

15. S. Yu. Davydov, Fiz. Tverd. Tela (St. Petersburg) **46**, 1108 (2004) [Phys. Solid State **46**, 1141 (2004)].

16. J. E. Ortega and R. Miranda, Appl. Surf. Sci. **56–58**, 211 (1992).

17. A. W. Grant and C. T. Campbell, Phys. Rev. B **55**, 1844 (1997).

18. M. Preitsch, M. Domke, C. Laubschat, *et al.*, Z. Phys. B **74**, 21 (1989).

19. S. Yu. Davydov and A. V. Pavlyk, Zh. Tekh. Fiz. **74** (4), 98 (2004) [Tech. Phys. **49**, 475 (2004)].

20. J. R. Waldrop and R. W. Grant, J. Appl. Phys. **72**, 4757 (1992).

Translated by É. Smorgonskaya

Photoelectric Properties of Surface-Barrier Structures Based on $Zn_{2-2x}Cu_xIn_xSe_2$ Films Obtained by Selenization

V. Yu. Rud'**^, Yu. V. Rud'*, V. F. Gremenok***, E. P. Zaretskaya***, and O. N. Sergeeva***

*Ioffe Physicotechnical Institute, Russian Academy of Sciences, Politekhnicheskaya ul. 26, St. Petersburg, 194021 Russia
**St. Petersburg State Technical University, Politekhnicheskaya ul. 29, St. Petersburg, 195251 Russia
^e-mail: rudvas@spbstu.ru
****Institute of Solid-State and Semiconductor Physics, Belarussian Academy of Sciences,
ul. Brovki 17, Minsk, 220072 Belarus*
Submitted December 16, 2004; accepted for publication December 30, 2004

Abstract—p-$Zn_{2-2x}Cu_xIn_xSe_2$ (ZCIS) polycrystalline films 1–2 μm thick have been obtained by selenization. Photosensitive surface-barrier In/p-ZCIS structures are fabricated based on the films. The spectra of relative quantum efficiency of the structures obtained by selenization of the initial ZnSe/(Cu–In) and (Zn–Cu–In) films are examined. The optical band gap of the $Zn_{2-2x}Cu_xIn_xSe_2$ films is determined. Conclusions are reached on the prospects for the use of the obtained films as broadband photoconverters of natural optical radiation. © *2005 Pleiades Publishing, Inc.*

1. INTRODUCTION

Studies of the nearest crystallochemical analogues to II–VI compounds, whose formation can be clearly illustrated by a scheme involving the cross-substitutions of two Group II atoms of the Periodic system with Groups I and II atoms (2II ⟶ I + III), has led to synthesis of an extensive class of I–III–VI$_2$ ternary compounds [1, 2]. The study of ternary and more complex positionally ordered phases both solved the problem of extending the series of materials used in modern semiconductor electronics and resulted in progress in a number of relevant fields of electronics. For example, thin-film solar cells with unprecedentedly high efficiency (η = 19.2%) and extraordinary radiation stability have been fabricated based on Cu(In,Ga)Se$_2$ quaternary alloys with a chalcopyrite lattice [3–5]. For further improvement of the properties of such photoconverters, it is necessary to reveal the interrelations between technological approaches and the parameters of the structures and to use new alloys based on binary compounds.

This study is concerned with the fabrication and examination of the photosensitivity of structures based on $Zn_{2-2x}Cu_xIn_xSe_2$ (ZCIS) thin films, which were synthesized for the first time by selenization [6–9]. Such films were previously grown only by pulsed laser evaporation of synthesized (CuInSe$_2$)$_x$(2ZnSe)$_{1-x}$ targets. It is shown that a continuous series of solid solutions exists in the system and that the band gap varies from 2.67 eV (ZnSe) to 1.04 eV (CuInSe$_2$) [10, 11].

2. EXPERIMENTAL

A specific feature of selenization is the fact that the synthesis proceeds in an atmosphere of one of the most volatile components that form the selected system while the other components are deposited as thin films on a solid carrier, specifically, glass plates. As the temperature increases, the components of the films react with each other and with the coexisting vapor phase and, thus, form a uniform film of the required composition. Selenium is used for the vapor phase, and, as a result, this process was called selenization.

For fabrication of the $Zn_{2-2x}Cu_xIn_xSe_2$ films, we studied two variants of preparation of the initial components for selenization, which were deposited on a glass substrate surface. In one of these variants, we deposited ZnSe films and films consisting of a Cu–In mixture 0.6–0.8 μm thick on the surface of borosilicate glass plates. The ZnSe film was formed on the glass surface via vacuum sublimation of the compound from a separate Ta heater. The charge of powderlike ZnSe was determined from the requirement of providing the specified $Zn_{2-2x}Cu_xIn_xSe_2$ composition after selenization. The Cu–In films (with 99.999% purity) were deposited by thermal evaporation under a residual pressure of $\sim 7 \times 10^{-4}$ Pa at the glass substrate temperature $T_s \approx$ 100°C. Metals were deposited from a common molybdenum boat at an average rate of 0.05 μm/min. The Cu and In contents in the obtained film were determined from the charge of these metals, which was selected empirically.

Selenization of the thus prepared ZnSe/(Cu–In) structures was carried out using the interaction between the films during Se diffusion from the vapor phase. This process was performed in inert gas (N$_2$) in a furnace with a special temperature profile [9]. The ZCIS single-phase films were fabricated by a two-stage thermal treatment along with Se. At the first stage, selenization
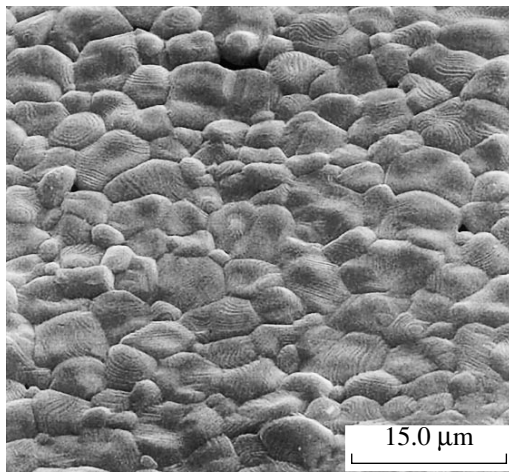
Fig. 1. Typical surface morphology of the $Zn_{2-2x}Cu_xIn_xSe_2$ films.

was carried out for substrates kept at 240–270°C for t = 10–30 min. At the second stage, the substrates were kept at 460–540°C for t = 15–40 min.

In the second variant of film synthesis, the Zn, Cu, and In charges were simultaneously evaporated from three sources and followed by a two-stage thermal selenization.

The structural properties and phase composition of the layers prior to and after selenization were studied by X-ray powder diffraction analysis in the angle range $2\theta = 15°–100°$ using CuK_α radiation with a Ni filter. The phases in the films were identified via comparison of the experimental interplanar spacings d with the data from the JCPDS tables [12]. The surface microprofile, microstructure, and transverse cleaved surfaces of the films were studied by scanning electron microscopy using an H-800 microscope (Hitachi, Japan) with a resolution of 0.2 nm. The elemental composition of the film material was determined by X-ray dispersion spectroscopy using a Stereoscan-360 system (UK) equipped with an AH 10000 EDX spectrometer (Link Analytic,

UK) with a resolution of 1 μm and sensitivity 0.1 at %. Qualitative and quantitative analyses of the elemental composition of the films was carried out using a PHI-660 scanning Auger microscope (Perkin-Elmer, USA) with a probe diameter of 0.1 μm and sensitivity of 0.1 at % and an IMS-4F ion microprobe (Cameca). The quantitative analysis was carried out by the method of high-purity standards, in which the intensity of the currents of the Auger electrons is corrected for the elemental sensitivity coefficient.

3. RESULTS AND DISCUSSION

The developed selenization conditions of the initial glass/ZnSe/(Cu–In) and glass/(Zn–Cu–In) structures allowed us to obtain ZCIS layers 1.0–2.0 μm thick and 10×10 mm² in area with a chalcopyrite lattice. These layers were similar to those obtained in [10, 11], where a substance was synthesized at a rather high temperature ($T \approx 1100°C$) and then deposited via laser evaporation. The X-ray powder diffraction analysis showed that the films obtained using both variants of selenization were uniform and had a lattice parameter corresponding to the bulk crystals [9, 10]. The crystal lattice of the ZCIS layers corresponded to an ordered chalcopyrite structure, which was confirmed by the presence of the typical reflections (112), (220/204), and (116/312), and the reflections of the chalcopyrite superlattice (101), (103), and (201).

The examinations allowed us to establish that the chemical composition of the $Zn_{2-2x}Cu_xIn_xSe_2$ films depended on the ratio between the initial components and the synthesis conditions. A typical surface microprofile and the chemical composition of certain ZCIS films obtained under the optimal conditions of selenization are shown in Fig. 1 and listed in Table 1. Figure 1 shows that the synthesized films have a dense structure formed by crystallites of more than 3 μm in size. The chosen selenization conditions provided a uniform distribution of the components over the layer thickness, which indicates that the interaction between the com-

Table 1. Composition and resistivity of the *p*-ZCIS films at T = 300 K

State of initial samples	Sample no.	Film composition after selenization						(Cu + In + Zn)/Se	ρ, Ω cm
		Molar fractions of components	Cu, at %	In, at %	Zn, at %	Se, at %			
Glass/ZnSe/(Cu–In)	Z4.1	$Cu_{0.92}In_{1.02}Zn_{0.18}Se_{1.88}$	22.95	25.56	4.49	47.00		1.128	1820
	2Z4.1	$Cu_{0.79}In_{0.85}Zn_{0.48}Se_{1.88}$	19.62	21.25	12.03	47.10		1.123	1680
	2Z4.1	$Cu_{0.79}In_{0.92}Zn_{0.40}Se_{1.89}$	19.65	22.99	10.04	47.32		1.113	5000
	3Z5.1	$Cu_{0.70}In_{0.82}Zn_{0.57}Se_{1.91}$	17.52	20.48	14.29	47.71		1.096	110
Glass/(Zn–Cu–In)	1ZK27	$Cu_{1.04}In_{0.89}Zn_{0.16}Se_{1.91}$	25.95	22.31	4.084	47.66		1.069	0.24
	1ZK28	$Cu_{0.85}In_{0.73}Zn_{0.49}Se_{1.93}$	21.18	18.14	12.36	48.32		1.026	56
	2ZK27	$Cu_{1.03}In_{0.90}Zn_{0.17}Se_{1.90}$	25.79	22.66	4.159	47.40		1.11	108
	2ZK28	$Cu_{0.80}In_{0.79}Zn_{0.39}Se_{2.02}$	19.85	19.73	9.919	50.61		0.976	150

ponents was complete and confirms the X-ray powder diffraction data. These data show that it is indeed possible to control the atomic composition of such films and vary the concentration ratio between the atoms occupying various sites in the chalcopyrite lattice. Table 1 also allows us to conclude that both the studied variants of preparation of the initial components for selenization yield practically identical homogenous $Zn_{2-2x}Cu_xIn_xSe_2$ thin films. In general, these studies show the potential of using selenization for obtaining thin films of quaternary selenides. Such technology can be used in the development of commercial methods for obtaining large-area films for employment as absorbing layers in thin-film solar cells.

According to the sign of the thermoelectric power, all the ZCIS films obtained by selenization exhibited p-type conductivity, similarly to the case of laser evaporation of a preliminary synthesized substance [11]. This circumstance does not contradict the assumption that the low-temperature interaction between the metals under the conditions of Se diffusion from the vapor phase preferentially causes the formation of acceptor lattice defects in such materials.

Table 1 also lists the resistivity ρ values of some of the $Zn_{2-2x}Cu_xIn_xSe_2$ alloy films obtained by selenization. It can be seen that the developed selenization conditions make it possible to vary the value of ρ in a rather wide range, specifically, from 0.2 to 500 Ω cm, at $T = 300$ K. Apparently, this wide range of variations in the film resistivity is caused by variations in their composition (Table 1), which shows that the film properties can be controlled by selecting the selenization parameters.

The initial studies of the contact phenomena for the $Zn_{2-2x}Cu_xIn_xSe_2$ films obtained by selenization led to observation of a photovoltaic effect at the contacts between the surface and pure In. The In thin films (~1 μm) were deposited on the surface of the ZCIS films by vacuum thermal deposition. As a rule, the photovoltage was at its highest when the barrier contact side of the In/p-ZCIS structures was illuminated; this contact was always negatively charged relative to the p-type films. This fact is consistent with the rectification direction in such structures.

The results of studies of the photovoltaic effect for typical structures based on ZCIS films obtained by selenization of two types of initial film structures, namely, glass/ZnSe/(Cu–In) and glass/(Zn–Cu–In) structures, are given in Table 2. It can be seen that the highest voltaic sensitivity S_U^m, which is always attained if the barrier-contact side of the obtained surface-barrier structures is illuminated, varies within the range of three orders of magnitude. For the best structures, $S_U^m = 1380$ V/W at $T = 300$ K. This value is substantially larger than that for similar structures based on $Zn_{2-2x}Cu_xIn_xSe_2$ films grown by pulsed laser evaporation of homogeneous bulk crystals of an identical composition [11]. The observed wide range of variation in

Table 2. Photoelectric properties of the In/p-$Zn_{2-2x}Cu_xIn_xSe_2$ surface-barrier structures ($T = 300$ K)

Sample no.	S_U^m, V/W	$\hbar\omega^m$, eV	$\hbar\omega'$, eV	$\delta_{1/2}$, eV	φ_b, eV	E_g^d, eV
Z4.1	8	1.3–2.0	0.95	1.8	0.85	0.95
2Z4.1	8	1.0–2.0	0.96	1.9	0.87	1.20
2Z4.1	1380	1.3–1.7	1.05	2.4	0.95	1.02
3Z5.1	60	1.3–2.2	1.03	2.5	0.93	1.00
1ZK28	160	1.7–2.4	1.02	2.5	0.94	1.23
2ZK28	360	1.6–1.8	1.03	2.0	0.95	1.21

the value of S_U^m for the obtained structures should be related to variations in the film composition (Table 1), the structure of the film systems prior to selenization, etc. This issue is rather complicated and requires detailed studies of the interrelation between the technology and the properties of the films grown.

The spectra of the relative quantum efficiency of photoconversion $\eta(\hbar\omega)$ for typical In/p-ZCIS structures fabricated using the two variants of preparation of the initial film system on a glass substrate for selenization are shown in Figs. 2 and 3. Certain photoelectric parameters of these structures and semiconductors forming the basis of their fabrication are given in Table 2.

The main results of our studies of the obtained In/p-ZCIS structures are the following. The use of two variants of preparation of the initial films on glass substrates for selenization does not introduce any substantial distinctions into the spectral dependences of photo-
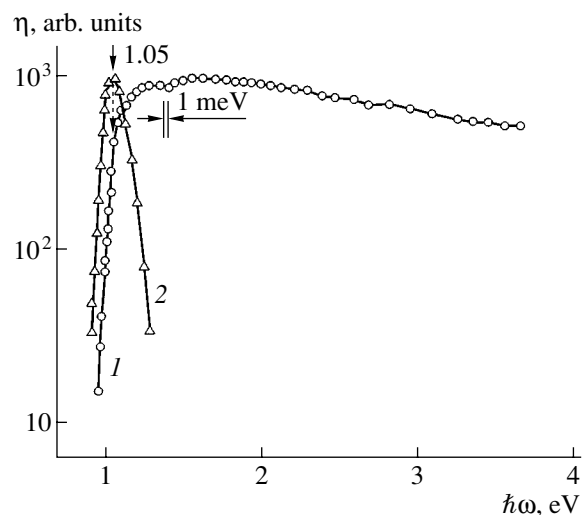

Fig. 2. Spectral dependences of the relative quantum efficiency of photoconversion for the In/p-ZCIS structure (sample no. 3Z4.1) in nonpolarized radiation under illumination of the barrier contact (curve *1*) and of the ZCIS film (curve *2*) at $T = 300$ K. The film was obtained by selenization of a glass/ZnSe/(Cu–In) sample.
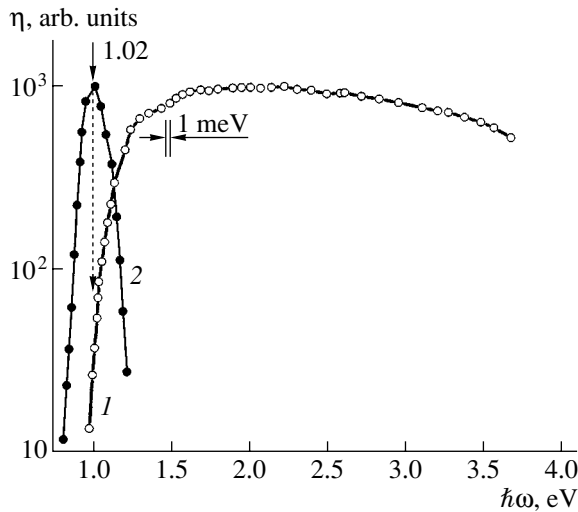
Fig. 3. Spectral dependences of the relative quantum efficiency of photoconversion for the In/*p*-ZCIS structure (sample no. 1ZK28) in nonpolarized radiation under illumination of the barrier-contact side (curve *1*) and of the ZCIS-film side (curve *2*) at $T = 300$ K. The film was obtained by selenization of a glass/(Zn–Cu–In) sample.

Fig. 4. Dependences $(\eta\hbar\omega)^{1/2} = f(\hbar\omega)$ (curves *1–3*) and $(\eta\hbar\omega)^2 = f(\hbar\omega)$ (curves *4–6*) for the In/*p*-ZCIS structures at $T = 300$ K. Curves *1* and *4* correspond to sample 3Z5.1, curves *2* and *5* correspond to sample 3Z4.1, and curves *3* and *6* correspond to sample 1ZK28.

sensitivity of the structures obtained (Figs. 2, 3). It can be seen that the photosensitivity sharply increases under illumination of the barrier-contact side of the structures for the photon energy $\hbar\omega \geq 0.90$–0.95 eV. This increase follows the exponential law to energies as high as $\hbar\omega'$ and exhibits a steep slope $S = \dfrac{\delta(\ln\eta)}{\delta(\hbar\omega)} = 30$–$40$ eV^{-1}. On the basis of [13, 14], we can assume the existence of direct band-to-band optical transitions in the thin-film quaternary phases whose atomic composition is given in Table 1. Deviations from the exponential law in the spectrum $\eta(\hbar\omega)$ emerge at the photon energy $\hbar\omega'$, which is indicated in Table 2 and by arrows in Figs. 2 and 3. The full width of the spectra $\eta(\hbar\omega)$ at the half-height $\delta_{1/2}$ points to a broadband spectrum of photoconversion in barriers based on the obtained polycrystalline films. For the best structures, $\delta_{1/2} \approx 2.5$ eV (Table 2). The highest value of the relative quantum efficiency of photoconversion for the best structures is also attained in a wide spectral range (the quantity $\hbar\omega^m$ in Table 2). It is clearly seen from Figs. 2 and 3 that the high photosensitivity of barriers based on the phases obtained by selenization manifests itself in a wide spectral range, specifically, from 1.3 to 3.6 eV. These values substantially exceed similar data for structures based on films obtained by laser evaporation [11]. In our opinion, this circumstance provides evidence of the higher crystal quality of the $Zn_{2-2x}Cu_xIn_xSe_2$ thin films obtained by selenization.

Figures 2 and 3 (curves *2*) clearly show that, if the semiconductor-film side (instead of the barrier-contact side) of the Schottky barriers is illuminated, the spectra $\eta(\hbar\omega)$ become highly selective. In this case, $\hbar\omega^m \approx \hbar\omega'$,
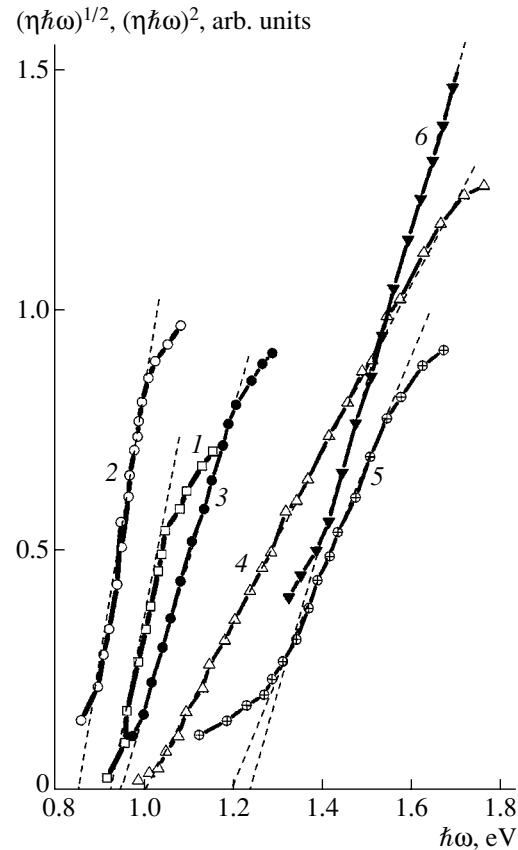
and $\delta_{1/2} \approx 0.15$–$0.25$ eV for various structures. The abrupt short-wavelength falloff in the photosensitivity of the structures is associated with the emergence of strong optical absorption in the films as $\hbar\omega'$ is approached; this effect is related to the onset of direct band-to-band transitions. As a result, the layer of photogenerated pairs recedes from the active area of the structures, which leads to the emergence of an abrupt short-wavelength falloff of η at $\hbar\omega > \hbar\omega'$ in this photodetection geometry. The analysis of the spectra $\eta(\hbar\omega)$ of the structures obtained showed that the short-wavelength portion of the spectra follows the Fowler law $(\eta\hbar\omega)^{1/2} = f(\hbar\omega)$, which is characteristic of Schottky barriers (Fig. 4, curves *1–3*) [15]. The extrapolation of these dependences $(\eta\hbar\omega)^{1/2} \longrightarrow 0$ yields the potential barrier height φ_b (Table 2).

The short-wavelength portion of the spectra of the relative quantum efficiency of photoconversion for the structures studied, as can be seen from Fig. 4 (curves *4–6*), follows the quadratic dependence $(\eta\hbar\omega)^2 = f(\hbar\omega)$. Therefore, this dependence can be attributed to direct band-to-band transitions [15, 16], as in the case of the $CuInSe_2$ compound [2]. Extrapolation of the type

$(\eta\hbar\omega)^2 \longrightarrow 0$, as can be seen from Fig. 4 (curves *4–6*), yields the cutoff energy. In turn, according to [15, 16], this energy allows us to determine the band gap E_g^d of the $Zn_{2-2x}Cu_xIn_xSe_2$ films grown by selenization (Table 2). Since the Zn concentration range in the ZCIS films obtained by selenization is very narrow (Table 1), it is impossible to analyze the band gap E_g^d as a function of the film composition. We can only note that a tendency towards an increase in the value of E_g^d is evident for the films obtained relative to a positionally ordered $CuInSe_2$ compound with a near-stoichiometric composition [2, 17]. It is also noteworthy that the largest values, $E_g^d \approx 1.27$ eV (Table 2), for the ZCIS films obtained by selenization are close to those for the $Cu(In,Ga)Se_2$ layers used in solar cells. Currently, these layers have the highest photoconversion efficiency [17].

4. CONCLUSIONS

$Zn_{2-2x}Cu_xIn_xSe_2$ thin films were grown by a two-stage temperature annealing in a mixture of Se vapor and inert gas (N_2). The developed modes of selenization of the initial glass/ZnSe/(Cu–In) and glass/(Zn–Cu–In) structures allowed us to obtain p-ZCIS layers with a chalcopyrite structure 1.0–2.0 μm thick. On the basis of these obtained $Zn_{2-2x}Cu_xIn_xSe_2$ films, In/p-ZCIS thin-film surface-barrier photosensitive structures were fabricated. The studies carried out showed that the structures obtained can be used for the development of broadband photoconverters of nonpolarized radiation whose long-wavelength edge of photosensitivity can be controlled by the technology parameters of the process of obtaining the $Zn_{2-2x}Cu_xIn_xSe_2$ thin films.

ACKNOWLEDGMENTS

REFERENCES

1. N. A. Goryunova, *The Chemistry of Diamond-like Semiconductors* (Leningr. Gos. Univ., Leningrad, 1963; Chapman and Hall, London, 1965).

2. J. L. Shay and J. H. Wernick, *Ternary Chalcopyrite Semiconductors: Growth, Electronic Properties and Applications* (Pergamon, Oxford, 1975).

3. H. W. Schock and R. Noufi, Prog. Photovoltaics **39**, 151 (2000).

4. U. Rau and H. W. Schock, Ser. Photoconvers. Solar Energy **1**, 277 (2001).

5. K. Ramanathan, M. A. Contreras, C. L. Perkins, *et al.*, Prog. Photovolt. Res. Appl. **11**, 225 (2003).

6. B. M. Basol and V. K. Kapur, in *Proceedings of 21st IEEE Photovoltaic Specialists Conference* (IEEE, New York, 1990), p. 546.

7. T. Wada, T. Megami, and M. Nishitani, Jpn. J. Appl. Phys. Suppl. **32** (2), 41 (1993).

8. A. Gupta, T. Ohno, T. Karia, *et al.*, Jpn. J. Appl. Phys. Suppl. **32** (3), 74 (1993).

9. V. F. Gremenok, E. P. Zaretskaya, O. N. Sergeeva, *et al.*, Poverkhnost: Rentgen. Sinkhrotron. Neĭtron. Issled. **7**, 45 (2004).

10. V. F. Gremenok, W. Schmitz, I. V. Bodnar, *et al.*, Jpn. J. Appl. Phys. Suppl. **39** (1), 277 (2000).

11. V. Yu. Rud', Yu. V. Rud', R. N. Bekimbetov, *et al.*, Fiz. Tekh. Poluprovodn. (St. Petersburg) **34**, 576 (2000) [Semiconductors **34**, 558 (2000)].

12. *Powder Diffraction File, Joint Committee on Powder Diffraction Standards* (ASTM, Philadelphia, PA, 1998).

13. V. Yu. Rud' and Yu. V. Rud', Fiz. Tekh. Poluprovodn. (St. Petersburg) **31**, 1336 (1997) [Semiconductors **31**, 1151 (1997)].

14. V. Yu. Rud' and H. W. Schock, Solid State Phenom. **67–68**, 391 (1999).

15. S. M. Sze, *Physics of Semiconductor Devices*, 2nd ed. (Wiley, New York, 1981; Mir, Moscow, 1984), Vol. 2.

16. Yu. I. Ukhanov, *Optical Properties of Semiconductors* (Nauka, Moscow, 1977) [in Russian].

17. V. Yu. Rud', Yu. V. Rud', V. F. Gremenok, and G. A. Il'chuk, Pis'ma Zh. Tekh. Fiz. **30** (18), 21 (2004) [Tech. Phys. Lett. **30**, 762 (2004)].

Translated by N. Korovin

Simulation of Special Features of the Drift-Mobility Saturation in Submicrometer Silicon Structures

V. A. Gergel', Yu. V. Gulyaev, and M. N. Yakupov^

Institute of Radio Engineering and Electronics, Russian Academy of Sciences, ul. Mokhovaya 18, Moscow, 125009 Russia
^e-mail: yamt@mail.ru

Abstract—Special characteristics of the high-field drift of electrons in submicrometer n^+–n–n^+ structures are studied by mathematical simulation methods in the quasi-hydrodynamic approximation. Alternative dependences of the mobility and energy-relaxation time on the electron temperature are used to calculate the profiles of the potential, temperature, drift mobility, and density of the thermal-energy flux of electrons. It is shown that, in a submicrometer configuration, a large part of the thermal energy acquired by an electron in a high-resistivity n-type region is dissipated in a low-resistivity n^+-type contact. This effect reduces the rate of increase in the electron temperature in the drift region as the voltage increases, brings about an increase in the effective mobility, and prevents saturation of the drift velocity, as is shown by the calculated current–voltage characteristics. © 2005 Pleiades Publishing, Inc.

The saturation of the charge-carrier drift mobility in silicon and other semiconductors was recognized even at the outset of the development of semiconductor physics [1] and was interpreted [2] as a manifestation of the field dependence of the mobility, for example,

$$\mu = \mu_0 \left[1 + \left(\frac{E}{E_S} \right)^2 \right]^{-1/2}. \tag{1}$$

Here, $\mu_0 \approx 1500$ cm^2/(V s) is a low-field mobility and the characteristic field $E_S = v_S/\mu_0 \approx 0.7 \times 10^4$ V/cm, where $v_S \approx 10^7$ cm/s is the saturation velocity. In turn, the field dependence of mobility is treated [3] as a manifestation of the corresponding dependence of the mobility on the electron temperature T. This temperature increases when the electric field is strengthened as a result of Joule heating of the electron subsystem and is determined from the well-known condition for the energy balance that corresponds to compensation of Joule heating by the transfer of excess thermal electron energy to the phonon subsystem of the crystal; i.e., we have

$$j_n E = \mu n E^2 = \frac{n(T - T_0)}{\tau_e}, \tag{2}$$

$$T = T_0 + \mu(T)\tau_e(T)E^2, \tag{3}$$

where n is the electron concentration; τ_e is the energy-relaxation time; and T_0 is the lattice temperature, which, it is assumed, corresponds to the equilibrium state.

Equation (2) is then rewritten under the assumption that the temperature dependences of the mobility and relaxation time follow the power law:

$$\mu = \mu_0 \left(\frac{T_0}{T} \right)^\alpha, \quad \tau_e = \tau_0 \left(\frac{T}{T_0} \right)^\beta, \tag{4}$$

$$T = T_0 + \left(\frac{T_0}{T} \right)^{\alpha - \beta} \mu_0 \tau_0 E^2. \tag{5}$$

It is worth noting that, in (4) and (5), only the quantity μ_0 can be considered as a well-defined physical parameter (determined from experiments and from microscopic-scale description of the momentum relaxation), whereas the value of the exponent α is determined to a lower accuracy, since only theoretical estimates obtained under the condition of absolute prevalence of a particular scattering mechanism exist. The quantities τ_0 and β, which effectively describe a complex combination of various multiphonon processes of the electron-energy relaxation, are in fact adjustable parameters whose numerical values should ensure the required asymptotic behavior of the mobility in high fields $\mu \longrightarrow v_S/E$. This requirement yields the expression $\tau_0 = \mu_0 T_0 / v_S^2$ and the well-known relation between the exponents $\beta = 1 - \alpha$. It is noteworthy that the pair $\{\beta = 1/2, \alpha = 1/2\}$ is the most physically reasonable of all the feasible combinations of these exponents and corresponds to the mechanism of scattering of momentum by acoustic phonons. In contrast, the pair $\{\beta = 0, \alpha = 1\}$ does not feature an unambiguous physical inter-

pretation like the pair above but yields the field dependence of mobility

$$\mu = \mu_0 \left[\frac{1}{2} + \sqrt{\frac{1}{4} + \left(\frac{E}{E_S}\right)^2} \right]^{-1}, \quad (6)$$

which, from the standpoint of a comparison with the experimental dependences of the drift mobility on the electric field, is practically no different from the corresponding dependence yielded by formula (1) with {1/2, 1/2}.

It was expected, at the initial stage of submicrometer-technology development, that the drift-velocity saturation under consideration would appreciably limit the characteristics of submicrometer transistors, in the active regions of which ultrahigh electric fields on the order of 10^5 V/cm appear. However, it was found that the effect of the drift-velocity saturation was largely suppressed in submicrometer structures; as a result, in present-day models of transistor structures, formulas (1) and (6) with $E_S \approx 10^5$ V/cm (which would correspond to the very high saturation velocities $\sim 10^8$ cm/s) are used.

It is self-evident that this remarkable behavior of the electron subsystem in submicrometer structures is caused by the corresponding lag in the heating of electrons, which manifests itself in a situation where the time of flight of electrons over the distance between the low-resistivity contact regions becomes comparable to the energy-relaxation time. This lag manifests itself under steady-state conditions in the nonlocality of the thermal balance in the case where an appreciable fraction of the electron thermal energy acquired in the high-resistivity flight region is dissipated in the low-resistivity contact region. In order to adequately take into account the above nonlocality, we should supplement condition (2) with the corresponding divergence of the heat flow and, thus, formulate the so-called quasi-hydrodynamic model of electron transport, which is similar to the model suggested by Stratton in his pioneering publication [4].

To date, quite a number of studies concerned with a quasi-hydrodynamic simulation of the electron drift have been published (see, e.g., [5]). However, the incompleteness of the numerical simulation results reported in these publications makes it impossible to reveal the distinctive physical special features in the resulting current–voltage (I–V) characteristics that can be used when comparing these results with experimental data and verifying the parameters of the employed models of mobility. The identification of these specific features of the high-field drift in submicrometer structures is precisely the aim of this study. We intend to attain this aim by comparing the results of a simulation (that consecutively complicates the drift description) and using both the alternative models of mobility with $\alpha = 1/2$ or $\alpha = 1$.

As the subject of our simulation, we used the simplest possible silicon n^+–n–n^+ structure with a drastic difference in its impurity concentration ($10^{19}/10^{18}$ cm^{-3})

and the extent of the high-resistivity region $L_1 = 0.25$ μm. Correspondingly, we can write the expressions for the electron-density flux

$$j_n = \mu_\alpha n \left[\frac{d\phi}{dx} - (1 - \alpha)\frac{dT}{dx} \right] - \mu_\alpha T \frac{dn}{dx} \quad (7)$$

and the electron-temperature flux

$$j_T = \left(\frac{5}{2} - \alpha\right)\left(\mu_\alpha n T \frac{dT}{Dx} + j_n T\right) \quad (8)$$

in the clearest form. Here, ϕ is the potential and T is the electron temperature expressed in energy units.

Under steady-state conditions, a system consisting of a Poisson equation and equations of current continuity and thermal balance is written as

$$\begin{cases} \dfrac{d^2\phi}{dx^2} = \dfrac{(N-n)}{L_D^2}\dfrac{T_0}{N_D^+}, \\[2ex] \dfrac{dj_n}{dx} = 0, \\[2ex] \dfrac{dj_T}{dx} = j_n\dfrac{d\phi}{dx} - \dfrac{n(T-T_0)}{\tau}, \end{cases} \quad (9)$$

where N and N_D^+ are the donor concentrations in the n- and n^+-type layers, respectively;

$$L_D = \sqrt{\frac{\varepsilon\varepsilon_0 T_0}{q_e N_D^+}}$$

is the Debye length; and $\varepsilon\varepsilon_0$ is the permittivity.

Introducing the dimensionless quantities $x \longrightarrow x/L_D$, $\phi \longrightarrow \phi/T_0$, $T \longrightarrow T/T_0$, and $N \longrightarrow N/N_D^+$ for the donor concentration, and $n \longrightarrow n/N_D^+$ for the electron concentration, we can rewrite Eqs. (9) as

$$\begin{cases} \dfrac{d^2\phi}{dx^2} = (N-n), \\[2ex] \dfrac{dj_n}{dx} = 0, \\[2ex] \dfrac{dj_T}{dx} = j_n\dfrac{d\phi}{dx} - \dfrac{n(T-T_0)}{N_D^+\tau\mu_0}. \end{cases} \quad (10)$$

In order to discretize system of Eqs. (10), we use the method of integral identities:

$$\begin{cases} \left(\dfrac{d\phi}{dx}\right)^{i+1} - \left(\dfrac{d\phi}{dx}\right)^i = (N-n)0.5(a_i + a_{i+1}), \\[2ex] j_n^{i+1} - j_n^i = 0, \\[2ex] j_T^{i+1} - j_T^i = \left[j_n^i\left(\dfrac{d\phi}{dx}\right)^i - \dfrac{n(T-T_0)}{N_D^+\tau\mu_0} \right]0.5(a_i + a_{i+1}). \end{cases} \quad (11)$$
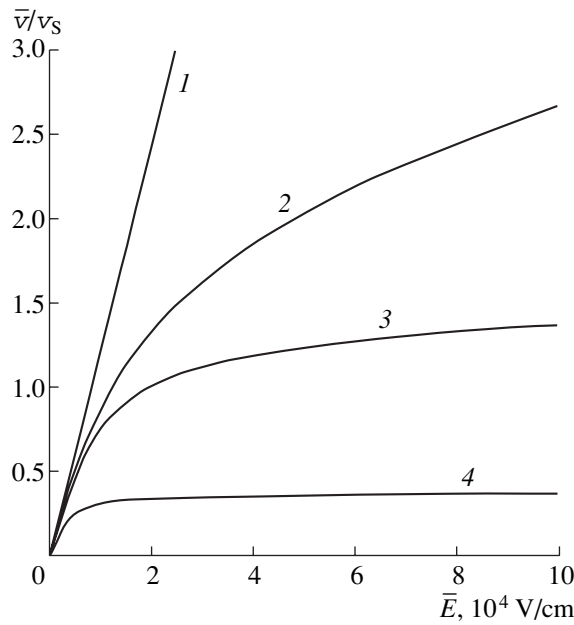
Fig. 1. Current–voltage characteristics of an n^+–n–n^+ structure in the models of (*1*) constant mobility, (*2*, *3*) energy transport, and (*4*) local temperature. $L_1 = 0.25$ μm and $T_0 = 0.025$ eV.
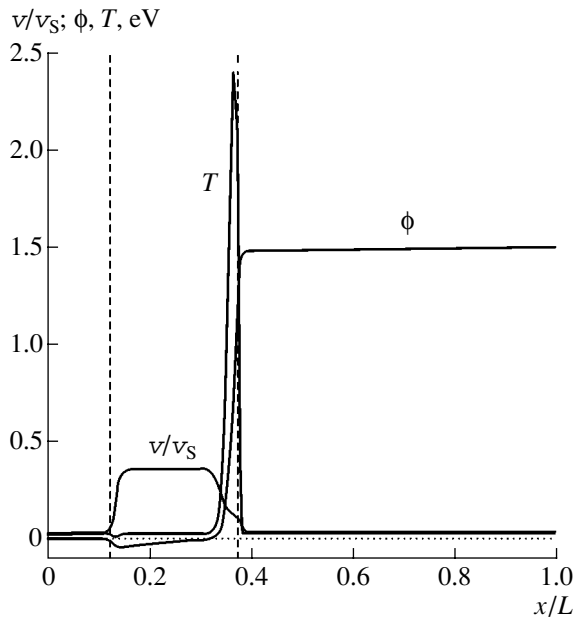

Fig. 2. Typical distributions of the potential ϕ, electron temperature T, and drift velocity v in the local-temperature approximation. $V = 1.5$ V and $T_0 = 0.025$ eV.

Here,

$$a_i = x_i - x_{i-1}, \quad \left(\frac{d\phi}{dx}\right)^i = \phi_i - \phi_{i-1},$$

and the densities of the electron current and thermal flux are given by

$$j_n^i = \mu_\alpha^i n^i \left[\left(\frac{d\phi}{dx}\right)^i - (1-\alpha)\left(\frac{dT}{dx}\right)^i\right] - \mu_\alpha^i T^i \left(\frac{dn}{dx}\right)^i,$$

$$j_T^i = \left(\frac{5}{2} - \alpha\right)\left[\mu_\alpha^i n^i T^i \left(\frac{dT}{dx}\right)^i - j_n^i T^i\right],$$

(12)

where

$$\left(\frac{dn}{dx}\right)^i = n_i - n_{i-1}, \quad \left(\frac{dT}{dx}\right)^i = T_i - T_{i-1}.$$

System of Eqs. (11) should be supplemented with boundary conditions at $x = 0$ and $x = L$:

$$\phi(0) = 0, \quad \phi(L) = V,$$
$$T(0) = T(L) = T_0.$$

(13)

Here, V is the voltage applied to the structure, T_0 is the lattice temperature, $N_D^+ = 10^{19}$ cm^{-3} is the donor concentration in the n^+-type layer, and $L = 1$ μm is the dimension of the structure under consideration with allowance for n^+-type contact regions.

System of Eqs. (11) with boundary conditions (13) was solved using a modified Newton method. We used a uniform impurity distribution combined with a gradual transition to abrupt n–n^+ boundaries as the initial approximation. In addition, calculation of the corresponding distributions and currents for the sequence of test voltages in the range 0–2.5 V began from small values. For each successive value of the voltage, the appropriately corrected final approximation of the preceding step was used as the initial approximation for the potential. This procedure assures a reasonably good convergence of the iterative process; specifically, we had to use no more than five to six Newton iterations for each new value of the applied voltage V.

In Fig. 1, we show the calculated *I–V* characteristics represented, for clarity, as the dependence of the average relative velocity $\dfrac{\overline{v}}{v_S} = \dfrac{j_n}{q N_D v_S}$ on the average field $\overline{E} = \dfrac{V}{0.26L}$. Curve *1* corresponds to the drift model for the constant mobility $\mu = \mu_0 = 1500$ cm^2/(V s); curve *4* corresponds to the drift–diffusion approximation for a local temperature; and curves *2* and *3* correspond to the quasi-hydrodynamic models for $\alpha = 1/2$ and 1, respectively.

It is worth noting that a clearly pronounced saturation effect is exhibited only in curve *4*, which corresponds to the local-heating model. In this model, however, the effective saturation velocity is equal to ~3 × 10^6 cm/s; i.e., it is a factor of 3 lower than the initial saturation velocity $v_S = 10^7$ cm/s. The inadequacy of the model including local heating in regard to submicrome-
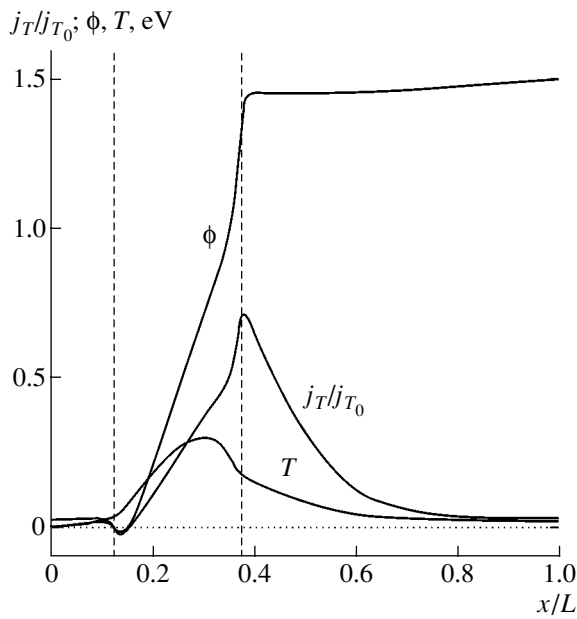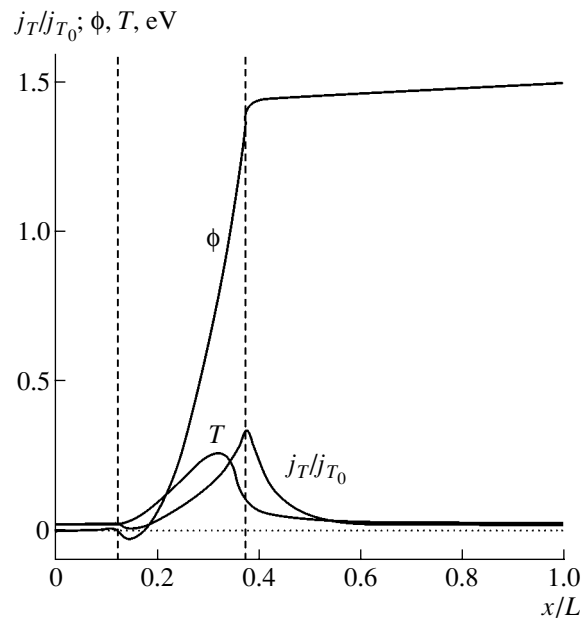
Fig. 3. Distributions of the potential ϕ, electron temperature T, and thermal-flux density j_T in the quasi-hydrodynamic approximation with $\mu \propto T^{-1/2}$.

Fig. 4. Distributions of the potential ϕ, electron temperature T, and thermal-flux density j_T in the quasi-hydrodynamic approximation with $\mu \propto T^{-1}$.

ter structures is illustrated by the curves in Fig. 2, where the distributions of the potential, temperature, and local charge-carrier velocity at $V = 1.5$ V are shown; the boundaries of the drift region with $N_D = 10^{18}$ cm^{-3} are indicated by vertical dashed lines. These results show that consideration of the diffusion-related component of the current in the context of the model involving local heating leads to an appreciable redistribution of the potential in the n-type region and to formation of a so-called static high-field domain at the anode. The main part of the applied voltage and an anomalously high electric field and electron temperature are concentrated in this region. However, the large gradient of increase in the electron concentration in this domain gives rise to a considerable diffusive counterflow, which is exactly what causes the resulting difference of the effective charge-carrier velocity from v_S. In our opinion, the fact that the average thermal energy of electrons in the domain is found to be higher than the energy supplied by the applied voltage most clearly indicates that approximation of the local temperature is inadequate.

Figures 3 and 4 illustrate the main results of this study corresponding to the hydrodynamic consideration of the electron drift. The distributions of the potential, temperature, and energy-flux density are shown in relative units in Figs. 3 and 4. These distributions correspond to the model of energy transport under the alternative variants with $\alpha = 1/2$ and $\alpha = 1$. The following specific properties can be mentioned: relative uniformity of the temperature profile in the high-resistivity n-type region, a characteristic shift of the peak to

the anode in the temperature distributions, and a noticeable penetration of hot electrons into the n^+-type anode contact. This penetration means that an appreciable fraction of the electrons heated in the high-resistivity part of the structure dissipate their excess thermal energy in the n^+-type contact bulk.

It is worth noting that the energy dissipation in the contact region brings about a shift of the temperature peak by a significant distance from the n–n^+ boundary. The first term in formula (8) corresponds to the thermal-conductivity component of the electron-temperature flux and plays an important role in the quasi-hydrodynamic models. It is this term that gives rise to the strange (at first sight) effect of a decrease in the temperature in the near-anode region while the temperature flux continues to increase until it reaches the geometric boundary of the contact, as is shown, at a high magnification, in Fig. 5. We can also mention, as a positive factor, the fact that the highest electron temperature in both cases amounts to approximately a fifth of the potential, whereas, according to the simplified (convective) model used in our previous study [6], we would expect an appreciably higher temperature $T \approx V/2$.

Comparing the results of calculations based on the above alternative models of mobility, we can only note that the model with $\alpha = 1/2$ yields somewhat higher temperatures in the drift region and a higher drift mobility. In the model with $\alpha = 1$ and a constant relaxation time, we obtain a lower charge-carrier velocity owing to the heavier temperature dependence of the carrier mobility. It should be emphasized that the qualitative closeness of the calculation results from both
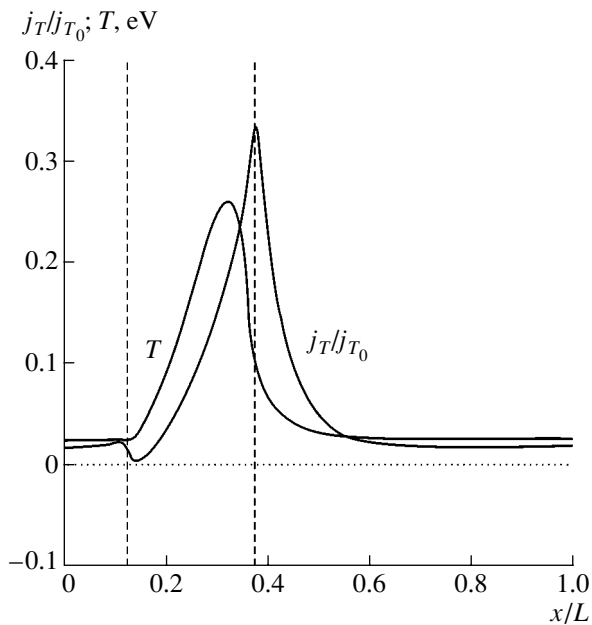
Fig. 5. Characteristic shift of distributions of the electron temperature T and thermal-flux density j_T caused by the electron thermal conductivity.
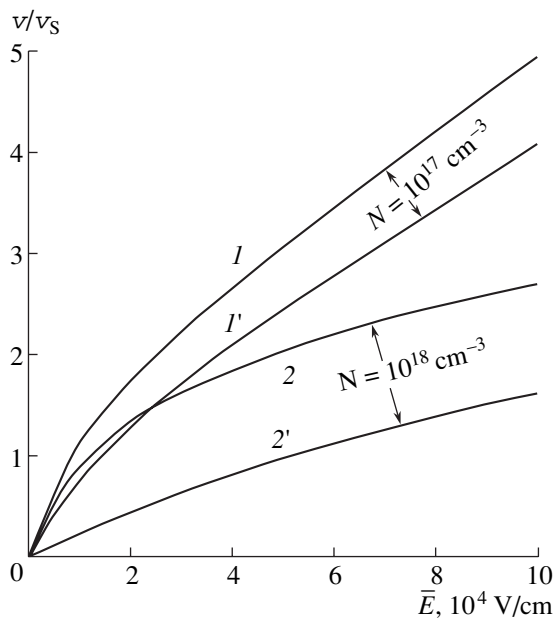

Fig. 6. Current–voltage characteristics calculated taking into account the dependence of mobility on the donor concentration. The calculations were carried out (*1*, *2*) disregarding and (*1'*, *2'*) taking into consideration scattering by impurities.

mobility models makes it impossible to give any physically justified preference to one of these models. The best choice of model can be probably made in future using the results of corresponding experiments.

In this context, we considered it worthwhile to increase the complexity of the description of the high-field drift in the energy-transport model by including the mechanism of the electron scattering by charged impurities in our consideration using the interpolation formula

$$\mu = \mu_0\left[\left(\frac{N}{10^{17}}\right)+\left(\frac{T}{T_0}\right)^{2\alpha}\right]^{-1/2}, \qquad (14)$$

which, in general, is close to the dependence suggested by Hänsch [7]. It is important that, in Eq. (7), α should be replaced with $\dfrac{\partial \ln \mu}{\partial \ln T}$. The corresponding calculated *I–V* characteristics (in the model with $\alpha = 1/2$) are shown in Fig. 6 for the donor concentrations $N = 10^{17}$ and 10^{18} cm^{-3} in the drift region. The similar characteristics obtained when disregarding scattering by impurities are also shown for comparison. We can note the expected decrease in the slope of the corresponding curves at the initial stage and their equidistant behavior in higher fields. It is also worth noting that the appreciably higher carrier velocities observed when $N = 10^{17}$ cm^{-3} are possibly caused, to an extent, by the injection of electrons from the cathode contact into the drift region.

REFERENCES

1. J. L. Moll, *Physics of Semiconductors* (McGraw-Hill, New York, 1964).

2. S. Sze, *Physics of Semiconductor Devices*, 2nd ed. (Wiley, New York, 1981; Mir, Moscow, 1984).

3. K. Hess, *Theory of Semiconductors Devices* (IEEE, Piscataway, New York, 2000).

4. R. Stratton, Phys. Rev. **126**, 2002 (1962).

5. T. Grasser, T. W. Tang, H. Kosina, and S. Silberher, Proc. IEEE **91**, 251 (2003).

6. V. A. Gergel', Yu. V. Gulyaev, A. P. Zelenyĭ, and M. N. Yakupov, Fiz. Tekh. Poluprovodn. (St. Petersburg) **38**, 237 (2004) [Semiconductors **38**, 232 (2004)].

7. W. Hänsch and M. Miura-Mattausch, J. Appl. Phys. **60**, 650 (1986).

Translated by A. Spitsyn

LOW-DIMENSIONAL
SYSTEMS

Influence of an Increase in the Implantation Dose of Erbium Ions and Annealing Temperature on Photoluminescence in AlGaN/GaN Superlattices and GaN Epitaxial Layers

**A. M. Emel'yanov*, N. A. Sobolev*^, E. I. Shek*, V. V. Lundin*,
A. S. Usikov*, and E. O. Parshin****

*Ioffe Physicotechnical Institute, Russian Academy of Sciences, St. Petersburg, 194021 Russia
^e-mail: nick@sobolev.ioffe.rssi.ru
**Institute of Microelectronics and Informatics, Russian Academy of Sciences, Yaroslavl, 150007 Russia

Abstract—Room-temperature photoluminescence (PL) has been studied in AlGaN/GaN superlattices and GaN epitaxial layers implanted with 1-MeV erbium at a dose of 3×10^{15} cm^{-2} and annealed in argon. The intensity of PL from Er^{3+} ions in the superlattices exceeds that for the epitaxial layers at annealing temperatures of 700–1000°C. The strongest difference (by a factor of ~2.8) in PL intensity between the epitaxial layers and the super-lattices and the highest PL intensity for the superlattices are observed upon annealing at 900°C. On raising the annealing temperature to 1050°C, the intensity of the erbium emission from the superlattices decreases substan-tially. This circumstance may be due to their thermal destruction. © *2005 Pleiades Publishing, Inc.*

The main advantage of light-emitting structures based on semiconductors doped with rare-earth (RE) elements is that the luminescence line is narrow and the emission wavelength is temperature-independent. Erbium impurity is of particular interest because the wavelength of erbium emission ($\lambda \approx 1.54$ μm) corre-sponds to the minimum loss and lowest dispersion in fiber-optic communication lines. For the basic material applied in semiconductor electronics, i.e., single-crys-tal silicon with a relatively narrow energy gap, a strong quenching (by several orders of magnitude) of the PL from Er^{3+} ions is observed when the temperature is raised from 77 to 300 K. It has been experimentally established that the magnitude of this effect decreases as the energy gap increases, to become virtually insig-nificant in GaN [1]. Therefore, erbium-doped layers of GaN and other Group III nitrides have been studied intensively [2]. It has been found, however, that the intensity of luminescence from Er^{3+} ions is insuffi-ciently high in these layers. This problem may be due to low excitation efficiency of the luminescence from RE ions in the semiconductor bulk, since optical transi-tions between f states are partially forbidden by the selection rules. In [3], it was theoretically shown that the excitation of f electrons at the heterointerface is more efficient than that in the semiconductor bulk [3]. Recently, we observed, for the first time, an effect that consists in an increase in the PL intensity from Er^{3+} ions in AlGaN/GaN superlattices, compared with epitaxial GaN layers, at an implantation dose of 1×10^{15} cm^{-3} [4]. The aim of the present study was to examine the influence exerted by an increased (by a factor of 3) implantation dose of erbium ions and an elevated

annealing temperature on the PL in superlattices and epitaxial layers.

Al$_{0.26}$Ga$_{0.74}$N/GaN superlattices (with a layer thick-ness of 5 nm and 148 periods) were grown by metal-organic chemical vapor deposition (MOCVD) on a modified Epiquip VP-50 RP machine with a horizontal quartz reactor and a graphite holder with an induction heater. The growth process commenced with deposition of a low-temperature (500°C) nucleation layer of AlGaN onto a (0001) sapphire substrate, with subse-quent epitaxial growth at 1050°C and a pressure of 200 mbar. The structures consisted of a 20-nm-thick AlGaN nucleation layer, a 200-nm-thick GaN buffer layer, and a superlattice with GaN wells and AlGaN barriers of the same thickness. For comparison, 3-μm-thick Si-doped GaN layers were grown in the same modes. The epitaxial growth conditions are described in more detail in [4]. Erbium ions with an energy $E = 1$ MeV at dose of 3×10^{15} cm^{-2} were implanted at room temperature. According to data furnished by a method involving Rutherford backscattering (RBS) of 200-keV protons, the implanted layer did not undergo amor-phization. The annealing treatments were performed in the temperature range 700–1050°C at steps of 100°C for 5 min at each temperature in a flow of argon. The PL was excited by light from a halogen lamp, with $\lambda > 360$ nm, separated by a bandpass filter made of SZS-24 optical glass [4]. The intensity of light focused by a sys-tem of lenses onto a sample was kept constant (~50 mW) in all the experiments. The PL in the spectral range 0.95–1.65 μm was recorded using an MDR-23 monochromator and an uncooled InGaAs photodetec-tor. The light flux from the halogen lamp was modu-
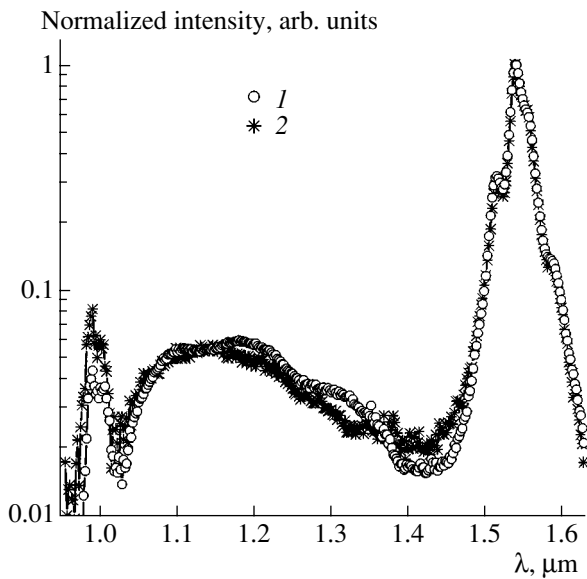
Normalized intensity, arb. units

Fig. 1. PL spectra of (*1*) a superlattice and (*2*) an epitaxial layer upon annealing at (700 + 800 + 900)°C. The spectra are normalized to the maximum intensity of each spectrum.
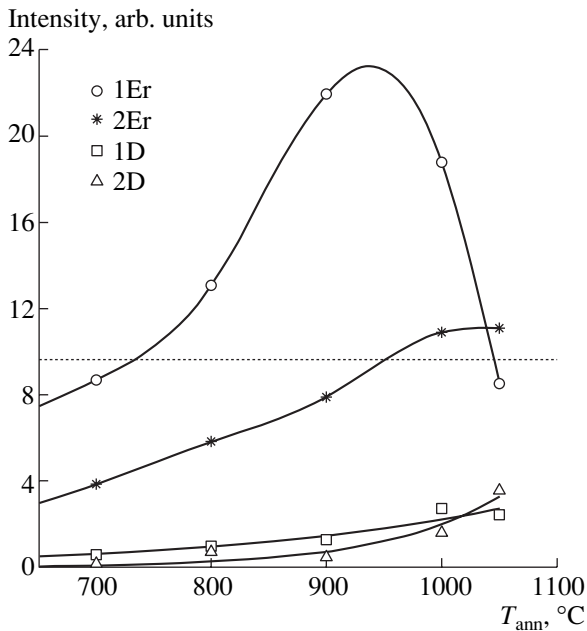
Intensity, arb. units

Fig. 2. PL intensities associated with Er^{3+} ions at $\lambda = 1.542\ \mu m$ (1Er and 2Er) and defects at $\lambda \approx 1.2\ \mu m$ (1D and 2D) vs. the annealing temperature for a superlattice (1Er and 1D) and an epitaxial layer (2Er and 2D).

lated with a chopper at a frequency of 36 Hz. The photocurrent pulses from the photodetector were transformed into an ac voltage, which was recorded with a selective voltmeter. The spectral resolution of the setup was ~7 nm.

Figure 1 shows the PL spectra of an AlGaN/GaN superlattice and an epitaxial GaN layer, both of which were implanted with erbium ions at a dose of $3 \times 10^{15}\ cm^{-2}$. The spectra were measured at 300 K upon annealing in a temperature mode of (700 + 800 + 900)°C and normalized to the maximum PL intensity for each sample. The highest-intensity peak at $\lambda = 1.542\ \mu m$ is due to a transition of Er^{3+} ions from the first excited state ($^4I_{13/2}$) to the ground state ($^4I_{15/2}$).

It is important to note that the shape of the spectra and the peak positions of these bands are the same for a superlattice and an epitaxial layer. The broad band at 1.05–1.4 μm, peaked at $\lambda \approx 1.2\ \mu m$, is associated with PL related to defects introduced in the course of implantation and the subsequent annealing treatments, as a similar band has been observed after annealing GaN layers implanted with ions of erbium [4], neodymium [5], and chromium [6]. The peak at ~0.994 μm is due to radiative transitions from the second excited state of Er^{3+} ions ($^4I_{11/2}$) to the ground state ($^4I_{15/2}$). The shapes and positions of the peak coincide for a superlattice and an epitaxial layer, similarly to the case of transitions from the first excited state to the ground state.

Figure 2 shows how the intensity of PL from Er^{3+} ions ($\lambda = 1.542\ \mu m$) and from the defects formed during implantation and annealing (at the maximum of the spectral distribution, $\lambda \approx 1.2\ \mu m$) depends on the annealing temperature T_{ann} for both an AlGaN/GaN superlattice and a GaN epitaxial layer implanted with erbium ions at a dose of $3 \times 10^{15}\ cm^{-2}$. As can be seen in Fig. 2, the intensity of the erbium PL in a superlattice exceeds that in single-crystal GaN at annealing temperatures of $700 \leq T_{ann} \leq 1000$°C. The highest PL intensity was obtained at $T_{ann} \approx 900$°C in a superlattice and at $T_{ann} \gtrsim 1000$°C in an epitaxial layer. The strongest difference in the intensity of erbium PL between a superlattice and epitaxial layer (by a factor of ~2.8) was observed upon annealing at 900°C. As the annealing temperature was raised to 1050°C, the intensity of the erbium PL in the superlattice substantially decreased, which may be due to thermal destruction of the layers constituting the superlattices (interface smearing). The intensity of the defect-related PL in the superlattices and epitaxial layers increased with temperature.

The dashed line in Fig. 2 shows the highest PL intensity produced by erbium ions, reached in the superlattices at an implantation dose of $1 \times 10^{15}\ cm^{-2}$. The results obtained from studies carried out at this dose were reported in detail in [4]. As can be seen from Fig. 2, raising the implantation dose by a factor of 3 leads to a ~2.3-fold increase in the maximum PL intensity.

Thus, it has been established that, at an erbium ion implantation dose of $3 \times 10^{15}\ cm^{-2}$, the intensity of PL from Er^{3+} ions in superlattices increases by up to a factor of 2.8 compared with epitaxial layers at equal temperatures of postimplantation annealing. This increase in intensity is presumably due to more efficient excitation of *f* electrons near the heterointerfaces, as was theoretically predicted in [3].

ACKNOWLEDGMENTS

REFERENCES

1. P. N. Favennec, H. L'Harridon, D. Moutonnet, *et al.*, Jpn. J. Appl. Phys. **29**, L524 (1990).

2. A. J. Steckl and J. M. Zavada, MRS Bull. **24**, 33 (1999).

3. G. G. Zegrya and V. F. Masterov, Appl. Phys. Lett. **73**, 3444 (1998).

4. N. A. Sobolev, A. M. Emel'yanov, V. I. Sakharov, *et al.*, Physica B (Amsterdam) **340–342**, 1108 (2003).

5. E. Silkowski, Y. K. Yeo, R. L. Hengehold, *et al.*, Mater. Res. Soc. Symp. Proc. **422**, 69 (1996).

6. S. Kim, S. J. Rhee, D. A. Turnbull, *et al.*, Appl. Phys. Lett. **71**, 231 (1997).

Translated by M. Tagirdzhanov

A Spin Filter with a Quantum Point Contact in a Dilute Magnetic Semiconductor

S. A. Ignatenko^ and V. E. Borisenko

Belarussian State University of Informatics and Radioelectronics, ul. Brovki 17, Minsk, 220013 Belarus
^e-mail: s2ign@tut.by
Submitted October 14, 2004; accepted for publication December 17, 2004

Abstract—Within the context of the suggested quantum-mechanical description of hole transport in the ballistic mode, the feasibility of using a quantum point contact as a spin filter in dilute magnetic semiconductors is analyzed. By studying the example of a dilute ferromagnetic $Ga_xMn_{1-x}As$ semiconductor, it is established that even smoothing the potential shape does not allow one to attain a 100% spin polarization of the current; in particular, at a constriction width of 3.5 nm, the polarization is 82%. It is shown that the operation region of such a spin filter lies in the narrow range of constriction widths ~3.5–4.0 nm, and, at large constriction widths, damped oscillations of the spin polarization of the current occur. The spin–orbit splitting in $Ga_xMn_{1-x}As$ is sufficient for real operation of a quantum point contact as a spin filter in this material. An increase in the splitting does not produce a substantial increase in the degree of polarization of the incoming current. © *2005 Pleiades Publishing, Inc.*

1. INTRODUCTION

The use of electron spin and charge for storage, processing, and transfer of information forms the basis of spintronics, a new area of development in modern electronics [1]. One of the important problems under discussion in spintronics is the creation of a stable source of spin-polarized charge carriers that can be injected into the bulk of a semiconductor. Several approaches to the solution of this have been suggested, including the injection of spins from a ferromagnetic metal into a semiconductor through a Schottky barrier [2] or a dielectric tunneling barrier [3]. Another approach uses an entirely semiconductor form of spin filter, which can operate under Rashba's effect [4], interband tunneling in a resonance tunneling diode [5], or the effect of Zeeman splitting in a quantum point contact (QPC) [6].

A classical QPC contains two electron tanks connected to each other by an ultranarrow constriction [7]. Due to transverse quantization, only a discrete set of modes (standing waves) can propagate through the constriction under the conditions of conductance quantization in such a channel. In the absence of spin degeneracy, the conductance is quantized in units of $e^2/\hbar$ [8].

In spintronics, there are thought to be good prospects for dilute magnetic semiconductors, which are usually represented by binary III–V or II–VI compounds with a small amount of magnetic Mn^{2+}, Fe^{2+}, or Co^{2+} ions [1, 9]. Impurity ions replace the atoms of the semiconductor at the sites of the crystal lattice and play the role of acceptors, thus producing a semiconductor with *p*-type conductivity. Spin polarization of holes arises because of their interaction with the localized spins of magnetic ions. Furthermore, a strong *s(p)–d*

exchange interaction gives rise to an indirect (*d–d*) exchange between magnetic ions, which determines the magnetic properties of a compound [9].

A highly promising dilute magnetic semiconductor is $Ga_xMn_{1-x}As$. The value of this semiconductor is related to the possibility of growing layers on semiconductor substrates in a production cycle, the ease of integration into the existing technology, and its relatively high Curie temperature, $T_C \approx 160$ K [10]. $Ga_xMn_{1-x}As$ compounds have the properties of a ferromagnetic semiconductor [9, 10], for which the Fermi energies for spin-up and spin-down carriers are different, even in the absence of a magnetic field. This difference is determined by the spin–orbit splitting $\Delta_{SO} = |E_{F\uparrow} - E_{F\downarrow}|$. For a $Ga_{0.976}Mn_{0.024}As$ compound with a hole concentration of 3×10^{20} cm^{-3}, the value of Δ_{SO} is 34 meV [11]. Thus, according to theoretical estimations [12], the degree of spin polarization of holes in the bulk of the material, $P = (\rho_\uparrow - \rho_\downarrow)/(\rho_\downarrow + \rho_\uparrow) \approx (k_{F\uparrow} - k_{F\downarrow})/(k_{F\downarrow} + k_{F\uparrow})$, is only ~5% ($\rho$ and k_F are the density of states and the wave vector at the Fermi level).

From the above arguments, it might be possible to conclude that, having attained the conductance of a $Ga_xMn_{1-x}As$ QPC equal to $e^2/\hbar$, it is possible to obtain a 100% spin-polarized current. The absence of any additional materials and layers makes such a design more attractive compared to the other possibilities [2–5] and makes the application of an external magnetic field unnecessary. However, more rigorous estimation of the efficiency of spin polarization in a QPC in a magnetic semiconductor taking into account its actual geometry is necessary.

In this study, we use a quantum-mechanical description of charge carrier transport in the ballistic mode to estimate the parameters of a QPC-based spin filter in a dilute magnetic semiconductor with regard to a smoothed geometrical shape of the conducting channel and analyze the effect of the width of the constriction and of the value of the spin–orbit splitting in a semiconductor on the degree of spin polarization of the current.

2. MODEL

For theoretical calculations, we choose a QPC of smoothed geometrical shape (Fig. 1). Such a QPC is usually realized in split-gate devices [7], where two Schottky barriers are connected in parallel to form a split contact and produce a depletion in the two-dimensional electron gas under the barriers. The application of a negative bias to the gate increases the depletion region under the Schottky barriers both in the longitudinal and in transverse directions and changes not only the width of the constriction w_0 but also the thickness l_0 of the impenetrable walls of the QPC. In order to take this effect into account, we choose the following approximation for the shape of the depletion region [13]:

$$\frac{w_q(x)}{w} = \begin{cases} \dfrac{w_0}{(w - w_0)\cos^4(\pi x/2l) + w_0}, & |x| \le l, \\ 1, & |x| > 1. \end{cases} \quad (1)$$

Here, $w_1(x)$ is the coordinate of the boundary, w is the width of the semi-infinite electrodes, and l is the half-length of the QPC (Fig. 1). We assume that the QPC has a fourth-order mirror symmetry with respect to the point A ($x = 0$ and $y = 0$). Using approximation (1), we can investigate the experimentally observed effect of depletion-region expansion without additionally complicating the calculations [7, 14].

The procedure for the conductance calculation described below is the same for the two spin components of the current. The difference in the results of the simulation is determined only by the difference in the initial data, namely, in the Fermi energy. Therefore, to simplify the formulas, we omit the spin index σ where it is not essential.

We assume that charge carrier transport mode is coherent (ballistic) in the conducting channel that passes through the constriction. The conductance in the linear-response mode is calculated using the Landauer–Büttiker formula (the temperature is disregarded) [8]

$$g = \frac{e^2}{\hbar} \sum_{m, n} |t_{mn}|^2, \quad (2)$$

where t_{mn} is the transmission factor of the wave from mode m in the left-hand electrode to mode n in the right-hand electrode. This factor is related to the Green's function of the system $G = (E - H)^{-1}$, where E
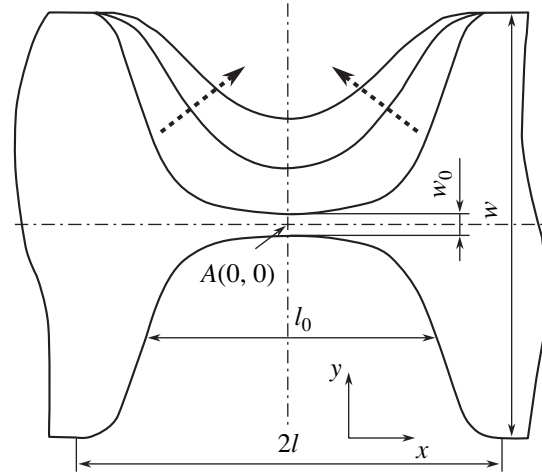
Fig. 1. Configuration of a quantum point contact formed in split-gate structures. Two symmetry axes (dash-dotted lines) intersect at the point A, with the coordinates $x = 0$ and $y = 0$. The arrows indicate the variation in the geometrical shape as the constriction width w_0 increases (see Eq. (1)).

is the Fermi energy and H is the Hamiltonian of the system [15]:

$$t_{mn} = -i\hbar\sqrt{\nu_m \nu_n} \int_0^w dy_1$$

$$\times \int_0^w dy_2 \phi_n^*(y_1)\phi_m(y_2)G(y_1, y_2, k_F). \quad (3)$$

Here, ν_n is the mobility of mode n in an electrode of width w, k_F is the Fermi wave vector, and $\phi_n(y)$ is the transverse wave function in the electrode,

$$\phi_n(y) = \sqrt{\frac{2}{w}}\sin\left(\frac{\pi n y}{w}\right). \quad (4)$$

For the factor of the reflection of electron waves r_{mn}, we write an expression similar to (3) [15].

A one-electron "tight-binding" Hamiltonian for the system under study is written as [14]

$$H = \sum_{m, n} (|m, n\rangle \varepsilon_0 \langle m, n|$$

$$- u\{|m, n\rangle\langle m + 1, n| + h.c.\}, \quad (5)$$

where u is the hopping integral between the nodes of the grid and ε_0 is the energy of a charge carrier at a node of the grid. The probability of finding a charge carrier at a node (m, n) is determined by the matrix element $\langle m, n|\Psi\rangle$, where $m = ax$; $n = ay$; a is the step of the grid; and x and y are the longitudinal and transverse coordinates, respectively. In the calculations, we set $\varepsilon_0 = 4u$. Choosing $u = \hbar^2/2m^*a^2$ (m^* is the charge-carrier effective mass), we see that, in the limit $a \longrightarrow 0$, the tight-

Parameters used for simulation of a QPC in $Ga_xMn_{1-x}As$

Parameters	Value
QPC width, w	30 nm
QPC length, $2l$	30 nm
Constriction width, w_0	0.5–15 nm
Number of points of the spatial discretization grid	240×240
Fermi level, E	150 [11] meV
Spin-orbit splitting, Δ_{SO}	34 [11] meV
Hole effective mass, m^*	$0.15 m_e^-$ [16]

binding approach yields the standard Schrödinger equation in the effective mass approximation.

In order to calculate the Green's functions, we used a standard recursive method [14] based on the Dyson equation. In this case, the transmission and reflection factors t_{mn} and r_{mn} assume the form

$$t_{mn} = -2iu\sqrt{\sin(k_n a)\sin(k_m a)}G_{nm}^{M+1,0}, \qquad (6)$$

$$r_{mn} = -2iu\sqrt{\sin(k_n a)\sin(k_m a)}G_{nm}^{0,0}$$
$$- \delta_{mn}\sqrt{\frac{\sin(k_m a)}{\sin(k_n a)}}, \qquad (7)$$

where k_m and k_n are the wave vectors for the longitudinal motion, $G_{nm}^{M+1,0}$ and $G_{nm}^{0,0}$ are the full Green's functions of the structure [14], and δ_{mn} is the Kronecker delta. The number of modes in the electrodes and the values of the wave vectors k_n (and, accordingly, of k_m) are determined using the dispersion relation and the value of the Fermi energy (we assume that the electrodes are ideal) [14]:

$$E = 4u - 2u\left(\cos k_n + \cos\frac{\pi n}{N+1}\right). \qquad (8)$$

Here, N is the number of transverse nodes. If k_n is a complex number, then we have a propagating wave; if k_n is purely imaginary, then we have a decaying wave.

The accuracy of the calculations was checked using the following criteria: (i) the sum of transmission factor (6) and reflection factor (7) must be equal to the number of propagating modes, and (ii) the factor of transmission through a straight waveguide section without any confining potential must be unity.

The degree of spin polarization of the current P is estimated as [12]

$$P = \frac{J_\uparrow - J_\downarrow}{J_\uparrow + J_\downarrow} = \frac{g_\uparrow - g_\downarrow}{g_\uparrow + g_\downarrow}, \qquad (9)$$

where $J_\uparrow(J_\downarrow)$ is the current created by spin-up (spin-down) polarized charge carriers and $g_\uparrow(g_\downarrow)$ are the corresponding channel conductances calculated from (2).

3. SIMULATION RESULTS

As the subject of our simulation, we chose a QPC of smoothed geometrical shape in $Ga_xMn_{1-x}As$. The parameters of this QPC are listed in the table. One of the aspects of the study is the establishment of the dependence of conductance (2) on the constriction width w_0 with regard to spin. However, it should be borne in mind that a change in only one parameter w_0 in (1) affects the entire shape of the QPC, as indicated in Fig. 1 by two arrows. The value of w_0 was chosen to vary from the minimal value determined by the step of the grid of spatial discretization to $0.5w$ (see table). The widths of the electrodes w were chosen so as to accomodate approximately 10 modes. With regard to this fact, the number of sites of the discretization grid must not be less than 100×100. Otherwise, large calculation errors arise related to transformation (1) from a continuous analytical form to a discrete form.

The choice of Fermi energy and spin–orbit splitting determines the Fermi energies for spin-up and spin-down carriers: $E_\uparrow = E + \Delta_{SO}/2$ and $E_\downarrow = E - \Delta_{SO}/2$. Having calculated conductances (2) for the two components, we determined the degree of spin polarization using formula (9).

In Fig. 2a, the dependence of the conductance of a $Ga_xMn_{1-x}As$ QPC on the width of the constriction is shown. The curve with circles is calculated for spin-up polarized holes, and the curve with triangles for the spin-down polarized holes. A stepped characteristic is typical of QPCs; it was observed experimentally [7] and discussed theoretically [13]. A certain integral number of propagating modes, which are accommodated across a constriction of width w_0, correspond to each step of the conductance. At small w_0 (less than 2.5 nm, Fig. 2a), no mode can pass from one electrode to the other. Thus, the total transmission factor (see (2)) is very small and varies from 10^{-22} at $w_0 = 0.5$ nm to 10^{-4} at $w_0 = 2.5$ nm. Increasing w_0 to 4–5 nm, we can accommodate one transverse mode in the constriction, and a step of $g = e^2/\hbar$ appears in the characteristic in Fig. 2a. Similar conditions arise for the other steps in the dependence of the conductance g on the constriction width w_0 [14].

From Fig. 2a, we can see that the characteristics for the two spin channels are different. This behavior manifests itself in a displacement of the curve for spin-down holes to the right along the w_0 axis, which is attributed to the difference Δ_{SO} between the Fermi energies for spin-up and spin-down charge carriers. Spin-up polarized holes have a higher energy, which corresponds to the large number of modes accommodated in the transverse direction. The passage of one mode at the QPC constriction is possible at smaller values of w_0.

By Δw, we denote the difference between constriction widths when one spin channel is open and the sec-

ond is closed (Fig. 2a). If the constriction width w_0 increases, the difference Δw increases: $\Delta w_1 < \Delta w_2 < \Delta w_3$. If we choose a QPC whose constriction width corresponds to one of the intervals Δw, then the total conductance is dominated by one of the spin components. In our case, this is the spin-up component, $g_\uparrow > g_\downarrow$.

Figure 2b shows the dependence of the degree of spin polarization P on the width of the QPC constriction. For a comparative analysis, we indicated the ranges Δw of the variation of the constriction width from Fig. 2a. For a constriction width of $w_0 = 3.5$ nm, the degree of spin polarization of the current is as high as 82%. At larger values of w_0, the value of P first abruptly falls to zero and, then, spikes are observed in the characteristic. As iw_0 increases, the spike amplitudes decrease. Such behavior is related to the increase in the magnitude of the QPC conductance, while the relative change in g of the two spin components does not exceed $e^2/\hbar$. At large values of w_0 (not shown in Fig. 2b), the oscillations are quickly damped and the polarization approaches the average value of $P = 5\%$, in agreement with the predictions of the theory [12].

The maximum spin polarization is attained at the instant when one of the spin channels is open and the other is completely closed. In a practical realization of a $Ga_xMn_{1-x}As$ QPC-based spin filter, the operation region lies in the range Δw_1. Although, at $w_0 < 3$ nm, the values of P are rather large, the application of the device encounters some difficulties related to the extremely small values of the conductance, i.e., of the current (see above). Here, it should be noted that one must carefully choose the operation point of the spin filter because of the strong dependence of P on w_0. In the split-gate configurations of a QPC, a smooth variation in the constriction width is attained by a corresponding variation in the negative bias at the gate [7, 14]. Except for the operation region Δw_1 specified above, the use of other regions, Δw_2 and Δw_3, is also possible. However, in these cases, the degree of spin polarization is four to five times lower than in the case of Δw_1.

Simulation was performed for the case where the Fermi energy for spin-up polarized holes is greater than for spin-down carriers, $E_\uparrow > E_\downarrow$. In this case, a QPC operates as a filter that is transparent for spin-up and nontransparent for spin-down polarized holes (Figs. 2a, 2b). In order to change the spin orientation of the current, one must reverse the direction of the magnetization vector in $Ga_xMn_{1-x}As$. This reversal can be produced by remagnetization of the material in an external magnetic field. The Fermi energy $E_\downarrow$ becomes greater than $E_\uparrow$ but the difference between the levels remains the same and equal to Δ_{SO}. Thus, when reversing the direction of the external magnetic field, a QPC can be a source of either spin-up or spin-down polarized charge carriers.

The effect of the magnitude of spin–orbit splitting Δ_{SO} in a magnetic semiconductor on the degree of spin polarization is illustrated in Fig. 3. The range of varia-
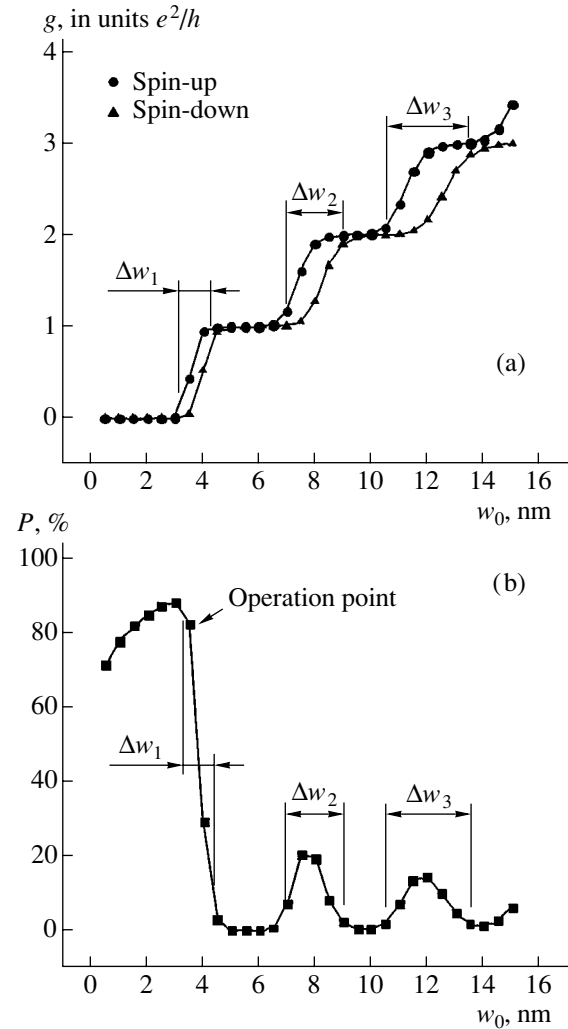

Fig. 2. Effect of the constriction width w_0 in a quantum point contact (a) on the conductance for two spin components of the current and (b) on the degree of spin polarization of the current. The operation point corresponds to the most effective operating mode of a spin filter based on a quantum point contact.

tion in Δ_{SO} is varied from 0.01 to 0.05 eV, and the constriction width w_0 is fixed at 3.5 nm, which corresponds to the optimum operation mode of the spin filter (Fig. 2b). As Δ_{SO} increases, the degree of spin polarization increases nonlinearly. The largest increase is observed at the initial portion of the curve; then, the increase becomes slower, thus indicating the approach to the saturation value of $P = 100\%$. Obviously, the experimental value of $\Delta_{SO} = 0.034$ eV for $Ga_xMn_{1-x}As$ [11] is, in principle, sufficient and attempts to further increase Δ_{SO} will not yield a significant increase in the polarization P in QPC-based spin filters.

At present, a basic obstacle to the practical application of QPCs in $Ga_xMn_{1-x}As$ as spin filters remains the low Curie temperature $T_C \approx 160$ K [10]; this fact, how-
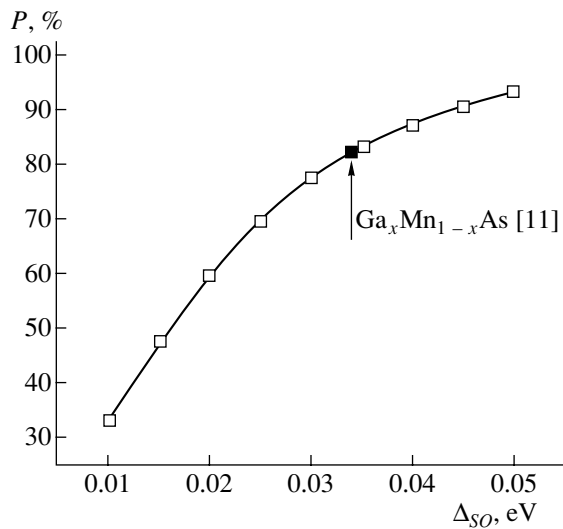
Fig. 3. Dependence of the degree of spin polarization of the current through a quantum point contact in a magnetic semiconductor on the spin–orbit splitting.

ever, does not prevent the realization of spintronic devices operating at liquid-nitrogen temperature.

4. CONCLUSION

The suggested quantum-mechanical two-dimensional model of the ballistic transport of charge carriers in QPCs on the basis of the Green's functions formalism makes it possible to take into account not only the spin of charge carriers but also the geometrical shape of the contact.

We estimated the efficiency of QPC spin filters on the basis of dilute magnetic semiconductors. In particular, we established that, for $Ga_xMn_{1-x}As$ at a constriction width of 3.5 nm, the degree of spin polarization of the current is 82%. This value is smaller than the complete (100%) spin polarization reported in [6] and is due to the smooth (without sharp steps) dependence of the QPC conductance on the constriction width. We note that the theoretical predictions in [6] are based on simple analytical expressions, whereas we have solved a rigorous quantum-mechanical problem. Thus, it is rather difficult to experimentally obtain a completely (100%) spin-polarized current in the classical QPC design. One of the solutions to this difficulty can be an increase in the length of the constriction (l_0 in Fig. 1); however, in this case, undesirable conductance oscillations appear [17].

We showed that the dependence of the polarization of the current on the constriction width has a complicated nonlinear character. The polarization attains a maximum value at low widths and, then, as the width increases, exhibits damped oscillations. Maximum values, i.e., the operation region of a spin filter, lie in a narrow range of QPC constriction widths (~3.5–4.0 nm).

Hence, when experimentally realizing this situation, special attention should be paid to the constriction width.

We established that the value of the spin–orbit splitting ($\Delta_{SO} = 0.034$ eV) attained at present in $Ga_xMn_{1-x}As$ [11] is sufficiently large for the fabrication of QPC-based spin filters, and a further increase in this quantity will not yield a substantial gain in the degree of polarization of the current.

REFERENCES

1. V. E. Borisenko and S. Ossicini, *What is What in the Nanoworld* (Wiley–VCH, Weinheim, 2004).
2. H. J. Zhu, M. Ramsteiner, H. Kostial, *et al.*, Phys. Rev. Lett. **87**, 016601 (2001); A. T. Hanbicki, B. T. Jonker, G. Itskos, *et al.*, Appl. Phys. Lett. **80**, 1240 (2002).
3. P. R. Hammar and M. Johnson, Appl. Phys. Lett. **79**, 2591 (2001).
4. T. Koga, J. Nitta, H. Takayanagi, and S. Datta, Phys. Rev. Lett. **88**, 126601 (2002).
5. M. Kohda, Y. Ohno, K. Takamura, *et al.*, Jpn. J. Appl. Phys. **40**, L1274 (2001); E. Johnston-Halperin, D. Lofgreen, R. K. Kawakami, *et al.*, Phys. Rev. B **65**, 041306 (2002).
6. M. J. Gilbert and J. P. Bird, Appl. Phys. Lett. **77**, 1050 (2000).
7. B. J. van Wees, H. van Houten, C. W. J. Beenakker, *et al.*, Phys. Rev. Lett. **60**, 848 (1988); D. A. Wharam, T. J. Thornton, R. Newbury, *et al.*, J. Phys. C **21**, L209 (1988).
8. R. Landauer, IBM J. Res. Dev. **1**, 223 (1957); M. Buttiker, Phys. Rev. Lett. **57**, 1761 (1986).
9. P. Kacman, Semicond. Sci. Technol. **16**, R25 (2001).
10. K. W. Edmonds, P. Boguslawski, K. Y. Wang, *et al.*, Phys. Rev. Lett. **92**, 037201 (2004).
11. J. Szczytko, W. Mac, A. Twardowski, *et al.*, Phys. Rev. B **59**, 12935 (1999); C. Rüster, T. Borzenko, C. Gould, *et al.*, Phys. Rev. Lett. **91**, 216602 (2003).
12. M. Julliere, Phys. Lett. A **54A**, 225 (1975).
13. E. Castano and G. Kirczenow, Phys. Rev. B **45**, 1514 (1992).
14. D. K. Ferry and S. M. Goodnick, *Transport in Nanostructures* (Cambridge Univ. Press, Cambridge, 1997).
15. A. D. Stone and A. Szafer, IBM J. Res. Dev. **32**, 384 (1988); R. A. Jalabert, H. U. Baranger, and A. D. Stone, Phys. Rev. Lett. **65**, 2442 (1990).
16. P. Yu and M. Cardona, *Fundamentals of Semiconductors* (Springer, Berlin, 1996; Fizmatlit, Moscow, 2002).
17. S. A. Ignatenko, Izv. Belorus. Inzh. Akad., No. 2(18)/2, 63 (2004).

Translated by I. Zvyagin

<div align="center">

LOW-DIMENSIONAL
SYSTEMS

</div>

The Stark Shift of the Hole States in Separate InAs/GaAs Quantum Dots Grown on (100) and (311)A GaAs Substrates

M. M. Sobolev^, G. E. Cirlin, Yu. B. Samsonenko, N. K. Polyakov, and A. A. Tonkikh

Ioffe Physicotechnical Institute, Russian Academy of Sciences, Politekhnicheskaya ul. 26, St. Petersburg, 194021 Russia
^e-mail: m.sobolev@mail.ioffe.ru

Submitted December 7, 2004; accepted for publication December 22, 2004

Abstract—Deep-level transient spectroscopy is used to study charge-carrier emission from the states of separate quantum dots in InAs/GaAs p–n heterostructures grown on (100)- and (311)A-oriented GaAs substrates in relation to the reverse-bias voltage U. It is established that the structures under consideration exhibit different bias-voltage dependences of the Stark shift for the energy levels of the quantum-dot states on the value of U. © 2005 Pleiades Publishing, Inc.

1. INTRODUCTION

In recent years, there has been an ever increasing interest in studies of the effect of an electric field on the electronic properties of InAs/GaAs heterostructures with self-organizing quantum dots (QDs). Such studies are important from both the basic and the application-related standpoints [1–13]. The results of studies performed in various laboratories have shown that the systems under consideration exhibit a high degree of freedom when controlling the energy-band and optical properties by using an external and a built-in internal electric field. Attention was drawn to the fact that the energy-band structure of systems with QDs can be controlled for the first time in [1–3], where the effect of a built-in electric field generated by a bistable dipole formed by charge carriers localized in a QD and by ionized point defects located very close to a QD was observed. In our studies of InAs/GaAs heterostructures with both vertically coupled QDs (VCQDs) and separate QDs (SQDs) using deep-level transient spectroscopy (DLTS), we observed a shift of the DLTS peak related to the emission of charge carriers from a quantum state of the VCQDs and SQDs to a higher-temperature region of the spectrum as the electric-field strength increased [1, 11]. The magnitude of the temperature shift of the DLTS peak was much larger in a structure with VCQDs than in one with SQDs. Recently, studies of the electric-field dependence of the photoluminescence (PL) spectra and photocurrent of self-organized QDs located in an InGaAs/GaAs system and grown on GaAs planes with various Miller indices have been reported [4–8]. A red shift of the energy of optical transitions in an electric field was observed [4–8]. The phenomenon responsible for this shift has come to be known as the quantum-constrained Stark effect. In the case of SQD structures obtained on GaAs substrates with large Miller indices, this effect was found to be related to a combination of a piezoelectric field and a permanent dipole located within a QD and caused by a spatial separation of the wave functions for electrons and holes [4, 5]. The Stark effect observed [6] for SQD structures on GaAs (100) substrates was attributed solely to dipoles resulting from a spatial separation of the wave functions for electrons and holes. Lemaitre *et al.* [7] assumed that the observed enhancement of the binding of excitons to LO phonons and the shift of excitonic spectral lines (the Stark effect) were caused by charged defects within and near the QDs. It should be borne in mind that the Stark effect in structures with QDs is more than just a new physical phenomenon; in addition, this effect has application-related potential. Thus, it is of interest to use the DLTS method to experimentally study the electric-field dependence of the above effect for self-organized QDs located in an InAs/GaAs system and grown on GaAs planes with different Miller indices.

In this paper, we report the results of measuring the capacitance–voltage (C–U) characteristics and of DLTS studies of the hole emission from the quantum states of SQDs in InAs/GaAs semiconductor heterostructures grown on substrates with (100) and (311)A orientations (here, A stands for the Ga sublattice). This emission is studied in relation to the reverse-bias voltage U, conditions of isochronous annealing both under the application of and without a bias voltage, and the presence of illumination. The InAs/GaAs heterostructures under study contained SQDs and were grown by the method of molecular-beam epitaxy (MBE) using self-organization effects.

2. EXPERIMENTAL

The InAs/GaAs heterostructures with SQDs under study were formed by MBE on n^+-GaAs substrates with (100) and (311)A orientations. The array of SQDs was formed as a result of a single-stage deposition of two
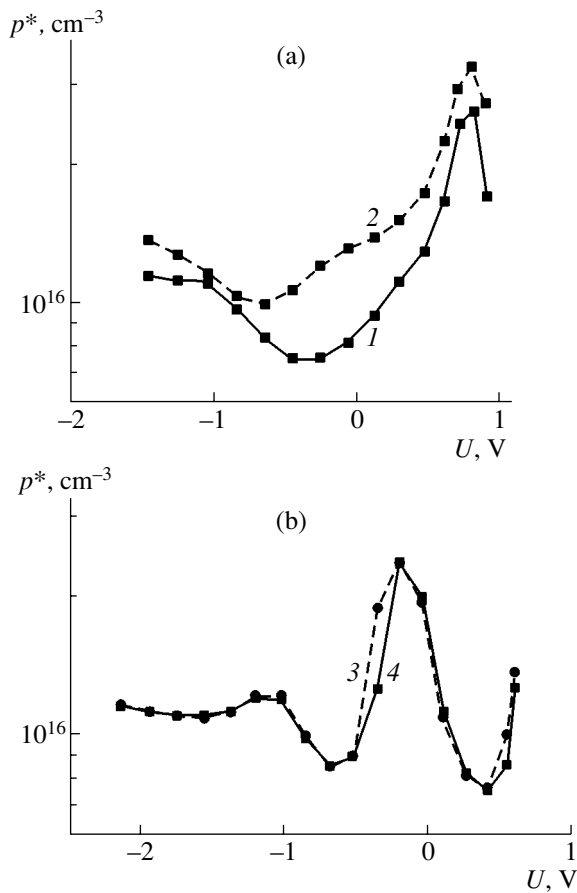
Fig. 1. Concentration profiles $p^*(U)$ for InAs/GaAs p–n heterostructures with separate quantum dots formed on GaAs (a) (311)A and (b) (100) substrates. The profiles were determined from capacitance–voltage measurements at $T = 82$ K after a preliminary isochronous annealing at a temperature of 350 K and at $U_a < 0$. The measurements were performed (*1, 3*) in the dark and (*2, 4*) under an exposure to white light.

InAs monolayers. The SQDs were positioned in the middle of a 0.90-μm-thick p-GaAs layer doped with Be at a concentration of 2×10^{16} cm^{-3}. The p-GaAs layer was coated with a 0.2-μm-thick p^+-GaAs layer doped with Be at a concentration of 2×10^{17} cm^{-3}. The DLTS studies were carried out using a DL4600 spectrometer (BIO-RAD Co.) that operated in a regime of two-gate integration. In order to measure the capacitance, we used a Boonton-72B bridge that operated at a frequency of 1 MHz. The sensitivity of this setup was $\Delta C/C \approx 10^{-4}$. In order to carry out the DLTS measurements, we thermally deposited ohmic contacts onto the n^+-GaAs substrate and the p^+-GaAs layer. The sample was annealed isochronously for 1 min at a fixed temperature, either under an applied reverse-bias voltage ($U_a < 0$) or without it ($U_a = 0$), before each DLTS measurement. Preliminarily, the sample was heated to 350 K; kept at this temperature for 1 min at $U_a = 0$ if the annealing was carried out at $U_a < 0$; and, finally, cooled to the annealing

temperature. If the sample was annealed with $U_a = 0$, it was preliminarily kept at 350 K under the conditions of $U_a < 0$. The annealing temperature was varied from 80 to 350 K. The sample was then cooled to 80 K under the conditions of either $U_a < 0$ or $U_a = 0$. The DLTS measurements were then performed in the dark or under exposure to white light. In order to determine the concentration profile of charge carriers in the heterostructure, we measured the capacitance–voltage characteristics. The thermal-activation energy E_a for deep levels and the cross sections σ_p for the capture of charge carriers by these levels were determined from the Arrhenius equation using the rate-window method for standard DLTS measurements.

3. RESULTS AND DISCUSSION

We measured the capacitance–voltage (C–U) characteristics of the InAs/GaAs p–n heterostructures with SQDs at a temperature $T = 82$ K. Variations in the capacitance C as the bias voltage U is varied for structures on (311)A and (100) GaAs substrates is known to be typical behavior for localized states [1, 2]. We observed a single peak related to emptying of the QD states in each of the free-hole concentration profiles $p^*(U)$ (Fig. 1a, 1b) calculated using the data obtained from the capacitance measurements at $T = 82$ K. Illumination had a clearly pronounced effect on the results of the C–U measurements for the structure grown on a GaAs (311)A substrate (Fig. 1a, curve *2*); however, the effect of the conditions of the isochronous annealing carried out before the measurements was less pronounced (this effect is not shown in Fig. 1). This behavior of the C–U characteristics for the structure on a GaAs (311)A substrate is consistent with the results of our previous studies [3, 13] and indicates that, in a GaAs matrix containing SQDs, there are point defects with deep levels whose concentration is comparable to that of shallow levels of the background impurity. It is the optical recharging of these deep levels that brings about appreciable changes in the C–U characteristics, since this causes changes in the Fermi level position. In the case of the SQD structures on a GaAs (100) substrate, the effect of illumination on the C–U characteristic was much less profound (Fig. 1b, curve *4*).

We used the results of the C–U measurements to determine the range of bias voltages for which signals related to the emission of charge carriers from the SQD states should be observed in the DLTS spectra. In order to determine the spatial localization of the DLTS signals and the nature of the levels responsible for these signals, we measured the DLTS spectra at a constant amplitude of the filling voltage pulse U_f and at a variable amplitude of the voltage pulse U that corresponded to the measurement of the DLTS signal (Figs. 2a, 2b). The DLTS spectra of an SQD structure on the GaAs (311)A substrate included two peaks (HD1$_{(311)A}$ and HD2$_{(311)A}$) related to the emission of holes accumulated

at deep traps (Fig. 2a). The measurements carried out under different conditions of preliminary isochronous annealing ($U_a < 0$ or $U_a = 0$) showed that the amplitudes of the DLTS $HD1_{(311)A}$ and $HD2_{(311)A}$ peaks after annealing with $U_a = 0$ were not significantly larger than in the case of annealing with $U_a < 0$; however, this increase became significant if the sample was illuminated during the DLTS measurements. The observed increase in the amplitudes of the $HD1_{(311)A}$ and $HD2_{(311)A}$ peaks as a result of annealing at $U_a = 0$ and illumination is related (as in the case of the $C–U$ measurements) to a change in the Fermi level position resulting from recharging of the deep-level defects in the GaAs matrix [3, 13]. In accordance with the conclusions drawn in [3, 13], the DLTS peaks $HD2_{(311)A}$ and $HD1_{(311)A}$ are caused by spatially localized states of holes. These states are related to the ground and excited hole states in an SQD, respectively. In addition to these two peaks, another peak was also observed in the DLTS spectra (this peak is not shown in Fig. 2a). The parameters of a deep-level defect responsible for the appearance of this peak were determined from the Arrhenius equation ($E_a = 331$ meV and $\sigma_p = 4.5 \times 10^{-16}$ cm^2) and were found to be close to the parameters of HL7 and HL11 defects [14]. HL7 and HL11 defects are typically formed in GaAs layers obtained by MBE and from the melt, respectively. In addition, the parameters of the defect HL11 are very close to those of the defect HL5 [14], which, according to [15], is a complex of intrinsic defects and includes an arsenic vacancy V_{As}. We previously observed this defect in GaAs/InAs heterostructures that included SQDs and were formed by MBE [13]. The DLTS spectra of the structures with SQDs formed on a GaAs (100) substrate (Fig. 2b) also included three peaks: an $ED1_{(100)}$ peak related to the emission of electrons from the trap levels in the upper half of the band gap and $HD1_{(100)}$ and $HD2_{(100)}$ peaks related to the emission of holes from the trap levels located in the lower half of the band gap. We also measured the DLTS spectra for different conditions of preliminary isochronous annealing ($U_a < 0$ or $U_a = 0$). These measurements showed that a shift in temperature was observed for all three peaks if the conditions of isochronous annealing were changed. The DLTS-peak shift is caused by the presence of electrostatic dipoles formed by the charge carriers localized in an SQD and by ionized defects with deep levels. This shift gives grounds for identification of the $ED1_{(100)}$, $HD1_{(100)}$, and $HD2_{(100)}$ peaks with those related to the SQD states or to the interfacial states [3, 13]. The relation of the $ED1_{(100)}$ and $HD1_{(100)}$ peaks to the SQD states is confirmed by the fact that the spatial localization of these DLTS peaks coincides with the peak in the concentration profile for free holes $p^*(U)$ (Fig. 1b) that is related to the emission of charge carriers from the QD states. The range of spatial localization of the $HD2_{(100)}$ peak coincides with the boundary between the wetting layer
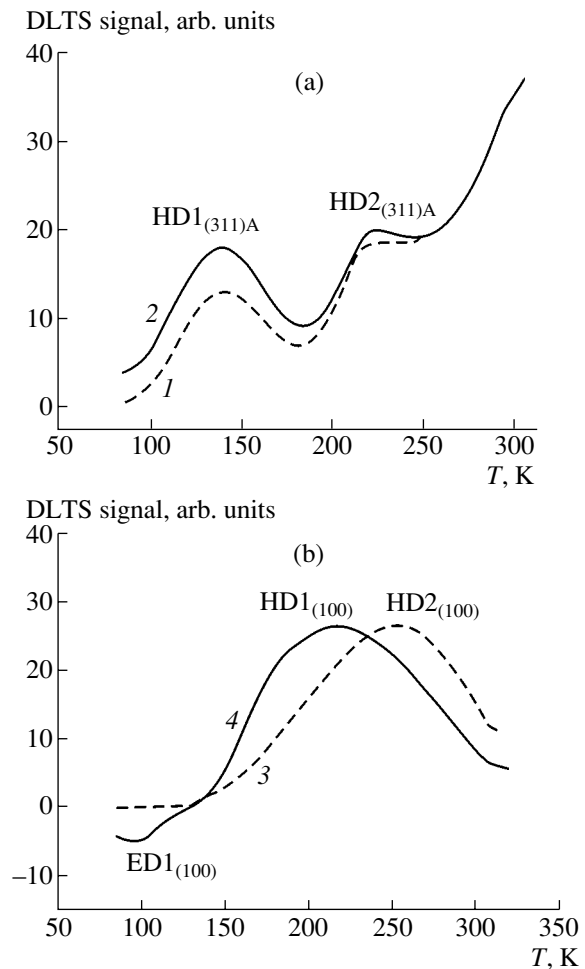

Fig. 2. DLTS spectra of InAs/GaAs $p–n$ heterostructures formed on GaAs substrates with orientations of (a) (311)A and (b) (100). The spectra were obtained at the following amplitudes of the reverse-bias voltage pulse U: (*1, 2*) –0.25, (*3*) –0.22, and (*4*) –0.64 V. All the spectra were measured using the emission-rate window 1000 cm^{-1}, the filling-pulse amplitude $U_f = 0.42$ V, and the pulse width 25 µs after a preliminary isochronous annealing at 350 K and $U_a < 0$. Spectrum *1* was obtained with a sample exposed to white light and spectra *2–4* were obtained for a sample kept in the dark.

and an SQD. We plotted the dependences of the temperature positions of the DLTS peaks T_{max} on the value of U for all the structures (Fig. 3). The peaks $HD1_{(311)A}$ and $HD2_{(311)A}$ are shifted to higher temperatures as the magnitude of U increases (Fig. 3; curves *1, 2*); this behavior corresponds to changes in the thermal-activation energies from 52 to 61 meV ($HD1_{(311)A}$) and from 303 to 308 meV ($HD2_{(311)A}$). In the case of an SQD structure on a GaAs (100) substrate, we also observed a shift of the positions of the DLTS peaks (Fig. 3): the peak $HD2_{(100)}$ shifted to higher temperatures as the bias voltage changed from +0.22 to –0.40 V (curve *3*); the peak $HD1_{(100)}$ first shifted to lower temperatures as U changed from –0.52 to –0.75 V (curve *4*) and, then,
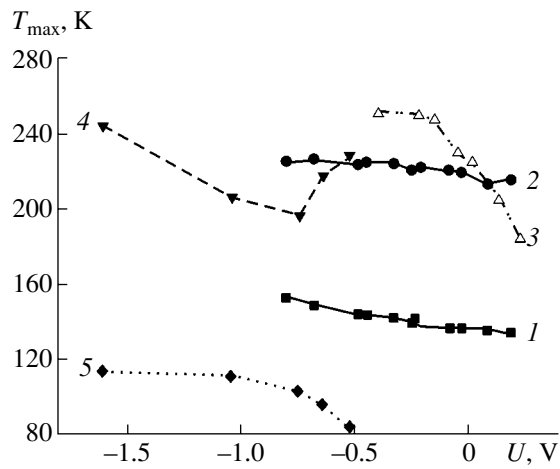
T_{max}, K

Fig. 3. Dependences of the temperature positions of the DLTS peaks on the voltage-pulse amplitude U. Curve *1* is for peak $HD1_{(311)A}$; curve *2*, for peak $HD2_{(311)A}$; curve *3*, for $HD2_{(100)}$; curve *4*, for $HD1_{(100)}$; and curve *5*, for $ED1_{(100)}$.

to higher temperatures as U changed from –0.75 to –1.61 V. This behavior corresponds to variations in the thermal-activation energy from 217 to 288 meV for the level related to the peak $HD2_{(100)}$ and from 239 to 156 meV and then to 215 meV for the level related to the peak $HD1_{(100)}$. The $ED1_{(100)}$ peak shifted to higher temperatures as the magnitude of U increased (Fig. 3, curve *5*). At $U = -0.75$ V, the thermal-activation energy for the level corresponding to this DLTS peak was equal to 192 meV and the cross section of the electron capture was 8.0×10^{-13} cm^2. The observed dependences of the positions of the DLTS peaks associated with the emission of holes from the quantum states of QDs on the bias voltage U applied to an SQD structure on a GaAs (311)A substrate are related to a manifestation of the Stark shift effect for the levels of the quantum-state energy in an SQD [4, 5]. As was ascertained by Gurioli *et al.* [5], the Stark shift in this case is apparently governed by a combination of the *p–n*-junction electric field and a piezoelectric field that arises in epitaxial GaAs layers grown on substrates with a large Miller index, the latter field being no higher than 10 meV. In the case of an SQD structure on a GaAs (100) substrate, the dependences of the positions of the DLTS peaks arising as a result of the hole emission on the bias voltage U applied to the structure (Fig. 3) were similar to those previously observed for structures with two vertically coupled QDs also grown on GaAs (100) substrates [12]. These dependences were related to the following phenomena, which can manifest themselves in structures with SQDs and can make opposing contributions to the thermal-activation energies determined from the DLTS measurements as the electric field increased:

(i) the field effect, which reduces the barrier height for thermal emission [16], and

(ii) the Stark effect, which shifts the energy levels of a quantum state in an SQD [4–8].

For the SQD structure under consideration, we observed an appreciable increase in the Stark shift for the ground state of holes in an SQD (this shift became as large as ~60 meV). A strong field dependence of the thermal-activation energy for emission of holes from this state also appeared, which was almost unobservable for an SQD structure on a GaAs (311)A substrate. An interfacial state at the boundary between the wetting layer and the SQD was detected; we also observed a large Stark shift for this state. In addition to the quantum states of holes, we also observed a quantum state of electrons for the SQD structures on GaAs (100) substrates. This state manifested itself in the $ED1_{(100)}$ DLTS peak, which also experienced a pronounced Stark shift.

4. CONCLUSION

Thus, the results of our DLTS studies of SQD (separate-quantum-dot) heterostructures formed on GaAs (311)A and (100) substrates show that the structures differ with respect to the energies of quantum-state levels in an SQD that exhibit different Stark shifts. In addition, in an SQD structure on a GaAs (100) substrate, we observed a field dependence of the thermal-activation energy for the hole emission from this quantum state in an SQD and ascertained that there existed an interfacial state at the heteroboundary between the wetting layer and an SQD; a pronounced Stark shift was also observed for this state. These differences between the properties of the two structures can be related to differences between the geometric shape of the SQDs [17] and between the conditions of SQD formation [3] and can be caused by different orientation of the substrate surface on which the heterostructures with SQDs were grown [18]. A special feature of the formation of SQD structures on (100) GaAs substrates can also consist in the presence of either point lattice defects located near an SQD [1–3] or a potential barrier for the capture of charge carriers [9, 10, 19].

REFERENCES

1. M. M. Sobolev, F. R. Kovsh, V. M. Ustinov, *et al.*, Fiz. Tekh. Poluprovodn. (St. Petersburg) **31**, 1249 (1997) [Semiconductors **31**, 1074 (1997)].
2. M. M. Sobolev, I. V. Kochnev, V. M. Lantratov, *et al.*, Physica B (Amsterdam) **273–274**, 959 (1999).

3. M. M. Sobolev, I. V. Kochnev, V. M. Lantratov, *et al.*, Fiz. Tekh. Poluprovodn. (St. Petersburg) **34**, 200 (2000) [Semiconductors **34**, 195 (2000)].

4. A. Patanè, A. Levin, A. Polimeny, *et al.*, Appl. Phys. Lett. **77**, 2979 (2000).

5. M. Gurioli, S. Sanguinetti, and M. Henini, Appl. Phys. Lett. **78**, 931 (2001).

6. P. W. Fry, I. E. Itskevich, D. J. Mowbray, *et al.*, Phys. Rev. Lett. **84**, 733 (2000).

7. A. Lemaitre, A. D. Ashmore, J. J. Finley, *et al.*, Phys. Rev. B **63**, 161309 (2001).

8. W. Sheng and J.-P. Leburton, Appl. Phys. Lett. **78**, 1258 (2001).

9. M. M. Sobolev, I. V. Kochnev, V. M. Lantratov, and N. N. Ledentsov, Fiz. Tekh. Poluprovodn. (St. Petersburg) **35**, 1228 (2001) [Semiconductors **35**, 1175 (2001)].

10. M. M. Sobolev and V. M. Lantratov, Physica B (Amsterdam) **308–310**, 1113 (2002).

11. M. M. Sobolev, V. M. Ustinov, and G. E. Cirlin, Physica B (Amsterdam) **340–342**, 1103 (2003).

12. M. M. Sobolev, G. E. Cirlin, Yu. B. Samsonenko, *et al.*, Fiz. Tekh. Poluprovodn. (St. Petersburg) **39**, 131 (2005) [Semiconductors **39**, 119 (2005)].

13. M. M. Sobolev, F. R. Kovsh, V. M. Ustinov, *et al.*, Fiz. Tekh. Poluprovodn. (St. Petersburg) **33**, 184 (1999) [Semiconductors **33**, 157 (1999)].

14. A. Mitonneau, G. M. Martin, and A. Mircea, Electron. Lett. **13**, 666 (1977).

15. P. N. Brunkov, S. Gaĭbullaev, S. G. Konnikov, *et al.*, Fiz. Tekh. Poluprovodn. (Leningrad) **25**, 338 (1991) [Sov. Phys. Semicond. **25**, 205 (1991)].

16. S. Anand, N. Carlsson, M.-E. Pistol, *et al.*, Appl. Phys. Lett. **67**, 3016 (1995).

17. W. Sheng and J.-P. Leburton, Physica E (Amsterdam) **17**, 50 (2003).

18. M. Henini, III–Vs Rev. **11**, 48 (1998).

19. H. L. Wang, F. H. Yang, S. L. Feng, *et al.*, Phys. Rev. B **61**, 5530 (2000).

Translated by A. Spitsyn

LOW-DIMENSIONAL SYSTEMS

Electronic Structure of Titanium Disulfide Nanostructures: Monolayers, Nanostripes, and Nanotubes

V. V. Ivanovskaya*, G. Seifert**, and A. L. Ivanovskiĭ*^

*Institute of Solid State Chemistry, Russian Academy of Sciences (Ural Branch), Yekaterinburg, 620219 Russia
^e-mail: ivanovskii@ihim.uran.ru
**Institut für Physikalische Chemie, Technische Universität, Dresden D-01062, Germany
Submitted January 11, 2005; accepted for publication January 13, 2005

Abstract—Atomic models for quasi-1D planar (nanostripe) and cylindrical (nanotube) nanostructures consisting of $1T$ and $2H$ TiS_2 phases are suggested. By using a self-consistent band approach to the electron-density functional in the tight-binding approximation, specific features of the electronic spectrum of these nanostructures and the conditions necessary for their stability are studied in comparison with 2D (molecular monolayer) and 3D (crystal) TiS_2 forms. The possibility of $1T \longleftrightarrow 2H$ phase transitions in the nanostructures is analyzed for the first time. It is established that the octahedral atomic surrounding characteristic of a stable $1T$ TiS_2 crystalline phase is retained in the 2D and 1D nanostructures. In contrast to 3D TiS_2, all the stable 2D and 1D nanostructures are semiconductors. The regular modifications of the energy-band spectrum of the TiS_2 nanostructures in relation to their type and atomic arrangement are found. © 2005 Pleiades Publishing, Inc.

1. INTRODUCTION

Titanium disulfide TiS_2 belongs to a wide group of layer-structured d-metal dichalcogenides MX_2, where M denotes the metal and X = S or Se. Depending on the composition of the metal sublattice, these materials can exhibit metal (and superconductor) or semiconductor properties (see [1]).

It is known that the TiS_2 structure is composed of packed S–Ti–S molecular layers. The constituent atoms inside the layers are bonded by strong interactions, partially covalent and ionic in nature. Separate layers are linked by a weak van der Waals interaction [2–4]. The layer structure and the anisotropy of interatomic bonding in these crystalline materials are considered as indicating that there is a possibility of obtaining quasi-1D (nanotubes) and quasi-0D (fullerene-like molecules) nanostructures [5–10] based on them.

Recently [11], a low-temperature gas-phase synthesis ($TiCl_4 + 2H_2S \longrightarrow TiS_2 + 4HCl$) was successfully used to produce the first TiS_2 nanotubes. Analysis of their morphology and structure showed that the tubes were composed of coaxial titanium sulfide layers, with an interlayer spacing of ~0.57 nm and Ti-to-S atomic ratio [Ti] : [S] = 1 : 2. The nanotubes were open at both ends, and their average outer and inner diameters (D) were about 20–30 and 10 nm, respectively. In [12, 13], the intercalation of TiS_2 nanotubes with lithium and hydrogen was studied, and the potential of these materials as hydrogen accumulators was discussed.

The material-science prospects for various categories of nanostructures are defined, in many respects, by their electronic properties, which may essentially differ from those of the corresponding 3D crystal phases; in turn, these properties depend on the atomic arrangement and geometry of the nanostructures. For instance, MoS_2 or WS_2 nanotubes are semiconductors whose band gap essentially depends on the diameter and atomic configuration of the walls, i.e., on the so-called chirality. In contrast, NbS_2 nanotubes are metallic in their conduction mechanism [14–16].

Regarding d-metal disulfides, the two most stable polytypes are known: the $1T$ and $2H$ phases, which are different in their local atomic arrangement. For disulfides from the Group VI d metals (MoS_2 or WS_2), the $2H$ phases, where the metal atoms are located in a trigonal prism-like surrounding of S atoms, are more stable. In contrast, disulfides from the Group IV d metals, such as Ti or Zr, are characterized by octahedral coordination of the metal atoms ($1T$ polytype). Disulfides from the Group V metals can exist in the form of both the $1T$ and $2H$ polytypes [1, 17].

So far, the type of local atomic coordination in disulfide nanostructures, i.e., the possibility of $1T \longleftrightarrow 2H$ "phase transitions" when the crystalline state is replaced by a nanoscale structure, has not been studied. When simulating NbS_2, MoS_2, and WS_2 nanotubes in [14–16], it was a priori assumed that the local atomic structure of the tubes was the same as that in the relevant crystalline $2H$ disulfides.

In this study, we suggest, for the first time, atomic models for a series of 1D and 2D titanium disulfide nanostructures with different local atomic arrangements (octahedral or trigonal prism-like configurations). In the context of a self-consistent band approach to the electron density functional in the tight-binding approximation, the electron energy properties of such

nanostructures are studied in comparison to each other. As a result, the possibility of a change in the atomic surrounding during the transition from the TiS$_2$ crystal to its nanostructure state is analyzed. Special features of the energy-band spectrum of the 1D nanostructures (nonchiral *zigzag* and *armchair* TiS$_2$ nanotubes and proportioned atomic stripes) in comparison with the band spectrum of the 2D molecular monolayers consisting of 1T and 2H phases are established for the first time.

2. STRUCTURAL MODELS AND THE COMPUTATIONAL METHOD

The structure of a stable 1T phase of TiS$_2$ ($P\bar{3}m$ symmetry group) is formed by three-atom S–Ti–S molecular layers that consist of Ti hexagonal atomic networks confined between planar networks of S atoms (Fig. 1). The layers are packed in such a manner that the Ti atoms are located above each other along the z axis. The coordination numbers of the Ti and S atoms are 6 and 3, respectively, and the Ti atoms are located in the centers of [TiS$_6$] octahedrons whose faces are in contact. The unit cell contains a single formula unit ($Z = 1$), and the Ti and S atoms are located at the sites 1a(0, 0, 0) and 2d(1/3, 2/3, 0.2501), respectively. The lattice parameters are $a = 0.3402$ nm and $c = 0.5698$ nm [1].

A metastable 2H TiS$_2$ phase ($C6/mmc$ symmetry group) is also formed by S–Ti–S molecular layers that consist of conjugated trigonal prisms [TiS$_6$]. The atomic positions in the unit cell ($Z = 2$) are as follows: (0, 0, 0) and (0, 0. 1/2) for the two Ti atoms and (1/3, 1/3, ±z) and (–1/3, –1/3, 1/2, ±z) for the four S atoms.

In the initial stage of the treatment, we optimized the structures and calculated the energy bands for the three-atom molecular layers consisting of 1T and 2H TiS$_2$ phases. Based on the results, we developed structural models for infinite nanotubes. For this purpose, molecular stripes were "cut off" from a layer and then twisted, resulting in the formation of "three-wall" tubes. This procedure is similar to that commonly used
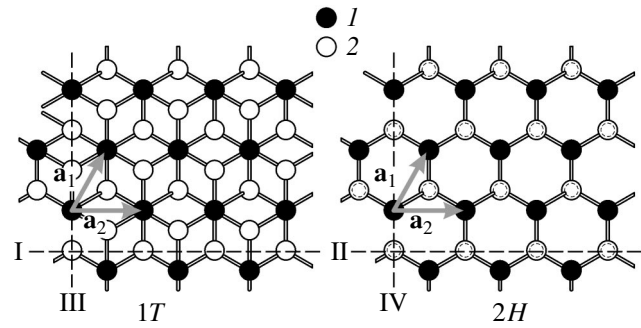

Fig. 1. Structures of 1T- and 2H-TiS$_2$ phase molecular layers. Titanium and sulfur atoms are schematically shown as (*1*) closed and (*2*) open circles, respectively. The basis vectors (**a**$_1$ and **a**$_2$) used when constructing the atomic models of the NTs are shown. The dashed lines show "sections" of the I–IV nanostripes (see text for details).

to form carbon nanotubes from graphene stripes [7–10, 18, 19]. The TiS$_2$ tubes consist of three coaxial cylinders of S, Ti, and S atoms (Fig. 2). According to the scheme adopted in [18, 19], the geometric parameters of the TiS$_2$ nanotubes (NTs) are described by the basic vectors of the hexagonal network of Ti atoms, **a**$_1$ and **a**$_2$ (see Fig. 1), specifying the so-called chiral vector **c**$_h$ = n**a**$_1$ + m**a**$_2$ equal to the perimeter of the cylinder of Ti atoms.

By using a well-known classification (see [18, 19]), the large variety of TiS$_2$ NTs constructed in the above manner can be divided into three groups of structures: the so-called nonchiral *armchair* (n, n) and *zigzag* (n, 0) NTs (Fig. 2) and chiral (n, m) NTs. We considered nonchiral *zigzag* (20, 0) NTs and *armchair* (20, 20) NTs. The band structures were calculated for unit cells consisting of 120 atoms. The diameters of the central atomic cylinders in the tubes D(Ti) are listed in Table 1.

In addition, the band structure of the infinite TiS$_2$ molecular stripes from which the above described (20, 0)

Table 1. The diameter D(Ti), band gap (BG), total energy E_{tot}, and strain energy E_{st} for optimized structures of the 1T and 2H TiS$_2$ nanotubes and nanostripes

Phase	Nanostructure	D(Ti), nm	BG, eV	$-E_{tot}$, eV/atom	E_{st}, eV/atom
1T	Tube (20, 0)	2.174 (2.161)*	1.28	55.703	0.063
	Stripe I**	–	1.38	55.766	–
	Tube (20, 20)	3.733 (3.743)*	1.54	55.759	0.012
	Stripe III**	–	1.48	55.771	–
2H	Tube (20, 0)	2.072 (2.161)*	1.12	55.378	0.117
	Stripe II**	–	0.87	55.495	–
	Tube (20, 20)	3.478 (3.743)*	1.21	55.499	–0.018
	Stripe IV**	–	Metal	55.481	–

Note: The symbol * indicates the diameters of the "central" cylinders formed by Ti atoms in the TiS$_2$ NTs. (The values of D(Ti) before structural optimization are given in parentheses). I**–IV** correspond to the types of nanostripes (see text).
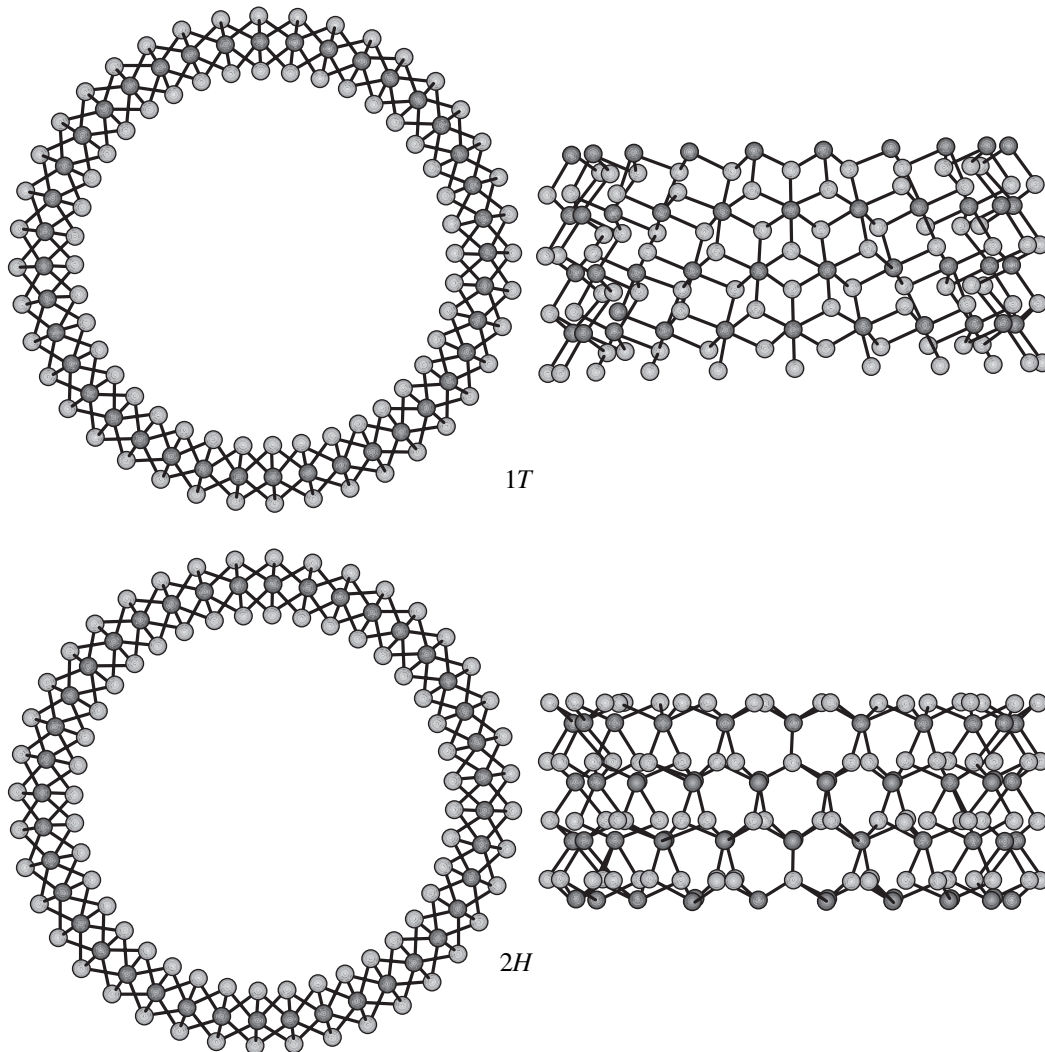
Fig. 2. Fragments of optimized atomic structures of the (20, 0) *zigzag* nanotubes constructed from 1*T* and 2*H* TiS$_2$ molecular layers.

and (20, 20) NTs were twisted was calculated. By performing this calculation, we pursued two principal goals.

First, it was interesting to compare the electron energy states in the 1*T* and 2*H* TiS$_2$ nanostripes, which exhibit three types of sections: those composed of only S, only Ti, or both S and Ti atoms; moreover, it was of interest to find the most stable configurations. Such edge structures in TiS$_2$ NTs can be formed due to extended atomic defects (dislocations) in the NT walls along the NT axis or to deviations in the NT shape from a cylindrical form as a rolllike morphology is developed. It is worth noting that "nanorolls" have been detected by scanning electron microscopy in a number of nanomaterials, e.g., *d*-metal oxides [20–23]. The edge states can promote semiconductor–metal transitions. In fact, metal-like states have recently been found in sections of semiconductor monomolecular MoS$_2$ stripes, and the corresponding atomic chains have been interpreted as 1D conductors [24].

Second, comparison of the energy states in proportionate nanostripes with those in the NTs allows discussion of the stability of these systems in terms of the strain energy E_{st} (see, e.g., [14–16]), which is representative of the energy effect of twisting a planar layer or a stripe into a cylinder.

We considered, as model systems, four infinite molecular stripes of types I–IV. These were used to construct 1*T*- and 2*H*-like TiS$_2$ NTs, specifically, *zigzag* (20, 0) NTs (types I and III) and *armchair* (20, 20) NTs (types III and IV) consisting of an equal number of atoms (120) in their unit cell. The directions in which the 1*T* and 2*H* TiS$_2$ monolayers were "cut" are shown in Fig. 1. With such directions, the planar sections of stripes I and II contain Ti or S atoms, whereas those of stripes III and IV contain both Ti and S atoms.

We calculated the electron structures of all of the above nanosystems using a self-consistent band theory of the electron density functional in the tight-binding

Table 2. Calculated band structure parameters (in eV) for the 1T and 2H TiS$_2$ monolayers in comparison to earlier results for a 1T TiS$_2$ crystal

Band width	Monolayer			Crystal			
	1T*	2H*	1T [4]	[4]	[26]	[27]	[28]
S-3s	1.96	2.22	1.9	–	2.0	2.1	1.4
Band gap S-3s–S-3p	6.44	6.38	6.4	–	6.2	6.5	6.7
S-3p (up to E_F)**	4.93	4.70	5.1	5.31	5.3	5.5	5.1
BG***	1.65	1.25	1.0	sm	sm	sm	sm
(Band overlap)	–	–	–	0.4	0.1	–	–

Note: The symbol * indicates the results of the DFT–TB calculations carried out in this study; the symbol ** indicates the results of band calculations using the NB-LMTO approach [4], the method of spherical waves (LSWs) [26], and the full-potential method of augmented plane waves (LAPWs) [27, 28]; and the symbol *** marks where, for the semimetal (sm) TiS$_2$ crystal, the overlap of the bands S 3p and Ti 3d around E_F is given.

approximation (DFT–TB) [25]. We optimized the structures of the nanosystems in order to minimize the total energy. As a result, the electron energy bands, the total and partial electron density of states (DoS), and the total energies of the systems (E_{tot}) were calculated.

3. RESULTS AND DISCUSSION

Before describing the results, it is worth noting that the band structure of a crystalline 1T TiS$_2$ phase has been studied both experimentally and theoretically and reported in a number of papers (for reviews, see [3, 4, 26–28]). In the earlier studies it was concluded that 1T TiS$_2$ falls into the category of narrow-gap semiconductors [2]. In contrast, the more accurate estimates obtained in the recent years show that titanium disulfide is a semimetal. It has this form due to the overlap between the S p and Ti d bands near the Fermi level (Table 2, [4, 26–28]). A critical analysis of the available calculations and the XPS and electrical conductivity data for TiS$_2$ was given in [26, 27]. At the same time, band calculations using the method of linear muffin-tin orbitals (LMTOs) for a single molecular 1T TiS$_2$ monolayer [4] showed that such a monolayer is a semiconductor. The transition to the metal-like state occurs for "a plate" of more than ten molecular layers.

We have no information on the electron structure of metastable 2H TiS$_2$.

3.1. 1T and 2H Monolayers

Figure 3 shows the DFT–TB energy bands for a 1T TiS$_2$ monolayer. The two lowest bands (from –13.86 to –11.90 eV) correspond to quasi-core bands and are largely composed of the contributions from S 3s states. The splitting between the bonding and antibonding s-like bands at the high-symmetry points Γ and M of the Brillouin zone is no larger than 1.96 eV. In the range –5.46 to –0.53 eV, there are six filled bonding bands, to which the major contribution is made by the S 3p states. The upper and lower edges of the entire band are at the points M and Γ of the Brillouin zone. There are three antibonding Ti 3d bands of symmetry t_{2g} above the Fermi level (E_F); these bands form the bottom of the conduction band. It is worth noting that the dispersion of these bands in k is very small (Fig. 3). A 1T TiS$_2$ monolayer is a semiconductor and it exhibits the indirect transition Γ–M and has a band gap E_g equal to ~1.65 eV.

The band spectrum of the 2H TiS$_2$ monolayer exhibits some essential differences. At the same time, this spectrum is, in many respects, similar to the band struc-
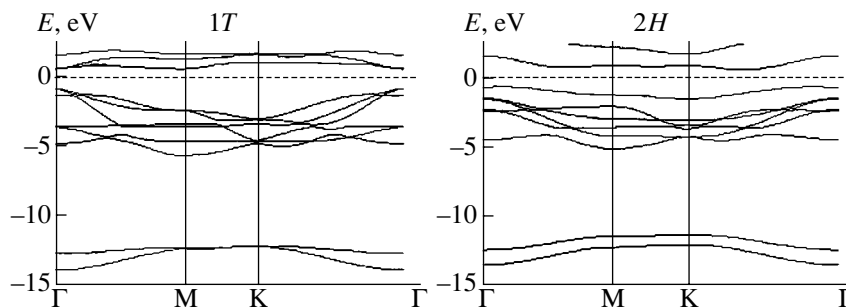
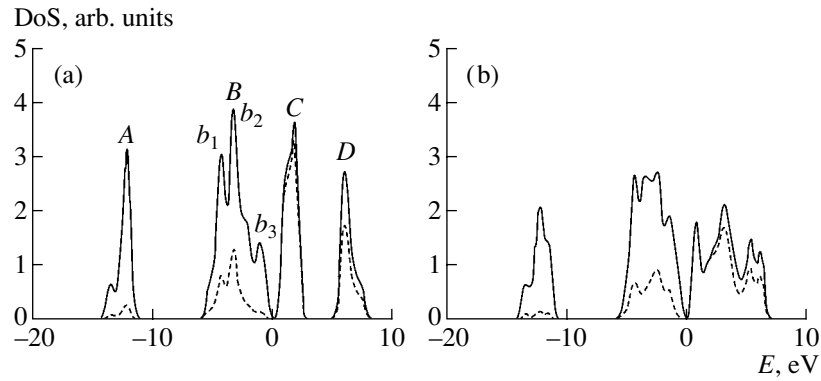**Fig. 3.** Energy bands for the 1T and 2H TiS$_2$ molecular layers.

Fig. 4. Total (solid lines) and Ti $3d$ partial (dashed lines) densities of states for (a) the $1T$ and (b) $2H$ TiS$_2$ monolayers.

ture of the other $2H$ disulfides [29–31]). Specifically, the dispersion of the S $3p$ bands in k is smaller than that for a $1T$ monolayer, and the band gap is also narrower (~1.25 eV).

We now compare the energy distributions of the total and partial DoS for the $1T$ and $2H$ monolayers (Fig. 4). The high peak at –12.4 eV (peak A) for a $1T$ TiS$_2$ monolayer is formed by the S $3d$ states. The peak near –3.41 eV (peak B) is formed by the S $3p$ states but with a noticeable contribution from the Ti $3d$ states. The lowest DoS peaks of the conduction band, C and D, are predominantly composed of Ti $3d(t_{2g})$ and Ti $3d(e_g)$ states with an admixture of antibonding S $3p$ and Ti sp states. These DoS bands show a number of substructures. For instance, the DoS profile of the S $3p$-like band (peak B) shows three maximums (b_1, b_2, and b_3), which are evident in the spectrum of the crystal as well [32]. These maximums are attributed to the bonding S $3p$–Ti $4s$, $4p$ and S $3p$–Ti $3d$ states, and the antibonding S $3p$ states, respectively. From the DoS distribution derived for a $3H$ monolayer, it is evident that the above peaks (A–D) are less intense, and subbands C and D merge into one antibonding band of a mixed type: Ti $3d(t_{2g} + e_g)$–S $3p$.

The dispersion and DoS distribution in the bands for a $1T$ TiS$_2$ monolayer are, in many respects, similar to those of the crystal [4, 20–22] (see Table 2). This result is a manifestation of the fact that the basic features of the distribution of electrons in TiS$_2$ are controlled by strong covalent-ion "intralayer" interactions. Nevertheless, the electronic properties of a monolayer and crystal are different: as mentioned above, the TiS$_2$ crystal is a semimetal while the monolayer is a semiconductor with a band gap of 1.65 eV. The change in the type of local atomic coordination, $1T \longleftrightarrow 2H$, does not lead to a change in the semiconductor properties of the monolayer and affects only the type and energy of the interband transitions.

Finally, our calculations show that the total energy of a $1T$ TiS$_2$ monolayer (–55.785 eV/atom) is lower than that of a $2H$ monolayer (–55.587 eV/atom). This

result means that the octahedral coordination favorable (in energy terms) for the TiS$_2$ crystal remains favorable for a single TiS$_2$ monolayer.

3.2. 1T and 2H Nanostripes

The results of the calculations are shown in Figs. 5 and 6 and are listed in Table 1. The band structure near the Fermi level for the stripes of types I and III and for the $1T$ TiS$_2$ monolayer are similar; the stripes remain semiconductors. We note only some lowering of the lowest empty quasi-planar Ti $3d(t_{2g})$ band. This effect is due to a decrease in the splitting of the e_g–t_{2g} states of Ti atoms in a section of the nanostripes due to some distortion in their environment.

At the same time, the bands of a $2H$ TiS$_2$ stripe (type IV) intersect the Fermi level E_F (Fig. 5), resulting in the formation of 1D metal states similar to the states observed for $2H$ MoS$_2$ stripes of the same structure [24]. Analysis of the composition (partial DoS) of these bands (Fig. 6) suggests that they are formed mainly from the $3d$ states of Ti atomic chains in a section of the stripe. Furthermore, a certain contribution is made by the $3d$ states of two parallel S chains at the edges of the stripe. These states are split off from the common hybrid Ti $3d$–S $3p$ valence band. As in the case of the monolayers, the octahedral configuration of Ti atoms appears to be preferable, and the $1T$-like nanostripes are more stable than their $2H$ analogues (Table 1).

3.3. 1T and 2H Nanotubes

As a result of DFT–TB minimization of the total energy E_{tot} for the (20, 0) and (20, 20) $1T$ and $2H$ TiS$_2$ NTs, we find that all the NTs are stable, and their optimized structures remain cylindrical in contrast to, e.g., NiCl$_2$ NTs [33]. The diameters of the optimized $1T$ TiS$_2$ NTs differ from the initial diameters, obtained when "twisting" the corresponding nanostripes, by 0.3–0.6%. For metastable $2H$ TiS$_2$ NTs, the effects of structural relaxation are much more pronounced: the above-men-
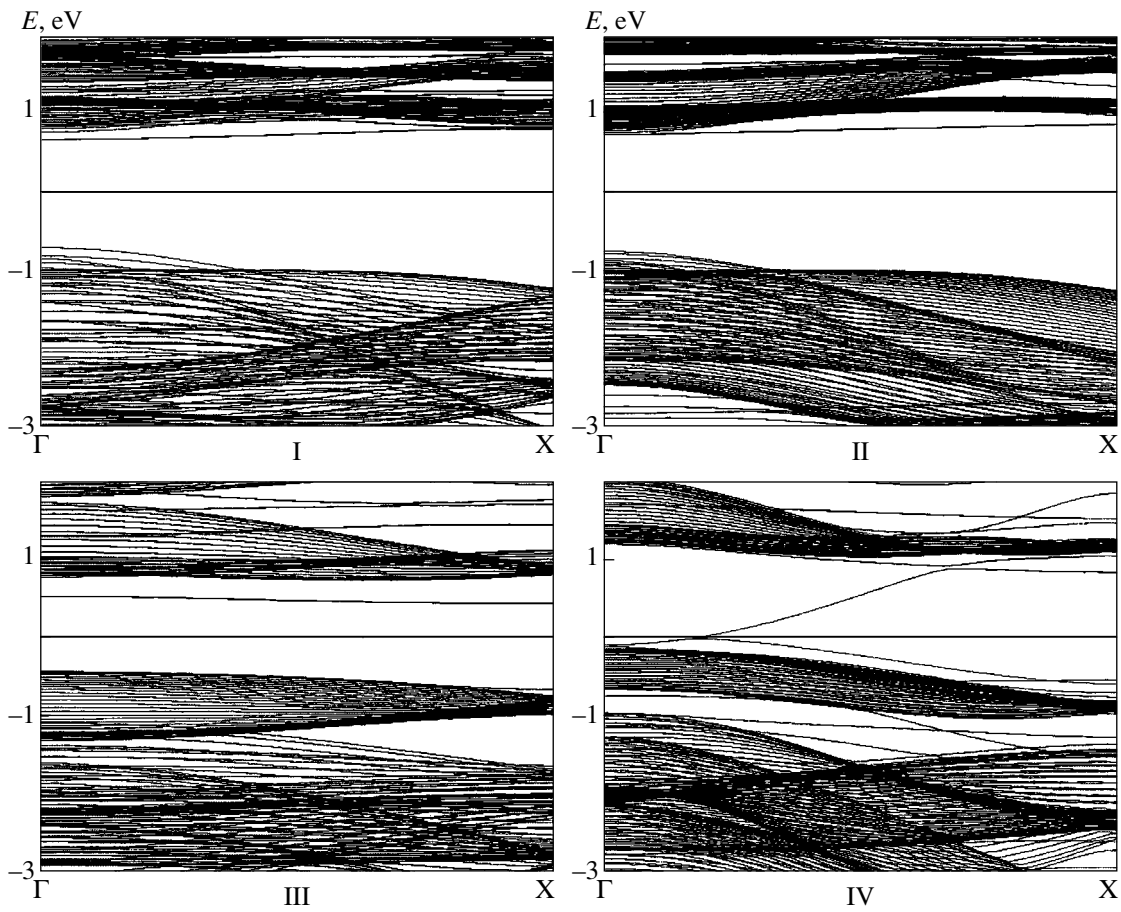
Fig. 5. Energy bands for the 1T (types I and II) and 2H (types III and IV) TiS$_2$ nanostripes.
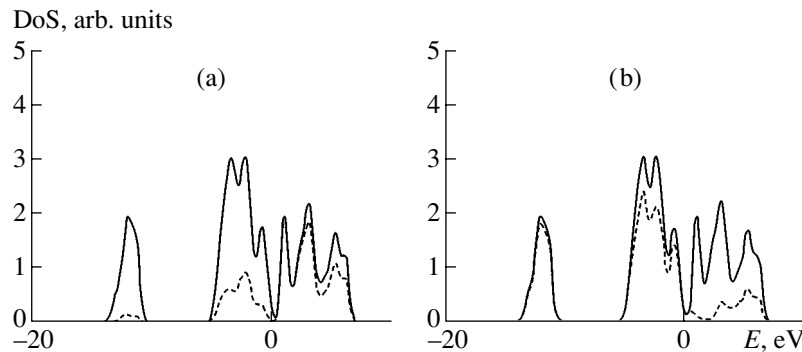

Fig. 6. Total (solid line) and partial (dashed lines) DoS for a 2H TiS$_2$ nanostripe of type V (see text). The partial DoS for (a) Ti 3d and (b) S 3p states are shown.

tioned difference in diameter can be as high as 4.5–7% (Table 1).

The relative stability of the tubular TiS$_2$ nanostructures can be inferred from the values of E_{tot} listed in Table 1. The tubes are less stable than the corresponding 1T or 2H monolayers; in turn, the NTs with an octahedral atomic arrangement of their walls (1T-like NTs) are more stable than the NTs "twisted" from 2H monolayers.

We now consider the strain energy (E_{st}). We define E_{st} as the difference between a NT and a corresponding nanostripe in relation to their total energy, i.e.,

$$E_{st} = E_{tot}(\text{TiS}_2 \text{ NT}) - E_{tot}(\text{TiS}_2 \text{ nanostripe}).$$

The values of E_{st} are listed in Table 1. Using these values, we can assess the relative role of the competitive energy effects controlling the preferential formation of particular structures, namely, the 1D planar nanostripes
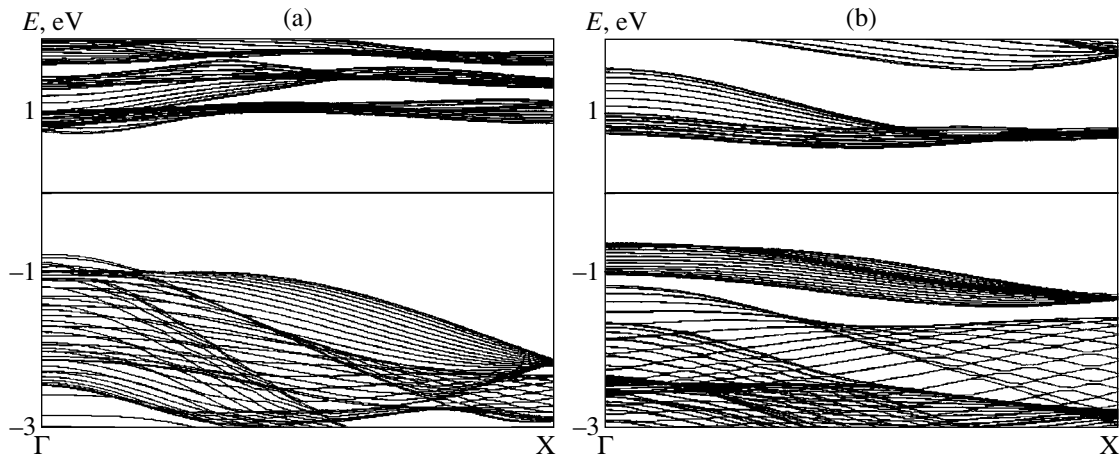
Fig. 7. Energy bands for *armchair* (20, 20) nanotubes based on (a) $1T$ and (b) $2H$ TiS$_2$ phases.

or the tubular nanostructures. For the 1D nanostripes, the destabilizing factor is generated by the dangling bonds of the edge atoms. For the NTs, this effect is excluded; however, the formation of the cylindrical structures requires extra energy to be spent to deform the planar layer. It is interesting that the values of E_{st} are substantially different for the $1T$- and $2H$-like NTs. It is evident from Table 1 that the $1T$ TiS$_2$ nanostripes are more stable than the NTs; however, the E_{st} values are small and decrease as the NT diameter increases. It is believed that this trend promotes the formation of predominantly multilayered TiS$_2$ NTs with relatively large diameters. Furthermore, there exists an additional mechanism of stabilization of multilayered NTs due to the van der Waals interaction between the neighboring walls of coaxial "molecular" S–Ti–S cylinders. It should be noted that such multilayered TiS$_2$ NTs have actually been experimentally observed [11–13]. Although the strain energy E_{st} for a (20, 20) $2H$ TiS$_2$ NT is negative, i.e., the formation of such an NT is favorable compared to a corresponding nanostripe of type IV (Table 1), these $2H$ TiS$_2$ NTs are less likely to be formed than the $1T$-like NTs, since they are less stable (lower E_{tot}) (see above).

We now consider the electronic properties of TiS$_2$ NTs (see Fig. 7 and Table 1). We can conclude that all these NTs are semiconductors, and their band gaps are wider for larger sizes D. The structural form of the walls ($1T$ or $2H$) and the NT configuration (*zigzag* or *armchair*) profoundly affect the band topology near the Fermi level, thus defining the types of transitions, i.e., direct or indirect (Fig. 7). As the NT diameter increases, the NT band gap generally approaches the band gap for the corresponding $1T$ or $2H$ molecular monolayers.

4. CONCLUSIONS

In this study, atomic models for quasi-1D planar (nanostripe) and cylindrical (nanotube) TiS$_2$ nanostruc-

tures are suggested. By using the DFT–TB approach, the electron energy spectra and the stability conditions are analyzed for these nanostructures in comparison with 2D (monolayer) and 3D (crystal) TiS$_2$ forms. The possibility of $1T \longleftrightarrow 2H$ phase transitions in the 2D and 1D TiS$_2$ nanostructures is theoretically studied for the first time. It is shown that the octahedral atomic surrounding typical of a stable $1T$ TiS$_2$ crystal is preserved in the nanostructures. In contrast to the TiS$_2$ crystal, all the stable 2D and 1D nanostructures are semiconductors.

The next research task would be to study the electronic properties of TiS$_2$ nanotubes in relation to the number of constituent molecular layers and the defects in these layers. An interesting area for further development of the theory of TiS$_2$ NTs and NTs of other d-metal disulfides could be simulation of the structure and electronic properties of as yet unknown multilayered "composite" NTs that consist of cylinders of different d-metal disulfides. For example, one can readily anticipate that, similarly to the well-known nanotubular materials based on carbon NTs (see [18, 19, 34]), "composite" TiS$_2$/NbS$_2$ NTs could form an appropriate system for producing quasi-1D semiconductor–metal heterojunctions.

REFERENCES

1. G. V. Samsonov and I. M. Vinitskiĭ, *Handbook of Refractory Compounds* (Metallurgiya, Moscow, 1976; Plenum, New York, 1980).
2. L. F. Mattheiss, Phys. Rev. B **8**, 3719 (1973).

3. D. G. Clerc, R. D. Poshusta, and A. C. Hess, J. Phys. Chem. **100**, 15735 (1976).

4. Z. Y. Wu, F. L. Lemoigno, P. Gressier, *et al.*, Phys. Rev. B **54**, 11009 (1996).

5. A. Zettl, Adv. Mater. **8**, 443 (1996).

6. P. M. Ajayan and O. Z. Zhou, Carbon Nanotubes **80**, 391 (2001).

7. V. V. Pokropivnyǐ, Poroshk. Metall. (Kiev), No. 9/10, 50 (2001); Poroshk. Metall. (Kiev), No. 11/12, 51 (2001).

8. R. Tenne, Chem. Eur. J. **8**, 5297 (2002).

9. A. L. Ivanovskiǐ, Usp. Khim. **71**, 203 (2002).

10. C. N. R. Rao and M. Nath, J. Chem. Soc. Dalton Trans., No. 1, 1 (2003).

11. J. Chen, S. L. Li, Z. L. Tao, and F. Gao, Chem. Commun. **8**, 980 (2003).

12. J. Chen, Z. L. Tho, and S. L. Li, Angew. Chem. Int. Ed. Engl. **42**, 2147 (2003).

13. J. Chen, S. L. Li, Z. L. Tao, *et al.*, J. Am. Chem. Soc. **125**, 5284 (2003).

14. G. Seifert, H. Terrones, M. Terrones, *et al.*, Phys. Rev. Lett. **85**, 146 (2000).

15. G. Seifert, H. Terrones, M. Terrones, and T. Frauenheim, Solid State Commun. **115**, 635 (2000).

16. G. Seifert, H. Terrones, M. Terrones, *et al.*, Solid State Commun. **114**, 245 (2000).

17. H. I. Starnberg, Mod. Phys. Lett. **13**, 455 (2000).

18. *The Science and Technology of Carbon Nanotubes*, Ed. by K. Tanaka, T. Yamabe, and K. Fuku (Elsevier, Oxford, 1999).

19. P. J. F. Harris, *Carbon Nanotubes and Related Structures: New Materials for the Twenty-first Century* (Cambridge Univ. Press, Cambridge, 1999).

20. F. Krumeich, H. J. Muhr, M. Niederberger, *et al.*, Z. Anorg. Allg. Chem. **626**, 2208 (2000).

21. H.-J. Muhr, F. Krumeich, U. P. Schonholzer, *et al.*, Adv. Mater. **12**, 231 (2000).

22. M. Niederberger, H. J. Muhr, F. Krumeich, *et al.*, Chem. Mater. **12**, 1995 (2000).

23. G. T. Chandrappa, N. Steunou, S. Cassaignon, *et al.*, J. Sol-Gel Sci. Technol. **26**, 593 (2003).

24. M. V. Bollinger, J. V. Lauritsen, K. W. Jacobsen, *et al.*, Phys. Rev. Lett. **87**, 196803 (2001).

25. D. Porezag, Th. Frauenchaim, Th. Kohler, *et al.*, Phys. Rev. B **51**, 12947 (1995).

26. C. M. Fang, R. A. de Groot, and C. Haas, Phys. Rev. B **56**, 4455 (1997).

27. S. Sharma, T. Nautiyal, G. S. Singh, *et al.*, Phys. Rev. B **59**, 14833 (1999).

28. H. Matrinez, Y. Tison, I. Baraille, *et al.*, J. Electron Spectrosc. Relat. Phenom. **125**, 181 (2002).

29. A. Klein, S. Tiefenbacher, V. Eyert, *et al.*, Phys. Rev. B **64**, 205416 (2001).

30. K. Kobayashi and J. Yamauchi, Phys. Rev. B **51**, 17085 (1995).

31. P. Raybaud, H. Hafner, G. Kresse, and H. Toulhoat, Phys. Rev. Lett. **80**, 1481 (1998).

32. Y. S. Kim, J. Li, I. Tanaka, *et al.*, Mater. Trans., JIM **41**, 1088 (2000).

33. Y. R. Hacohen, R. Popovitz-Biro, Y. Prior, *et al.*, Phys. Chem. Chem. Phys. **5**, 1644 (2003).

34. A. L. Ivanovskiǐ, *Quantum Chemistry in Materials Science: Nanotubular Forms of Matter* (Ural. Otd. Ross. Akad. Nauk, Yekaterinburg, 1999) [in Russian].

Translated by É. Smorgonskaya

Exciton States in Semiconductor Spherical Nanostructures

S. I. Pokutnyi

Ilyichevsk Scientific Training Center, Mechnikov Odessa National University, Ilyichevsk, 68001 Ukraine
e-mail: univer@ivt.ilyichevsk.odessa.ua

Abstract—The results of theoretical studies of the energy spectra of excitons moving in semiconductor spherical quantum dots are described. The contributions of the kinetic electron and hole energies, the energy of the Coulomb interaction between an electron and hole, and the energy of the polarization interaction between them to the energy spectrum of an exciton in a quantum dot with a spherical (quantum dot)–(insulator medium) interface is analyzed. © 2005 Pleiades Publishing, Inc.

1. INTRODUCTION

Progress in solid-state technology has made it possible to fabricate crystalline structures whose linear size is comparable to de Broglie's wavelengths of an electron and hole and/or to their Bohr radii. At nanoscale geometrical parameters of semiconductor systems, the phenomena of quantum confinement of charge carriers play an important role in optical and electrooptical processes [1–4].

Since the energy gap of semiconductors is much smaller than that of semiconductor (insulator) matrices, the motion of charge carriers in a spherical quantum dot is restricted in all three directions to the bulk of the quantum dot (QD); i.e., charge carriers move in a three-dimensional spherical potential well. It follows that neither an electron and a hole together nor an exciton in a QD have a quasi-momentum. Therefore, we can only deal with the states of quasiparticles in a QD. In what follows, by an exciton in a QD, we imply an exciton state that has no quasi-momentum.

The optical and electrooptical properties of such heterophase systems are, to a large extent, determined by the energy spectrum of a spatially confined electron–hole pair (exciton) [4–8]. The energy spectrum of charge carriers in a QD is completely discrete, starting from the dot size a on the order of Bohr radii of an electron a_e or hole a_h or smaller [9–11]. Therefore, such QDs are also called "superatoms" [12]. Under these conditions, the interface between a QD and the insulator matrix can give rise to quantum confinement of electrons and holes in the QD. This phenomenon is related both to a purely spatial restriction of the confinement region [5, 6, 13] and to the polarization interaction of charge carriers with the QD surface [9–11, 14–20].

At the present time, the theory of exciton states in quasi-zero-dimensional systems is not sufficiently developed. Therefore, we study the contribution of the kinetic energies of an electron and hole, the energy of the Coulomb interaction between them, and the energy of the polarization interaction of an electron and hole with the spherical interface between a QD and the insulator medium to the energy spectrum of an exciton in a QD.

2. SPECTRUM OF AN EXCITON IN A QUASI-ZERO-DIMENSIONAL SEMICONDUCTOR SYSTEM

Following [14–20], we consider a simple model of a quasi-zero-dimensional system: a neutral semiconductor spherical QD of radius a with permittivity ε_2 surrounded by a medium with permittivity ε_1, the permittivity of the QD ε_2 being much greater than the permittivity ε_1 of the medium (i.e., $\varepsilon_2 \gg \varepsilon_1$). An electron e and a hole h with the effective masses m_e and m_h (r_e and r_h are the distances of the electron and hole from the center of the QD) move in the bulk of the QD (see Fig. 1). We assume that the electron and hole bands are parabolic.
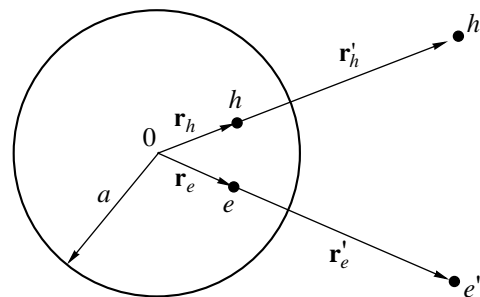

Fig. 1. Schematic diagram of an exciton in a spherical semiconductor nanocrystal. The radius vectors $\mathbf{r}_e$ and $\mathbf{r}_h$ determine the distance of the electron e and the hole h from the center of a nanocrystal of radius a. The image charges $e' = (a/r_e)e$ and $h' = -(a/r_h)e$ are located at the distances $r'_e = (a^2/r_e)$ and $r'_h = (a^2/r_h)$ from the center of the nanocrystal 0 and represent point image charges of the electron and hole, respectively.

The characteristic scales of the problem are a, a_e, a_h, and a_{ex}, where

$$a_e = \frac{\varepsilon^2 \hbar^2}{m_e e^2}, \quad a_h = \frac{\varepsilon^2 \hbar^2}{m_h e^2}, \quad a_{ex} = \frac{\varepsilon^2 \hbar^2}{\mu e^2}$$

are the Bohr radii of an electron, hole, and exciton, respectively, in an infinite semiconductor with permittivity ε_2; e is the elementary charge; and

$$\mu = \frac{m_e m_h}{m_e + m_h}$$

is the reduced exciton effective mass. The fact that all the characteristic scales of the problem are much greater than the interatomic distance a_0 [21], i.e.,

$$a, a_e, a_h, a_{ex} \gg a_0,$$

makes it possible to consider the motion of the electron and hole in the QD in the effective-mass approximation.

In [14, 17–19], the spectrum of an exciton in a QD was obtained under the assumption that, for an electron and hole moving in the bulk of the QD, the QD is an infinitely deep potential well. Thus, the QD radius a is bounded by the conditions

$$a_h \ll a \le a_e \approx a_{ex}. \tag{1}$$

Under conditions (1), we can use the adiabatic approximation (where the hole effective mass m_h is much greater than the electron effective mass m_e, i.e., $m_h \gg m_e$), assuming that the kinetic energy of an electron in the QD is

$$T^e_{n_{e,0}}(S) = E^e_{n_{e,0}}(S) = \frac{\pi^2 n_e^2}{S^2}, \tag{2}$$

where

$$S = \frac{a}{a_{ex}}$$

is the reduced radius of the QD. We also assume that energy (2) is the highest energy in the problem. Using only first-order perturbation theory, the authors of [17–19] obtained the exciton spectrum $E^{n_h, l_h, m_h = 0}_{n_e, l_e = 0, m_e = 0}(S)$ in a QD of radius S in the following state: n_e, $l_e = 0$, $m_e = 0$ and n_h, l_h, $m_h = 0$. Here, n_e, l_e, m_e and n_h, l_h, m_h are the principal, orbital, and magnetic quantum numbers of the electron and hole,

$$E^{t_h}_{n_e, 0, 0}(S)$$

$$= E_g + T^e_{n_e, 0}(S) \left[1 + \frac{\overline{U}^{n_e, 0, 0}_{pol}(S)}{T^e_{n_e, 0}(S)} - \frac{\widetilde{\overline{V}}^{n_e, 0, 0; t_h}_{eh}(S)}{T^e_{n_e, 0}(S)} \right]. \tag{3}$$

In (3), the energy of the polarization interaction of the electron and hole with the QD surface $\overline{U}^{n_e, 0, 0}_{pol}(S)$ aver-

aged over the electron wave functions for a spherical well of infinite depth is

$$\overline{U}^{n_e, 0, 0}_{pol}(S) = \overline{V}_{hh'}(S) + \overline{V}^{n_e, 0, 0}_{ee'}(S)$$

$$+ [\overline{V}^{n_e, 0, 0}_{eh'}(S) + \overline{V}^{n_e, 0, 0}_{he'}(S)] = \frac{Z_{n_e, 0} + (\varepsilon_2/\varepsilon_1) - 1}{S}. \tag{4}$$

We write the expressions for the average values of the energies of interaction of the electron with its own image [17–19] as

$$\overline{V}^{n_e, 0, 0}_{ee'}(S) = \frac{Z_{n_e, 0}}{S},$$

$$Z_{n_e, 0} = \frac{\varepsilon_2}{\varepsilon_1} + 2 \int\limits_2^1 \frac{dx \sin^2 \pi n_e x}{1 - x^2}; \tag{5}$$

of the hole with its own image as

$$\overline{V}_{hh'}(S) = \frac{1 + (\varepsilon_2/\varepsilon_1)}{S}; \tag{6}$$

of the electron with the hole image and the hole with the electron image as

$$\overline{V}^{n_e, 0, 0}_{eh'}(S) + \overline{V}^{n_e, 0, 0}_{he'}(S) = -\frac{2}{S}; \tag{7}$$

and the energy of the Coulomb interaction between the electron and hole as

$$\widetilde{\overline{V}}^{n_e, 0, 0; t_h}_{eh}(S) = -\frac{2}{3}[\ln(2\pi n_e) + \gamma - \text{Ci}(2\pi n_e)]$$

$$+ \omega(S, n_e)\left(t_h + \frac{3}{2}\right), \tag{8}$$

where the frequency of the vibrations of the hole is

$$\omega(S, n_e) = 2\left(1 + \frac{2}{3}\pi^2 n_e^2\right)^{1/2}\left(\frac{m_e}{m_h}\right)^{1/2} S^{-3/2}. \tag{9}$$

In formula (8), $t_h = 2n_{r_h} + l_h = 0, 1, 2, \ldots$ is the principal quantum number of the hole, $n_{r_h} = 0, 1, 2, \ldots$ is the radial quantum number of the hole, $\text{Ci}(y)$ is the integral cosine, and $\gamma = 0.577$ is Euler's constant. In what follows, the energy is measured in units of $\text{Ry}_e = \hbar^2/2m_e a_e^2$ and a dimensionless QD radius $S = a/a_e$ is used.

It should be noted that formulas (4)–(8) were obtained in [17–19] by averaging the corresponding expressions for the interaction energies with wave functions of the QD (of a spherical well of infinite depth).

The representation of the exciton spectrum $E^{t_h}_{n_e, 0, 0}(S)$ in form (3) makes it possible to compare the contribution of the energy of Coulomb interaction (8) between the electron and hole and the energy of polarization interaction (4) with the contribution of electron kinetic energy (2) to the exciton spectrum.
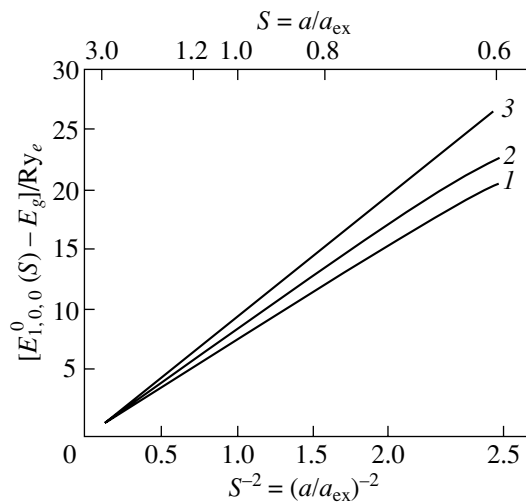
Fig. 2. The dependence of the exciton energy spectrum $E_{1,0,0}^0(S)$ on the size of the nanocrystal $S = a/a_{ex}$: (*1*) experimental exciton spectrum taken from [5, 8]; (*2*) exciton spectrum $E_0(a)$ obtained by a variational method in [20]; and (*3*) the electron kinetic energy $T_{1,0}^e(S)$ (Eq. (2)).

Expression (3), obtained for the exciton spectrum, is valid only for the lowest exciton states (n_e, 0, 0; t_h) under which the inequality

$$E_{n_e,0,0}^{t_h}(S) - E_g \ll \Delta V(S) \qquad (10)$$

is satisfied; here, $\Delta V(S)$ is the depth of the potential well for electrons in the QD (e.g., for a CdS QD with a radius in range (1), the quantity $\Delta V = 2.3$–2.5 eV [7]).

In [20], rather than restricting the analysis to the adiabatic approximation, we found the spectrum $E_0(a)$ of the exciton ground state in a QD of radius a for a simple model of a quasi-zero-dimensional system (see Fig. 1) using the variational method. In contrast to [14, 17–19], the radius of the QD a in this case was not bounded by conditions (1). The results of a variational calculation of the spectrum are shown in Fig. 2. Note that the spectrum $E_0(a)$ in a QD of radius a was obtained in [20] under condition (10), which corresponds to the conditions of the experiments carried out in [5–8].

3. CONTRIBUTIONS OF THE KINETIC, POLARIZATION, AND COULOMB ENERGIES TO THE SPECTRUM OF AN EXCITON IN A QUANTUM DOT

In [5, 8], peaks of interband absorption were observed for spherical CdS QDs ($\varepsilon_2 = 9.3$) with radii a ranging from 1.2 to 30 nm dispersed in a transparent matrix of silicate glass (with a permittivity $\varepsilon_1 = 2.25$). The effective masses of an electron m_e, hole m_h, and the reduced mass of an exciton μ in CdS were $m_e/m_0 = 0.205$, $m_h/m_0 = 5$, and $\mu/m_0 = 0.197$, respectively. In [5, 8], the dependence of the positions of the QD absorption lines resulting from interband transitions to the electron quantum-confinement levels ($n_e = 1$ and $l_e = 0$), ($n_e = 1$ and $l_e = 1$), and ($n_e = 1$ and $l_e = 2$) in the conduction band on the QD radius a were experimentally determined.

Table 1 lists the parameters of the exciton spectrum $E_{1,0,0}^{t_h}(S)$ according to Eq. (3) under the conditions of the experiments carried out in [5, 8] for CdS QDs with radii $a = 1.5$–3.0 nm. According to expressions (4), (8), and (2), the ratios of the energy of the polarization interaction $\overline{U}_{pol}^{1,0,0}(S)/T_{1,0}^e(S)$ and the energy of Cou-

Table 1. The contribution of the energy of the Coulomb interaction of the electron and hole $\widetilde{V}_{eh}^{1,0,0;t_h}(a)/T_{1,0}^e(a)$ (Eq. (8)) and the energy of the polarization interaction $\overline{U}_{pol}^{1,0,0}(a)/T_{1,0}^e(a)$ (Eq. (4)) to the exciton spectrum $E_{1,0,0}^{t_h}(a)$ (Eq. (3)) in comparison with the contribution of the electron kinetic energy $T_{1,0}^e(a)$ (Eq. (2)). The values refer to CdS QDs with radii $a = 1.5$–3.0 nm under the conditions of the experiments carried out in [5, 8]

a, nm (S)	$\dfrac{T_{1,0}^e(S)}{Ry_e}$	t_h	$\dfrac{\widetilde{V}_{eh}^{1,0,0;t_h}(S)}{T_{1,0}^e(S)}$, %	$\dfrac{\overline{U}_{pol}^{1,0,0}(S)}{T_{1,0}^e(S)}$, %	$\dfrac{E_{1,0,0}^{t_h}(S) - E_g}{Ry_e}$
1.5	23.35	0	17.4	55.8	35.08
(0.624)		1	8.5		37.34
2.0	14.26	0	25.6	74.4	21.21
(0.83)		1	15.3		22.68
2.5	9.13	0	34.0	93.0	14.51
(1.04)		1	22.5		15.56
3.0	6.34	0	42.6	111.5	10.71
(1.25)		1	30.0		11.51

Table 2. The contributions of the energy of the interaction of the electron with its own image $\bar{V}_{ee'}^{1,0,0}(a)$ (Eq. (5)), the energy of the interaction of the hole with its own image $\bar{V}_{hh'}^{1,0,0}(a)$ (Eq. (6)), and the energy of the interaction of the electron with the image of the hole and of the interaction of the hole with the image of the electron $\bar{V}_{eh'}^{1,0,0}(a) + \bar{V}_{he'}^{1,0,0}(a)$ (Eq. (7)) to the energy of the polarization interaction $\bar{U}_{\mathrm{pol}}^{1,0,0}(a)$ (Eq. (4)), as well as of the ratio of the energy of the Coulomb interaction to the energy of the polarization interaction $\tilde{\bar{V}}_{eh}^{1,0,0;\,t_h}(a)/\bar{U}_{\mathrm{pol}}^{1,0,0}(a)$ (8) and (4)). The values correspond to CdS quantum dots with radii $a = 1.5$–3.0 nm under the conditions of the experiments carried out in [5, 8]

a, nm (S)	$\dfrac{\bar{U}_{\mathrm{pol}}^{1,0,0}(S)}{\mathrm{Ry}_e}$	$\dfrac{\bar{V}_{ee'}^{1,0,0}(S)}{\bar{U}_{\mathrm{pol}}^{1,0,0}(S)}$, %	$\dfrac{\bar{V}_{hh'}^{1,0,0}(S)}{\bar{U}_{\mathrm{pol}}^{1,0,0}(S)}$, %	$\dfrac{\left|\bar{V}_{eh'}^{1,0,0}(S) + \bar{V}_{he'}^{1,0,0}(S)\right|}{\bar{U}_{\mathrm{pol}}^{1,0,0}(S)}$, %	t_h	$\dfrac{\left|\tilde{\bar{V}}_{eh}^{1,0,0;\,t_h}\right|}{\bar{U}_{\mathrm{pol}}^{1,0,0}(S)}$, %
1.5	14.14	64.5	58.2	22.7	0	31.2
(0.624)					1	15.2
2.0	10.61	64.5	58.2	22.7	0	34.3
(0.83)					1	20.5
2.5	8.49	64.5	58.2	22.7	0	36.6
(1.04)					1	24.2
3.0	7.07	64.5	58.2	22.7	0	38.2
(1.25)					1	26.9

lomb interaction $\tilde{\bar{V}}_{eh}^{1,0,0;\,t_h}(S)/T_{1,0}^e(S)$ to the increase in the electron kinetic energy with the QD radius S are proportional to S and $S^{1/2}$, respectively. The behavior of these ratios is confirmed by the simulation results listed in Table 1.

It follows from Table 1 that the major contribution to exciton spectrum (3) is made by the energy of the polarization interaction $\bar{U}_{\mathrm{pol}}^{1,0,0}(S)/T_{1,0}^e(S)$ (Eq. (4)). This contribution varies from 55.8% for $a = 1.5$ nm to 112% for $a = 3$ nm. However, the energy of the Coulomb interaction $\tilde{\bar{V}}_{eh}^{1,0,0;\,t_h}(S)/T_{1,0}^e(S)$ (Eq. (8)) makes only a small negative contribution, whose magnitude changes from 17.4% ($t_h = 0$) and 8.5% ($t_h = 1$) at $a = 1.5$ nm to 42.6% ($t_h = 0$) and 30% ($t_h = 1$) at $a = 3$ nm. The results listed in Table 1 are also confirmed by the results of a variational calculation of the exciton spectrum $E_0(a)$ in a QD of radius a, which were obtained in [20] without using the adiabatic approximation under the conditions of the experiments carried out in [5, 8].

The main contribution to the energy of the polarization interaction $\bar{U}_{\mathrm{pol}}^{1,0,0}(S)$ (Eq. (4)) is made by the energy of the interaction of the electron with its image $\bar{V}_{ee'}^{1,0,0}(S)/\bar{U}_{\mathrm{pol}}^{1,0,0}(S) \approx 64.5\%$ (Eq. (5)) and the energy of the interaction of the hole with its image $\bar{V}_{hh'}^{1,0,0}(S)/\bar{U}_{\mathrm{pol}}^{1,0,0}(S) \approx 58.2\%$ (Eq. (6)). The contribution $[\bar{V}_{eh'}^{1,0,0}(S) + \bar{V}_{he'}^{1,0,0}(S)]/\bar{U}_{\mathrm{pol}}^{1,0,0}(S)$ (Eq. (7)) of the energy of the interaction of the electron with the hole image and the energy of the interaction of the hole with

the electron image is negative and its magnitude is equal to 22.7% (see Table 2). It is important that these contributions do not depend on the QD radius S.

The energy of the Coulomb interaction $\tilde{\bar{V}}_{eh}^{1,0,0;\,t_h}(S)$ (Eq. (8)) yields a much smaller contribution to exciton spectrum (3) than the energy of the polarization interaction $\bar{U}_{\mathrm{pol}}^{1,0,0}(S)$ (Eq. (4)). The ratio of these energies $\tilde{\bar{V}}_{eh}^{1,0,0;\,t_h}(S)/\bar{U}_{\mathrm{pol}}^{1,0,0}(S)$ is negative, and its magnitude changes from 31% ($t_h = 0$) and 15% ($t_h = 1$) at $a = 1.5$ nm to 38% ($t_h = 0$) and 27% ($t_h = 1$) at $a = 3$ nm (see Table 2).

The authors of [5] claimed that, at large radii a of a CdS QD, starting with a size of $a \geq 2.0$ nm, the experimental exciton spectrum could be adequately described by the kinetic energy of an electron in a QD $T_{1,0}^e(a)$ (Eq. (2)). Actually, it follows from Table 1 that, at $2 \leq a \leq 3$ nm, the ratio of the sum of the polarization and Coulomb interaction energies to the kinetic energy of an electron is large:

$$\frac{\left|\bar{U}_{\mathrm{pol}}^{1,0,0} + \tilde{\bar{V}}_{eh}^{1,0,0;\,t_h}(S)\right|}{T_{1,0}^e(S)} \approx 49\text{–}69\%.$$

Even for smallest experimentally realized QDs of radius $a = 1.5$ nm, this ratio is substantial: ~38% (see Table 1).

Thus, in the context of a simple model of a quasi-zero-dimensional system, we showed that, even for smallest experimentally realized QDs of radius $a < a_{\mathrm{ex}}$,

the contribution of the electron kinetic energy $T_{1,0}^{e}(a)$ (Eq. (2)) to the spectrum of an exciton in a QD $E_{1,0,0}^{t_h}(a)$ (Eq. (3)) is of the same order of magnitude as the contributions of the energies of the polarization $\overline{U}_{\text{pol}}^{1,0,0}(a)$ (Eq. (4)) and Coulomb $\widetilde{\overline{V}}_{eh}^{n_e,0,0;\,t_h}(a)$ (Eq. (8)) interactions. Therefore, describing the exciton spectrum for a QD of size a satisfying conditions (1) using only the expression for the electron kinetic energy $T_{1,0}^{e}(a)$ (Eq. (2)) is not quite justified.

4. CONCLUSIONS

In this study, we mainly considered simple quasi-zero-dimensional systems. Nevertheless, the obtained results make it possible to understand features of the optical processes in complex multilayer spherical nanosystems related to electron and exciton states [1–4].

REFERENCES

1. Zh. I. Alferov, Fiz. Tekh. Poluprovodn. (St. Petersburg) **32**, 3 (1998) [Semiconductors **32**, 1 (1998)].

2. A. D. Yoffe, Adv. Phys. **42**, 173 (1993).

3. S. V. Gaponenko, Fiz. Tekh. Poluprovodn. (St. Petersburg) **30**, 577 (1996) [Semiconductors **30**, 315 (1996)].

4. S. I. Pokutniĭ, *The Theory of Excitons in Quasi-Zero-Dimensional Semiconductor Systems* (Astroprint, Odessa, 2003) [in Russian].

5. A. I. Ekimov and A. A. Onushchenko, Pis'ma Zh. Éksp. Teor. Fiz. **40** (8), 337 (1984) [JETP Lett. **40**, 1136 (1984)].

6. A. I. Ekimov, A. A. Onushchenko, and Al. L. Éfros, Pis'ma Zh. Éksp. Teor. Fiz. **43**, 292 (1986) [JETP Lett. **43**, 376 (1986)].

7. V. Ya. Grabovskis, Ya. Ya. Dzenis, and A. I. Ekimov, Fiz. Tverd. Tela (Leningrad) **31** (1), 272 (1989) [Sov. Phys. Solid State **31**, 149 (1989)].

8. D. Chepik, A. Efros, and A. Ekimov, J. Lumin. **47** (3), 113 (1990).

9. N. A. Efremov and S. I. Pokutniĭ, Fiz. Tverd. Tela (Leningrad) **27**, 48 (1985) [Sov. Phys. Solid State **27**, 27 (1985)].

10. S. I. Pokutniĭ, Fiz. Tverd. Tela (St. Petersburg) **35**, 257 (1993) [Phys. Solid State **35**, 129 (1993)].

11. S. I. Pokutniĭ, Fiz. Tekh. Poluprovodn. (St. Petersburg) **31**, 1443 (1997) [Semiconductors **31**, 1247 (1997)].

12. E. A. Andryushin and A. P. Silin, Fiz. Tverd. Tela (Leningrad) **33**, 211 (1991) [Sov. Phys. Solid State **33**, 123 (1991)].

13. Al. L. Éfros and A. L. Éfros, Fiz. Tekh. Poluprovodn. (Leningrad) **16**, 1209 (1982) [Sov. Phys. Semicond. **16**, 772 (1982)].

14. N. A. Efremov and S. I. Pokutniĭ, Fiz. Tverd. Tela (Leningrad) **32**, 1637 (1990) [Sov. Phys. Solid State **32**, 955 (1990)].

15. N. V. Tkach and V. A. Golovatskiĭ, Fiz. Tverd. Tela (Leningrad) **32**, 2512 (1990) [Sov. Phys. Solid State **32**, 1461 (1990)].

16. G. V. Grigoryan, A. V. Rodina, and Al. L. Éfros, Fiz. Tverd. Tela (Leningrad) **32**, 3512 (1990) [Sov. Phys. Solid State **32**, 2037 (1990)].

17. S. I. Pokutniĭ, Fiz. Tekh. Poluprovodn. (Leningrad) **25**, 628 (1991) [Sov. Phys. Semicond. **25**, 381 (1991)].

18. S. I. Pokutnyi, Phys. Lett. A **168**, 433 (1992).

19. S. I. Pokutniĭ, Fiz. Tekh. Poluprovodn. (Leningrad) **30**, 1952 (1996) [Semiconductors **30**, 1015 (1996)]; Ukr. Fiz. Zh. **42** (1), 111 (1997).

20. S. I. Pokutniĭ, Fiz. Tverd. Tela (St. Petersburg) **38**, 2667 (1996) [Phys. Solid State **38**, 1463 (1996)].

21. V. M. Agranovich and V. L. Ginzburg, *Crystal Optics with Spatial Dispersion, and Excitons*, 2nd ed. (Nauka, Moscow, 1979; Springer, New York, 1984).

Translated by I. Zvyagin

High-Frequency Nonlinear Response of Double-Well Nanostructures

V. F. Elesin and I. Yu. Kateev

Moscow Engineering Physics Institute (State University), Moscow, 115409 Russia
Submitted November 2, 2004; accepted for publication January 19, 2005

Abstract—A theory on the high-frequency nonlinear response of a double-well nanostructure in a constant electric field has been developed. Such a structure is the next simplest in form after a single-well structure (a resonant-tunnel diode) but less complex than a superlattice with a one-band "Stark ladder." By solving the Schrödinger equation numerically, the polarization current over wide ranges of frequencies and fields, including high fields, is found for model and real structures. It is shown that the response of a double-well nanostructure is much higher (by one or two orders of magnitude) than that of a resonant-tunnel diode. A new optimal mode of generation, similar to that based on interlevel transitions in a coherent laser, is predicted. © *2005 Pleiades Publishing, Inc.*

1. INTRODUCTION

Resonant tunneling appears to show considerable promise for application in nanostructure-based lasers, integrated circuits, and logic devices [1–3]. The satisfied conditions for coherent tunneling offer fundamentally new opportunities in this field. Examples include coherent lasers [4], in which population inversion is not necessary, and oscillators based on the effect of a two-band "Stark ladder" [5], which provide generation in the bulk.

The present-day level of technology has already made it possible to accomplish coherence over long lengths (up to ten quantum wells (QWs) [6]). Furthermore, the simple condition for coherent tunneling $\tau_\Gamma < \tau_{ph}$, where $\tau_\Gamma = \hbar/\Gamma$, Γ is the level width, and τ_{ph} is the coherence degradation time, can be too strict. In fact, a detailed theoretical consideration shows that, under certain conditions, electron–phonon interaction does not affect the damping of the Bloch oscillations [7] and that resonant tunneling remains coherent even at $\tau_\Gamma \gg \tau_{ph}$ [8]. Consequently, it is of interest to search for ways to develop oscillators operating under the conditions for resonant tunneling and to gain insight into the physical processes occurring in them.

The purpose of this study was to develop a theory for the high-frequency nonlinear response of a double-well nanostructure (DWNS) under a dc bias. Such a structure can be considered as the next simplest in form after a single-well structure, or resonant-tunnel diode (RTD), but before a superlattice with a one-band Stark ladder. In addition, a DWNS is of interest in its own right. First, it exhibits fundamentally new features resulting from level splitting and from interference between the wells. Second, the high-frequency response of a DWNS due to the transitions between the levels can be more intense than the response of an RTD [9, 10], making

DWNSs rather promising for application as generators in the terahertz frequency range.

Recently [10], an analytical theory of linear response for a DWNS has been developed in the context of a model previously used in [11]. Simple expressions were derived for the transmission coefficient and the average polarization current [10].

In this study, the equations of the theory developed in [10] are solved numerically and, as a result, the polarization current in high fields is determined for wide ranges of frequencies and structural parameters, including those of practical QW structures.

The results of the numerical calculations are in good agreement with those obtained analytically for low fields. On the basis of these results, a number of new effects in high fields are predicted. In addition, these results make it possible to calculate the output power of DWNS-based oscillators.

2. FORMULATION OF THE PROBLEM AND THE NUMERICAL PROCEDURE

We follow [10] and consider a structure consisting of two identical QWs of width a confined by δ barriers of strength α. Let a dc bias V_{dc} be applied to the structure (Fig. 1). A steady flow of electrons of energy ε and amplitude q is supplied to the structure on its left side. An ac electric field E of potential $V(x, t)$ acts in the region of the structure:

$$V(x, t) = U(x)\cos\omega t,$$

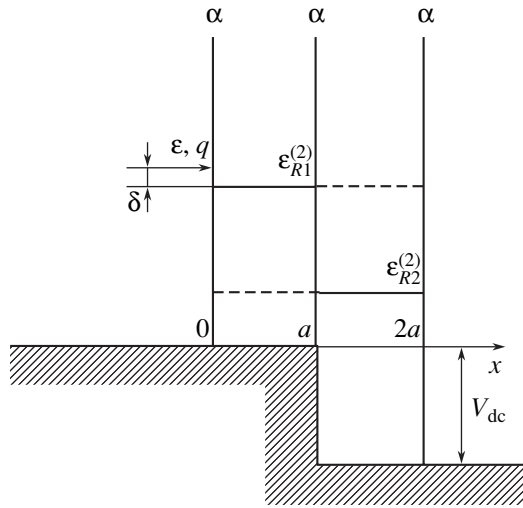$$U(x) = \begin{cases} 0, & x < 0 \\ -eEx, & 0 \le x \le 2a \\ -2eEa = -V_{ac}, & x > 2a. \end{cases}$$

Fig. 1. A double-well nanostructure under an external voltage V_{dc}.

Here, e is the elementary charge and ω is the frequency of the external field.

The electron wave function $\Psi(x, t)$ obeys the one-dimensional time-dependent Schrödinger equation

$$i\hbar\frac{\partial\Psi}{\partial t} = -\frac{1}{2m^*}\frac{\partial^2\Psi}{\partial x^2}$$
$$+ \alpha[\delta(x) + \delta(x-a) + \delta(x-2a)]\Psi \qquad (1)$$
$$+ [V(x, t) - V_{dc}\Theta(x-a)]\Psi.$$

Here, Θ is the unit-step function and m^* is the electron effective mass in the structure. The boundary conditions for the Schrödinger equation (1) can be written as

$$\begin{cases} \Psi(0, t)\left(1 - \dfrac{\alpha}{ip}\right) + \dfrac{1}{ip}\dfrac{\partial\Psi(0, t)}{\partial x} = 2q\exp\left(-\dfrac{i\varepsilon t}{\hbar}\right), \\ \Psi(2a, t)\left(1 - \dfrac{\alpha}{ip_1}\right) - \dfrac{1}{ip_1}\dfrac{\partial\Psi(2a, t)}{\partial x} = 0, \end{cases} \qquad (2)$$

where

$$p = \sqrt{\frac{2m^*\varepsilon}{\hbar^2}} \quad \text{and} \quad p_1 = \sqrt{\frac{2m^*(\varepsilon + V_{ac})}{\hbar^2}}$$

are the electron wave vectors to the left and right of the structure, respectively.

The reduced current of the nth well J_n is given by

$$J_n(t) = \frac{e\hbar}{2m^*}\frac{1}{a}\int\limits_{a(n-1)}^{an} dx\,\text{Im}\left\{\Psi^*(x, t)\frac{\partial\Psi(x, t)}{\partial x}\right\},$$

where $n = 1$ and 2. Under the effect of the ac electric field, an active polarization current J_c, which is in phase with the external field, and a reactive current J_s flow

through the structure. The active current (amplification) can be calculated using the formula

$$J_{nc} = \frac{\omega}{\pi}\int\limits_0^{2\pi/\omega} dt\,J_n(t)\cos(\omega t). \qquad (3)$$

Thereafter, we set $\hbar = 2m^* = q = 1$.

In order to solve Eq. (1) numerically, we take a discrete rectangular mesh with certain steps along the coordinate $dx = 2a/(N_X - 1)$ and time (dt) axes. (Here, N_X is the number of coordinate nodes in the mesh.) We use the finite difference method [12]. Then, for each fixed time layer j, the problem is reduced to the solution of the matrix equation

$$\begin{pmatrix} 1 - \dfrac{1}{ipdx} & \dfrac{1}{ipdx} & 0 & \dots & \dots & \dots & \dots & 0 \\ \dfrac{1}{dx^2} & A_2 & \dfrac{1}{dx^2} & 0 & \dots & \dots & \dots & 0 \\ \dots & \dots & \dots & \dots & \dots & \dots & \dots & \dots \\ 0 & \dots & \dots & \dfrac{1}{dx^2} & A_k & \dfrac{1}{dx^2} & \dots & 0 \\ \dots & \dots & \dots & \dots & \dots & \dots & \dots & \dots \\ 0 & \dots & \dots & \dots & \dots & 0 & 1 - \dfrac{1}{ip_1 dx} & \dfrac{1}{ip_1 dx} \end{pmatrix}$$

$$\times \begin{pmatrix} \Psi(1, j) \\ \Psi(2, j) \\ \dots \\ \Psi(k, j) \\ \dots \\ \Psi(1, N_x) \end{pmatrix} = \begin{pmatrix} f(1, j) \\ f(2, j) \\ \dots \\ f(k, j) \\ \dots \\ f(N_x, j) \end{pmatrix},$$

$$f(k, j) = \Psi(k, j-1)\left[\frac{2i}{dt} + U(k, j-1) - \varepsilon\right]$$
$$- \frac{\Psi(k-1, j-1) - 2\Psi(k, j-1) + \Psi(k+1, j-1)}{dx^2},$$

where $\Psi(k, j)$ is the wave function to be found, $U(k, j) = V_{ac}(k, j) + V_{dc}(k)$ are the known values of the potential at the nodal points of the mesh corresponding to the coordinate k and the time j, and $i = \sqrt{-1}$.

The symbols A_2 and A_k denote the matrix elements

$$A_2 = \frac{2i}{dt} - \frac{2}{dx^2} + \varepsilon - U(2, j) - \frac{\alpha}{dx}$$

and

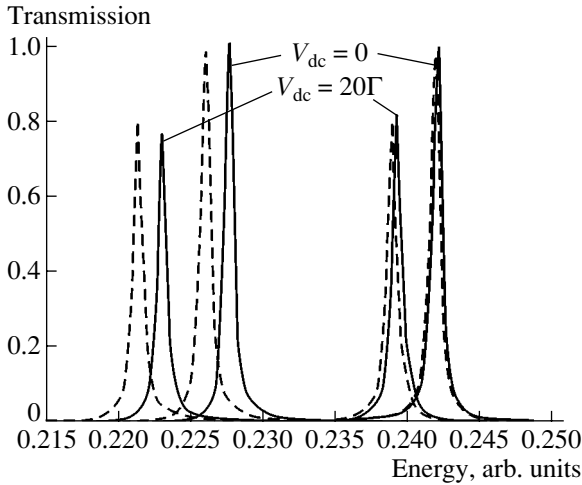$$A_k = \frac{2i}{dt} - \frac{2}{dx^2} + \varepsilon - U(k, j) - \frac{\alpha}{dx}.$$

Fig. 2. Dependences of the propagation coefficient T on the energy of incident electrons ε at $V_{ac} = 0$. The solid and dashed lines refer to the numerical and analytical solutions, respectively.
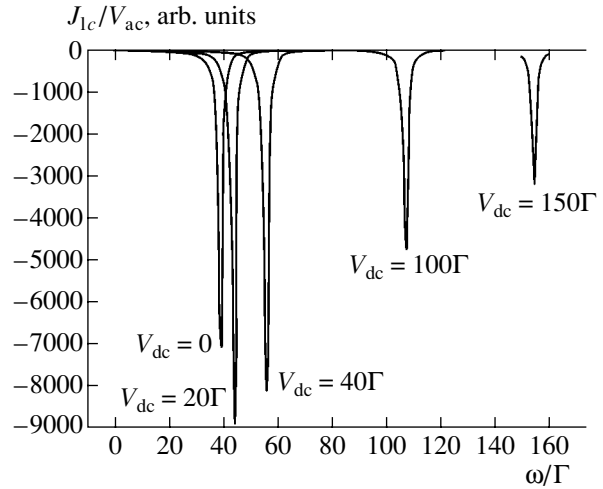

Fig. 3. Dependences of the linear response of the first well, J_{1c}/V_{ac}, on the frequency ω at $V_{ac} = 0.01\Gamma$ for different values of V_{dc}.

The solution to the above matrix equation is searched for by the sweep method [12]. Once the function $\Psi(k, j)$ has been found using this procedure, we progress to the next time layer $j + 1$ and so on, thus obtaining the solution to the problem formulated by Eqs. (1) and (2). The symmetric six-point procedure developed by Crank and Nicholson [13] yields a high accuracy of the solution over a wide range of external field frequencies.

The calculations were performed for a structure with barriers of strength $\alpha = 5$, 10, and 15 and width $a = 2\pi$. For a separate well with $\alpha = 10$, the energy of the resonant ground state is $\varepsilon_R^{(1)} \approx 0.235$ and the half-width (damping constant) is $\Gamma^{(1)} = 7 \times 10^{-4}$.

3. ENERGY SPECTRUM AND TRANSMISSION COEFFICIENT

The energy and the half-width of the resonant levels can be found directly from the dependence of the transmission coefficient T on the electron energy ε (Fig. 2). As can be seen from Fig. 2, the dependence features two peaks at the energies $\varepsilon_{R1}^{(2)} \approx 0.228$ and $\varepsilon_{R2}^{(2)} \approx 0.242$; the widths of the peaks are $\Gamma_1^{(2)} = 3.3 \times 10^{-4}$ and $\Gamma_2^{(2)} = \Gamma = 3.7 \times 10^{-4}$. (The above-listed numerical results correspond to $V_{dc} = 0$). The energy separation between the peaks increases as V_{dc} increases. From this trend, the energy spectrum of the structure can be found. It is worth noting that the quantity $\varepsilon_{R1}^{(2)}$ decreases as V_{dc} increases, while the quantities $\Gamma_1^{(2)}$ and $\Gamma_2^{(2)}$ remain almost unchanged. These results are in good agreement with the relevant analytical calculations [10]. For illustration, comparison between the numerical and analytical results for the transmission coefficient $T(\varepsilon)$ is

shown in Fig. 2. Some discrepancy between the results derives from the fact that the analytical formula taken for the comparison does not involve corrections quadratic in the parameter p/α.

4. LINEAR RESPONSE OF A DOUBLE-WELL STRUCTURE

First, we find the currents in the first and second wells, J_{1c} and J_{2c}, under a weak field $V_{ac} \ll \Gamma$ at $\varepsilon = \varepsilon_{R2}^{(2)}$ in relation to the parameters of the structure, the frequency ω, and the voltage V_{dc}. This step allows us to compare the results with those obtained analytically [10]. Figure 3 shows the dependence of the response J_{1c}/V_{ac} on ω under various voltages V_{dc} for the average current of the first well J_{1c}. (The current of the second well is virtually the same as that of the first well.) From Fig. 3, we notice that the response shows a sharp peak at certain frequencies ω_m that are nearly equal to the energy separations between resonant levels. (It is worthwhile comparing this finding with the energy dependence of the transmission coefficient shown in Fig. 2.) The peak response first increases with voltage, attains a maximum at $V_{dc} \approx 20\Gamma$, and then decreases.

It should be noted that the peak response here is considerably stronger than the response of an RTD (see [14]). Calculation of the response for different values of α/p shows that it increases proportionally to $(\alpha/p)^3$.

The above results are in good agreement with the analytical calculations [10], including the dependence of the response on the voltage V_{dc}. We can conclude that this finding confirms the correctness of the above numerical computations.
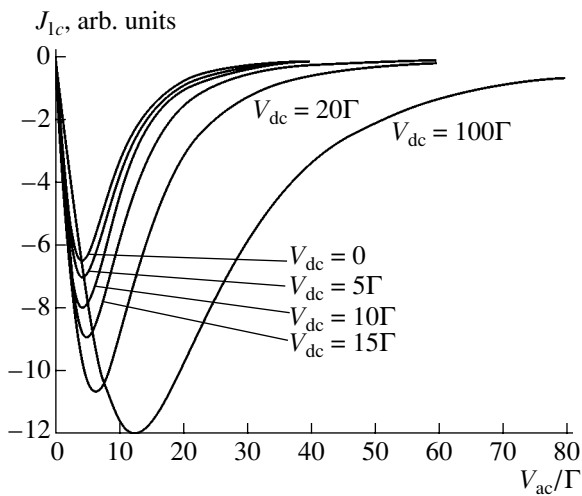
Fig. 4. Dependences of the polarization current J_{1c} on the ac electric field amplitude V_{ac} at the frequencies $\omega = \omega_m$ for different values of V_{dc}.

5. NONLINEAR RESPONSE OF A DOUBLE-WELL STRUCTURE

In order to obtain the output power in the generation mode, the current under high fields, i.e., for $V_{ac} > \Gamma$, should be determined. Typical results of the calculations for different V_{dc} at the frequencies $\omega = \omega_m$ are shown in Fig. 4. We can see that, at certain values of V_{ac}^m, the absolute value of the current J_{1c} exhibits a peak that shifts in accordance with an increase in V_{dc}. As V_{dc} increases, the peak value of the current increases as well. The resultant dependences of J_{1c} on the ac field V_{ac} allow us to find the generation output power, e.g., by applying the method used in [4, 14]. Analysis shows that the output power may attain rather large values, especially under a high bias voltage V_{dc}. Taking into account the fact that variations in the voltage V_{dc} affect the resonant frequency, we can conclude that DWNSs show considerable potential as oscillators in the terahertz frequency range.

Since the radiative transitions in DWNSs occur between two levels, the generation should exhibit a "laser" behavior, with the frequency being much lower than the frequency of the transition between the resonant levels of one well. Therefore, certain special features typical of the coherent lasers in high electric fields [4] can be expected. In particular, we can expect a sharp dependence of the current J_{1c} on the energy of electrons supplied to the structure. This feature is a result of the splitting of the resonant levels in high ac fields.

Figures 5a and 5b show the results of calculations of the quantity $J_{1c}V_{ac} = Q$ as a function of the detuning $\delta = \varepsilon = \varepsilon_R$ at different values of V_{ac}. At $V_{dc} = 0$ and $V_{ac} = 8\Gamma$, Q shows a minimum (a maximum in absolute value) at $\delta = 0$. If V_{ac} is higher than 8Γ, there are two minimums that pull apart, with the separation being proportional
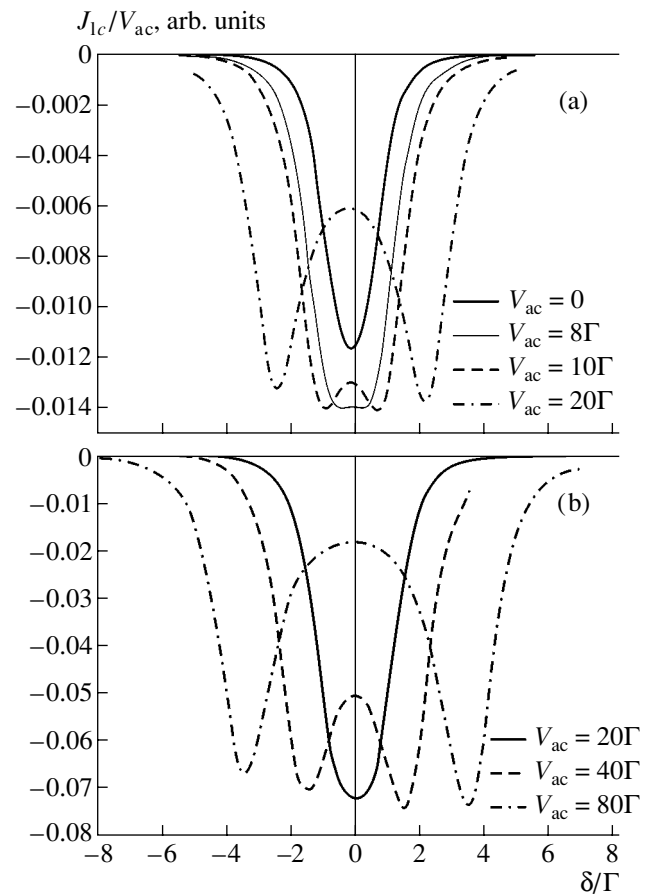

Fig. 5. Dependences of the quantity $J_{1c}V_{ac}$ on the detuning δ for different values of V_{ac} at the frequencies $\omega = \omega_m$. $V_{dc} =$ (a) 0 and (b) 100Γ.
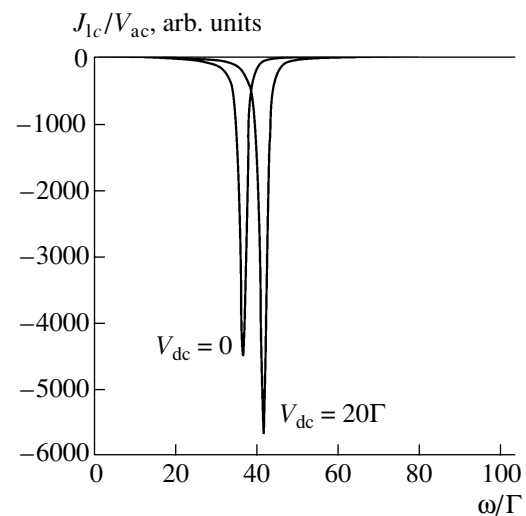

Fig. 6. Dependences of the linear response J_{1c}/V_{ac} on the frequency ω for a real structure with rectangular barriers under different biases V_{dc}.

to V_{ac}. Thus, a DWNS exhibits behavior similar to that of a coherent laser that operates by transitions between the resonant levels of one well. Because of this circumstance, there should exist an optimal mode of generation with a fine adjustment, as predicted in [4]. At the same time, there are some differences, namely, an asymmetry in the behavior of Q at $\delta > 0$ and $\delta < 0$ and a decrease in minimal Q as V_{ac} increases. At high V_{dc} (Fig. 5b), the asymmetry is less pronounced, and the quantity $J_{1c}V_{ac}$ at the minimums remains nearly constant.

6. CONCLUSIONS

The results presented above are obtained in the context of a simple model with δ-like barriers. We believe that the qualitative content of the results will not change for actual structures. In order to verify this conclusion explicitly, we calculated the linear response of a structure with the following parameters: a well width $a = 150$ Å, barrier width $b = 16$ Å, and barrier height $V_b = 2$ eV. The parameters were chosen so that we had $\alpha/p \approx 10$ and $\alpha = V_b b$. The results of the calculation are shown in Fig. 6. It is clear that the frequency dependence of the response is similar to that in Fig. 3 and that the response is of the same order of magnitude.

ACKNOWLEDGMENTS

REFERENCES

1. A. Kazarinov and R. Suris, Sov. Phys. Semicond. **5**, 207 (1971).
2. J. Fainst, F. Capasso, D. Sivco, *et al.*, Science **264**, 553 (1994).
3. J. P. Sun, G. I. Haddad, P. Mazumder, and J. N. Schulman, Proc. IEEE **86**, 644 (1998).
4. V. F. Elesin, Zh. Éksp. Teor. Fiz. **112**, 483 (1997) [JETP **85**, 264 (1997)].
5. V. F. Elesin and Yu. V. Kopaev, Zh. Éksp. Teor. Fiz. **123**, 1308 (2003) [JETP **96**, 1149 (2003)].
6. S. Haas *et al.*, Phys. Rev. B **57**, 14 860 (1998).
7. I. A. Dmitriev and R. A. Suris, Fiz. Tekh. Poluprovodn. (St. Petersburg) **36**, 1449 (2002) [Semiconductors **36**, 1375 (2002)].
8. V. F. Elesin, Zh. Éksp. Teor. Fiz. **123**, 1096 (2003) [JETP **96**, 966 (2003)].
9. V. F. Elesin, V. V. Kapaev, Yu. V. Kopaev, and A. V. Tsukanov, Pis'ma Zh. Éksp. Teor. Fiz. **66**, 709 (1997) [JETP Lett. **66**, 742 (1997)].
10. V. F. Elesin, Zh. Éksp. Teor. Fiz. (2005) (in press).
11. V. F. Elesin, Zh. Éksp. Teor. Fiz. **116**, 704 (1999) [JETP **89**, 377 (1999)].
12. A. A. Samarskiǐ and E. S. Nikolaev, *Methods for Solving Finite-Difference Equations* (Nauka, Moscow, 1978) [in Russian].
13. J. Crank and P. Nicholson, Proc. Cambridge Philos. Soc. **50**, 43 (1947).
14. V. F. Elesin, I. Yu. Kateev, and A. I. Podlivaev, Fiz. Tekh. Poluprovodn. (St. Petersburg) **34**, 1373 (2000) [Semiconductors **34**, 1321 (2000)].

Translated by É. Smorgonskaya

Polarization of the Optical Emission of Polaron Excitons in Anisotropic Quantum Dots

A. Yu. Maslov and O. V. Proshina

Ioffe Physicotechnical Institute, Russian Academy of Sciences, St. Petersburg, 194021 Russia
Submitted December 27, 2004; accepted for publication February 4, 2005

Abstract—A theory of large polarons in ellipsoidal quantum dots is developed. The optical spectrum of polaron excitons and its dependence on the degree of anisotropy of a quantum dot are analyzed. It is shown that the polaron ground state exhibits specific anisotropic polarization of the medium. The symmetry of the wave function of the ground state depends on the band structure of the material and on the shape of the quantum dot. The conditions under which strong polarization of the zero-phonon emission line produced by interband optical transitions occurs are determined. The possible polarization of this line is determined for various relationships between the polaron energy and the energy of the exchange interaction. © 2005 Pleiades Publishing, Inc.

The optical properties of quantum dots (QDs) controlled by interband electronic transitions are closely related to a profound localization of charge carriers in the region defined by the QD radius R. Such localization involves the enhancement of both electron–electron interaction and electron–phonon coupling. The manifestation of each of these effects in the optical spectra of QDs has undergone extensive theoretical study. In this paper, we consider the possible influence that these types of interaction have on each other.

In the case of enhanced effective electron–electron interaction, the excitonic effects become more pronounced. The average energy of a Coulomb interaction between two charged particles in a QD is much higher than the exciton binding energy in the bulk of the same crystal if the following condition for strong localization is satisfied [1]:

$$\frac{R}{a_B} \ll 1. \tag{1}$$

Here, a_B is the exciton Bohr radius in the bulk.

Along with the direct Coulomb interaction, the effects of the exchange interaction are also considerably enhanced for the excitons localized in a QD [2, 3]. In this case, the corresponding exchange splitting is much more pronounced than that in the bulk material if condition (1), i.e., the same condition that defines the enhancement of the direct Coulomb interaction, is satisfied.

In semiconductors that exhibit a high degree of ionic bonding, the strong interaction of electrons with polar optical phonons results in polaronic effects [4]. In semiconductor nanostructures, the polaron interaction manifests itself most clearly in a series of intense lines of phonon replicas. These lines have been observed in CdSe QDs embedded in a vitreous matrix [5, 6].

The condition for appreciable enhancement of the polaronic effects in QDs in comparison to those in bulk

materials can be expressed [7, 8] by an inequality similar to (1), namely,

$$\frac{R}{a_0} \ll 1, \tag{2}$$

where a_0 is the polaron radius in the bulk. Condition (2) can be referred to as the strong localization condition for a polaron.

Conditions (1) and (2) can be simultaneously satisfied for different relationships between polaron and exciton binding energies or, equivalently, for different relationships between the radii a_B and a_0. In this study, we show how these differences can manifest themselves in the optical spectra of exciton transitions in QDs.

We begin with a consideration of the relation between the polaron and exciton effects in a spherical QD. We assume that the energy states of electrons and holes can be described, with reasonable accuracy, using the approximation of a potential well with an infinitely high barrier. For typical semiconductors, the spectrum of electrons in the conduction band is nondegenerate and can be characterized by the effective mass m_e. The valence band for the same materials is, as a rule, four-fold degenerate at the Γ point in the Brillouin zone. In this case, the spectrum of the states of a free hole with the moment **p** can be described by the spherical Luttinger Hamiltonian [9]

$$\hat{H}_L = \frac{1}{m_0}\left[\frac{\hat{\mathbf{p}}^2}{2}\left(\gamma_1 + \frac{5}{2}\gamma\right) - \gamma(\hat{\mathbf{p}}\hat{\mathbf{J}})^2\right], \tag{3}$$

where γ and γ_1 are the Luttinger parameters, which are well known for most semiconductors; m_0 is the free electron mass; and $\hat{\mathbf{J}}$ is an operator of the proper hole momentum equal to 3/2. For electrons and holes in a spherical potential well with infinitely high barriers, the

quantum-confinement energy levels and wave functions are known. For the electron ground state, we have [1]

$$\Psi_{s_z}^{(e)}(\mathbf{r}_e) = \frac{2\pi}{R} j_0\left(\frac{\pi r}{R}\right)|s_z\rangle, \qquad (4)$$

where $j_l(x)$ is a spherical Bessel function of order l and $|s_z\rangle$ is the spin wave function.

The states of holes in a symmetric potential well are characterized by certain values of the total momentum $\hat{\mathbf{F}} = \hat{\mathbf{L}} + \hat{\mathbf{J}}$, where $\hat{\mathbf{L}}$ is the operator of the angular momentum. For the hole ground state, the total momentum is $\hat{\mathbf{F}} = 3/2$, and the wave function has the following form [10]:

$$\Psi_{F_z}^{(h)}(\mathbf{r}_h) = 2\sum_l (-1)^{l-3/2+F_z} R_{F,l}(r)$$

$$\times \sum_{m,\mu}\begin{pmatrix} l & 3/2 & 3/2 \\ m & \mu & -F_z \end{pmatrix} Y_{lm}(\vartheta,\varphi)\chi_\mu. \qquad (5)$$

Here, F_z is the component of the momentum $\hat{\mathbf{F}}$ along the axis of quantum confinement z, χ_μ is the eigenvector of the matrix J_z, μ is the corresponding eigenvalue $(J_z\chi_\mu = \mu\chi_\mu)$, and $\begin{pmatrix} l & 3/2 & 3/2 \\ m & \mu & -F_z \end{pmatrix}$ is Wigner's $3j$ symbol. The summation in Eq. (5) is performed over the values of the quantum number $l = 0$ and 2 and values of m and μ that satisfy the condition $m + \mu = F_z$. The radial wave functions are given by [11]

$$R_{3/2,0} \equiv R_0(r)$$

$$= A(\beta)\left[j_0\left(k\frac{r}{R}\sqrt{\beta}\right) + \frac{j_2(k\sqrt{\beta})}{j_2(k)}j_0\left(k\frac{r}{R}\right)\right]$$

and

$$R_{3/2,2} \equiv R_2(r)$$

$$= A(\beta)\left[j_2\left(k\frac{r}{R}\sqrt{\beta}\right) - \frac{j_2(k\sqrt{\beta})}{j_2(k)}j_2\left(k\frac{r}{R}\right)\right],$$

where the parameter $\beta = (\gamma - 2\gamma_1)(\gamma + 2\gamma_1)$ characterizes the ratio between the masses of light and the heavy holes, $A(\beta)$ is a normalization factor equal to

$$A(\beta) = \left(\int_0^R (R_0^2(r) + R_2^2(r))r^2 dr\right)^{-1/2}, \qquad (6)$$

and the quantity $k = R\sqrt{2m_h E_n}/\hbar$ is defined by the quantum-confinement energy E_n and by the heavy-hole mass m_h.

It is worth noting that simultaneous fulfillment of conditions (1) and (2) implies that, in a zeroth approxi-

mation, the energies and wave functions of the states are defined by the condition of quantum confinement for the spectrum of charged particles. The energy of the electron–electron interaction appears to be smaller than the energy of the state quantized in parameter (1). Similarly, the energy of the electron–phonon coupling is lower than the energy of the state quantized in parameter (2).

Known wave functions (4) and (5) can be used for constructing the wave function of the ground state of an electron–hole pair (exciton) for any relationships between the quantities a_B and a_0.

The essential difference between electron wave functions (4) and (5) lies in their different degrees of degeneracy in the angular momentum component that represents the symmetry of the band states for typical semiconductors. The electron states are twofold degenerate in spin, while a hole ground state with the total momentum $\hat{\mathbf{F}} = 3/2$ is fourfold degenerate. Consequently, disregarding the Coulomb interaction and electron–phonon coupling, the ground state of an electron–hole pair is eightfold degenerate. In line with the general rules for addition of momenta, the states of an electron and a hole coupled by a Coulomb interaction can have the total momentum $I_{exc} = 1$ and 2. In this case, the state with $I_{exc} = 1$ is optically active in the dipole approximation, while the state with $I_{exc} = 2$ is optically inactive. These states differ with respect to energy due to the exchange interaction [2, 3]. The most interesting case occurs when the energy of exchange splitting is higher than the polaron energy; otherwise, the polaron interaction tends towards a mixing of all the possible exciton states, with the result that the polaron exciton spectrum appears as it would without the exchange interaction [7].

In what follows, we deal only with an optically active state where $I_{exc} = 1$. The wave function of such state is given by [12]

$$\Psi_{I_z}^{(exc)}(\mathbf{r}_e, \mathbf{r}_h) = \sqrt{3}(-1)^{I_z-1}$$

$$\times \sum_{s_z+F_z=I_z}\begin{bmatrix} 1/2 & 3/2 & 1 \\ s_z & F_z & -I_z \end{bmatrix}\Psi_{s_z}^{(e)}(\mathbf{r}_e)\Psi_{F_z}^{(h)}(\mathbf{r}_h). \qquad (7)$$

The state of an electron–hole pair described by wave function (7) is threefold degenerate in the $I_{exc} = 1$ momentum component along an arbitrary axis. It should be noted that the exact form of wave function (7) is independent of the relation between a_B and a_0 and is defined by the symmetry of the states and by conditions for strong localization (1) and (2). If electron–phonon coupling is taken into account along with the Coulomb interaction, further reduction of the symmetry of the wave function can occur. In the case of strong electron–

phonon coupling, the energy of the exciton ground state in a QD is shifted by the polaron shift [7, 8]

$$\Delta E = -\frac{e^2}{2\varepsilon_{opt}}\int\frac{\left|\phi_e^2(r)-\phi_h^2(r)\right|\left|\phi_e^2(r')-\phi_h^2(r')\right|}{|\mathbf{r}-\mathbf{r}'|}d^3r\,d^3r'. \quad (8)$$

Here,

$$\phi_e^2(\mathbf{r}_e) = \int\left|\Psi^{(exc)}(\mathbf{r}_e,\mathbf{r}_h)\right|^2 d^3r_h,$$

$$\phi_h^2(\mathbf{r}_h) = \int\left|\Psi^{(exc)}(\mathbf{r}_e,\mathbf{r}_h)\right|^2 d^3r_e,$$

and the optical permittivity ε_{opt} characterizes the interaction of charged particles with polar optical phonons and obeys the relation $1/\varepsilon_{opt} = 1/\varepsilon_0 - 1/\varepsilon_\infty$. Expression (8) for the polaron energy was derived by the same procedure as in [7, 8], taking into account wave function (7) corresponding to a certain value of the total momentum of an electron–hole pair. This expression differs from that obtained previously in that, if the exchange effects are taken into account, it involves the modified electron and hole densities $\phi_e^2(\mathbf{r}_e)$ and $\phi_h^2(\mathbf{r}_h)$, which generally depend on the quantum numbers of the exciton state.

Since, for a zeroth-approximation exciton, wave function (7) is degenerate, the correct functions of the first approximation should be written, according to the general rules of quantum mechanics, as linear combinations of functions of type (7),

$$\Psi^{(exc)}(\mathbf{r}_e,\mathbf{r}_h) = C_{-1}\Psi_{-1}^{(exc)}(\mathbf{r}_e,\mathbf{r}_h)$$
$$+ C_0\Psi_0^{(exc)}(\mathbf{r}_e,\mathbf{r}_h) + C_1\Psi_1^{(exc)}(\mathbf{r}_e,\mathbf{r}_h), \quad (9)$$

with the arbitrary coefficients C_i. These coefficients are determined from the condition that polaron energy (8) takes its minimal value. It is found that this condition for ΔE in Eq. (8) is attained under anisotropic polarization of the medium. In such a case, the minimal energy is realized using a combination of wave functions (9), such that $C_{-1} = \pm C_1$, which corresponds to the condition

$$\langle(I_{exc})_z\rangle = 0. \quad (10)$$

Condition (10) implies that recombination of an electron and hole in the relevant state produces nonpolarized light emission. It should be noted that, in this case, the binding energy of a polaron exciton, ΔE, is equal to the same value E_{pol}, which was obtained in [7, 8] by disregarding the exchange interaction:

$$\Delta E \equiv E_{pol} = -\frac{e^2}{\varepsilon_{opt}R}B(\beta). \quad (11)$$

The dimensionless function $B(\beta)$ is given in [7, 8]. The absolute value of the binding energy of a polaron exiton, ΔE, controls the distribution of phonon replicas in the optical spectra of QDs. Thus, the simultaneously considered polaron coupling and exchange interaction in a spherical QD do not produce any qualitative changes in the spectrum of exciton optical transitions.

The situation can be reversed if a QD has lower, e.g., ellipsoidal symmetry. Let the equation for the QD boundary in the principal axes x, y, and z have the following form:

$$\frac{x^2+y^2}{b^2}+\frac{z^2}{c^2} = 1. \quad (12)$$

Here, $b = R(1 - \varepsilon/3)$, $c = R(1 + 2\varepsilon/3)$, and ε is the non-spherical-shape parameter. We will assume that this parameter is small; i.e.,

$$|\varepsilon| \ll 1. \quad (13)$$

In this case, the electron and hole states can be characterized by certain values of the anglular momentum. In an approximation that is linear in the small nonspherical-shape parameter, the fourfold degenerate hole state is split into two doublets corresponding to $F_z = \pm3/2$ and $F_z = \pm1/2$. Because of the relatively high symmetry of such a QD, the centroids of the quantum-confinement levels are not shifted [12]. Such splitting for ellipsoidal QDs was considered in detail in [13]. It was found that the splitting of the hole doublets ΔE_{hole} is proportional to the energy E_n of the quantum-confinement level:

$$\Delta E_{hole} = \varepsilon E_n f(\beta). \quad (14)$$

Here, the factor $f(\beta)$ depends only on the ratio β between the masses of the light and heavy holes. The dependence $f(\beta)$ was plotted in [13]. It is significant that the function $f(\beta)$ reverses its sign and passes through zero at $\beta = \beta_0 \approx 0.14$.

In the vicinity of the mass ratio $\beta = \beta_0$, splitting due to the non-spherical shape of a QD is negligible. This range of β should be considered separately in more detail (see below).

Outside the range around $\beta = \beta_0$, the quantum-confinement energy of a hole, E_n, is parametrically high compared to the polaron energy as given by inequality (2). In addition to E_n, splitting of the hole levels $\Delta E_{hole} < E_{pol}$ (14) is defined by the nonspherical-shape parameter ε. If ε is very small, meaning that the condition $\Delta E_{hole} < E_{pol}$ is satisfied, the polaron state appears to be the same as in the case of a spherical QD. The optical spectrum of a QD can essentially be modified under the condition

$$|\varepsilon| \gg \frac{R}{a_B}, \quad (15)$$

which is compatible with the condition of small non-spherical-shape parameter (13) as a result of inequality (1). When constructing wave function (7) for the exciton ground state in this case, the states of only one hole doublet, which has a minimal energy, should be taken into account.

If the conditions

$$\varepsilon > 0 \text{ and } \beta > \beta_0 \text{ or } \varepsilon < 0 \text{ and } \beta < \beta_0 \quad (16)$$

are satisfied, the ground state of a hole in a nonspherical QW is a doublet with the momentum component $F_z = \pm1/2$. In this case, there are no qualitative changes in the

optical spectra of interband transitions. The exciton ground state corresponds to the coefficients C_i that lead to condition (10). The optical emission due to recombination of such states is nonpolarized. In contrast, under the conditions

$$\varepsilon > 0 \text{ and } \beta < \beta_0 \text{ or } \varepsilon < 0 \text{ and } \beta > \beta_0 \qquad (17)$$

the ground state of a hole is a doublet with the momentum component $F_z = \pm 3/2$. When taking into account the polarization of the medium, the exciton ground state is described by solutions of type (9). In this case, however, the coefficients found by minimizing polaron energy (8) are

$$|C_{-1}| = 1 \text{ or } |C_1| = 1, \qquad (18)$$

which are consistent with the conditions $\langle (I_{exc})_z \rangle = \pm 1$. Recombination of an electron and a hole in this state produces polarized emission. For a single QD, the degree of polarization of the zero-phonon line should as high as 100%.

In the range $\beta \propto \beta_0$, the symmetry of the ground state is largely defined by polaron effects. The splitting of the quantum-confinement levels of a hole due the nonspherical shape of a QD is small compared to the polaron interaction and, thus, can be disregarded. Consideration of this range is of special interest because it is typical of a number of II–VI compounds (e.g., CdSe and CdS), in which polaron effects have been experimentally observed.

In the linear approximation, with respect to the small nonspherical-shape parameter ε, the energy of the polaron state of an electron does not change. Therefore, we take into account only possible changes in the energy of the hole states. Conditions (1) and (2) allow us to study the electron–phonon coupling in a QD independently of exciton effects.

We now consider the interaction of a hole with the polar optical phonons in an ellipsoidal QD whose boundaries obey Eq. (12). After substituting variables in the form $x = (x'b)/R$, $y = (y'b)/R$, and $z = (z'c)/R$, the QD boundary is transformed into a sphere of radius R. Under the same substitution of variables, the conventional operator of the electron–phonon coupling from [7] takes the form

$$\hat{V}_{h-ph} = -e\sqrt{\frac{2\pi\hbar}{V\varepsilon_{opt}}}\sum_{\mathbf{q}}\sqrt{\omega(\mathbf{q})}$$
$$\times \frac{1}{q}[\hat{a}_{\mathbf{q}}\exp[i\mathbf{q}'\cdot\mathbf{r}_h] + \hat{a}_{\mathbf{q}}^+\exp[-i\mathbf{q}'\cdot\mathbf{r}_h]], \qquad (19)$$

where $\hat{a}_{\mathbf{q}}^+$ and $\hat{a}_{\mathbf{q}}$ are the phonon creation and annihilation operators. In Eq. (19), we used the notation

$$\mathbf{q}' = \left(\frac{b}{R}q_x, \frac{b}{R}q_y, \frac{c}{R}q_z\right) \qquad (20)$$

for the above substitution of the variables x, y, and z.

We now account for the polaron coupling by the method described in detail in [7, 8]. It is necessary to average the Hamiltonian of the system with respect to the fast motion of electrons and to make the unitary transformation $\hat{S} = \exp[\hat{U}_h]$, where

$$\hat{U}_h = \sum_{\mathbf{q}}\frac{e}{q}\sqrt{\frac{2\pi}{V\varepsilon_{opt}\hbar\omega(\mathbf{q})}}[\rho_h(\mathbf{q}')\hat{a}_{\mathbf{q}}^+ - \rho_h^*(\mathbf{q}')\hat{a}_{\mathbf{q}}]; \qquad (21)$$

as a result, we convert the phonon Hamiltonian into a diagonal form and obtain the following expression for the binding energy of a hole polaron:

$$\Delta E_h = -\frac{e^2}{2\varepsilon_{opt}}\frac{1}{2\pi^2}\int\frac{d^3q}{q^2}|\rho_h(\mathbf{q}')|^2. \qquad (22)$$

Here, the Fourier component of the hole density is given by

$$\rho_h(\mathbf{q}') = \int d^3r|\Psi_{F_z}^{(h)}(\mathbf{r})|^2\exp[i\mathbf{q}'\cdot\mathbf{r}]. \qquad (23)$$

Expanding expression (20) in series up to a term that is linear in nonspherical-shape parameter (13), we use Eq. (23) to obtain the following expression:

$$\rho_h(\mathbf{q}') = \int d^3r|\Psi_{F_z}^{(h)}(\mathbf{r})|^2\exp[i\mathbf{q}\cdot\mathbf{r}]$$
$$\times\left[1 - \frac{i\varepsilon}{3}(\mathbf{q}\cdot\mathbf{r} - 3q_zr_z)\right]. \qquad (24)$$

In the zeroth approximation with respect to the parameter ε, expressions (22) and (24) yield the binding energy of a hole polaron in a spherical QD, which was derived in [7]. In the linear approximation in ε, the hole ground state, initially fourfold degenerate, splits into two doublets with the momentum components $F_z = \pm 1/2$ and $F_z = \pm 3/2$. At the same time, in the linear approximation in ε, the centroid of the levels is shifted along with the above-mentioned splitting. This shift is determined by the formula

$$\Delta E_{shift} = \frac{e^2}{2\varepsilon_{opt}R}\varepsilon F_1(\beta). \qquad (25)$$

The dependence of the shift in Eq. (25) on the mass ratio β of light and heavy holes was calculated using wave functions (5). The result takes the form

$$F_1(\beta) = \frac{32}{75\pi}(A(\beta))^4\int_0^R\int_0^R\int_0^\infty\left(j_1(qr) + \frac{3}{7}j_3(qr)\right)$$
$$\times j_2(qr')qr^3r'^2R_0(r)R_2(r)R_0(r')R_2(r')dqdr'dr. \qquad (26)$$

The dimensionless function $F_1(\beta)$ is plotted in Fig. 1. Although the shift is rather small, it can be important, since it produces a change in the energy of the interband optical transitions in an ellipsoidal QD as compared to a spherical QD of the same volume. Taking this shift
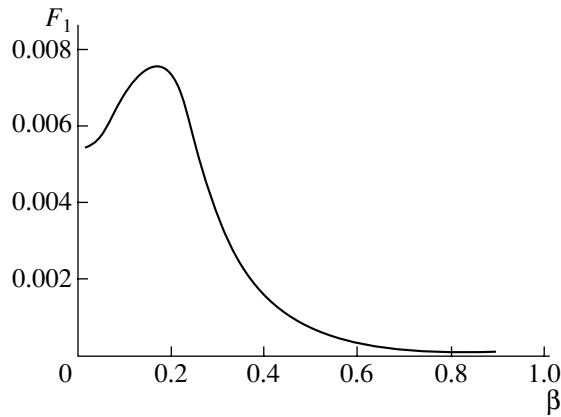
Fig. 1. Shift of the energy levels of the ground state for a hole exciton in an ellipsoidal QD versus the ratio between the masses of light and heavy holes.
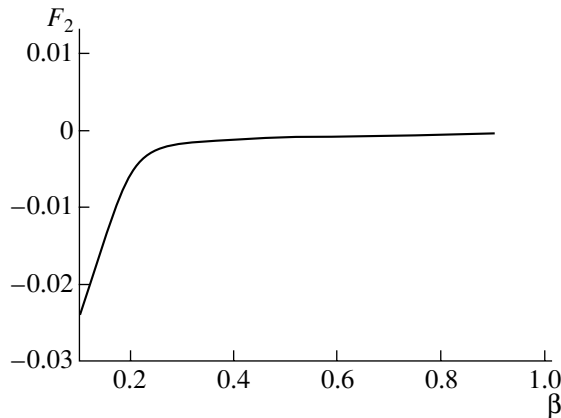

Fig. 2. Splitting of the energy levels of holes with the momentum components $F_z = \pm 3/2$ and $F_z = \pm 1/2$ in an ellipsoidal QD versus the ratio between the masses of light and heavy holes.

into account can be important when analyzing the experimental spectra of the interband optical transitions.

The splitting of the hole levels at the energies $E_{\pm 3/2}$ and $E_{\pm 1/2}$ is given by

$$\Delta E_{split} = E_{\pm 3/2} - E_{\pm 1/2} = \frac{e^2}{2\varepsilon_{opt}R}\varepsilon F_2(\beta), \qquad (27)$$

where the dimensionless function $F_2(\beta)$, dependent on the mass ratio, is expressed in terms of radial wave functions of the hole ground state for a QD in the following way:

$$F_2(\beta) = \frac{16}{15\pi}(A(\beta))^4 \int\limits_0^R \int\limits_0^R \int\limits_0^\infty [(R_0^2(r') + R_2^2(r'))$$

$$\times R_0(r)R_2(r)j_0(qr') - (R_0^2(r) + R_2^2(r)) \qquad (28)$$

$$\times R_0(r')R_2(r')j_2(qr')]j_1(qr)qrdqdr'dr.$$

The function $F_2(\beta)$ is plotted in Fig. 2. The symmetry of the states resulting from polaron-induced splitting is the same as in the case of splitting due to the quantum-confinement effects considered above. Depending on parameter (2), the splitting induced by quantum confinement can be larger than that described by Eq. (27). Therefore, Eq. (27) actually describes splitting of the hole levels only in a rather narrow range of mass ratios, where $\beta \approx \beta_0$. As follows from the calculated values of the function $F_2(\beta)$, the symmetry of the polaron ground state in this case is the same as the symmetry in the range defined by inequalities (17).

In the approximation that is linear in the small non-spherical-shape parameter ε, the corrections to the polaron exciton energies are the same as above-derived corrections (25) and (27) to the hole polaron energy. For the polarized emission controlled by interband optical transitions to be observed, it is necessary that the exciton ground state corresponds to a hole doublet with the momentum components $F_z = \pm 3/2$. This situation takes place under condition (17). If this condition is satisfied, the emission from a single QD will be completely polarized; i.e., the degree of polarization will be 100%.

Emission from arrays of QDs is commonly observed experimentally. These QDs can differ in shape and size. In this case, the degree and type of polarization of the emission is governed by the properties of a particular array. Polarized emission from an array can serve as an optical indicator of a rather high density of constituent nonspherical QDs, for which the nonspherical-shape parameter obeys condition (15). This opens up new possibilities for determining the parameters of QDs from optical measurements.

REFERENCES

1. Al. L. Éfros and A. L. Éfros, Fiz. Tekh. Poluprovodn. (Leningrad) **16**, 1209 (1982) [Sov. Phys. Semicond. **16**, 772 (1982)].

2. T. Takagahara, Phys. Rev. B **47**, 4569 (1993).

3. S. V. Gupalov and E. L. Ivchenko, Fiz. Tverd. Tela (Leningrad) **42**, 1976 (2000) [Phys. Solid State **42**, 2030 (2000)].

4. S. I. Pekar, *Investigations on Electron Theory of Crystals* (GITTL, Moscow, 1951; Report AEC-tr-5575, U.S. Atomic Energy Commission, 1963).

5. M. C. Klein, F. Hache, D. Ricard, and C. Flytzanis, Phys. Rev. B **42**, 11 123 (1990).

6. V. Yungnickel and F. Henneberger, J. Lumin. **70**, 238 (1996).

7. I. P. Ipatova, A. Yu. Maslov, and O. V. Proshina, Fiz. Tekh. Poluprovodn. (St. Petersburg) **33**, 832 (1999) [Semiconductors **33**, 765 (1999)].

8. I. P. Ipatova, A. Yu. Maslov, and O. V. Proshina, Europhys. Lett. **53**, 769 (2001).

9. J. M. Luttinger, Phys. Rev. **102**, 1030 (1956).

10. B. I. Shklovskiǐ and A. L. Éfros, *Electronic Properties of Doped Semiconductors* (Nauka, Moscow, 1979; Springer, New York, 1984).

11. Al. L. Efros, Phys. Rev. B **46**, 7448 (1992).

12. L. D. Landau and E. M. Lifshitz, *Course of Theoretical Physics*, Vol. 3: *Quantum Mechanics: Non-Relativistic Theory*, 4th ed. (Nauka, Moscow, 1989; Pergamon, Oxford, 1977), Chap. 14.

13. Al. L. Efros and A. V. Rodina, Phys. Rev. B **47**, 10005 (1993).

Translated by É. Smorgonskaya

A Millimeter–Submillimeter Phonon-Cooled Hot-Electron Bolometer Mixer Based on Two-Dimensional Electron Gas in an AlGaAs/GaAs Heterostructure

D. V. Morozov, K. V. Smirnov, A. V. Smirnov^, V. A. Lyakhov, and G. N. Goltsman

Moscow State Pedagogical University, ul. Malaya Pirogovskaya 1, Moscow, 119992 Russia

^e-mail: cleviy@mail.ru

Submitted September 27, 2004; accepted for publication October 14, 2004

Abstract—Experimental results obtained by studying the main characteristics of a millimeter–submillimeter-wave mixer based on the hot-electron effect in a two-dimensional electron gas in a AlGaAs/GaAs heterostructure with a phonon-scattering cooling mechanism for charge carriers are reported. The gain bandwidth of the mixer is 4 GHz, the internal conversion losses are 13 dB, and the optimum local-oscillator power is 0.5 µW (for a mixer area of 1 µm^2). It is shown that a millimeter–submillimeter-wave receiver with a noise temperature of 1900 K can be developed on the basis of a AlGaAs/GaAs mixer. This mixer also appears to be promising for use in array receiver elements. © 2005 Pleiades Publishing, Inc.

1. INTRODUCTION

Heterodyne receivers show great potential as devices for the detection of electromagnetic radiation in the frequency range 0.5–6.0 THz. At present, these detectors are used to facilitate the realization of projects such as HERSHEL, SOFIA, TELIS [1], etc., aimed at the development of submillimeter-wave-band radio telescopes and spectrometers that can be earth-, balloon-, and space-based. At the same time, the field of possible applications of terahertz-radiation detectors is much wider, including medicine, fire departments, navigation systems, security systems, and so on. Expansion of the market for heterodyne detectors is primarily impeded by the necessity of ensuring complex special conditions for the operation of these detectors. For example, mixers that exhibit a record-breaking value of noise temperature and are based on a superconductor–insulator–superconductor junction (SIS mixers) [2] and mixers based on electron-induced heating in a thin superconductor film (HEB mixers) [3] need cooling to temperatures of ~4.2 K and lower, which adds complications when dealing with these mixers. The noise temperature of widely known mixers based on Schottky diodes increases drastically at frequencies higher than 1 THz, even if these mixers operate at room temperature [4]. In addition, the mixers based on Schottky diodes require an appreciable (~1 mW) power for their local-oscillator source, which makes the development of array detector components based on these mixers impossible, although these components undoubtedly extend the field of application for mixers that operate in the millimeter- and submillimeter-wave (MM–SMM) bands.

A new type of a mixer designed for the MM–SMM band and based on the effect of heating a two-dimen-sional (2D) electron gas in AlGaAs/GaAs semiconductor structures was suggested by Yang *et al.* [5, 6]. The mechanism of operation of a submillimeter AlGaAs/GaAs mixer is based on the heating of the electron subsystem in the heterostructure produced by absorption of electromagnetic radiation. This heating brings about a variation in the charge-carrier mobility and resistivity of a sample and, as a result, the appearance of a photoconductivity signal P_{IF} at the intermediate frequency (IF) Δf, i.e., the difference between the frequency of radiation of the local-oscillator source and that of the object under study. The IF bandwidth of the mixer is controlled by the relaxation time for the temperature of nonequilibrium ("hot") electrons. In the case of a phonon-related mechanism of cooling at a lattice temperature of 77 K, this relaxation occurs via the transfer of excess energy to the optical phonons of the lattice. If the sample length l satisfies the condition $l < \pi\sqrt{D\tau_{e-ph}}$, where D is the diffusion coefficient and τ_{e-ph} is the time of electron–phonon interaction, the conditions are then satisfied for a diffusion-related escape of nonequilibrium charge carriers to the contacts. In our experiment, we studied the rate of electron–phonon interaction. Yang *et al.* [5, 6] (in addition, see [7, 8]) studied the electron–phonon interaction in AlGaAs/GaAs heterostructures and showed that the conversion bandwidth of an AlGaAs/GaAs mixer should be equal to ~3 GHz at 77 K if the phonon-related mechanism of cooling of hot electrons is used. Lee *et al.* [9] reported the design of a mixer based on an AlGaAs/GaAs heterostructure with ballistic cooling of charge carriers; for this mixer, the signal-conversion bandwidth was as large as ~40 GHz. Theoretical estimation of the noise temperature T_n for a receiver based on an

AlGaAs/GaAs mixer yielded $T_n \approx 1500$–2000 K at a local-oscillator frequency of 1 THz [8], which is comparable with the best characteristics of mixers based on superconductors. Estimation of the optimum local-oscillator power for an AlGaAs/GaAs mixer [8] yielded the value $P_{het} \approx 1$ μW at submicrometer sizes of the mixer, which makes it feasible to fabricate mixers that consist of arrays of receiver sections based on AlGaAs/GaAs.

In this paper, we report the results of experimental studies of the main parameters of a mixer based on heating of a 2D electron gas in an AlGaAs/GaAs heterostructure with a phonon-related mechanism of charge-carrier cooling. The parameters under consideration include the conversion losses, the conversion bandwidth, and the optimum local-oscillator power.

2. THE STRUCTURES UNDER STUDY

The structures were fabricated on the basis of a separate $Al_xGa_{1-x}As$/GaAs heterojunction grown by molecular-beam epitaxy. The molar fraction of Al in the $Al_xGa_{1-x}As$ compound was $x = 0.28$–0.3. A schematic representation of the structure is shown in Fig. 1. In order to improve the ohmic contact to the 2D electron gas, we used a heavily doped 50-nm-thick n-GaAs layer (the concentration of the doping impurity was 1×10^{18} cm^{-3}). The structures were obtained by the conventional technology sequentially using the following operations: wet chemical etching of the mesa structure, explosive photolithography while forming the contact metallization, thermal deposition of the AuGe alloy with subsequent annealing at a temperature of 400°C in an inert-gas atmosphere, and removal of the top shunting GaAs layer. The typical contact resistances of the structures were equal to 10^{-3} Ω/cm^2. The mobility μ and the surface electron concentration n_s were determined from the results of measurements of the Shubnikov–de Haas oscillations and were recalculated for the temperature $T = 77$ K. The obtained values of μ and n_s, as well as the length l and width W of the structures, are listed in the table.

3. THE CONVERSION BANDWIDTH OF AN AlGaAs/GaAs MIXER

The experimental setup for measuring the mixer bandwidth is shown schematically in Fig. 2. Radiation from the signal generator, with a frequency of 129.2 GHz, and radiation from the local oscillator, whose frequency was varied in the range from 129.2 to 139.2 GHz, were supplied to the mixer through a quasi-optical channel that included a beam splitter. The local-oscillator power exceeded the signal-generator power by ~7 dB. A direct bias current was fed to the mixer via a cooled wideband bias adapter. The IF signal was extracted using a section of a semirigid coaxial line and was fed to uncooled broadband amplifiers with a frequency range from 0.1 to 10 GHz and gain of ~50 dB. The amplified signal was detected using a thermistor-based power meter.
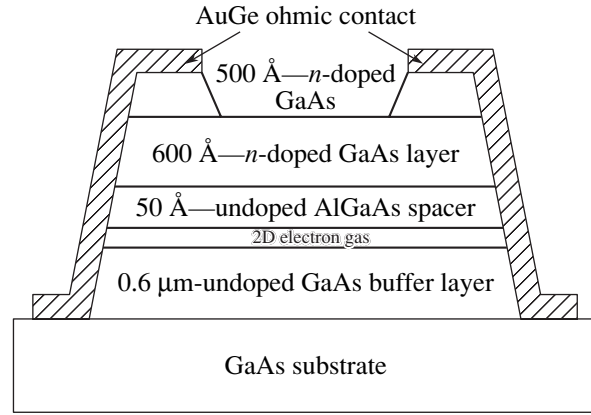
Fig. 1. Schematic representation of the AlGaAs/GaAs heterostructure under study.
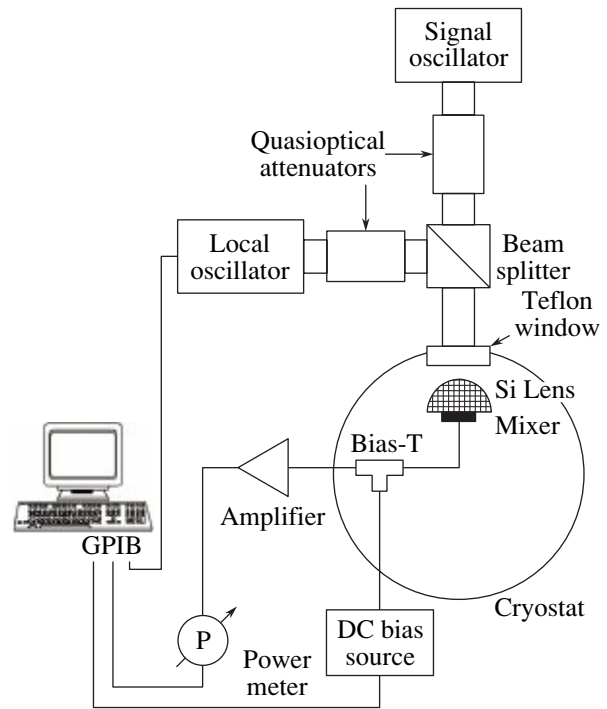

Fig. 2. Schematic circuit diagram of the system for measuring the conversion bandwidth of a mixer based on an AlGaAs/GaAs heterostructure.

The IF bandwidth of the mixer was determined from the frequency dependence of the mixer signal P_{IF} (at fixed power levels of both the signal and local-oscilla-

Table

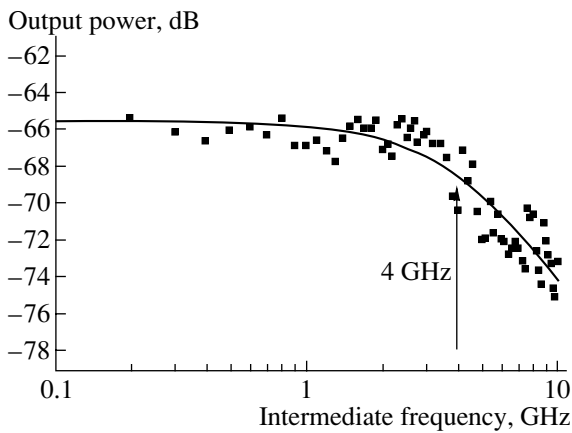| Structure no.	$m_{77\,K}$, cm^2 V^{-1} s^{-1}	$n_{s,\,77\,K}$ cm^{-2}	l, μm	W, μm
15	2.5×10^4	2.5×10^{11}	35	100
5	1.1×10^5	3.5×10^{11}	190	60
1	2.3×10^5	3×10^{11}	1600	300
760	7.7×10^4	7.5×10^{11}	1000	500

Output power, dB

Fig. 3. Dependence of the output-signal power on the intermediate frequency for structure 6 (in reference to 1 mW).
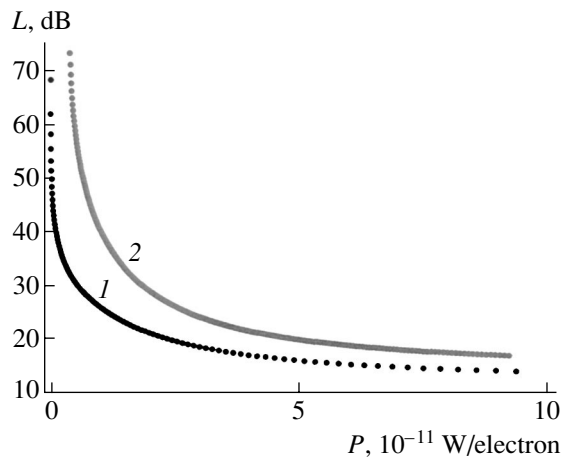

Fig. 4. Conversion-loss factor for structures 1 and 760 at $T = 77$ K as a function of the total absorbed power per electron. Curve *1* corresponds to structure 1, with the electron mobility $\mu = 2.3 \times 10^5$ cm^2/(V s), and curve *2* corresponds to structure 760, with $\mu = 7.7 \times 10^4$ cm^2/(V s).

tor sources) using the expression [10] $P_{IF}(f)/P_{IF}(0) = 1/(1 + (f/f_{3\,dB}))^2$, where $f_{3\,dB}$ is the frequency at which the signal decreases by a factor of 2. We measured the frequency dependence of P_{IF} at 77 K for an AlGaAs/GaAs mixer (structure 5) with the 2D electron concentration $n_s = 3.5 \times 10^{11}$ cm^{-2} and electron mobility $\mu = 1.1 \times 10^5$ cm^2/(V s); this dependence is shown in Fig. 3. The IF bandwidth was ~4 GHz, and the corresponding time of electron–phonon interaction was equal to $\tau_{e-ph} = 0.04$ ns.

4. CONVERSION LOSSES OF AN AlGaAs/GaAs MIXER

We determined the conversion-loss factor of a mixer $L = 10 \log (P_{in}/P_{IF})$, where P_{in} is the absorbed power of microwave radiation, using the method of isotherms

[10]; in this method, it is assumed that heating a 2D electron gas by microwave radiation is equivalent to heating by a constant bias current. In this case, if the mixer is completely matched to the IF amplifier, we have $L = 10 \log (8 (R_{op}/KP_0)^2)$, where R_{op} is the sample resistance at the operating point, P_0 is the total power absorbed by the mixer at the operating point, and $K = (dR/dP)_{P = P_0}$ [10]. According to [10], at the optimum operating point of the mixer, we have $0.5 P_0 = P_{het} = P_{bi}$; here, P_{het} and P_{bi} are the values of the power absorbed by the mixer related to the local oscillator and the constant bias current, respectively. The parameters R_{op}, P_0, and K were determined from the current–voltage characteristics of the mixers under consideration.

Figure 4 shows the dependences of the conversion-loss factor for an AlGaAs/GaAs mixer based on structure 1 with $\mu = 2.3 \times 10^5$ cm^2/(V s) and structure 760 with $\mu = 7.7 \times 10^4$ cm^2/(V s) on the power absorbed by the mixers (per electron); we measured these dependences at 77 K. It can be seen from Fig. 4 that the smallest conversion-loss factor for both structures is obtained in the region of high absorbed power, i.e., in the region of high heating of the electron gas. The lowest conversion losses, $L = 13$ dB, correspond to the mixer with a higher mobility of the 2D electron gas. The curves shown in Fig. 4 also indicate that the same values of the conversion-loss factor are attained for mixers with different electron mobilities at a different level of heating of the 2D electron gas; moreover, a much higher absorbed power is required in the case of a mixer with a lower electron mobility.

It is worth noting that, if we take into account the requirement for matching the structure resistance to the resistance of the IF circuit and for constancy of the local-oscillator power when choosing the operating point, the conversion losses depend only on the coefficient K. In turn, this coefficient (taking into account the constancy of the 2D electron concentration in the range of electron temperatures under consideration) is controlled by the temperature dependence of the charge-carrier mobility. At temperatures of ~77 K, the relaxation of the hot-electron momentum in an AlGaAs/GaAs heterostructure is possible only as a result of scattering by either the residual impurities in GaAs or polar optical phonons. We confirmed this inference by experimentally measuring the dependences of the mobility μ on the temperature T in the range $T = 4.2–200$ K for structures 1, 5, and 15 (Fig. 5). The theoretical calculated dependence $\mu(T)$ [11] for an AlGaAs/GaAs heterostructure in the case of scattering of 2D electrons by optical phonons is also shown in Fig. 5. The dependences shown in Fig. 5 indicate that the transition to the prevalence of optical-phonon scattering for AlGaAs/GaAs structures with a higher mobility of the 2D electron gas occurs at lower temperatures than for structures with a lower mobility. Consequently, in order to obtain the largest possible value of $\partial\mu/\partial T$ (and the smallest possible value of L) governed
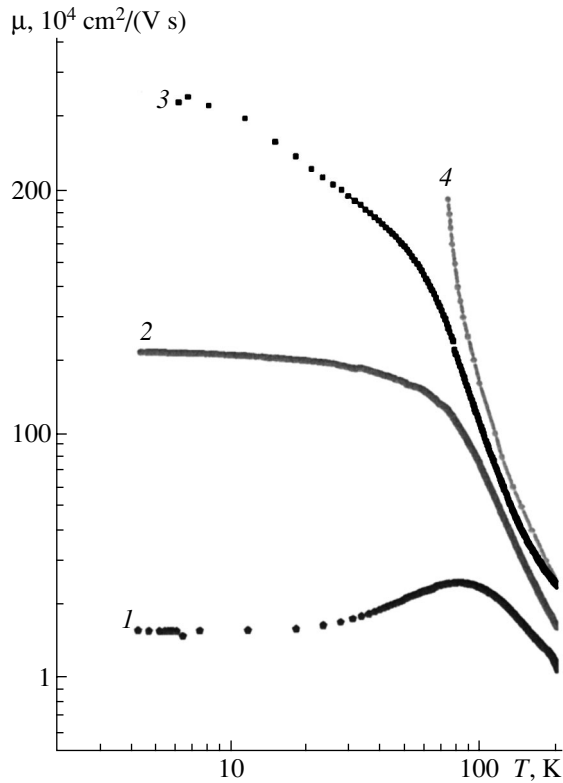
Fig. 5. Temperature dependence of the mobility for structures (*1*) 15, (*2*) 5, and (*3*) 1. Curve *4* represents the result of the calculation.

Fig. 6. Dependence of the conversion-loss factor on the total absorbed power per 1 μm^2 for an AlGaAs/GaAs mixer at $T = 77$ K for structures 1 and 760. Curve *1* corresponds to structure 1, with the electron mobility $\mu = 2.3 \times 10^5$ cm^2/(V s), and curve *2* corresponds to structure 760, with $\mu = 7.7 \times 10^4$ cm^2/(V s).

by the optical-phonon scattering, we have to apply a lower power of the local-oscillator source P_{het} to samples with a higher mobility μ. This behavior completely confirms the above temperature dependences for the samples with different mobilities of 2D electrons.

Estimations of noise temperature for a receiver based on an AlGaAs/GaAs mixer were carried out on the basis of the determined conversion-loss factor. The two-band noise temperature of the receiver is obtained from the following conventional expression [12]:

$$T_n = L_{sing}/2(T_{out} + T_{IF}). \qquad (1)$$

Here, L_{sing} are the total losses of a single-band mixer, T_{IF} is the noise temperature of the IF amplifier, and T_{out} is the noise temperature at the mixer output. According to Gerecht *et al.* [12], the two major contributions to T_{out} are made by the thermal-fluctuation noise T_{fl} and the Johnson noise T_J. As was shown by Gershenzon *et al.* [13], the thermal-fluctuation noise in a mixer based on an AlGaAs/GaAs heterostructure $T_{fl} \approx 70$ K, while T_J is equal to the electron temperature (in the case under consideration, ~100 K) in the first approximation. Consequently, $T_{out} \approx 170$ K. The typical value of T_{IF} is $T_{IF} \approx 20$ K at $T = 77$ K. The total mixer losses can be represented by the sum of the conversion losses of the sensitive element (the value $L \approx 13$ dB obtained by us) and
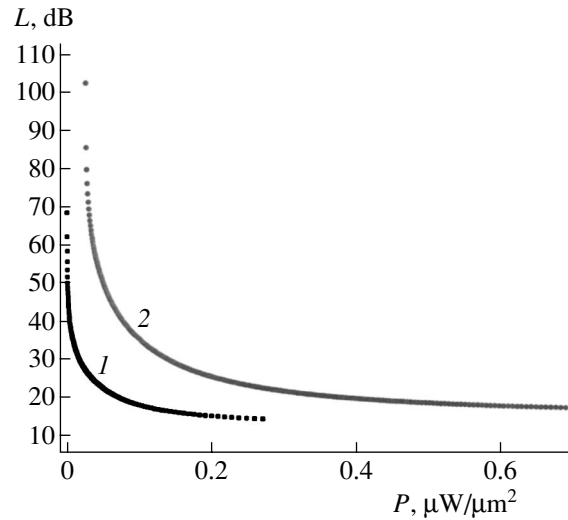
the losses in the high- and intermediate-frequency channels, with the latter losses amounting to ~7 dB in present-day receivers at frequencies of ~1 GHz [14]. The noise temperature obtained using expression (1) for an AlGaAs/GaAs mixer is equal to ~1900 K. This temperature indicates that further studies of the most important characteristic of the mixer, i.e., the noise temperature, are very important and that further improvement of the results already obtained is possible.

5. OPTIMAL LOCAL-OSCILLATOR POWER FOR AN AlGaAs/GaAs MIXER

When estimating the optimal local-oscillator power required for the operation of a mixer based on an AlGaAs/GaAs heterostructure, it is convenient to represent the conversion-loss factors obtained for structures with different mobilities of the 2D electron gas as dependences on the active mixer area. In Fig. 6, we show the dependence of L on the total absorbed power per 1 μm^2 for structures 1 and 760. It can be seen that, for structure 1, which has a lower concentration and higher mobility of the 2D electron gas, the conversion-loss factor levels off and takes a nearly constant value of 13 dB at absorbed power in excess of 0.2 $\mu W/\mu m^2$. For structure 760, the dependence $L(P_0)$ levels off at much larger values of absorbed power. Taking into account the measurements of optical losses in a submillimeter-range receiver based on a local-oscillator mixer [14], we can state that the necessary power of the local-oscillator source for an AlGaAS/GaAs mixer with an area of 1 μm^2 should be ~0.5 μW. If structures with submicrometer planar sizes were fabricated on the basis of

an AlGaAs/GaAs heterojunction with a higher mobility and a lower concentration of 2D electrons, the above value of the optimal absorbed power could be reduced even more. This reasoning makes the development of submillimeter-multielement-array receiving systems based on AlGaAs/GaAs mixers promising.

6. CONCLUSION

The main characteristics of millimeter- and submillimeter-band mixers based on a separate AlGaAs/GaAs heterojunction with $\mu = 2.3 \times 10^5$ cm²/(V s) and $n_s = 3 \times 10^{11}$ cm⁻² at $T = 77$ K were found to be the following: a conversion-loss factor $L \approx 13$ dB, conversion bandwidth of a mixer $f_{3\,dB} \approx 4$ GHz, and optimal local-oscillator absorbed power per 1 µm² of area $P_{het} = 0.2$ µW. In order to improve the mixer characteristics, it is necessary to use the heterojunctions with a higher mobility and lower concentration of 2D electron gas. With the above parameters of an AlGaAs/GaAs mixer, the main characteristics of a millimeter- and submillimeter-band receiver operating at $T = 77$ K would be the following: a receiver noise temperature $T_n \approx 1900$ K, receiver conversion bandwidth $f_{3\,dB} = 4$ GHz, and optimal power of the local-oscillator source for a mixer with an area of 1 µm² $P_{het} = 0.5$ µW. This consideration makes the fabrication of multielement-array receiving sections and their use in thermal-imaging systems possible.

ACKNOWLEDGMENTS

REFERENCES

1. TELIS home page: http://telis.af.op.dlr.de/; HERSCHEL home page: http://astro.estec.esa.nl/SA-general/Projects/Herschel/; SOFIA home page: http://sofia.arc.nasa.gov/.

2. A. Karpov, J. Blondel, M. Voss, and K. Gundlach, IEEE Trans. Appl. Supercond. **9**, 4456 (1999).

3. A. Semenov, G. N. Goltsman, and R. Sobolewski, Lab. Laser Energ. Rev. **87**, 134 (2002).

4. T. W. Crowe, R. J. Mattauch, H. P. Raser, *et al.*, Proc. IEEE **80**, 1827 (1992).

5. J. X. Yang, F. Agahi, K. S. Yngvesson, *et al.*, IEEE Trans. Microvawe Theory Tech. **41**, 581 (1993).

6. J. X. Yang, C. F. Musante, and K. S. Yngvesson, Appl. Phys. Lett. **66**, 1983 (1995).

7. G. N. Gol'tsman and K. V. Smirnov, Pis'ma Zh. Éksp. Teor. Fiz. **74**, 532 (2001) [JETP Lett. **74**, 474 (2001)].

8. K. S. Yngvesson, Appl. Phys. Lett. **76**, 777 (2000).

9. M. Lee, L. N. Pfeffer, and K. W. West, Appl. Phys. Lett. **81**, 1243 (2002).

10. F. Arams, C. Allen, B. Peyton, and E. Sard, Proc. IEEE **54**, 612 (1966).

11. K. Hirakawa and H. Sakaki, Appl. Phys. Lett. **49**, 889 (1986).

12. E. Gerecht, C. F. Musante, H. Jian, *et al.*, in *Proceedings of 10th International Symposium on Space THz Technology* (Univ. Virginia, Charlottesville, 1999), p. 200.

13. E. M. Gershenzon, G. N. Gol'tsman, I. G. Gogidze, *et al.*, Sverkhprovodimost: Fiz. Khim. Tekhnol. **3**, 1711 (1990).

14. A. D. Semenov, H.-W. Hubers, J. Shubert, and G. N. Goltsman, J. Appl. Phys. **88**, 6758 (2000).

Translated by A. Spitsyn

PHYSICS OF SEMICONDUCTOR DEVICES

Semiconductor WGM Lasers for the Mid-IR Spectral Range

V. V. Sherstnev*^, A. M. Monakhov*, A. P. Astakhova*, A. Yu. Kislyakova*, Yu. P. Yakovlev*, N. S. Averkiev*, A. Krier**, and G. Hill***

Ioffe Physicotechnical Institute, Russian Academy of Sciences, St. Petersburg, 194021 Russia
^e-mail: V.SHERSTNEV@mail.ioffe.ru
**Lancaster University, Lancaster, LA1 4YB, UK*
***University of Sheffield, Sheffield, S1 3JD, UK*
Submitted November 22, 2004; accepted for publication December 6, 2004

Abstract—Disk-cavity whispering-gallery-mode (WGM) semiconductor lasers for the mid-IR spectral range have been developed. The specific properties of these devices are investigated. © *2005 Pleiades Publishing, Inc.*

1. INTRODUCTION

Semiconductor lasers for the IR spectral range have been actively studied during the last ten years. The mid-IR (2–8 μm) range is of considerable practical interest because it includes the characteristic absorption lines of numerous toxic and harmful gases and liquids, explosives, etc. However, the advantage of optical detection of substances of this kind is not fully taken advantage of because of the lack of simple coherent light sources for this spectral range.

Usually, the active region of a 2–4 μm semiconductor laser is made of a narrow-gap semiconductor. In such semiconductors, in contrast to wider gap ones, nonradiative recombination is strong, which reduces the gain in the active region. In this case, the demands on the optical-cavity Q factor increase by virtue of the generator self-excitation condition $GF = 1$, where G is a single-pass gain and F is the energy feedback coefficient. The estimated single-pass gain along a beam path of ~100 μm is 1.4 [1], which is not sufficient for the onset of lasing in a conventional stripe laser at room temperature.

Earlier [2], we reported the results of studies of ring lasers with an emission peak at the wavelength λ = 3.05 μm. Ring lasers for the visible range have been studied before (see [3] and the references therein). The specific feature of these devices was the use of a disc cavity with a whispering gallery mode (WGM).

The WGM in disc cavities has been studied both theoretically and experimentally [3]. It was found that the Q factor of the disc cavities can exceed 10^6 [4]. However, WGM lasers have not yet demonstrated decisive advantages as compared to conventional semiconductor lasers for the visible and near-IR range.

In our opinion, this circumstance is related to the fact that, in this spectral range, devices with a conventional configuration operate sufficiently well at room temperature for the high quality of WGM cavities not to offer a decisive advantage over the disadvantages typical of WGM lasers: a complicated design of beam outlet, instability of the ring cavity, and multimode (in a general case) operation.

In the mid-IR range, lasers of simple design just do not exist (recently, quantum-cascade lasers operating at 300 K were reported [5], but their design is very complicated). Therefore, the increase in quality provided by a disc cavity opens the way for fabrication of a device capable of lasing even when the optical gain in the active region is not high. Furthermore, since the wavelength in the range under study is λ ≈ 3 μm (~1 μm within the cavity), the demands on the surface finish are significantly lowered, and the treatment of the cavity surface can be reduced to the usual lithography and standard methods of finishing.

In this study, we discuss mid-IR WGM lasers emitting at a wavelength of 3–4 μm at the temperature $T = 70$–120 K. The obtained results give grounds to hope for the development of room-temperature devices.

2. SAMPLES AND EXPERIMENTAL METHODS

Light-emitting laser diodes were fabricated based on LPE-grown InAsSbP/InAs$_{1-x}$Sb$_x$/InAsSbP double heterostructures (DHs). The DHs were grown in a standard graphite holder on a (100) InAs substrate. The rectangular substrates used, which were 18×16 mm in size and had a dopant concentration from 2×10^{16} to 5×10^{18} cm^{-3}, were produced by Wafer Technology Ltd. The epitaxial growth was controlled by a PC using Lab-View software. The details of the technology are described in [6–8].

The active region of the DHs was composed of an InAs$_{1-x}$Sb$_x$ solid solution, with the Sb content x varying from 0 to 0.11. The carrier density in the active region was below 5×10^{15} cm^{-3}. This density was obtained owing to defect gettering in the active region doped with Yb, with Pb used as a neutral solvent. The active region thickness was 0.5–0.7 μm.
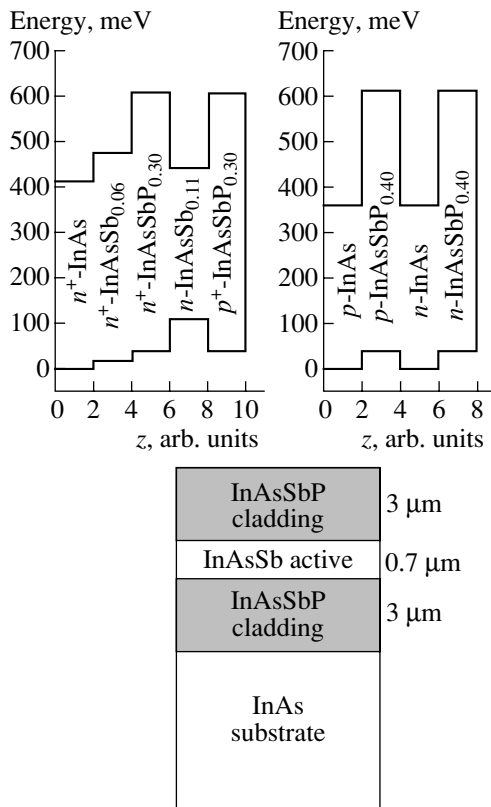
Fig. 1. Semiconductor structures used in the fabrication of lasers. z is the coordinate in the direction of layer growth.

Fig. 2. Micrograph of a mesa.

A Monospec 1000 high-resolution (1 Å) monochromator was used to study the mode structure of the spectra. In the measurement with a lower resolution, or in those that demanded a high focal power of the setup, a DK-480 monochromator (CVI Laser Corp.) with a resolution of 15 Å was used.

The emission was detected by a J10D-M204-R04M-60 cooled InSb photodiode with a PA-9 (Judson technologies) preamplifier. A Stanford Research SR850 lock-in instrument was used.

The active region was embedded between *n*- and *p*-type layers of a wide-gap InAsSbP solid solution. The wide-gap *n*- and *p*-type regions were doped, respectively, with Sn to 5×10^{18} cm^{-3} and with Zn (1×10^{18} cm^{-3}). Figure 1 shows a typical device configuration.

Laser diodes were fabricated from epitaxial structures using standard photolithography and reactive ion etching in a CH$_4$:H$_2$ gas medium. The mesa diameter ranged from 100 to 1000 μm. After etching, the surface of the mesa was passivated with Si$_3$N$_4$. Ohmic contacts were produced by thermal sputtering of AuZn:Au and AuTe:Au onto the *p*- and *n*-type layers, respectively. The top contact was a 30-μm-wide ring lying at a distance of 10 μm from the edge of the mesa. The crystal was soldered with In onto a TO-49 case. The emission was collected by a parabolic mirror. Figure 2 shows a micrograph of a laser diode produced in this way.

The electroluminescence spectra of the laser diodes were studied in pulsed and quasi-stationary modes. In the pulsed mode, the pulse width τ varied from 50 ns to 30 μs, and the repetition rate *f*, from 1 to 50 kHz. A current *I* of 0.1 to 10 A was passed through the device. The measurements were performed in the temperature range 4–300 K.

A laser diode was placed in a cryostat with a sapphire window, and the emission was focused by a system of fluorite lenses onto the monochromator slit.
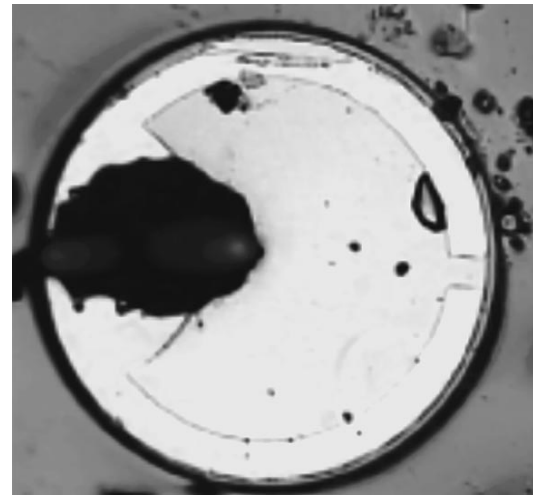
3. EXPERIMENTAL RESULTS AND DISCUSSION

3.1. Ring Lasers 200 μm in Diameter

In this study, we discuss two types of laser diodes: type 1, with an active region based on InAs, and type 2, with an InAs$_{0.89}$Sb$_{0.11}$ active region. The emission wavelength of the type-1 and type-2 devices was λ ≈ 3.04 and 3.9 μm, respectively, at the temperature *T* = 77 K. The type-1 devices were fabricated with a disc cavity of 200 and 400 μm in diameter, and, in the type-2 devices, the diameter of the cavity was 400μm.

Figure 3 shows the typical coherent emission spectra of a device with a diameter of 200 μm. It can be seen that the emission is multimode, with the mode spacing Δλ ≈ 40 Å.

In order to correlate the experimentally observed spectrum with the presumed spectrum of a WGM laser, it is necessary to recall that the strength of the *z* component of the electric field in a WGM is approximately described by the relation [3]

$$E_z = f(z)J_m\left(rn\frac{\omega_{mN}}{c}\right)e^{im\phi}, \qquad (1)$$

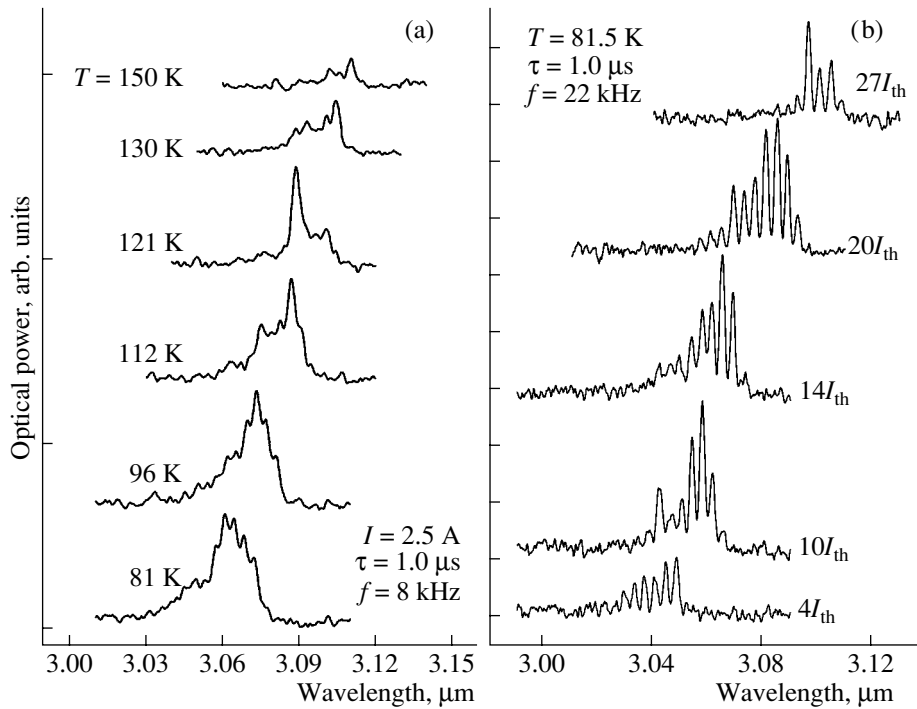where *r* is the distance along the radius, *n* is the refractive index, $\omega_{mN} = x_m^N c/nR$, x_m^N is the *N*th root of the

Fig. 3. Lasing spectra of a V2230R device 200 μm in diameter (a) at different temperatures and (b) at different currents. $I_{th} = 0.15$ A.

equation $J_m(x) = 0$, $J_m(x)$ is the Bessel function, and R is the mesa radius.

WG modes correspond to large m ($m \gg 1$) and $N \approx 1$. The specific feature of WGMs is that the field in these modes is concentrated near the cavity walls and their damping in the cavity is small. In the case under study, with a cavity diameter of 200 μm, wavelength of 3.04 μm in air, and the refractive index $n \approx 3.5$, m is about 600.

The mode spacing for the cavity under study can easily be estimated using the asymptotic expression for the roots of the Bessel function with a large index for m and $N = 1$:

$$x_m^1 \approx m + o(m^{1/3}).$$

Using this relation and expressing m in terms of λ, we obtain the mode spacing

$$\Delta\lambda_{WGM} = \frac{\lambda^2}{2\pi Rn}, \qquad (2)$$

which, in our case, yields $\Delta\lambda = 43$ Å, in perfect agreement with the experiment.

Another specific feature of the laser diodes under study is the fact that, in contrast to conventional lasers with Fabry–Perot cavities, they operate at a current exceeding the threshold value by a factor of 27 ($I = 27I_{th}$), and they remain operable at temperatures up to 150 K (a standard stripe laser fabricated from the same material becomes inoperative at 110 K).

Before we discuss the dependence of the optical output power of the laser on the driving current (the external quantum efficiency), it is necessary to note that the current density in a round mesa with a circular contact is highly nonuniformly distributed and to find this distribution for the given sample shape.

It is noteworthy that a laser diode is a nonlinear device that does not obey Ohm's law. (Moreover, since the active region is a double heterojunction with double charged layers on its interfaces, the standard theory of a p–n junction is not applicable to this device either.) Nevertheless, the current–voltage characteristic can be approximated by a straight line in the range of working voltages, and the current density distribution can be calculated assuming the existence of some additional voltage drop across the active region of a real device, which cannot be calculated in terms of a linear theory.

Formulated in this way, the problem of calculation of the current density distribution is reduced to the solution of the standard equation

$$\nabla(\sigma\nabla\varphi) = 0$$

with the boundary condition

$$\iint_{\partial\Omega} j_n dS = I$$

instead of setting the potential at the contacts (in this case, the potential at the contacts is assumed to be constant). Here, I is the current in the sample; j_n is the normal component of the current density; σ is the conductivity, which is different in different regions; and φ is
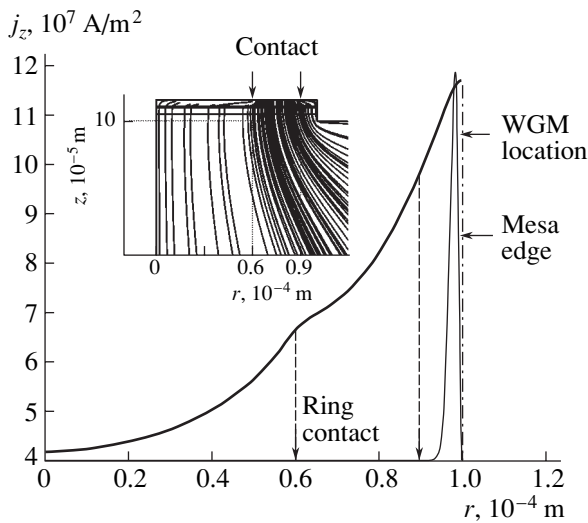
Fig. 4. Current density distribution along the radius of a round mesa with a ring contact. Inset: the distribution of current lines.

the potential. The integration is performed over any surface $\partial\Omega$ dividing the sample into two parts and passing between the contacts.

The thus calculated distribution of the normal component of the current density $j_n \equiv j_z$ on the interface of the active region is shown in Fig. 4. The same figure demonstrates the position of the WGM in respect to the mesa edge. The inset shows the scheme of current lines, which illustrates how such a distribution is attained. As can be seen in Fig. 4, the current density peaks exactly at the place where the WGM is localized.

Figure 5 shows the calculated current density distribution and a photo of the device under study in the LED mode, made using an IR photographic camera (at room temperature). Since the light intensity is proportional to the normal component of the current density, this photo indicates, at least, qualitative agreement between the calculation and the experiment.

Figure 6 shows the dependence of the laser output power on the current density in the active region (for definiteness, we plot the average current density in a ring ~10 μm in width and situated at the mesa edge along the x axis). Figure 6 also shows similar dependences for a stripe laser made of the same material (in this case, the current density is easily obtained by dividing the total current by the contact area) and for a ring of 400 μm in diameter. The last result will be discussed in the next section.

As can be seen in Fig. 6, the threshold current in a ring laser with a 200 μm diameter is severalfold smaller than that in a conventional stripe laser, which confirms the high quality of the disk cavity. At the same time, the slope of the curve for the stripe laser is significantly larger, which means that the external quantum efficiency of this device is higher.
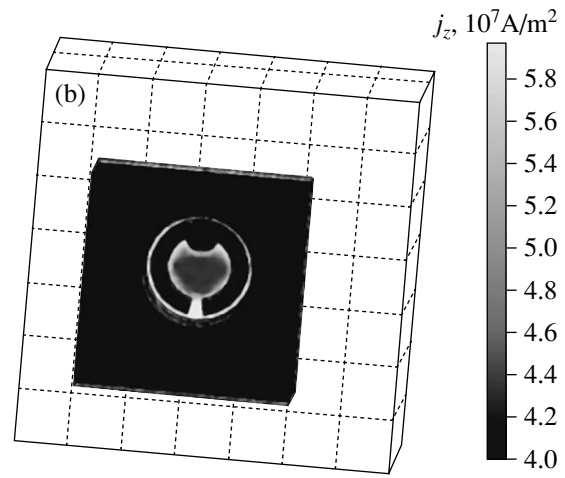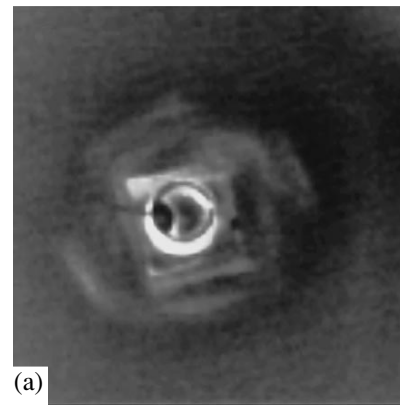

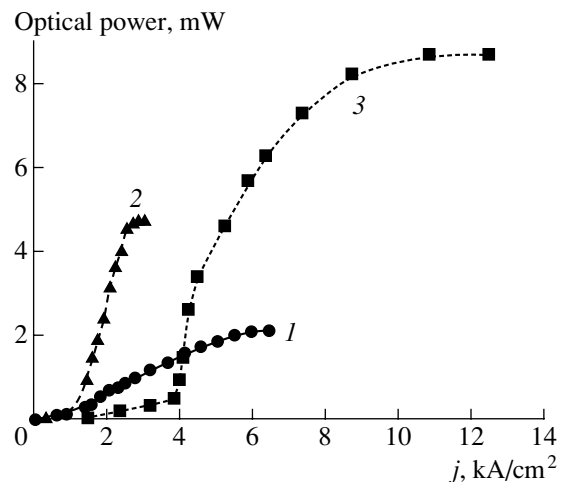**Fig. 5.** (a) IR photo of a LED and (b) the calculated current density distribution.

Fig. 6. Output power of the lasers vs. the current density j in the active region. (*1*) a 200-μm ring laser, (*2*) a 400-μm ring laser, and (*3*) a stripe laser.

We attribute the small experimental quantum efficiency of the ring laser to several factors. First, no special device was used for outcoupling light from the cav-
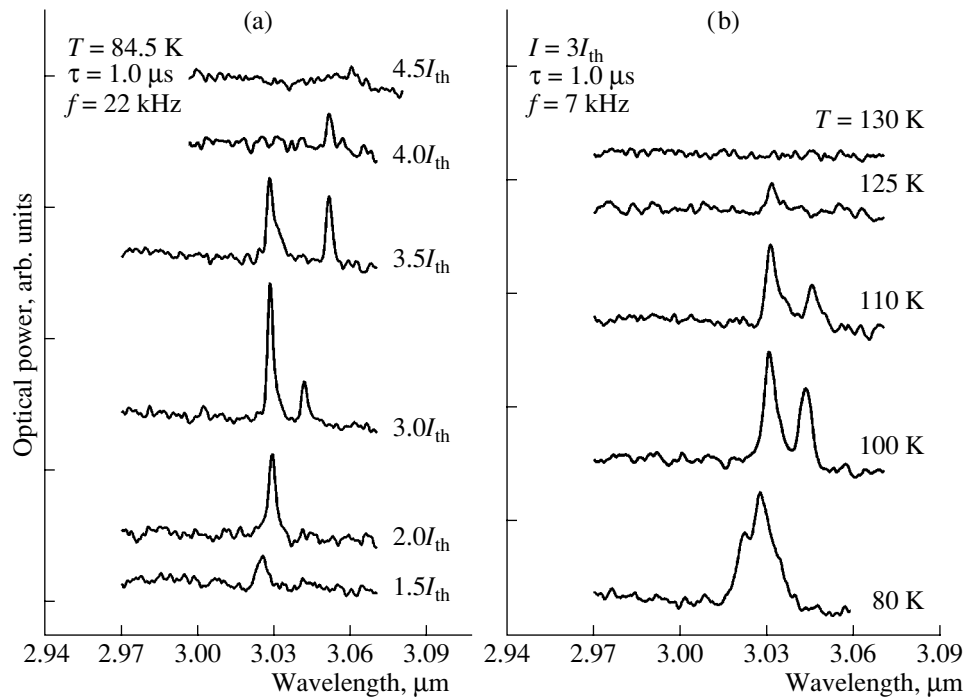
Fig. 7. (a) Mode positions at different currents and (b) emission spectra at different temperatures for an V2230R Device with a diameter of 400 μm and an InAs-based active region. $I_{th} = 0.65$ A.

ity; therefore, it seems probable that only a fraction of the optical output power was measured and the external quantum efficiency was underestimated. Second, the WGM is localized near the mesa edge, where centers of nonradiative recombination are also localized as a result of technological factors; therefore, indeed, the internal and, accordingly, the external quantum efficiency of a WGM laser must be lower than that of a stripe laser. The problem of which of these two factors is dominant needs further study.

3.2. Ring Lasers 400 μm in Diameter

Along with lasers with a diameter of 200 μm, we fabricated ring lasers with a diameter of 400 μm and an active region composed of InAs (Figs. 7, 8) and InAs$_{0.89}$Sb$_{0.11}$ (Fig. 9). The specific feature of these lasers is that, in contrast to the 200-μm-diameter lasers, their emission spectrum shows separate high-intensity modes (Figs. 8, 9). The spectral mode spacing ranges from 40 to 150 Å. The InAs-based laser demonstrates quasi-single-mode lasing at currents up to twice the threshold current.

Detailed study of the spectra of the 400-μm lasers reveals several other modes, which are suppressed in respect to the fundamental mode. For the nearest modes, the mode spacing is ~17 Å (see Fig. 8), which agrees with the mode spacing for the WGM as estimated from Eq. (2).

The dependence of the output power on the current density in the active region was studied using the

above-described method. As can be seen in Fig. 6, this dependence for the 400-μm lasers differs significantly from that for the 200-μm lasers. This observation suggests that the operating modes in these two cases are different and that the difference is related to the cavity size not to the structure of the active region: indeed, devices in which the active region is made up of different materials, which emit at significantly different wavelengths, demonstrate similar behavior.
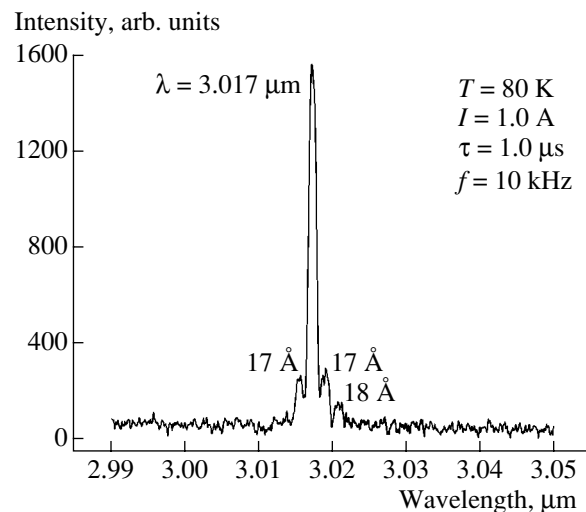

Fig. 8. High-resolution emission spectrum of a V2133R device with a diameter of 400 μm and an InAs-based active region. $I_{th} = 0.65$ A.
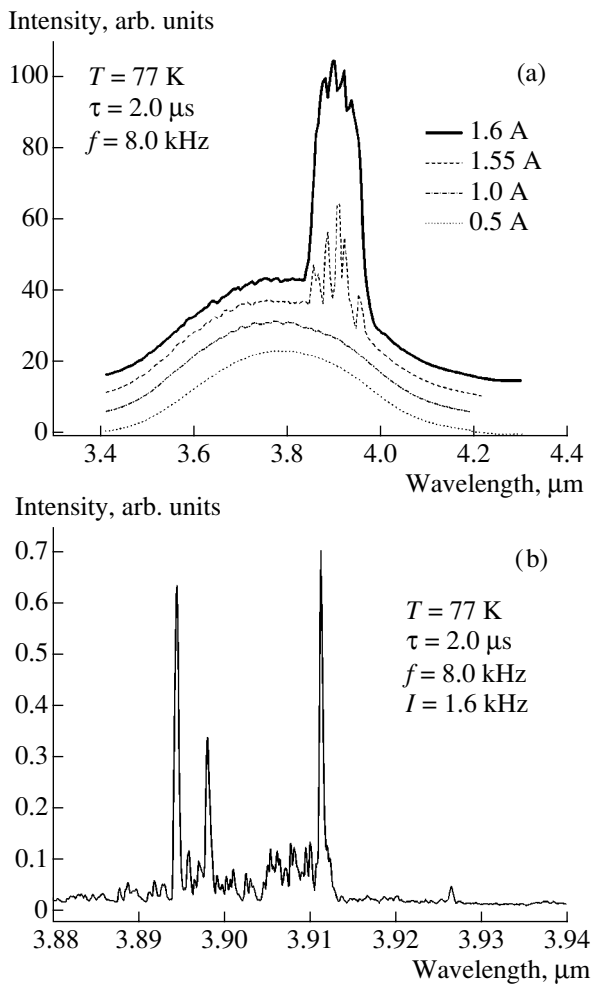
Intensity, arb. units

Fig. 9. (a) Mode positions at different currents, and (b) the mode structure of emission for a V2346-2 device with a diameter of 400 μm and an InAsSb-based active region.

The different behavior observed for the two sizes of WGM lasers can be explained in two plausible ways: first, the cavity modes generated in a 400-μm ring are not WGMs; second, certain nonlinear processes appear in the large disks, leading to preferential lasing in separate WGMs. The first assumption contradicts a simple estimation of the size of a cavity with the mode spacing Δλ:

$$L = \frac{\lambda^2}{2n\Delta\lambda},$$

which yields ~80–150 μm. In a round cavity of 400 μm in diameter, there exists no region of this size selected in any way. Furthermore, WGM peaks are observed in the spectra even though they are suppressed (Fig. 8).

Therefore, we believe that the described difference in the behavior of 200- and 400-μm WGM lasers is related to the development of nonlinear processes in a larger-diameter cavity. Unfortunately, we have not yet studied this effect in detail.

4. CONCLUSIONS

The first WGM lasers for the mid-IR range have been produced. An emission power of several milliwatts is obtained at a wavelength of 3–4 μm at temperatures up to 150 K. The threshold current is several times less than that in conventional stripe lasers of the same structure, which confirms the existing concept of the high Q factor of disk cavities. The lasers can operate at currents up to $27I_{th}$. Modification of the emission spectrum is observed as the size of the disk cavity increases. The origin of this effect needs further study. The obtained results indicate that WGM lasers are promising devices for IR-spectroscopy.

ACKNOWLEDGMENTS

REFERENCES

1. A. M. Monakhov, A. Krier, and V. V. Sherstnev, Semicond. Sci. Technol. **19**, 480 (2004).

2. V. V. Sherstnev, A. Krier, A. M. Monakhov, and G. Hill, Electron. Lett. **39**, 916 (2003); V. V. Sherstnev, A. M. Monakhov, A. Krier, and G. Hill, Appl. Phys. Lett. **77**, 3908 (2000); A. Krier, D. A. Wright, V. V. Sherstnev, and A. M. Monakhov, in *Abstracts Book of Sixth International Conference on Mid-Infrared Optoelectronics Materials and Devices, MIOMD-VI* (St. Petersburg, Russia, 2004), p. 72.

3. N. C. Frateschi and A. F. J. Levi, Appl. Phys. Lett. **66**, 2932 (1995); R. P. Wang and M. Dumitrescu, J. Appl. Phys. **81**, 3391 (1997); J. R. Davies and J. T. Mendonca, Phys. Rev. E **62**, 7168 (2000).

4. D. A. Cohen, M. Hossein-Zadeh, and A. F. J. Levi, Solid-State Electron. **45**, 1577 (2001).

5. A. N. Baranov, R. Teissier, D. Barate, *et al.*, in *Abstracts Book of Sixth International Conference on Mid-Infrared Optoelectronics Materials and Devices, MIOMD-VI* (St. Petersburg, Russia, 2004), p. 3.

6. A. Krier and V. V. Sherstnev, J. Appl. Phys. **33**, 101 (2000).

7. A. Krier, H. H. Gao, and V. V. Sherstnev, IEE Proc.: Optoelectron. **147** (3), 217 (2000).

8. A. Krier and V. V. Sherstnev, J. Phys. D: Appl. Phys. **36**, 1484 (2003).

Translated by D. Mashovets

Semiconductor–Insulator Structures in the Phototargets of Vidicons Sensitive in the Middle Infrared Region of the Spectrum

N. F. Kovtonyuk^, V. P. Misnik, and A. V. Sokolov

FGUP Kometa Research Institute, Moscow, 115280 Russia
^e-mail: ruslokum@mtu-net.ru
Submitted November 1, 2004; accepted for publication December 17, 2004

Abstract—The kinetics of electronic processes in vidicon phototargets based on semiconductor–insulator structures with a narrow-gap semiconductor is considered taking into account charge drain in the insulator layer and relaxation of the nonequilibrium depletion region in the semiconductor layer. The integration time, threshold sensitivity, and resolution at various intensities of incident radiation are estimated. © *2005 Pleiades Publishing, Inc.*

It has been suggested [1, 2] that, to extend the spectra-sensitivity range of vidicons to longer wavelengths (for example, to 2.5–5.5 μm), semiconductor–insulator structures could be used as phototargets. These structures should include a narrow-gap n-type semiconductor that operates under the conditions of nonequilibrium depletion. The insulator layer should exhibit some electrical conductivity, so that the negative charge induced by an electron beam in this layer can drain off during the frame time. The electrical conductivity of the insulator is chosen according to the requirement that the times of the charge drain-off and frame integration are comparable.

Such a phototarget is in fact a heterostructure that consists of wide- and narrow-gap semiconductors, which means that the concept of the "insulator layer" should be treated as just terminological.

The energy-band diagram of a metal–insulator–semiconductor (MIS) structure in the phototarget under consideration was considered in detail in [3].

If there is an input image, a charge profile is formed in the areas exposed to light during the existence of a depletion region. This profile is retained until the depletion-region thickness becomes equal to zero as a result of thermal generation. In the case of repeat scanning of the target with an electron beam, a videosignal appears across the load resistance during the period in which the charge-profile exists.

We now consider the kinetics of the electronic processes in phototargets in which a narrow-gap extrinsic semiconductor with a band gap $\Delta E_g = 0.2$–0.4 eV and free-electron concentration $n_0 = 10^{14}$–10^{15} cm^{-3} is used as the photosensitive layer. The possible thickness of the depletion layer, which exists for some time in such a semiconductor under the effect of voltage induced by the charge deposited on the insulator, is equal to $L \leq 10$ μm. We have to determine the integration time in the phototarget taking into account the leakage current in the insulator.

Distributions of the field, charge, and voltage are described by the equations [4]

$$\varepsilon_i E_i = 4\pi e n_0 L + 4\pi e N_s - 4\pi \Delta Q_i, \qquad (1)$$

$$U = U_0 - \frac{\Delta Q_i}{C} = U_i + U_s, \qquad (2)$$

$$U_s = \frac{4\pi e n_0 L^2}{\varepsilon_s}, \quad U_i = E_i L_i, \qquad (3)$$

where ε_i and ε_s are the dielectric constants of the insulator and semiconductor layers, L is the thickness of the depletion layer, L_i is the thickness of the insulator layer, N_s is the density of free charge carriers (holes) accumulated at the semiconductor–insulator boundary, ΔQ_i is the surface density of the charge that drains through the insulator layer, U is the voltage that arises at the phototarget in reference to the signal plate if there exists a charge on the insulator-layer surface, U_s and U_i are the voltages across the semiconductor and insulator layers, U_0 is the initial voltage at the phototarget, n_0 is the concentration of ionized impurities in the semiconductor, E_i is the electric-field strength in the insulator layer, and C is the phototarget capacitance. Since $L_i \ll L$, we have

$C = \dfrac{C_s C_i}{C_s + C_i} \approx C_s = \dfrac{\varepsilon_s S}{4\pi L}$, where C_s and C_i are the capacitances of the semiconductor and insulator layers, respectively.

Substituting the expressions for U_s and U_i from (1) and (3) into Eq. (2), we obtain

$$U_0 - \frac{\Delta Q_i}{C}$$

$$= \frac{L_i}{\varepsilon_i}(4\pi e n_0 L + 4\pi e N_s - 4\pi \Delta Q_s) + \frac{4\pi n_0 L^2 e}{\varepsilon_s}. \qquad (4)$$

Differentiating (4) with respect to time and taking into account that $\dfrac{dN_s}{dt} = G_T L$ and $\dfrac{d\Delta Q_i}{dt} = \sigma_i E_i$, we represent Eq. (4) as

$$-\frac{d}{dt}\left(\frac{\Delta Q_i}{C}\right)$$
$$= \frac{L_i}{\varepsilon_i}\left(4\pi e n_0 \frac{dL}{dt} + 4\pi e G_T L - 4\pi\sigma_i E_i\right) + \frac{8\pi e n_0 L dL}{\varepsilon_s}\frac{dL}{dt}. \quad (5)$$

Here, G_T is the thermal-generation rate for free charge carriers in the semiconductor; σ_i is the electrical conductivity of the insulator layer; and $\sigma_i = e\mu n_i$, where μ is the mobility of charges in the insulator and n_i is their concentration.

In order to simplify the solution to Eq. (5), we assume that the current in the insulator layer is time-independent, since the drift mobility in insulators and semiconductors attains saturation under the effect of high fields $>10^3$ V/cm. The voltage across the insulator layer varies from 0.1 to 10 V at $L_i \approx 10^{-5}$ cm, and, consequently, the electric-field strength $E_i \approx 10^4$–10^6 V/cm; as a result, the above assumption is reasonable.

In order to determine the value of the term $\dfrac{d}{dt}\left(\dfrac{\Delta Q_i}{C}\right)$ in Eq. (5), we use the following concepts. Thermal generation dominates over recombination in the depletion region of the semiconductor; as a result, a flow of holes, which eventually accumulate at the interface, arises.

If holes are accumulated with the density ΔN_s, the depletion-region thickness decreases by ΔL and the variation in the surface charge density is given by

$$\Delta Q_i = e n_0 \Delta L = e n_0 (L_0 - L), \quad (6)$$

where L_0 is the initial thickness of the depletion region.

Taking (6) into account at $L \gg L_i$, we can represent the first term in Eq. (5) as

$$\frac{d}{dt}\left(\frac{\Delta Q_i}{C}\right) = \frac{d}{dt}\left(\frac{4\pi e n_0 (L_0 - L) L}{\varepsilon_s}\right)$$
$$= \frac{4\pi e n_0 L_0}{\varepsilon_s}\frac{dL}{dt} - \frac{8\pi e n_0 L}{\varepsilon_s}\frac{dL}{dt}. \quad (7)$$

We then use the expressions for $\dfrac{d}{dt}\left(\dfrac{\Delta Q_i}{C}\right)$ and $\dfrac{d}{dt}\Delta Q_i$ to transform Eq. (5) into the following form:

$$-\left(\frac{e n_0 L_0 \varepsilon_i}{L_i \varepsilon_s} + e n_0\right)\frac{dL}{dt} = e G_T L - \sigma_i E_i. \quad (8)$$

A solution to Eq. (8) is written as

$$\ln\frac{e G_T L - \sigma_i E_i}{e G_T L_0 - \sigma_i E_i} = -t\frac{G}{n_0\left(\dfrac{\varepsilon_i L_0}{\varepsilon_s L_i} + 1\right)}. \quad (9)$$

For $L_0 \gg L$, we use formula (9) to obtain the dependence

$$L(t) = \frac{\sigma_i E_i}{e G} + \left(L_0 + \frac{\sigma_i E_i}{e G}\right)\exp\left\{-\frac{t}{T}\frac{\varepsilon_s L_i}{\varepsilon_i L_0}\right\}. \quad (10)$$

If $\sigma_i E_i \ll e G_T L$ and $\sigma_i E_i \ll e G_T L_0$, we use (10) to obtain

$$L(t) = L_0 \exp\left\{-\frac{t}{T}\frac{\varepsilon_s L_i}{\varepsilon_i L_0}\right\}, \quad (11)$$

and the integration time for the phototarget can be estimated using the formula

$$t_{int} = T\left(\frac{\varepsilon_i L_0}{\varepsilon_s L_i}\right) = \frac{n_0}{G_T}\left(\frac{\varepsilon_i L_0}{\varepsilon_s L_i}\right). \quad (12)$$

Using formula (12), we list the numerical estimates for the integration time. In structures composed of narrow-gap semiconductors (indium antimonide and indium arsenide), the thermal-generation rate $G_T \approx 10^{18}$–10^{20} cm^{-3} s^{-1} [4], $L_0 = 10^{-3}$ cm, $L_i = 10^{-5}$ cm, $\varepsilon_s \approx \varepsilon_i \approx 10$, and the impurity concentration $n_0 \approx 10^{14}$–10^{15} cm^{-3}. Substituting these values into formula (2), we find that the integration time can vary from 10^{-1} to 10^{-3} s. The experimentally measured integration times in InAs phototargets at ~80 K are equal to ~60 ms [2], while the integration time in InSb-based MIS structures has been found to be equal to ~1 ms [4].

When the phototarget is affected by an image, with the electron charge deposited on the insulator layer in the phototarget, a larger charge of holes is accumulated in the regions exposed to illumination with a higher intensity than in those exposed to illumination with a lower intensity; correspondingly, the depletion-region thickness decreases to a greater extent. In this case, the accumulated surface-charge density is given by

$$e\Delta N_s = e G_P L_0 t_{int}, \quad (13)$$

where G_P is the integrated photogeneration rate.

In the case of repeat electron-beam scanning, the illuminated element is additionally charged for the time τ_e; the additional charge is given by

$$e n \Delta L = e \Delta N_s j_S \tau_e. \quad (14)$$

As a result, a signal current with a density j_S appears across the load resistance R.

Since the values of the charge N_s in formulas (13) and (14) are the same, the value of the signal-current

density is given by the following expression, which is characteristic of integrating photodetectors:

$$j_S = eG_PL_0\frac{t_{int}}{\tau_e}. \qquad (15)$$

The highest possible signal current that can be collected from each element of a vidicon is limited by the maximum current obtained from the electron beam (1–5 μA) [3].

We now report an estimate of the threshold sensitivity and the detectivity of vidicons. The threshold sensitivity is controlled by an incident-radiation power P_i at which the photocurrent signal is equal to the noise signal. If the electron-beam current is equal to 1 μA and the bandwidth of the measured frequencies is $\Delta f = 10^6$ Hz, the noise current is $I_N \approx 10^{-9}$ A.

Comparing the noise current with the videosignal current defined by formula (15) and taking into account that the photogeneration rate G_t at the threshold power P_t is equal to $G_t = \dfrac{\gamma\alpha P_t}{h\nu S_e}$ in a single element, we can write the expression for the threshold sensitivity as

$$P_t = \frac{h\nu}{e\gamma}\frac{\tau_e}{t_{int}}I_N. \qquad (16)$$

By varying the parameters within reasonable ranges and taking into account the experimental data ($I_e = 10^{-5}$–10^{-6} A, $\tau_e = 10^{-6}$–10^{-7} s, $t_{int} = 10^{-3}$–10^{-2} s, $\gamma = 0.2$–0.7, and $h\nu = 0.36$ eV for InAs), we can use formula (16) to find that the values of the threshold power P_t and the threshold power density I_t can vary within the following ranges: $P_t = 10^{-13}$–10^{-14} W/element and $I_t = 5 \times 10^{-8}$–10^{-7} W/cm^2 (the element area $S_e = 6 \times 10^{-6}$–10^{-5} cm^2).

The experimental values of the threshold sensitivity obtained using vidicon samples with InAs-based phototargets at a temperature $T = 85$ K are equal to $(0.5$–$5) \times 10^{-13}$ W/element, which is consistent with the calculated values.

In order to calculate the specific detectivity D^*, we use the well-known formula [3]

$$D^* = \frac{\sqrt{S_e\Delta f}}{\text{NEP}}, \qquad (17)$$

where NEP is the noise-equivalent power.

In the case under consideration, the NEP $= P_i \approx 10^{-13}$–10^{-14} W/element, $S_e = 6 \times 10^{-6}$–10^{-5} cm^2, and $\Delta f \approx 10^6$ Hz. In this situation, the specific detectivity is equal to $\sim 10^{13}$ cm Hz$^{1/2}$ W^{-1} according to formula (17).

When the input images have low levels of illumination, the resolution of the semiconductor–insulator structures can be as high as hundred lines per millimeter. This behavior is related to the fact that a fairly high electric field can quickly push charge carriers to the interface and suppress charge-carrier diffusion in the transverse direction. Under these conditions, the resolution of the phototargets is mainly limited by the diameter of the sampling electron beam (15–30 μm). Photogenerated charge carriers can spread out in the transverse direction (due to bipolar diffusion) when the input images have high intensities of illumination, in which case the thickness of the depletion region vanishes (the potential well is completely filled).

Background radiation brings about not only an increase in the noise level but also overfilling of the potential well in the depletion region. The highest noise level of a vidicon is determined by an electron-beam shot noise amounting to $\sim 10^{-9}$ A/element. The possibility of accumulation in the potential well is limited by a deposited-charge density equal to $\sim 10^{12}$ e/cm^2. If background generation and thermal generation give rise to the same hole density in the accumulation time, a weak signal from the input image cannot be detected. For the input-radiation signal to be detected, the potential well should not be completely filled (instead, e.g., it should be half filled) by the combined effect of the background radiation and thermal generation. In order to realize this situation, it is necessary that the generation by signal radiation is either comparable with the generation caused by background radiation and by heat or amounts to several tenths of the total generation.

The use of two-layer semiconductor–insulator structures with nonequilibrium depletion of the semiconductor as phototargets in vidicons makes it possible to extend the spectral-sensitivity range of vidicons to the middle infrared region of the spectrum (2.5–5.5 μm). The accumulation time in the phototarget at liquid-nitrogen temperature can be $\sim(1$–$100)$ ms if the phototarget is made of a narrow-gap semiconductor with $\Delta E_g = 0.2$–0.4 eV. This consideration could lead to the design of infrared vidicons with a threshold sensitivity of $\sim(5 \times 10^{-8}$–$10^{-7})$ W/cm^2 and detectivity of $\sim 10^{13}$ cm $\sqrt{\text{Hz}}$/W.

REFERENCES

1. N. F. Kovtonyuk, Zh. Prikl. Spektrosk. **26**, 162 (1977).

2. N. F. Kovtonyuk and V. P. Misnik, Radiotekh. Élektron. (Moscow) **47**, 1145 (2002) [J. Commun. Technol. Electron. **47**, 1045 (2002)].

3. *The Infrared Handbook*, Ed. by W. L. Wolfe and G. J. Zissis (Environment. Res. Inst., Michigan, 1993; Mir, Moscow, 1999), Vol. 3.

4. N. F. Kovtonyuk, G. N. Savkov, and L. I. Vanina, Fiz. Tekh. Poluprovodn. (Leningrad) **9**, 1208 (1975) [Sov. Phys. Semicond. **9**, 805 (1975)].

Translated by A. Spitsyn

A Mechanism of Electroluminescence in Silicon Diodes with a High Dislocation Density

A. V. Sachenko and Yu. V. Kryuchenko^

Lashkarev Institute of Semiconductor Physics, National Academy of Sciences of Ukraine, Kiev, 03028 Ukraine
^e-mail: kryuchenko@isp.kiev.ua

Abstract—A new concept is suggested to explain the effect of dislocations on electroluminescence in silicon diodes. This concept is based on consideration of the spatial correlation between injected electrons and holes that recombine inside a dislocation core. This correlation leads to an increase in the probability of radiative recombination for electron–hole pairs. Two cases are analyzed. In the first case, the resulting current is controlled mainly by tunneling of electrons and holes along dislocations, which is followed by electron–hole recombination under the conditions of barrier lowering. In this situation, electroluminescence is not related to the fundamental absorption edge and the energy position of the electroluminescence band shifts to shorter wavelengths as either the temperature decreases or the applied voltage increases. In the second case, the diffusion-related component is prevalent in the total current. The radiative recombination of electron–hole pairs occurs in quasi-neutral regions and the electroluminescence exhibits an edge-related character. It is shown that the suggested mechanism may be responsible for a substantial enhancement of both the electroluminescence intensity and the quantum efficiency in silicon diodes with dislocations if the Shockley–Read–Hall lifetime is shorter than 10^{-3} s. © 2005 Pleiades Publishing, Inc.

1. INTRODUCTION

Appreciable progress has recently been made with regard to increasing the quantum efficiency of electroluminescence (EL) in silicon diode structures. Results that are encouraging with respect to practical applications have been obtained for structures of three types. The first type is represented by diode structures formed from high-quality silicon grown by the floating-zone method. For these structures, it has been possible to obtain an appreciable reduction of recombination losses related to the nonradiative multiphonon bulk and surface recombination of charge carriers [1, 2]. Diode structures obtained by boron implantation are assigned to the second type of devices under consideration [3–5]. Finally, the third type of devices includes diode structures of plastically deformed silicon [6, 7]. The EL mechanism is more or less clear only for the first type of structure, where this mechanism is apparently related to the radiative recombination of charge carriers in quasi-neutral regions of the emitter and base [1, 8–10]. In these structures, radiative recombination of spatially correlated electrons and holes is dominant at room and elevated temperatures [11, 12], whereas excitonic recombination is prevalent at low temperatures [9, 10]. The intense EL observed in the second and third types of structures is, in some way, related to the presence of dislocations. For example, it was suggested [3] that an increase in the EL intensity in the second type of structure (where, as is well known, a large number of dislocations are formed as a result of ion implantation) is related to an increase in the nonradiative lifetime of charge carriers due to appearance of barriers that limit the recombination.

The dislocation-related mechanism of EL and photoluminescence (PL) in silicon has been analyzed in a number of studies, whose results were summarized in [13]. It was shown that, if the dislocation density exceeds 10^6 cm^{-2}, the PL and EL intensities are higher than those in dislocation-free silicon. The so-called $D1$ band peaked at 0.8 eV was the main band observed at fairly low temperatures; as temperature increased, the EL and PL intensities decreased drastically, although the data on the temperature corresponding to the onset of appreciable falloff of the $D1$-band intensity were different in different publications.

In this study, we advance a hypothesis that makes it possible to account for the EL mechanism in the second and third types of structures using the same reasoning. The hypothesis is based on the assumption that, due to the spatial correlation between an electron and hole in the region of a dislocation, the probability of their radiative recombination at the dislocations increases drastically; in a number of cases, this increase can not only compensate for an increase in the probability of nonradiative recombination but even become prevalent. It is established that EL and PL in the third type of structures are typically observed in a situation in which the barrier does not completely vanish. We advance and theoretically justify the assumption that the EL mechanism in the third type of structure is related to radiative recombination of electrons and holes that tunnel along the dislocation cores, thus decreasing the distance between electrons and holes. It is shown that the position of the emission-band peak depends, in this case, on the extent to which the initial barrier height is lowered in the p–n junction. We compare the results of our cal-

culation with experimental data and show that there is qualitative agreement between them.

The EL related to the fundamental-absorption edge in the second type of structure is attributed to the diffusion component of the total current, whereas the EL band located at longer wavelengths and observed at fairly low temperatures is related to the tunneling component of the total current. This component is caused by tunneling of the charge carriers along the cores of dislocations.

2. FORMULATION OF THE PROBLEM

We assume that, in diodes with dislocations intersecting the p–n-junction space-charge region (SCR), a tunneling current, caused by multistage tunneling of charge carriers along the cores of dislocations, flows in addition to the diffusion- and recombination-related currents. The tunneling component of the total current is expressed in a "dislocation shunt" model, first suggested by Evstropov $et\ al.$ [14]. We carried out a theoretical calculation for a situation where the use of a model of equivalent diode's circuit with the lumped parameters is justified; in this case, the total-current density in the diode $J(V, T)$ can be written as

$$J(V, T) = J_{Sd}(T)\exp\left(\frac{q[V - I(V, T)R_s]}{kT}\right)$$

$$+ J_{Sr}(T)\exp\left(\frac{q[V - I(V, T)R_s]}{2kT}\right) \quad (1)$$

$$+ J_{St}(T)\exp\left(\frac{q[V - I(V, T)R_s]}{\varepsilon_t}\right).$$

Here, $J_{Sd}(T) = J_{Sd}(300)[n_i(T)/n_i(300)]^2$ is the density of the saturated diffusion-related current; $J_{Sr}(T) = J_{Sr}(300)(T/300)^{1/2}n_i(T)/n_i(300)$ is the density of the saturated recombination-related current; $n_i(T) = [N_c(T)N_v(T)\exp(-E_g(T)/kT)]^{1/2}$ is the charge-carrier concentration in an intrinsic semiconductor; $N_c(T)$ and $N_v(T)$ are the effective densities of states in the conduction and valence bands; R_s is the series resistance; and $I(V, T) = AJ(V, T)$, where A is the area of the diode structure. We used the following expression for the saturation tunneling-current density $J_{St}(T)$:

$$J_{St}(T) = qN_d\nu\exp\left(-\frac{qV_C(T)}{\varepsilon_t}\right). \quad (2)$$

Here, q is the elementary charge, N_d is the density of dislocations that intersect the p–n junction, ν is the frequency of collisions of tunneling electrons (or holes) with the barrier, $qV_C(T) = E_g(T) - kT\ln[(T/300)^{3/2}1.02 \times 10^{19}\ cm^{-3}/p_p] - kT\ln[(T/300)^{3/2}2.86 \times 10^{19}\ cm^{-3}/n_n]$ is the barrier height in the p–n junction, $E_g(T)$ is the silicon band gap, p_p and n_n are the majority-carrier concentrations expressed in cm^{-3}, and ε_t is the characteristic
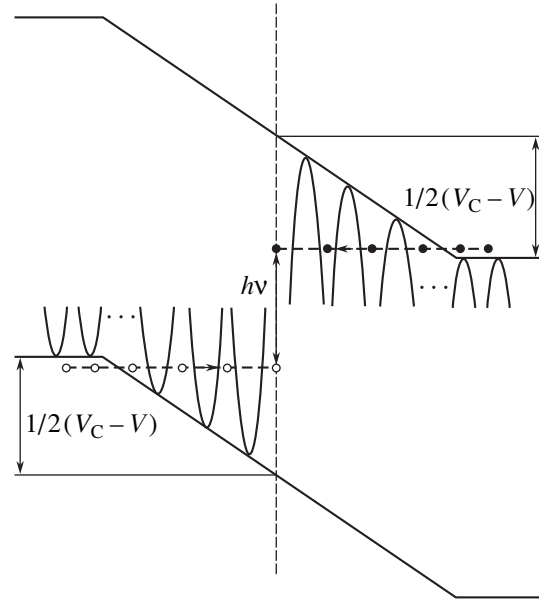
Fig. 1. Energy diagram of the p–n junction and a schematic representation of tunneling [14].

energy of tunneling. The energy-band diagram of the p–n junction and a schematic representation of the tunneling are shown in Fig. 1.

2.1. Theoretical Analysis of Electroluminescence for the Third Type of Structure

In Fig. 2, we show the calculated temperature dependences of the diffusion- and tunneling-related components of the total current at the bias voltage $V = 0.9$ V. Here, the dislocation density serves as a parameter and is varied in the range 10^4–10^8 cm^{-2}. It can be seen from Fig. 2 that, as the dislocation density increases, the temperature range in which the tunneling component of the current is prevalent widens; moreover, this component is dominant even at room temperature if the dislocation density is as high as $\sim 10^7$ cm^{-2}.

The integrated intensity of EL related to the radiative recombination of electrons and holes that tunnel along the dislocations is directly proportional to the tunneling-current density. This intensity is given by the following expression when the probability of tunneling is lower than that of recombination:

$$U = \frac{J_T}{q}\frac{\tau_{d1}^n}{\tau_{d1}^r}. \quad (3)$$

Here, J_T is the tunneling component of the current density and is defined by the third term on the right-hand side of formula (1), and τ_{d1}^r and τ_{d1}^n are the radiative and nonradiative times for recombination of electrons and holes that come into close proximity with each other in the course of tunneling within the dislocation core. The quantum yield for this EL component is equal
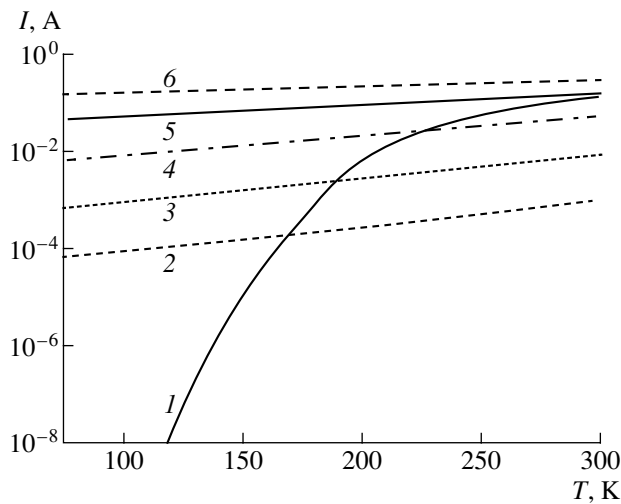
Fig. 2. Calculated temperature dependences of the (*1*) diffusion and (*2–6*) tunneling currents. The following values of the parameters were used in the calculations: the saturation-current density $J_{Sd} = 10^{-14}$ A/cm^2 at $T = 300$ K; $A = 10$ mm^2; $R_s = 1$ Ω; $\nu = 10^{13}$ s^{-1}; $\varepsilon_t = 0.08$ eV; $V = 0.9$ V; and $N_d = $ (*2*) 10^4, (*3*) 10^5, (*4*) 10^6, (*5*) 10^7, and (*6*) 10^8 cm^{-2}.

Fig. 3. (*1*) Theoretical and (*2*) experimental temperature dependences of the position of the EL-band peak. The following values of the parameters were used in the calculations: $A = 10$ mm^2, $\nu = 10^{13}$ s^{-1}, $R_s = 1$ Ω, $\varepsilon_t = 0.08$ eV, $N_d = 3 \times 10^6$ cm^{-2}, and $I_C = 10$ mA. Calculated dependences of the tunneling current on the dislocation density are shown in the inset; the following values of the parameters were used in the calculations: $T = 77$ K; $A = 10$ mm^2; $\nu = 10^{13}$ s^{-1}; $R_s = 1$ Ω; $\varepsilon_{t0} = 0.066$ eV; $\beta = 0.00014$ eV cm$^{1/2}$; $p_p = 10^{20}$ cm^{-3}; $n_n = 3 \times 10^{15}$ cm^{-3}; and $V = $ (*1*) 0.9, (*2*) 1.0, and (*3*) 1.1 V.

to $\tau^n_{d1} / \tau^r_{d1}$. We can estimate the position of the EL-band peak from the condition $E_m(T) \approx qV_x(T, I_C)$, where $V_x(T, I_C)$ is the voltage that should be applied to the structure at a given temperature T in order to obtain the current $I_C = AJ_C$ (A is the diode-structure area). The dependence $E_m(T)$ for the case of $I_C = 10$ mA was derived by solving transcendental Eq. (1); this dependence is shown in Fig. 3 (curve *1*). As can be seen from Fig. 3, this estimation for the photon energy at the tunneling-EL peak yields a value of approximately 0.76 eV at room temperature and at the values of the parameters used in the calculation. As the temperature is lowered, this energy increases to a value of about 0.9 eV at $T = 100$ K. In addition, as follows from Fig. 3, the barrier does not vanish completely, even at low temperatures, in the case under consideration; i.e., the injection-related mechanism of EL exists under the condition $V - I_C R_s < V_C(T)$.

The temperature dependence of the energy position of the EL-band peak in plastically deformed diodes is also shown in Fig. 3 (curve *2*); this dependence is drawn using the experimental data reported by Kreger *et al.* [6]. As can be seen, our theoretical estimates are consistent with the experimental data at a temperature close to 250 K. At lower temperatures, the experimental values of the energy corresponding to the peak of the EL band are smaller than those calculated under the assumption that the barrier vanishes completely. This disagreement is apparently caused by the appearance of a one-dimensional dislocation band [13] at fairly low temperatures. It is also noteworthy that, according to the results of our calculations, the energy corresponding to the EL-band
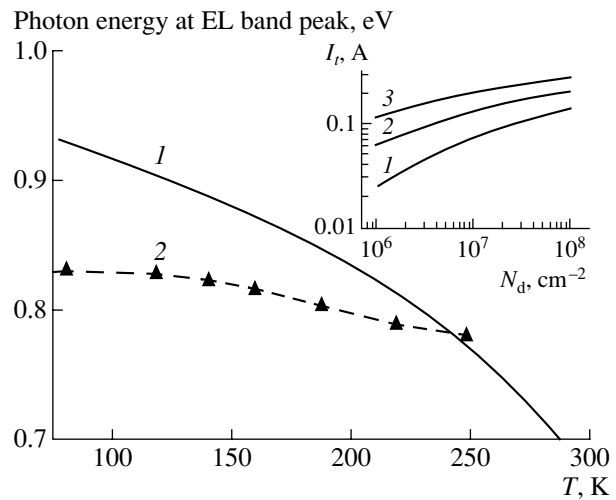
peak should increase as the total current at which the EL is measured increases. It is this behavior that is observed experimentally [6].

2.2. Theoretical Analysis of Electroluminescence When the Diffusion-Related Component of the Total Current Is Dominant

In this case, we should take into account the effect of dislocations on the effective lifetime of electron–hole pairs in the quasi-neutral regions of the base and emitter. We restrict the consideration to room-temperature cases and assume that the diffusion-related component is dominant in the total current.

In the case under consideration, an increase in the intensity and quantum yield of electroluminescence in the diode structures can be obtained under the condition that the inequality $\tau^n_{d2} / \tau^r_{d2} \ll \tau^n_0 / \tau^r_0$ is satisfied; here, τ^r_{d2} and τ^n_{d2} are the radiative and nonradiative lifetimes of charge carriers in the region of a dislocation, and τ^r_0 and τ^n_0 are the corresponding lifetimes in the dislocation-free region, which are governed only by conventional mechanisms of electron–hole recombination (for example, multiphonon recombination, radiative electron–hole recombination, excitonic recombination, and band-to-band Auger recombination).

When dislocations are arranged perpendicularly to the p–n junction and the criterion $(1/\tau_{d2}^n + 1/\tau_{d2}^r)d_d/(DN_d^{1/2}) \ll 1$ (where d_d is the diameter of the dislocation core and D is the diffusion coefficient in the base) is satisfied, the effective lifetime of holes in an n-type base is given by

$$\tau_{\text{eff}}^p \cong \left(\left(\frac{1}{\tau_0^{np}} + \frac{1}{\tau_0^{rp}}\right) + 4N_d^{1/2}d_d\left(\frac{1}{\tau_{d2}^n} + \frac{1}{\tau_{d2}^r}\right)\right)^{-1}. \quad (4)$$

Similarly, we can write the following expression for the lifetime of electrons in a p-type emitter:

$$\tau_{\text{eff}}^p \cong \left(\left(\frac{1}{\tau_0^{nn}} + \frac{1}{\tau_0^{rn}}\right) + 4N_d^{1/2}d_d\left(\frac{1}{\tau_{d2}^n} + \frac{1}{\tau_{d2}^r}\right)\right)^{-1}. \quad (5)$$

Using the notation of [9], we can express the diffusion lengths for electrons (L_n) and holes (L_p) as

$$L_n = \left[D_n\left(\frac{1}{\tau_{sn}} + \left(A_i + \frac{1}{n^*\tau_x}\right)p_p + C_p p_p^2 \right.\right.$$
$$\left.\left. + 4N_d^{1/2}d_d\left(\frac{1}{\tau_{d2}^n} + \frac{1}{\tau_{d2}^r}\right)\right)^{-1}\right]^{1/2}, \quad (6)$$

$$L_p = \left[D_p\left(\frac{1}{\tau_{sp}} + \left(A_i + \frac{1}{n^*\tau_x}\right)n_n + C_n n_n^2 \right.\right.$$
$$\left.\left. + 4N_d^{1/2}d_d\left(\frac{1}{\tau_{d2}^n} + \frac{1}{\tau_{d2}^r}\right)\right)^{-1}\right]^{1/2}. \quad (7)$$

Here, τ_{sp} and τ_{sn} the Shockley–Read–Hall lifetimes in the n- and p-type regions, respectively; A_i is the constant of the radiative electron–hole recombination; $n^* = (N_c N_v/N_x)\exp(-E_x/kT)$, where N_x is the effective density of excitonic states and E_x is the exciton binding energy; $\tau_x = (1/\tau_x^r + 1/\tau_x^n)^{-1}$, where τ_x^r is the radiative lifetime of excitons and τ_x^n is the nonradiative exciton lifetime related to the Auger recombination with the involve-

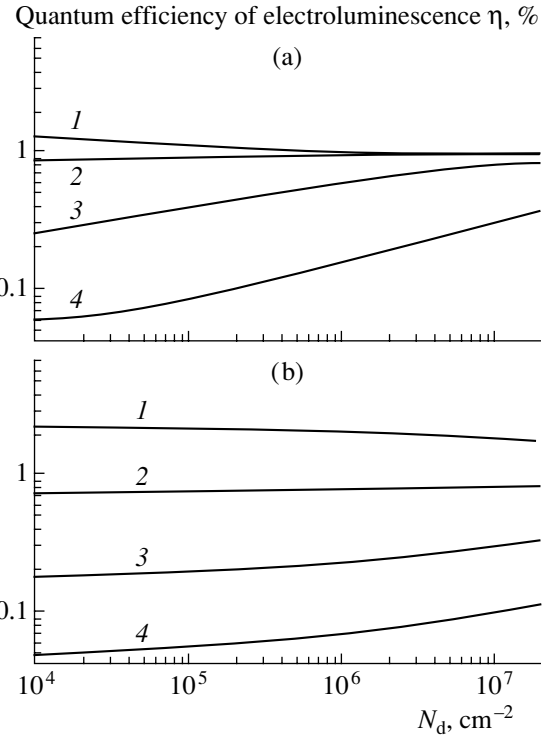Quantum efficiency of electroluminescence η, %

Fig. 4. Calculated dependences of the EL internal quantum efficiency in a silicon diode on the dislocation density for the cases of (a) transverse and (b) longitudinal arrangement of dislocations with respect to the p–n junction. The following values of the parameters were used in the calculation: $p_p = 10^{17}$ cm^{-3}; $n_n = 10^{16}$ cm^{-3}; $\tau_{sn} = 10^{-4}$ s; and $\tau_{sp} =$ (1) 10^{-2}, (2) 10^{-3}, (3) 10^{-4}, and (4) 10^{-5} s.

ment of a deep bulk level; and C_n and C_p are the coefficients of the band-to-band Auger recombination of electrons and holes in silicon.

In the case of a long-base diode, we take into account the dislocation-related EL and express the internal quantum yield of electroluminescence as

$$\eta = n_n p_p \frac{(L_p + L_n)(A_i + 1/n^*\tau_x^r) + 4N_d^{1/2}d_d(L_p/\tau_{d2}^r n_n + L_n/\tau_{d2}^n p_p)}{D_p p_p/L_p + D_n n_n/L_n}. \quad (8)$$

Analysis shows that taking into account the effect of dislocations can bring about both an increase in the EL quantum efficiency η and its decrease. The increase occurs when the Shockley–Read–Hall lifetimes of charge carriers in the emitter and base are fairly short, whereas the decrease is possible if these lifetimes are long. These lifetimes are on the order of 10^{-2} s for the values of the parameters used in the calculations. In Fig. 4a, we show the calculated dependences of η at $T = 300$ K on the dislocation density; these dependences illustrate the above reasoning. In the calculations, we

used the value of 2.5×10^{-15} cm^3 s^{-1} for the coefficient of the combined absorption-edge and excitonic radiative recombination $A_i + 1/n^*\tau_x^r$. The quantity $1/n^*\tau_x^n$, which characterizes the nonradiative excitonic Auger recombination, was assumed to be equal to $(2.7 \times 10^{-16}$ cm$^3)\tau_{sp}^{-1}$ in n-Si and $(1.3 \times 10^{-17}$ cm$^3)\tau_{sn}^{-1}$ in p-Si. For the coefficients of the band-to-band Auger recombination of electrons and holes in p-Si (C_p) and n-Si (C_n), we used the value $C_p = 10^{-31}$ cm^6 s^{-1} and the empirical dependence $C_n = (2.8 \times 10^{-31} + 2.5 \times$

$10^{-22}/n_n^{1/2}$) cm^6 s^{-1}, where the numerical value of n_n is expressed in units of cm^{-3} [9]. When plotting the curves in Figs. 4a and 4b, the diffusion coefficients for holes and electrons were assumed to be equal to $D_p = 10$ cm^2 s^{-1} and $D_n = 25$ cm^2 s^{-1}. We also used the values $d_d = 10^{-6}$ cm, $\tau_{d2}^n = 10^{-7}$ s, and $\tau_{d2}^r = 10^{-5}$ s in the calculation.

It is much more difficult to simulate a situation where the dislocations are arranged parallel to the p–n-junction plane. We can obtain a simple estimate of η in this case by assuming that the dislocations are distributed uniformly in the emitter bulk and are absent in the base. In order to calculate η, we can then use a modified form of expression (8) in which the effective quantity

$$L_p^* = \left[D_p \left(\frac{1}{\tau_{sp}} + \left(A_i + \frac{1}{n^* \tau_x} \right) n_n + C_n n_n^2 \right)^{-1} \right]^{1/2} \quad (9)$$

appears instead of the diffusion length L_p.

As can be seen from Fig. 4b, where the calculated dependences of η on the dislocation density are shown for the case under consideration, these dependences are similar to those shown in Fig. 4a for smaller values of τ_{sp}. However, as can be seen from Fig. 4b, the EL quantum yield decreases as the dislocation density increases if $\tau_{sp} \geq 10^{-3}$ s.

To conclude this subsection, we note that, in fact, both EL mechanisms can exist in the same diode structures. As can be seen from Fig. 2, at intermediate values of the dislocation densities, the diffusion-related mechanism of charge transport is dominant and the EL is related to the fundamental-absorption edge at high temperatures, whereas, in the region of low temperatures, the tunneling component of the current is prevalent and the energy of the emitted photons can be close to the value of $qV_x(T, I_C)$, where $V_x(T, I_C)$ is the voltage that should be applied to the structure in order to obtain the current I_C at a given temperature T. It is also noteworthy that our results are valid when dislocations are separated by distances that do not exceed the diffusion lengths for the minority charge carriers in the p- and n-type regions; for example, the corresponding diffusion length should be no shorter than 10 μm at a dislocation density of 10^6 cm^{-2}.

3. DISCUSSION OF EXPERIMENTAL AND THEORETICAL RESULTS

It was noted in [13] that dislocation-related PL and EL intensities depend on N_d randomly from the dislocation density $N_d \approx 10^6$ cm^{-2} onwards. This behavior can easily be explained in the context of the dislocation-shunt model. Indeed, according to [14], tunneling along dislocations occurs through a chain of barriers formed by decorating impurities. At a given impurity concentration, the heights of barriers for tunneling electrons (and holes) increase as the dislocation density increases; as a result, the value of ε_t increases. The cal-

culated dependences of the tunneling dislocation-related current for the model when the value of ε_t depends on the dislocation density according to the law $\varepsilon_t = \varepsilon_{t0} + \beta N_d^{0.25}$ are shown in the inset in Fig. 3. As can be seen from Fig. 3, the value of the tunneling current practically levels off in the region of $N_d \approx 10^8$ cm^{-2}, which is consistent with the experimental dependences.

We now analyze the differences between the conditions of EL observation in the second and third types of structures. In the second type of structure, experimental studies of the EL were carried out at fixed values of the current in the range 50–250 mA. The electrode diameter in diodes was on the order of 1 mm. Study of the EL for the third type of structure was performed at a dark current equal to 10 mA, and the electrode area was approximately ten times larger than in the case of the first type structure. Thus, the current density at which EL was measured in the second type of structure was higher than that in the third type of structure by at least 1.5–2 orders of magnitude. In addition, in the third type of structure, the dislocation density was higher than 10^8 cm^{-2} [7], which, according to our estimates, led to the predominance of the tunneling component of the total current even at room temperature. This inference is supported by the forward portions of the current–voltage (I–V) characteristics of silicon diodes formed from a plastically deformed material; these characteristics were reported in [15] for the case of $T = 300$ K. In the voltage range 0.1–0.7 V, the I–V characteristics reported in [15] obey the exponential law with a nonideality factor of ~3, which is highly indicative of the tunneling mechanism of the charge transport. The barrier does not disappear completely in the p–n junction in the third type of structure. However, the same can also be stated about the second type of structure if we take into account their high series resistance R_s. As the theoretical estimates reported in [3] show, the forward I–V characteristics can be simulated only under the condition that $R_s \approx 50$ Ω; in this case, the value of $V - IR_s$ is approximately equal to 0.6 V even at $V \approx 2$ V; i.e., the barrier indeed does not vanish completely. Since the dislocation density in the second type of structure is much lower than that in the third type of structure, the diffusion-related component of the total current should be dominant in the second type of structure at room temperature; in addition, the EL should be related to the fundamental-edge absorption. Such is indeed the case for the experimental observations. As temperature is lowered, the role of the tunneling component should become more important and, correspondingly, a band at longer wavelengths should appear. The EL tunneling component is especially pronounced at low temperatures in the case of diodes fabricated by implantation of boron [4]. The EL has been studied [4] in a wide range of temperatures and implantation doses. In addition to the edge EL, a long-wavelength EL band, with its peak located at ~0.96 eV at $T = 12$ K, was observed at low temperatures [4]. The temperature dependence of the

energy position of the peak for this band was consistent with the results shown in Fig. 3. The band under consideration is almost unobservable at room temperature, which, in our opinion, is due to a lower dislocation density in the ion-implanted diodes compared to the case of plastically deformed silicon. The integrated intensity of this band decreases as the temperature increases. This behavior, on the one hand, is accounted for by a decrease in the tunneling component of the current (compared to the diffusion-related component) as the temperature increases and, on the other hand, is probably related to the activation character of the nonradiative recombination of electrons and holes that migrate along dislocations.

The electroluminescence observed in all three types of structures at temperatures below 295 K is apparently related to excitons and is caused by the radiative recombination of correlated electron–hole pairs at room temperature.

The following considerations can be applied to the mechanism of radiative recombination involving dislocations. For electron–hole pairs in the vicinity of a dislocation, the factor of spatial restriction imposed on the motion of electrons and holes in a direction transverse with respect to the dislocation axis brings about an enhancement of the Coulomb component of the electron–hole interaction; i.e., the degree of correlation between the electron and hole states increases. As a result, the thermodynamic equilibrium between electron–hole pairs and excitons should shift towards an increase in the exciton concentration. This behavior can be also promoted by an increase in the probability of radiative recombination of excitons both with the involvement of phonons and as a result of pseudodirect zero-phonon transitions, in which case the law of conservation of momentum is satisfied owing to the dislocation itself. Therefore, the role of the excitonic component of emission in structures with dislocations should apparently become more important compared to that in dislocation-free diode structures.

4. CONCLUSIONS

In this study, we used the hypothesis that the probability of radiative recombination involving dislocations increases owing to an increase in the degree of spatial correlation between electrons and holes to suggest two mechanisms describing the appearance of dislocation-related electroluminescence in silicon diodes. These mechanisms allowed us to explain an increase in the quantum efficiency of electroluminescence in comparison with dislocation-free diodes.

The first mechanism involves the radiative recombination of electrons and holes that tunnel towards each other over dislocations in the p–n junction. This mechanism is prevalent even at room temperature in the case of plastically deformed diodes and manifests itself at low temperatures in diodes with a moderate dislocation density. Electroluminescence that is unrelated to the edge absorption and a shift of the emission-band peak to longer wavelengths are typical of this mechanism.

The second mechanism implies radiative recombination with the involvement of dislocations in quasineutral regions of the emitter and base. This mechanism is dominant at relatively high temperatures. In this case, electroluminescence is related to the edge absorption.

It follows from the above analysis that the electroluminescence intensity is directly proportional to the total-current density, whereas the quantum yield of electroluminescence is independent of this density.

REFERENCES

1. M. A. Green, J. Zhao, A. Wang, *et al.*, Nature **412**, 805 (2001).
2. T. Trupke, J. Zhao, A. Wang, *et al.*, Appl. Phys. Lett. **82**, 2996 (2003).
3. W. L. Ng, M. A. Lourenco, R. M. Gwilliam, *et al.*, Nature **410**, 192 (2001).
4. J. M. Sun, T. Dekorsy, W. Skorupa, *et al.*, Appl. Phys. Lett. **83**, 3885 (2003).
5. N. A. Sobolev, A. M. Emel'yanov, E. I. Shek, and V. I. Vdovin, Fiz. Tverd. Tela (St. Petersburg) **46**, 39 (2004) [Phys. Solid State **46**, 35 (2004)].
6. V. Kveder, E. A. Steinman, S. A. Shevchenko, and H. G. Grimmeis, Phys. Rev. B **51**, 10520 (1995).
7. V. V. Kveder, M. Badylevich, E. Steinman, *et al.*, Appl. Phys. Lett. **84**, 2106 (2004).
8. O. B. Gusev, M. S. Bresler, I. N. Yassievich, and B. P. Zakharchenya, in *Proceedings of NATO Workshop on Toward the First Silicon Laser* (Trento, 2002); M. S. Bresler, O. B. Gusev, B. P. Zakharchenya, and I. N. Yassievich, in *Proceedings of Workshop on Nanophotonics* (Nizhni Novgorod, Russia, 2003), Vol. 1, p. 59.
9. A. V. Sachenko, A. P. Gorban', and V. P. Kostylev, Fiz. Tekh. Poluprovodn. (St. Petersburg) **38**, 570 (2004) [Semiconductors **38**, 550 (2004)].
10. A. V. Sachenko, A. P. Gorban, V. P. Kostylyov, *et al.*, Semicond. Phys., Quantum Electron. Oproelectron. **7**, 5 (2004).
11. H. Schlangenotto, H. Maeder, and W. Gerlach, Phys. Status Solidi A **21**, 357 (1974).
12. M. Ruff, M. Fick, R. Lindner, *et al.*, J. Appl. Phys. **74**, 267 (1993).
13. *Electronic Properties of Dislocations*, Ed. by Yu. A. Osip'yan (Éditorial URSS, Moscow, 2000) [in Russian].
14. V. V. Evstropov, M. Dzhumaeva, Yu. V. Zhilyaev, *et al.*, Fiz. Tekh. Poluprovodn. (St. Petersburg) **34**, 1357 (2000) [Semiconductors **34**, 1305 (2000)].
15. V. G. Eremenko, V. I. Nikitenko, and E. B. Yakimov, Zh. Éksp. Teor. Fiz. **67**, 1148 (1974) [Sov. Phys. JETP **40**, 570 (1974)].

Translated by A. Spitsyn

A Combined Model of a Resonant-Tunneling Diode

I. I. Abramov^, I. A. Goncharenko, and N. V. Kolomeĭtseva

Belarussian State University of Informatics and Radioelectronics, ul. Brovki 17, Minsk, 220013 Belarus
^e-mail: nanodev@bsuir.edu.by
Submitted December 21, 2004; accepted for publication January 21, 2005

Abstract—A combined model of a resonant-tunneling diode is suggested. This model is based on the semiclassical and quantum-mechanical (the wave-function formalism) approaches. In addition to certain factors, important properties of the device heteroboundaries, in particular, the shape of the energy-band offset and the surface charge, are taken into account in the model. It is shown that the model can be used to obtain satisfactory agreement with experimental data when calculating the current–voltage characteristics of the diode. It is important that the peak voltages are determined with a good accuracy only if the resistances of extended passive regions and the surface charge of the heteroboundaries are taken into account. © 2005 Pleiades Publishing, Inc.

1. INTRODUCTION

The resonant-tunneling diode (RTD) is one of the most promising devices produced in the field of solid-state nanoelectronics [1]. For example, at present, analog, digital, and analog–digital multipurpose integrated circuits based on these devices are being developed [2]. Some of these circuits are already produced commercially [3]. The highest attained frequencies of RTD operation exceed 2.5 THz; i.e., this device exhibits an unprecedentedly fast response. This property makes it possible to use an RTD as a unique active element in microwave electronics. Unfortunately, in spite of the seemingly relatively simple principle of operation of the device under consideration [4, 5], the physics and simulation of this device are fairly complex. This circumstance is related to the very high sensitivity of the device under consideration to the effect of a great variety of factors. Therefore, there are many unresolved problems with regard to both the physics of RTD operation and the RTD simulation.

Basically, when constructing RTD models, one can use the following general quantum-mechanical formalisms [6]: (i) the formalism of wave functions; (ii) the formalism of density matrices; (iii) the formalism of the Wigner distribution functions, (iv) the formalism of the Green's functions, and (v) the formalism of the Feinman integrals over trajectories. When deriving simplified models, one begins, as a rule, with the formalism of wave functions [7–11]. More adequate and complex numerical models are typically developed in the context of the formalisms of wave functions [12–16], the Wigner distribution functions [17–21], and the Green's functions [22–24]. A great number of factors are often taken into account in the course of self-consistent calculation in the more adequate RTD models, the most important and most frequently used of these factors being the charge in various regions of the structure and the scattering [25]. Each of the three formalisms mentioned above has its own advantages and disadvantages. Without analyzing these formalisms in detail, we note that the formalisms of the Wigner and Green's functions lead to an increase in the number of variables and, therefore, require computers with a higher throughput when these formalisms are to be implemented numerically [19, 21, 24]. As a result, the corresponding models are of limited utility for widespread use.

In spite of the great efforts undertaken for, in fact, more than 30 years, it has been very rare that the results of calculations of the current–voltage (*I–V*) characteristics of an RTD could be made consistent with experimental data, even for models demonstrating a high adequacy in the context of the above three formalisms. The best results in this context were obtained using the models reported in [24–26].

We may speculate as to the cause of the poor agreement with the experimental data for the majority of models. In our opinion, there are two main causes in addition to those mentioned above, and the first of these is related the approximations used. The single-particle approximation and the effective-mass method are conventionally used in numerical models of all three formalisms. In addition, the models, as a rule, are one-dimensional; i.e., the passive regions are often not analyzed. Second, there have been no attempts made to take into account the properties of actual heteroboundaries in the RTD models in more detail [27]; in particular, the shape of the energy-band offset and the surface charge are disregarded.

In this paper, we describe a developed numerical combined RTD model that is based on the semiclassical and quantum-mechanical (the wave-function formalism) approaches and takes into account the effect of charge in different regions of the structure (including the surface charge at the heteroboundaries), the shape of the band offsets at the heteroboundaries, scattering in the quantum well, and resistances of the extended pas-

sive regions. The use of this model confirms the importance of taking into account all the above factors when calculating RTD *I–V* characteristics.

2. CONSIDERATION OF THE CHARGE (INCLUDING THE SURFACE CHARGE)

The suggested RTD numerical model is based on the self-consistent solution to the Schrödinger and Poisson equations and belongs to the class of combined models [6], since this model combines the semiclassical and quantum-mechanical approaches.

We first consider how the charge in various regions of the structure (including the surface charge) is taken into account in the model. First of all, the device is considered as consisting of three regions: contacts, near-contact regions, and an active region. The effect of the contacts is described using the contact-potential difference. In the near-contact regions that also include the spacer layers, the Boltzmann statistics instead of the Thomas–Fermi approximation is used for the charge-carrier mobility [28, 29]; as a result, the electron concentration is given by [6]

$$n = n_{ie}\exp[q(\Phi - F_n)/k_{\mathrm{B}}T], \qquad (1)$$

where n_{ie} is the effective intrinsic concentration, Φ is the electrostatic potential, F_n is the quasi-Fermi potential for electrons, k_{B} is the Boltzmann constant, T is temperature, and q is the elementary charge.

In an active region that includes barriers and a quantum well, the following Poisson and Schrödinger equations are solved self-consistently:

$$\frac{\partial}{\partial x}\left(\varepsilon_s\varepsilon_0\frac{\partial\Phi}{\partial x}\right) = -q(N_D - n), \qquad (2)$$

$$-\frac{\hbar^2}{2}\frac{\partial}{\partial x}\left(\frac{1}{m^*}\frac{\partial}{\partial x}\psi\right) + V\psi = E\psi. \qquad (3)$$

Here, $\varepsilon_s\varepsilon_0$ is the permittivity of the medium, N_D is the concentration of ionized donors, m^* is the effective electron mass, ψ is the wave function, E is the electron energy, and V is the potential energy of an electron. In the active region, the quantity n is calculated on the basis of the wave functions $\psi(E_k)$ and the electron concentration for each of the states k is calculated using the well-known formula given in [28], which, in the case under consideration, takes the form

$$n = \frac{m^*k_{\mathrm{B}}T}{\pi\hbar^2}$$

$$\times\sum_k|\psi(E_k)|^2\ln\left\{1 + \exp\left[-\frac{E_k + \Delta E_c - q(\Phi - F_n)}{k_{\mathrm{B}}T}\right]\right\}, \qquad (4)$$

where ΔE_c is the conduction-band offset in the barrier with respect to the quantum well.

The initial approximation for the potential Φ is specified according to the assumption that there is electroneutrality, relation (1) is satisfied for the entire device, and the quasi-potential F_n is constant in the near-contact regions and varies linearly in the active region. The latter assumption is also used below in the course of the self-consistent calculation.

The electron concentration in the active region is determined by solving Eq. (3) in the form of a transport problem [30, 31]. To this end, the wave functions are specified as a combination of incident (transmitted) and reflected waves [30] with general boundary conditions [32] at the boundaries of the solution domain for the Schrödinger equation. It is noteworthy that, in the known models, the values of the wave functions at the boundaries of the active region are specified as fixed (zero) when the self-consistent potential is determined. This procedure leads to errors [28] and also requires additional solution of the Schrödinger equation in the form of a transport problem in order to calculate the current density J in the final stage [14, 29].

In order to improve the convergence of the iterative process, we linearize Eq. (2); as a result, we obtain

$$\frac{\partial}{\partial x}\left(\varepsilon_s\varepsilon_0\frac{\partial\delta\Phi}{\partial x}\right) - q\frac{\partial n(\Phi)}{\partial\Phi}\delta\Phi$$

$$= -\left[\frac{\partial}{\partial x}\left(\varepsilon_s\varepsilon_0\frac{\partial\Phi}{\partial x}\right) + q(N_D - n(\Phi))\right]. \qquad (5)$$

Equation (5) is solved (for the entire device, including the near-contact and active regions) for the correction $\delta\Phi$ to the potential, and a new value of the potential Φ is then determined. In the course of the solution, we took into account the nonlinear dependence of the charge on the electrostatic potential both in the classical (near-contact) and quantum-mechanical (barriers and the well) regions using the derivative $\partial n(\Phi)/\partial\Phi$. This derivative was found on the basis of expressions (1) and (4). A flowchart for the method of a self-consistent concept [6] for iterative solution of the Schrödinger and Poisson equations was reported in [30].

When estimating the accuracy of simultaneous solution of the equations, we used the following two criteria: (i) a criterion based on the largest variation in the electrostatic potential from iteration to iteration $\max|\delta\Phi(x)| \le \varepsilon ps$ and (ii) a criterion related to the fulfillment of the electroneutrality of the RTD as a whole. After the self-consistent potential has been determined, we use the transmission coefficient [30] to calculate the current density with formulas derived in [5] for the case of finite temperatures ($T \ne 0$ K) and in the limit of $T \longrightarrow 0$ K.

We now consider how the surface charge at the heteroboundary is taken into account in the model. To this end, we use the Gauss law

$$\varepsilon_s^{\Gamma-}\varepsilon_0\frac{\partial\Phi}{\partial x}\bigg|^{\Gamma-} + \varepsilon_s^{\Gamma+}\varepsilon_0\frac{\partial\Phi}{\partial x}\bigg|^{\Gamma+} = \sigma_{\mathrm{sur}}, \qquad (6)$$

where the superscripts $\Gamma-$ and $\Gamma+$ indicate points to the left and right of the boundary and σ_{sur} is the surface-charge density. It is noteworthy that the nodal point of the spatial-discretization grid must be located at the boundary. As a result, the finite-difference approximation for Eq. (5) at a point i of the interface is expressed as

$$\delta\Phi_{i-1} + \delta\Phi_i\left[-1 - \frac{h_i\varepsilon_s^{\Gamma+}}{h_{i+1}\varepsilon_s^{\Gamma-}}\right.$$

$$\left. - \frac{qh_i}{2\varepsilon_0\varepsilon_s^{\Gamma-}}\left(h_i\frac{\partial n_i^{\Gamma-}}{\partial\Phi} + h_{i+1}\frac{\partial n_i^{\Gamma+}}{\partial\Phi}\right)\right] + \delta\Phi_{i+1}\frac{h_i\varepsilon_s^{\Gamma+}}{h_{i+1}\varepsilon_s^{\Gamma-}}$$

$$\tag{7}$$

$$= -\Phi_{i-1} - \Phi_i\left(-1 - \frac{h_i\varepsilon_s^{\Gamma+}}{h_{i+1}\varepsilon_s^{\Gamma-}}\right) - \Phi_{i+1}\frac{h_i\varepsilon_s^{\Gamma+}}{h_{i+1}\varepsilon_s^{\Gamma-}} - \frac{h_i\sigma_{\mathrm{sur}}}{\varepsilon_s^{\Gamma-}\varepsilon_0}$$

$$- \frac{qh_i}{2\varepsilon_0\varepsilon_s^{\Gamma-}}[h_i(N_{Di}^{\Gamma-} - n_i^{\Gamma-}) + h_{i+1}(N_{Di}^{\Gamma+} - n_i^{\Gamma+})],$$

where Φ_i is the value of the potential at the point i and h_i is the mesh width of the spatial-discretization grid. The approximation for internal points (outside the heteroboundaries) is a particular case of (7) at $\varepsilon_s^{\Gamma-} = \varepsilon_s^{\Gamma+}$, $N_{Di}^{\Gamma-} = N_{Di}^{\Gamma+}$, $n_i^{\Gamma-} = n_i^{\Gamma+}$, $\sigma_{\mathrm{sur}} = 0$. The finite-difference approximations of the linearized Poisson equation in the case where σ_{sur} depends on the potential Φ and of the Schrödinger equation can be found in [30]. The systems of linear algebraic equations that emerge at each step are solved using direct methods (see [30]).

3. CONSIDERATION OF THE BAND-OFFSET SHAPE AT THE HETEROBOUNDARIES

If the band-offset shape is taken into account, two basically different situations can arise, i.e., (i) the band offset is abrupt (steplike) and (ii) the band offset is more gradual. It is worth noting that both situations can also be described using a discrete model when the nodal point is located at the heteroboundary. The first situation was considered in detail in [30]. In this context, we consider the second situation, which is more attractive from the physical standpoint, of a more gradual offset.

In the approximations under consideration, we use the averaged value of the potential directly at the heteroboundary (at the ith point); specifically,

$$V_i = \frac{V_{i-1} + V_{i+1}}{2}, \tag{8}$$

where V_{i-1} and V_{i+1} are the values of the potential on opposite sides of the barrier. A hyperbolic approximation [33] (in addition to the linear approximation) has been also used to describe the barrier shape [34]. This approximation is similar to that often used when the image-force potential is taken into account in simpli-

fied models of the tunneling effect [34]. The approximation was carried out not only for the barriers but also for the quantum well between them. As a result, the modified initial potential profile is described by the expression

$$V_b(x) = V_{b0} \mp \beta\frac{d^2}{x(d-x)}, \tag{9}$$

where V_{b0} is the height of an equivalent rectangular barrier; the sign "–" corresponds to the barrier region; the sign "+" corresponds to the well region; β is a coefficient; d is the barrier width; and x is the coordinate for the barrier, with the result that $x \in (0, d)$. Division by 0 is possible at the interfacial points. Therefore, we used the linear approximation in order to describe the potential in the immediate vicinity of the interfacial points; as a result, expression (8) is valid in this case as well.

We emphasize that, in the described approximations, the band offset at the heteroboundaries is typically quite abrupt (as has been observed experimentally [27]) but is not steplike. This circumstance is related to the very small mesh width of the spatial-discretization grid in the active region of the device; as a rule, this width amounts to tenths or hundredths of a nanometer. Obviously, a great deal depends on the parameter β in expression (9).

4. CONSIDERATION OF SCATTERING

A complex Hamiltonian, in the context of various formalisms, is widely used at present to take into account the processes of inelastic scattering [25, 35]. Since the main mechanism of scattering in devices with resonant tunneling is believed to be related to scattering by optical phonons, our consideration of this scattering was performed according to the approach used in [14, 36]. In particular, after calculation of the self-consistent potential Φ, attained as a result of solving the Poisson (2) and Schrödinger (3) equations, a Schrödinger equation with a complex Hamiltonian is solved in the next stage in the quantum-well region; specifically [14, 36], we obtain

$$-\frac{\hbar^2}{2}\frac{\partial}{\partial x}\left(\frac{1}{m^*}\frac{\partial}{\partial x}\psi\right) - (E - V + iW_{\mathrm{op}})\psi = 0. \tag{10}$$

Here, W_{op} is the optical potential $W_{\mathrm{op}} = \hbar/2\tau$, where $1/\tau$ is the scattering rate. The potential V is taken from the previous stage (i.e., it depends on Φ), is calculated according to [30], and is corrected at the heteroboundaries according to the procedure described in Section 3.

In order to calculate the scattering rate, we extended the relations reported in [14, 36] to a case in which all the levels through which tunneling is possible are taken into account. In this case, we have

$$\frac{1}{\tau_l} = S_{\mathrm{op}l}\left[1 + \frac{2}{\exp(\hbar\omega_{\mathrm{op}l}/k_{\mathrm{B}}T) - 1}\right], \tag{11}$$

$$E - E_{Rl} \geq \hbar\omega_{\mathrm{op}l},$$

$$\frac{1}{\tau_l} = S_{\mathrm{op}l}\left[\frac{1}{\exp(\hbar\omega_{\mathrm{op}l}/k_{\mathrm{B}}T) - 1}\right], \qquad (12)$$

$$|E - E_{Rl}| < \hbar\omega_{\mathrm{op}l},$$

where $S_{\mathrm{op}l}$ is the scattering-rate coefficient, E_{Rl} is the energy corresponding to the lth resonant level, and $\hbar\omega_{\mathrm{op}l}$ is the energy of optical phonons for the lth level. The total scattering rate is given by

$$1/\tau = \sum_l 1/\tau_l, \qquad (13)$$

where the summation is performed over all the resonant levels l located within the specified energy range.

As a result of solving Eq. (10), we determine the wave functions. On the basis of these functions, we then calculate the transmission coefficient

$$T_{\mathrm{tot}} = T_{\mathrm{coh}} + T_{\mathrm{incoh}} = T_{\mathrm{coh}} + \frac{AT_R}{T_L + T_R}, \qquad (14)$$

where T_{coh} and T_{incoh} are the coherent and incoherent components of the transmission coefficient, A is the attenuation coefficient ($A = 1 - T_{\mathrm{coh}} - R_{\mathrm{coh}}$) ($R_{\mathrm{coh}}$ is the coherent component of the transmission coefficient), and T_L and T_R are the transmission coefficients for the left- and right-hand barriers. In order to determine the quantity T_{incoh}, we represent the wave functions as

$$\psi(x) = Ae^{ikx} + Be^{-ikx}, \qquad (15)$$

$$k(x) = \frac{1}{\hbar}\sqrt{2m^*[E - V(x) + iW_{\mathrm{op}}(x)]}. \qquad (16)$$

The quantity $k(x)$ is calculated on the basis of expression (16) with $W_{\mathrm{op}} = 0$ in the RTD active region outside the quantum well. Next, the transmission coefficient is determined according to [30], while the current density is determined according to the method described in Section 2. It is noteworthy that the wave function has previously [25, 36] been represented as

$$\psi(x) = Ae^{i(\kappa + i\gamma)x} + Be^{-i(\kappa + i\gamma)x}, \qquad (17)$$

where γ is the wave-function attenuation coefficient related to scattering and κ is the wave vector with the scattering disregarded. In this case, the coefficient γ is calculated on the basis of the optical potential and is assumed to be constant in the quantum well at a specified energy. In a strict sense, this assumption is valid only for a rectangular quantum well. Thus, the suggested modification also makes it possible to take into account an arbitrary profile of the quantum well.

5. CONSIDERATION OF RESISTANCES OF THE NEAR-CONTACT REGIONS

It was earlier assumed (as in many of the known models) that all applied voltage drops across the active region of the structure (see Section 2). It should be

noted that this assumption is indeed justified, since the near-contact (passive) regions are typically heavily doped; i.e., these regions are considered as belonging to contacts in the models under consideration.

Let us take into account the voltage drop across the RTD near-contact regions. Consideration of this voltage drop is necessitated by two factors. First, currents with very high densities can flow through the structure. Second, actual RTDs often exhibit fairly extended (generally, three-dimensional) passive regions that cannot be precisely taken into account in the context of one-dimensional numerical models.

We correct the voltage in the model suggested using the formula

$$U' = U + IR_e + IR_c, \qquad (18)$$

where U' is the voltage applied to the RTD, I is the current calculated using the model (see Sections 2–4) at a voltage U, and R_e and R_c are the resistances of the RTD near-contact regions. In order to estimate the values of these resistances, we can use the well-known model of a resistor for a slab of a uniformly doped semiconductor,

$$R = L/qs\mu_n N_D, \qquad (19)$$

where L is the length of the region, s is the cross-sectional area, and μ_n is the electron mobility. It is noteworthy that the near-contact RTD regions typically include several subregions with differing electrical conductivity; therefore, the total resistance should be estimated taking into account the above fact [38].

The software package that made it possible to compute the above-described combined RTD model was included in the NANODEV system of simulation of nanoelectronic devices [39], which is intended for personal computers (PCs). All the data reported below were obtained using this system and a PC based on a Pentium III processor.

6. RESULTS AND DISCUSSION

The effect of some of the above-considered factors on the results of the simulation has been discussed in a number of our publications [30, 31, 38–43]. For example, the established patterns of the effect of the width of different regions on the RTD I–V characteristics were described in the cases where the active-region charge is taken into account or is disregarded [30, 41]. It was found that, when calculating the I–V characteristics lying within the range of numerical values typical of actual RTDs, it is necessary to correctly take into account the charge in the active region. The results of calculations of the I–V characteristics are also profoundly affected by the shape of the band offset at the heteroboundaries [42]. In particular, for a two-barrier RTD based on $In_{0.52}Al_{0.48}As/In_{0.53}Ga_{0.47}As$, the calculated value of the peak current was approximately 47 times smaller in the case of a steplike band offset than in the case of using the averaged value of the
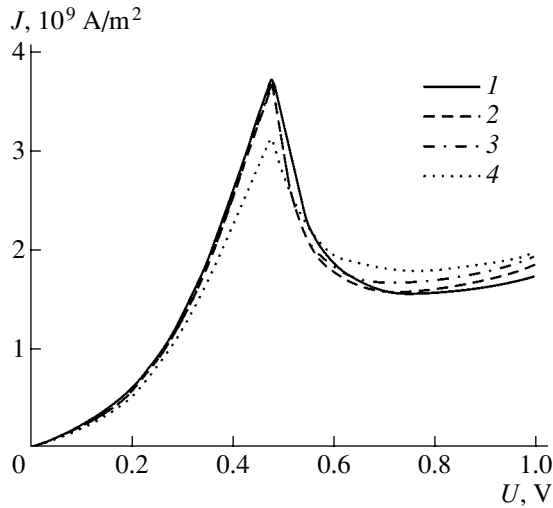
Fig. 1. Calculated *I–V* characteristics of an RTD (*1*) with scattering disregarded and (*2–4*) taking into account scattering with the optical-phonon energy $\hbar\omega_{op}$ = (*2*) 0.064, (*3*) 0.032, and (*4*) 0.016 eV.

potential at the interfacial point (see (8) and $\beta = 0$ eV in (9)). The peak voltage is higher by a factor of approximately 2.5 in the case of a steplike offset. If smooth approximations are used, the values of the peak currents and voltages (see Section 3, case (ii)) differ from each other but to a much lesser extent. As the coefficient β increases in (9), the barrier becomes more smoothed-out, with the result that its height and width decrease, which brings about an increase in the peak current and a decrease in the peak voltage. Simultaneously, the shape of the calculated *I–V* characteristic becomes closer to that of the experimental characteristic. These data indicate that it is important to develop models of the energy-band structure of heterojunctions so that these models can be applied to resonant-tunneling devices, in particular, to RTDs. At the same time, as has been shown recently [38, 43], it is necessary to take into account the insignificant (at first glance) resistances of the passive RTD regions when fitting the calculated *I–V* characteristics to the experimental data. It is also worth noting that the values of the resistances R_e and R_c are close to estimates calculated according to the concepts given in Section 5. Therefore, we can assume that these resistances are not, in fact, merely adjustable parameters in the model under consideration. The near-contact regions also profoundly affect the distributions of the charge and potential in the active region [43]; i.e., a correct description of the interaction between all three regions in an RTD is required for adequate simulation of the physical processes occurring in this device.

We now consider the effect of other factors that can be taken into account in the described combined model. The *I–V* characteristics were calculated for a GaAs/AlAs two-barrier RTD at $T = 300$ K [44]. The structure of this RTD consists of an active region that includes 2-nm-wide barriers and a 4.5-nm-wide quantum well confined by these barriers. The spacer regions on the sides of the emitter and collector contacts are not doped and have a width of 7 and 10 nm. The impurity concentration is equal to 2×10^{18} cm^{-3} in the emitter and collector near-contact regions, which have sizes of 600 nm; however, the 100-nm-thick layers near the spacers are an exception: the impurity concentration in these layers is as low as 10^{17} cm^{-3}. We used the following values of the parameters in the simulation: the barrier height 1.116 eV; $m^* = 0.068m_0$ and $\varepsilon_s = 13.18$ for GaAs; and $m^* = 0.172m_0$ and $\varepsilon_s = 10.06$ for AlAs.

We studied the effect of the parameters of the scattering model used on the results of calculations of the *I–V* characteristics. These parameters were assumed to be independent of *l* and included the energy of optical phonons $\hbar\omega_{op}$ and the scattering-rate coefficient S_{op}. An analysis of the available publications showed that the values of these parameters can vary widely. For example, we found that $S_{op} = 6.0 \times 10^{12}$ s^{-1} and $\hbar\omega_{op} = 0.32$ eV in [36], whereas $S_{op} = 1.25 \times 10^{13}$ s^{-1} and $\hbar\omega_{op} = 0.032$ eV in [14]. Therefore, in our studies, we varied the scattering parameters within the ranges close to the above experimental data.

In Fig. 1, we show the RTD *I–V* characteristics calculated using different values of $\hbar\omega_{op}$ at a fixed value of $S_{op} = 1.25 \times 10^{13}$ s^{-1}. Curve *1* corresponds to the case where scattering is disregarded. Curves *2–4* were calculated using the optical phonon energies 0.064, 0.032, and 0.016 eV. It can be seen that a decrease in $\hbar\omega_{op}$ leads to a decrease in the peak current and to an increase in the valley current (at a high voltage) of the *I–V* characteristic compared to the case where the scattering is disregarded. The most significant transformation in the shape of the *I–V* characteristic is observed at $\hbar\omega_{op} = 0.016$ eV. The ratios between the peak current and the current in the region of the valley in the *I–V* characteristic (the "contrast" of the *I–V* characteristic) are equal to 2.41 (curve *1*), 2.33 (curve *2*), 2.156 (curve *3*), and 1.744 (curve *4*). Thus, as the energy of optical phonons increases, the contrast of the *I–V* characteristic increases and attains its largest value if scattering is disregarded.

In Fig. 2, we show the results of the simulation at various values of S_{op}. Curve *1* corresponds to the *I–V* characteristic calculated with scattering disregarded. Curves *2–4* correspond to the cases where the values of S_{op} are equal to 0.625×10^{13}, 1.25×10^{13}, and 2.5×10^{13} s^{-1}. It can be seen that an increase in S_{op} brings about a decrease in the peak current and an increase in the valley current of the *I–V* characteristic. The contrast of the *I–V* characteristic decreases simultaneously and is equal to 2.237, 2.156, and 2.022 for curves *2*, *3*, and *4*.

At the same time, consideration of a various number of resonant levels when calculating the scattering rate
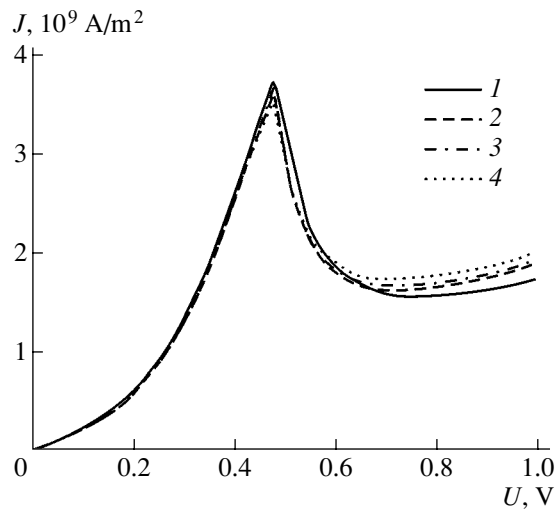
Fig. 2. Calculated *I–V* characteristics of an RTD (*1*) with scattering disregarded and (*2–4*) taking into account scattering with the scattering-rate coefficient $S_{op} =$ (*2*) 6.25×10^{12}, (*3*) 1.25×10^{13}, and (*4*) 2.5×10^{13} s^{-1}.
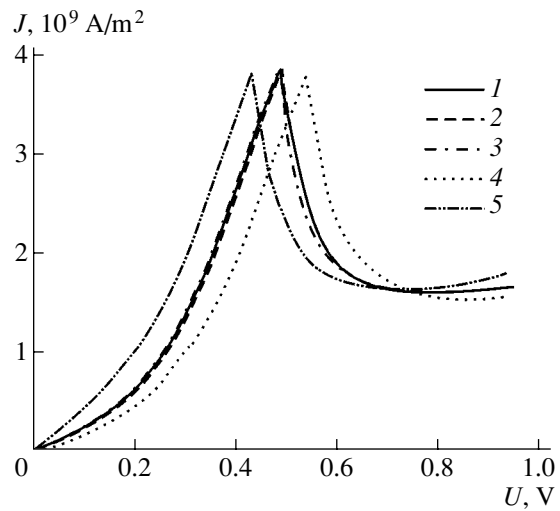

Fig. 3. RTD *I–V* characteristics calculated for various values of the surface-charge density σ_{sur} at the interface between the right-hand barrier and the quantum well: $\sigma_{sur} =$ (*1*) 0, (*2*) -10^{-5}, (*3*) 10^{-5}, (*4*) -10^{-4}, and (*5*) 10^{-4} C/m^2.

(see Section 4) made it possible to establish that the major contribution is made by scattering involving only the lowest level for the RTD under consideration. The effect of scattering also involving other resonant levels on the *I–V* characteristic is insignificant. Notwithstanding this circumstance, consideration of the effect of several resonant levels makes it possible to more adequately describe the real pattern of physical processes that occur in an RTD.

Figure 3 illustrates the calculated *I–V* characteristics of the same RTD for various values of the surface-charge density. In this case, scattering was disregarded in order to exclude its possible effects. Curve *1* was calculated with the surface charge disregarded. Curves *2–5* were obtained using the following values of σ_{sur} at the interface between the right-hand barrier and the quantum well: (*2*) -10^{-5}, (*3*) 10^{-5}, (*4*) -10^{-4}, and (*5*) 10^{-4} C/m^2. It follows from the results that the surface charge strongly affects the voltage V_{max} that corresponds to the peak values of the current. For example, a decrease in σ_{sur} from 10^{-4} C/m^2 (curve *5*) to -10^{-4} C/m^2 (curve *4*) brings about an increase in the voltage V_{max} from 0.43 to 0.54 V. This behavior can be accounted for by the fact that a negative charge at the heteroboundary retards the process of resonant tunneling; as a result, the voltage V_{max} increases.

Similar studies were carried out for cases where the surface charge at other heteroboundaries was taken into consideration, namely, the boundaries between the left-hand barrier and the emitter near-contact region, between the left-hand barrier and the quantum well, and between the right-hand barrier and the collector near-contact region. The results show that the observed general pattern is retained. In these cases, the charge

and potential are only redistributed in the active region, which insignificantly affects the voltage V_{max} at fixed values of σ_{sur}. In this context, it is sufficient to take into account the surface (effective) charge at only one of heteroboundaries in the course of calculating the voltage V_{max} for the RTD under consideration.

Finally, Fig. 4 shows a comparison of an *I–V* characteristic calculated with all the above factors taken into account (curve *1*) with the experimental data [44] (curve *2*). Satisfactory agreement with the experiment is attained at the following values of the parameters: the cross-sectional area $s = 1.5$ μm^2, the scattering-rate coefficient $S_{op} = 1.25 \times 10^{13}$ s^{-1}, the optical-phonon
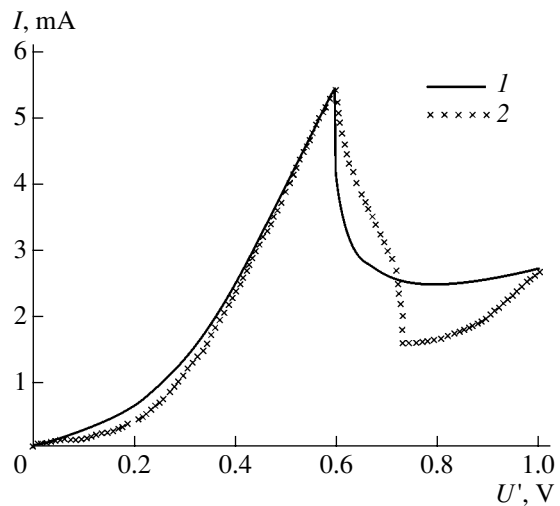

Fig. 4. Comparison of a calculated *I–V* characteristic (curve *1*) with experimental data [44] (curve *2*).

energy $\hbar\omega_{op} = 0.032$ eV, the shape factor for the barrier $\beta = 0$ eV, the surface-charge density $\sigma_{sur} = -10^{-4}$ C/m², and the resistances of the near-contact regions $R_e = R_c = 7$ Ω.

Let us analyze the results obtained. The number of adjustable parameters is no more than seven in the suggested combined RTD model; these parameters include s, S_{op}, $\hbar\omega_{op}$, β, σ_{sur}, R_e, and R_c. We believe that seven parameters cannot be considered as a large number. For example, there are 25 adjustable parameters in the well-known Gummel–Poon model of a bipolar transistor [37]. In one of the most adequate numerical models of submicrometer MOS transistors (based on the Monte Carlo method and intended for use by supercomputers), the number of adjustable parameters is equal to four just for the description of the transport properties of silicon [45], which was considered a considerable achievement. At the same time, only three parameters are really adjustable in the model we have suggested: s, β, and σ_{sur}. For example, as was mentioned above, the values of the parameters R_e and R_c are close to the estimates (see Section 5), while the scattering parameters S_{op} and $\hbar\omega_{op}$ are taken from the characteristic range of published experimental values because of a lack of other data. The cross-sectional area s is conventionally chosen on the basis of the best fit of the calculated peak current to the corresponding experimental values even in the well-known models. Such an approach is generally often used in one-dimensional numerical models of semiconductor devices [37]. In addition, data on the value of s were not reported in [44]. Unfortunately, there is almost no experimental information about the parameters β and σ_{sur} [27]. In this context, it is important to note that the model suggested can be used to determine these parameters indirectly.

At the same time, it is worth noting that consideration of the surface charge and resistances of the near-contact region made it possible to obtain very good agreement with the experimental data with respect to the voltage V_{max} (see Fig. 4), which is rarely attained in the known models. For example, the value of the voltage V_{max} is equal to about 0.48 V with the above factors disregarded and at various scattering parameters (see Fig. 2, curve *1*) and is equal to 0.59 V (Fig. 4, curve *1*) if these factors are taken into account. Consequently, consideration of both the surface charge and the resistances of the near-contact regions is important for a correct estimate of the RTD peak voltage.

In summary, we should comment on the valley region (or "plateau") and the internal bistability [46] of the *I–V* characteristic of an RTD, since it is in this region that the most significant difference between our calculations and the experimental results is observed (Fig. 4). First, it is established at present that this region can be adequately described using only nonstationary models (see, for example, [21]). Second, a more adequate description of this region can be obtained by varying the resistance [47] using models based on RTD equivalent circuits. Such a correction can also be easily applied in the model suggested; however, a radical improvement of the model from the physical standpoint is related to the consideration of nonstationary processes.

7. CONCLUSIONS

We suggested a numerical combined RTD model that is based on both the semiclassical and quantum-mechanical (the formalism of wave functions) approaches and can be implemented in calculations on personal computers. This model makes it possible to describe the joint effect of a number of factors, such as the charge in different regions of the structure (including the surface charge at the heteroboundaries), the shape of the band offset at the heteroboundaries, scattering in the quantum well for a number of resonant levels, and resistances of extended passive regions.

The performed studies of the effect of each of the above factors indicated that it is important to take into account these factors when simulating an RTD. Satisfactory agreement of the calculated *I–V* characteristic with the experimental data is attained if all the parameters are taken into account. The introduction, for the first time, of important parameters (the band-offset shape and the surface charge) of the heteroboundaries into the model suggests that it is necessary to take into account the characteristics of actual heterojunctions in more detail in order to adequately simulate RTDs. Good results of the analysis can be obtained in the context of the single-particle approximation and the effective-mass method using a one-dimensional model. Further refinement of the combined model suggested will be carried out by taking into account the effect of nonstationary processes in order to provide a more adequate description of both the valley region in the *I–V* characteristic and the internal bistability of an RTD.

REFERENCES

1. Zh. I. Alferov, A. L. Aseev, S. V. Gaponov, *et al.*, Mikrosist. Tekh., No. 8, 3 (2003).
2. P. Mazumder, S. Kulkarni, M. Bhattacharya, *et al.*, Proc. IEEE **86**, 664 (1998).
3. *Technology Roadmap for Nanoelectronics*, Ed. by R. Compano, 2nd ed. (European Commission, IST Programme, Future and Emerging Technologies, 2000).
4. L. V. Iogansen, Zh. Éksp. Teor. Fiz. **45**, 207 (1963) [Sov. Phys. JETP **18**, 146 (1964)].
5. R. Tsu and L. Esaki, Appl. Phys. Lett. **22**, 562 (1973).
6. I. I. Abramov, *Simulation of Physical Processes in Silicon Integrated Circuits* (Belorus. Gos. Univ., Minsk, 1999) [in Russian].

7. A. S. Tager, Élektron. Tekh., Ser. 1: Élektron. SVCh, No. 9, 21 (1987).

8. I. N. Dolmanov, V. I. Tolstikhin, and V. G. Elenskiĭ, Zarubezh. Radioélektron., No. 7, 66 (1990).

9. E. V. Buzaneva, *Microstructures of Integrated Electronics* (Radio i Svyaz', Moscow, 1990) [in Russian].

10. *Resonant Tunneling in Semiconductors: Physics and Applications*, Ed. by L. L. Chang, E. E. Mendez, and C. Tejedor (Plenum, New York, 1991).

11. V. P. Dragunov, I. G. Neizvestnyĭ, and V. A. Gridchin, *Fundamentals of Nanoelectronics* (Novosib. Gos. Tekh. Univ., Novosibirsk, 2000) [in Russian].

12. R. K. Mains, I. Mehdi, and G. I. Haddad, Appl. Phys. Lett. **55**, 2631 (1989).

13. Y. Fu, Q. Chen, M. Willander, *et al.*, J. Appl. Phys. **74**, 1874 (1993).

14. J. P. Sun and G. I. Haddad, VLSI Design **3**, 1 (1997).

15. A. A. Gorbatsevich, V. M. Koltyzhenkov, and A. G. Tsibizov, Izv. Vyssh. Uchebn. Zaved. Élektron., No. 4, 61 (2001).

16. O. Pinaud, J. Appl. Phys. **92**, 1987 (2002).

17. W. R. Frensley, Phys. Rev. B **36**, 1570 (1987).

18. N. C. Kluksdahl, A. M. Kriman, D. K. Ferry, and C. Ringhofer, Phys. Rev. B **39**, 7720 (1989).

19. K. L. Jensen and F. A. Buot, J. Appl. Phys. **65**, 5248 (1989).

20. B. A. Biegel and J. D. Plummer, Phys. Rev. B **54**, 8070 (1996).

21. P. Zhao, D. L. Woolard, B. L. Gelmont, and H.-L. Cui, J. Appl. Phys. **94**, 1833 (2003).

22. G. Klimeck, R. Lake, R. C. Bowen, *et al.*, Appl. Phys. Lett. **67**, 2539 (1995).

23. R. C. Bowen, G. Klimeck, R. K. Lake, *et al.*, J. Appl. Phys. **81**, 3207 (1997).

24. R. Lake, G. Klimeck, R. C. Bowen, and D. Jovanovich, J. Appl. Phys. **81**, 7845 (1997).

25. J. P. Sun, G. I. Haddad, P. Mazumder, and J. N. Schulman, Proc. IEEE **86**, 641 (1998).

26. I. A. Obukhov, Mikrosist. Tekh., No. 2, 23 (2001).

27. *Molecular Bean Epitaxy and Heterostructures*, Ed. by L. L. Chang and K. Ploog (Martimus Nishoff, Amsterdam, 1985; Mir, Moscow, 1989).

28. J. P. Sun, PhD Thesis (Dep. of EECS, Univ. of Michigan, Ann Arbor, 1993).

29. S. Mohan, J. P. Sun, P. Mazumder, and G. I. Haddad, IEEE Trans. Comput.-Aided Des. **14**, 653 (1995).

30. I. I. Abramov and I. A. Goncharenko, Élekromagn. Volny Élektron. Sist. **7** (3), 54 (2002).

31. I. I. Abramov and I. A. Goncharenko, in *Proceedings of 11th International Conference on Microwave Engineering and Telecommunication Technologies* (Sevastopol, Ukraina, 2001), p. 443.

32. I. I. Abramov and I. A. Goncharenko, Izv. Belorus. Inzh. Akad., No. 1(9)/2, 88 (2000).

33. I. I. Abramov and E. G. Novik, *Numerical Simulation of Metal Single-Electron Transistors* (Bestprint, Minsk, 2000) [in Russian].

34. *Tunneling Phenomena in Solids*, Ed. by E. Burstein and S. Lundqvist (Plenum, New York, 1969; Mir, Moscow, 1973).

35. *Nanostructure Physics and Fabrication*, Ed. by M. A. Reed and W. P. Kirk (Academic, San Diego, 1989).

36. Y. Zohta and T. Tanamoto, J. Appl. Phys. **74**, 6996 (1993).

37. I. I. Abramov, *Modeling of Integrated Circuits: A Course of Lectures* (Belorus. Gos. Univ., Minsk, 1999) [in Russian].

38. I. I. Abramov and I. A. Goncharenko, Izv. Belorus. Inzh. Akad., No. 2(14)/2, 170 (2002).

39. I. I. Abramov, I. A. Goncharenko, S. A. Ignatenko, *et al.*, Mikroélektronika **32**, 124 (2003) [Russ. Microelectronics **32**, 97 (2003)].

40. I. I. Abramov and I. A. Goncharenko, *Low-Dimensional Systems-2* (Grodn. Gos. Univ., Grodno, 2002), p. 21 [in Russian].

41. I. I. Abramov and I. A. Goncharenko, Izv. Belorus. Inzh. Akad., No. 1(11)/3, 77 (2001).

42. I. I. Abramov and I. A. Goncharenko, in *Proceedings of 12th International Conference on Microwave Engineering and Telecommunication Technologies* (Sevastopol, Ukraina, 2002), p. 464.

43. I. I. Abramov and I. A. Goncharenko, in *Proceedings of 13th International Conference on Microwave Engineering and Telecommunication Technologies* (Sevastopol, Ukraina, 2003), p. 534.

44. T. B. Boykin, R. C. Bowen, G. Klimeck, and K. L. Lear, Appl. Phys. Lett. **75**, 1302 (1999).

45. M. V. Fischetti and S. E. Laux, Phys. Rev. B **38**, 9721 (1988).

46. V. J. Goldman, D. C. Tsui, and J. E. Cunningham, Phys. Rev. Lett. **58**, 1256 (1987).

47. C. Y. Huang, J. E. Morris, and Y. K. Su, J. Appl. Phys. **82**, 2690 (1997).

Translated by A. Spitsyn

ATOMIC STRUCTURE AND NONELECTRONIC PROPERTIES OF SEMICONDUCTORS

Formation of Nanostructures in a Ga$_2$Se$_3$/GaAs System

N. N. Bezryadin*^, G. I. Kotov*, I. N. Arsent'ev**, and A. A. Starodubtsev*

Voronezh State Technological Academy, Voronezh, 394000 Russia
^e-mail: phys@vgta.vrn.ru
***Ioffe Physicotechnical Institute, Russian Academy of Sciences, Politekhnicheskaya ul. 26, St. Petersburg, 194021 Russia*
Submitted December 27, 2004; accepted for publication January 17, 2005

Abstract—The topology of GaAs(100) and GaAs(111) surfaces before and after short treatments in Se vapor is studied by atomic-force microscopy. On the basis of this study, as well as ellipsometry and electron microscopy, a mechanism for the formation and growth of Ga$_2$Se$_3$(110) nanoislands and a layer on the GaAs(100) and GaAs(111) surfaces is proposed. © *2005 Pleiades Publishing, Inc.*

The use of gallium arsenide in microelectronics is limited by the presence of a high density of surface electronic states on the actual surface of this semiconductor [1]. In order to decrease the surface-state density, chalcogenide passivation is used [1–3]. The first studies focusing on the passivation of GaAs surfaces in sulfide solutions showed a significant increase in the photoluminescence intensity of GaAs [2]. This effect is due to a significant decrease in the nonradiative surface recombination rate, which becomes comparable with the nonradiative recombination rate at the only known ideal interface: GaAs/AlGaAs [3]. Investigation of the electrical characteristics of Me–Ga$_2$Se$_3$(110)–GaAs Schottky diodes (Me represents a metal) by measuring capacitance–voltage and current–voltage (I–V) characteristics has shown that, as a result of chalcogenide passivation, the experimental value of the effective height of Al and Au Schottky barriers decreases from 0.75 to 0.50 eV and from 0.84 to 0.94 eV, respectively. These facts indicate that, due to the chalcogenide passivation, a decrease in the surface-state density and the detachment of the Fermi level near the GaAs surface occur [4]. The energies of electronic states with respect to the bottom of the conduction band in the bulk (0.20, 0.32, and 0.68 eV) and on the surface (0.40 eV) of GaAs have been determined by isothermal-scanning deep-level transient spectroscopy. It was shown that, after treatment of the surface in Se vapor, the level with an activation energy 0.40 eV, which is responsible for the surface-state density, is absent [5]. During thermal treatment of GaAs substrates in Se vapor, reconstruction of (100) and (111) polar surfaces occurs, followed by the formation of a thin pseudomorphic Ga$_2$Se$_3$(110) layer [5].

The authors of [5] believed that it is the formation of this layer, accompanied by the reconstruction of the GaAs surface, that is responsible for the decrease in the surface-state density. Indeed, the lowest surface-state density (~10^{11} cm^{-2} eV^{-1}) was observed at the minimum lattice mismatch in the heterostructure. This condition is satisfied for Ga$_2$Se$_{3x}$Te$_{3(1-x)}$/GaAs heterostruc-

tures at $x = 0.43$, since the Ga–Se–Te solid solution of this composition has the same lattice constant as GaAs. The surface reconstruction provides a passivating effect (minimum surface-state density) only when the duration of the treatment of the GaAs surface in Se vapor under the conditions described in [4–6] is shorter than 15 min. Thus, from the point of view of the electrical properties of the Ga$_2$Se$_3$(110)/GaAs interface (minimum surface-state density), samples subjected to short-term (shorter than 15 min) treatment are of prime interest. Thus, in this study, in order to clarify the mechanism of formation of Ga$_2$Se$_3$/GaAs heterostructures, the surface of GaAs was investigated before and after short-term treatments in Se vapor by atomic-force microscopy (AFM), ellipsometry, and transmission-electron microscopy (TEM).

Investigation in an H-800 transmission electron microscope was performed in order to choose samples with a single-crystal pseudomorphic gallium selenide layer for subsequent analysis of their surface by AFM using a FEMTOSCAN-001 instrument. In this case, the microdiffraction image of the surface corresponded to that shown in Fig. 1 in [5]. These samples were also studied by measuring the I–V characteristics of Schottky diodes formed by free thermal deposition of a metal (Al, Ni, Ag, or Au) on the substrate surface immediately after the treatment in Se vapor. Samples with I–V characteristics corresponding to those of GaAs samples without surface states [5] were chosen for AFM study.

Analysis of the ellipsometric data obtained on an LÉF-3M ellipsometer for the GaAs surface treated in Se vapor made it possible to establish a number of kinetic regularities for the initial stage of formation of GaAs(100)/Ga$_2$Se$_3$(110) systems. Specifically, the temperature dependences of the ellipsometric parameter, possessing the dimension of length (in what follows, thickness), showed that the growth rate of Ga$_2$Se$_3$ layers, depending on the treatment duration, is initially limited by the rate of the chemical reaction of heterov-
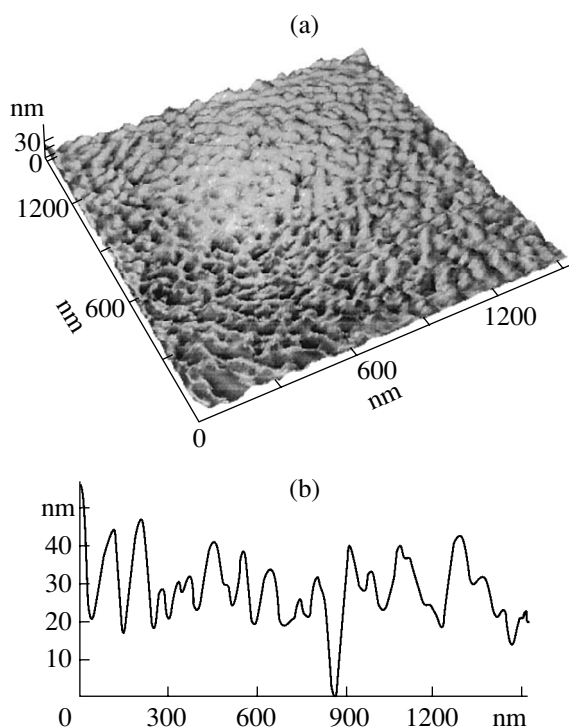
Fig. 1. (a) AFM image and (b) the cross section for the initial GaAs(100) surface.

Fig. 2. (a) AFM image and (b) the cross section for a GaAs(100) surface treated in Se vapor for 3 min.

alent substitution ($E_a = 4.75$ eV); then, as the layer thickness increases, the mechanism of limitation becomes mixed (diffusion–kinetic, $E_a = 1.04$ eV); furthermore, the growth rate is limited by the diffusion of Se or the reaction products ($E_a = 0.40$ eV) through the formed Ga_2Se_3 layer [7].

In this study, high-resistivity ($\sim 10^{16}$ cm^{-3}) n-GaAs substrates were used. The substrate surface was chemomechanically polished in a $H_2SO_4 : H_2O_2 : H_2O = 4 : 1 : 1$ solution; subsequently, residual oxides were removed in a $HCl : H_2O = 1 : 10$ solution. After this procedure, the substrates were rinsed in deionized water and dried in a centrifuge. The surface was scanned in an atomic-force microscope in the ranges 5000×5000, 1500×1500, and 600×600 nm. Figure 1 shows an AFM image and a cross section for the initial (immediately after the chemomechanical polishing) GaAs(100) surface.

After a 3-min treatment of GaAs, Ga_2Se_3(110)-phase islands were formed on the surface (Fig. 2). It can be seen that the islands formed on the GaAs(100) surface have lateral sizes of about 100–200 nm and heights of 50 to 70 nm; their density is 10^8 cm^{-2}.

With an increase in the treatment time, these islands expanded, with their lateral sizes attaining ~400–500 nm at treatment times of about 5 min (Fig. 3).

After a 10–15 min treatment of GaAs, the characteristic shape of the initial surface and islands was not observed and the surface became more uniform
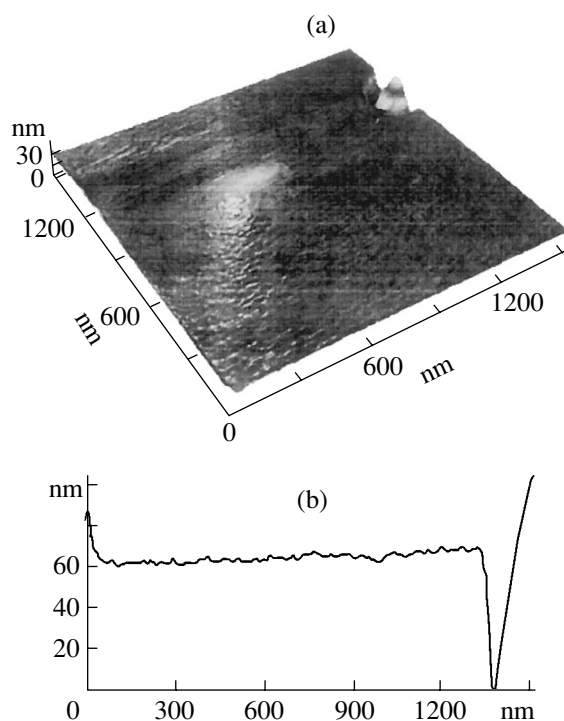
(Fig. 4). The roughness amplitude did not exceed 5 nm, in contrast to the initial GaAs(100) surface and the surface treated for periods lasting from several seconds to 10 min. As was noted above, we studied samples with a continuous single-crystal pseudomorphic Ga_2Se_3(110) layer on their surface [5]: microdiffraction images of all the surface regions contain reflections from the Ga_2Se_3(110) phase, and analysis of the I–V characteristics shows detachment of the Fermi level and, respectively, a decrease in the surface-state density for all the surface regions. Within the model considered in [5], these observations can be attributed to the presence of a continuous single-crystal Ga_2Se_3(110) layer on the surface. We should note that the correspondence of the composition of the layers formed in these processes to the stoichiometry of Ga_2Se_3 was earlier established in [8].

In order to explain the formation of islands on the heterostructure surface, we analyzed the ellipsometric data along with microscopic images of the same surface. New-phase islands formed at treatment times of ~3 min (Fig. 2) have sizes of ~$200 \times 200 \times 60$ nm and their surface density is 10^8 cm^{-2}. If we take the material of these islands to form a uniform Ga_2Se_3 layer, its thickness will be ~2.5 nm. The kinetic ellipsometric investigations of the same sample show that a layer formed in such a way should be ~7.5 nm thick. This ratio of thicknesses is retained for treatment times lasting up to 10 min, when individual islands from the Ga_2Se_3 phase can be detected (Figs. 2, 3). The revealed
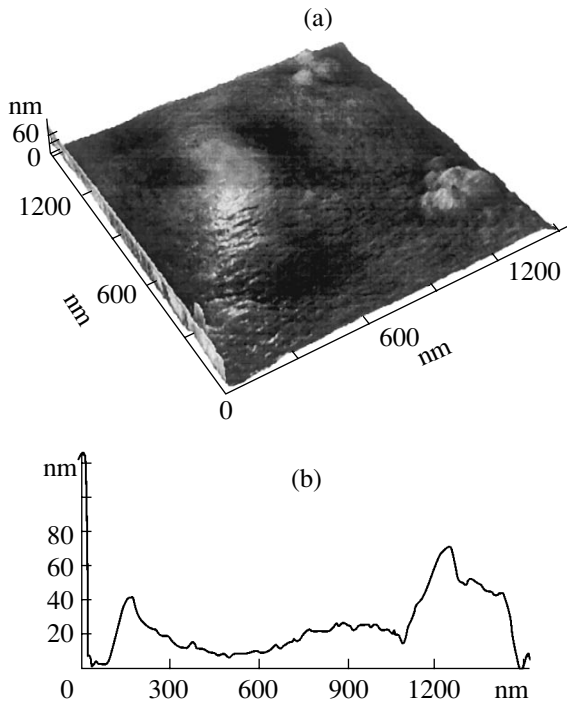
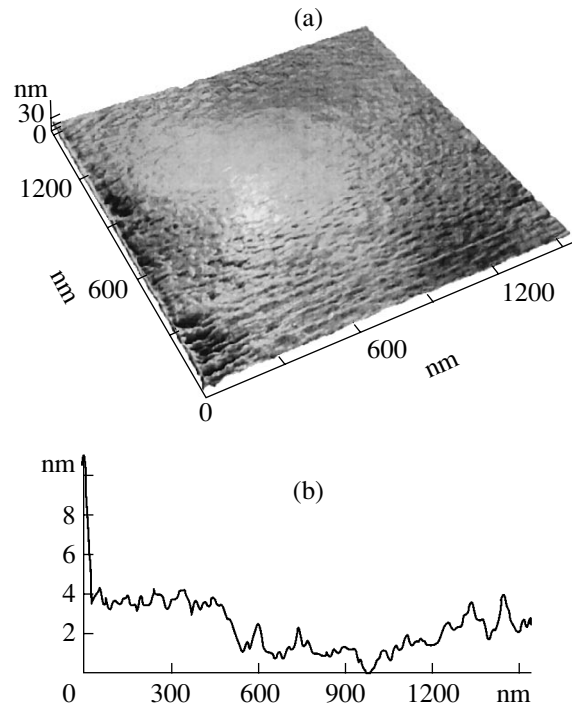**Fig. 3.** (a) AFM image and (b) the cross section for a GaAs(100) surface treated in Se vapor for 5 min.

Fig. 4. (a) AFM image and (b) the cross section for a GaAs(100) surface treated in Se vapor for 15 min.

feature of Ga$_2$Se$_3$ growth on the GaAs surface can be explained if we consider the growth process in terms of two interdependent mechanisms:

(i) Ga$_2$Se$_3$ is formed as a result of the heterovalent substitution of As in the GaAs lattice by Se (adsorbed on the sample surface) in accordance with the reaction

$$3GaAs + 3Se \longrightarrow Ga_2[V_{Ga}]Se_3 + Ga + 3As. \quad (1)$$
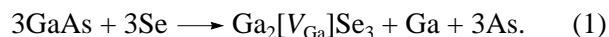
(ii) Gallium atoms (superstoichiometric for Ga$_2$Se$_3$) released after reaction (1) arrive at the sample surface and become involved in the formation of Ga$_2$Se$_3$, directly reacting with Se in accordance with the reaction

$$3Ga + 3Se \longrightarrow Ga_2[V_{Ga}]Se_3. \quad (2)$$

This reaction constitutes the second mechanism of formation of Ga$_2$Se$_3$ during the thermal treatment of GaAs in Se vapor.

Gallium (superstoichiometric for Ga$_2$Se$_3$) is supplied to the surface through the formed Ga$_2$Se$_3$ layer. This diffusion process seems quite likely because Ga$_2$Se$_3$, crystallizing in the sphalerite structure, has a large ($\sim 10^{21}$ cm^{-3}) concentration of stoichiometric cation vacancies.

Furthermore, gallium selenide is formed both in the bulk, by reaction (1), and on the surface, by reaction (2). With an increase in the process duration, the number of islands and their sizes increase, and they cover the GaAs (100) surface with a continuous layer from the Ga$_2$Se$_3$(110) phase (Fig. 4). Thus, under the chosen process conditions, the above-mentioned feature of

crystal growth is attributed to the fact that the larger part of the Ga$_2$Se$_3$ layer (with a thickness two-thirds of the value measured by the ellipsometric method) grows in the bulk of the GaAs substrate in accordance with reaction (1), while the rest (one-third) of the Ga$_2$Se$_3$(110) phase is formed from the released superstoichiometric Ga in accordance with reaction (2). Similar processes are observed under the annealing of GaAs(111) substrates in Se vapor, with the only difference being a shift of the temperature modes corresponding to the states of the GaAs(100) surface treated in Se vapor (see Figs. 2–4) to higher temperatures by about 20 K. This difference may be a consequence of the differing rate constants of the chemical reactions on the (100) and (111) GaAs surfaces.

Thus, analysis of ellipsometric and AFM data for a GaAs surface processed in Se vapor shows that the formation of nanoislands and a nanolayer from the Ga$_2$Se$_3$(110) phase occurs through two successive mechanisms and that stoichiometry is conserved. The number of islands, the rate of their nucleation, and, finally, the formation of a continuous Ga$_2$Se$_3$(110) layer are determined by the modes of treatment of the GaAs surface in Se vapor.

REFERENCES

1. V. N. Bessolov and M. V. Lebedev, Fiz. Tekh. Poluprovodn. (St. Petersburg) **32**, 1281 (1998) [Semiconductors **32**, 1141 (1998)].

2. B. J. Skromme, C. J. Sandroff, E. Yablonovich, and T. J. Gmitter, Appl. Phys. Lett. **51**, 2022 (1987).

3. E. Yablonovitch, C. J. Sandroff, R. Bhat, and T. Gmitter, Appl. Phys. Lett. **51**, 439 (1987).

4. B. I. Sysoev, N. N. Bezryadin, G. I. Kotov, and V. D. Strygin, Fiz. Tekh. Poluprovodn. (St. Petersburg) **27**, 131 (1993) [Semiconductors **27**, 69 (1993)].

5. B. I. Sysoev, N. N. Bezryadin, G. I. Kotov, and V. D. Strygin, Fiz. Tekh. Poluprovodn. (St. Petersburg) **29**, 24 (1995) [Semiconductors **29**, 12 (1995)].

6. B. L. Agapov, I. N. Arsent'ev, N. N. Bezryadin, *et al.*, Fiz. Tekh. Poluprovodn. (St. Petersburg) **33**, 712 (1999) [Semiconductors **33**, 658 (1999)].

7. N. N. Bezryadin, G. I. Kotov, I. N. Nazarenko, *et al.*, Kondens. Sredy Mezhfaz. Granitsy **6**, 225 (2004).

8. B. I. Sysoev, V. D. Strygin, G. I. Kotov, *et al.*, Phys. Status Solidi A **129**, 207 (1992).

Translated by Yu. Sin'kov

Microphotoluminescence of Undoped Single-Crystal Zinc Telluride Produced by Nonequilibrium Vapor-Phase Growth Techniques

V. V. Ushakov^ and Yu. V. Klevkov

Solid-State Physics Division, Lebedev Physical Institute, Russian Academy of Sciences,
Leninskiĭ pr. 53, Moscow, 119991 Russia
^e-mail: ushakov@mail1.lebedev.ru
Submitted November 22, 2004; accepted for publication December 6, 2004

Abstract—The properties of undoped bulk ZnTe crystals grown under nonequilibrium crystallization conditions by chemical synthesis from a vapor phase have been examined using microphotoluminescence spectral analysis and imaging. In spite of a considerable increase in the crystallization rate, the samples under study compare well, in terms of the concentration of different types of residual defects, with high-quality single crystals grown from a vapor phase under quasi-equilibrium conditions at much higher temperatures. At the same time, the absence of a luminescence contrast at the grain boundaries and the inefficiency of thermal annealing indicate that the main nonradiative growth defects in the materials obtained are low-mobility thermally stable complexes formed due to the association of stoichiometric defects and, possibly, background impurities. © 2005 Pleiades Publishing, Inc.

1. INTRODUCTION

Single-crystal zinc telluride, a direct-gap II–VI semiconductor compound with a band gap of ~2.3 eV, is useful for physical studies and applications as a material for visible-range light-emitting and electrooptical devices. However, in ZnTe crystals grown under quasi-equilibrium conditions, a straightforward relationship between their physical properties and their composition cannot be readily ensured. This problem is caused by the fact that, due to the retrograde behavior of the solidus line in the $T–x$ (temperature–composition) cross section of the phase diagram, the free-carrier concentration is determined by the interaction of stoichiometric defects with doping (background) impurities, which is not easily controlled. For example, because of the well-known problems related to growing a doped material of n-type conductivity, light-emitting devices with the best parameters have, so far, been based on MOS structures rather than on $p–n$ junctions [1]. Moreover, it should not be forgotten that the electrical and optical properties of real crystals are determined by the interplay between all the defects of thermodynamic origin, both point and extended (dislocations and boundaries).

An alternative is offered by opting for nonequilibrium growth techniques. Due to changes in the mechanisms of incorporation of both matrix and dopant atoms into the crystal lattice, this approach makes it possible to avoid limitations related to the shape of phase diagrams and to modify the system of defects and impurities in a way necessary for obtaining a material with the desired properties.

Earlier [2, 3], we investigated the properties of bulk CdTe crystals grown using nonequilibrium vapor-phase processes, including low-temperature synthesis from highly purified components and subsequent purification of the material under the conditions of congruent sublimation, gas-dynamic vapor flow, and high-rate condensation at low temperatures. In this study, different variants of nonequilibrium conditions for crystallization by chemical synthesis from a vapor phase were used to produce undoped bulk ZnTe. The properties of the material obtained were studied by low-temperature microphotoluminescence spectral analysis and imaging. These techniques combine high sensitivity to the presence of impurities and defects in the crystal with a high spatial resolution.

2. EXPERIMENTAL

Below, we briefly characterize the developed nonequilibrium vapor-phase techniques of growing bulk crystals at increased deposition rates.

The first method involves vacuum sublimation of an initially synthesized binary compound using a temperature gradient and shifting the material composition to the point of minimum pressure P_{min} in the $P–x$ (pressure–composition) cross section of the phase diagram.

In the gas-dynamic flow regime, the vapor-condensation rates at the temperatures 680–720°C were 200–250 μm/h (taking into account the condensation coefficient). Upon deposition in a dynamic vacuum, a textured material with a single-crystal grain size up to 1.5 mm and the predominant growth direction [111]

was obtained on the quartz walls of the reactor. Mass-spectrometry analysis indicates that, within the detectivity limits, the main background impurities in this material are O, C, Cu, and Li (at a concentration of $\sim 10^{15}$ cm^{-3}).

The second and third methods involve chemical synthesis from vaporized Zn and Te$_2$ components fed into the synthesis area from individual cells connected to the crystallizer.

The processes were carried out in a quasi-closed-type quartz reactor in dynamic vacuum. The vapor flux density of the components (supersaturation) and the ratio of the vapor fluxes (nonstoichiometry of the vapor phase in the synthesis area) were controlled by heating the cells with source components whose temperatures (vapor pressures) can be controlled independently. With vapor supersaturation in a crystallization area of 10^3–10^4 and under relatively small deviations of the vapor-phase composition towards an excess of Te (second method) or Zn (third method), bulk polycrystalline condensate was deposited on the walls of the quartz crystallizer at temperatures of 650–720°C and rates up to 3000 μm/h. The condensed material consisted of faceted crystallites with sizes up to 1 μm and a predominant {111} orientation. As revealed by etching and optical microscopy techniques, twins are main form of structural defects within single-crystal grains.

Luminescence was measured both for samples with natural-growth surfaces and for ones whose surface was ground and polished parallel to the crystallization front and, after removal of the damaged layer in bromomethanol solution, treated in a selective etchant (12.5N solution of NaOH, 80°C).

After the as-grown samples were studied, they were annealed for 72 h in an atmosphere of saturated Zn vapor at 840°C or in liquid zinc at 650°C.

Measurements were carried out using a microphotoluminescence scanner, which made it possible both to carry out a spectral analysis at chosen spots on the sample surface and to conduct luminescence imaging of the surface at a given wavelength. The combination of these two techniques enabled us not only to identify the nature of the impurity and defect centers but also to determine the mechanisms of their formation. The samples were mounted on a cold finger in a cryostat, with the temperature variable from 100 to 300 K. The luminescence was excited by a He–Cd laser ($\lambda = 415.6$ nm) using an optical focusing system. The power of the excitation radiation on the sample surface was 3.0 mW, and the spot diameter was 15 μm (at a half-maximum intensity level). Optical filters were used to reduce the excitation level. The luminescence spectra were recorded in a wavelength range up to 1 μm using an MDR-12 grating monochromator (1200 groove/mm) with the reciprocal linear dispersion 2.4 nm/mm; a cooled FÉU-83 photomultiplier was used as a detector, and the signal was finally fed to a lock-in amplifier. The position of the excitation spot on the sample surface

was monitored visually using a microscope-based optical system.

Spatial scanning was performed by moving, under computer control, a special table with a cryostat along two mutually perpendicular directions with respect to the excitation laser beam (which was fixed in space). The scan step could be varied according to the measurement requirements; in this study, the images were recorded at a 35-μm step. In the course of luminescence mapping, the data were displayed on a computer monitor using color representation of the luminescence intensity; at any spot of interest, the scan can be interrupted to obtain a record of the sample emission spectrum. Below, the recorded luminescence spectra are given with corrections made to take into account the spectral variation in the setup sensitivity.

3. RESULTS AND DISCUSSION

When analyzing the experimental results reported below, one should bear in mind that microluminescence measurements are typically characterized by high excitation levels. In this study, this level was $\gtrsim 10^{21}$ photons/(cm^2 s), which exceeds the intensities commonly used in "macroscopic" photoluminescence measurements by more than an order of magnitude. As a rule, this leads to relatively high intensities of the exciton-emission lines in the spectra in comparison to the impurity- and defect-related bands.

Another consequence of high excitation levels observed in this study was the photochromism of the freshly etched samples, manifested as a reduction of the luminescence intensity under the effect of the excitation laser beam (by a factor of 2–2.5 in 4–5 min). Thus, in order to avoid errors, all the luminescence spectra shown below were recorded under steady-state conditions, after the photostimulated processes of the formation of surface nonradiative recombination centers had come to an end.

The spectra of liquid-helium-temperature macroscopic luminescence of the samples under study are typical of the emission of undoped single-crystal p-type ZnTe, where lines of excitons bound to neutral acceptors are dominant [4, 5]. The intensities of the longer wavelength impurity and defect bands were low, which is indicative of the high quality of the material. This inference is also confirmed by observation of the luminescence from the crystals under study at room temperature (edge-emission band at ~ 2.27 eV).

As a wide-gap semiconductor, ZnTe features fairly large exciton binding energies. For free and neutral-acceptor-bound excitons, the binding energies are 13 and 6–7 meV, respectively, while the ionization energy of a hydrogen-like acceptor is ~ 62.5 meV [6, 7]. Due to the relatively large values of the binding energies, excitonic transitions can be observed at rather high temperatures, specifically, exceeding 100 K. Furthermore, the intensity of the excitonic emission depends nearly qua-

dratically on the excitation level, as compared to the (sub)linear dependence for the emission originating from the transitions to localized states [8]; thus, even at high temperatures, excitonic lines may still dominate over impurity- and defect-related bands under high-level excitation conditions (excitation by a pulsed laser, electron beam, etc.) (see [9, 10]).

Figure 1 shows the microluminescence spectra of the crystals under study at $T = 95$ K. It can be seen that all of these spectra are characterized by similar sets of spectral lines (note that the spectral resolution varies according to the magnitude of the signal). Under the given experimental conditions, the edge-emission lines at 2.0–2.4 eV are the strongest ones. Their intensities exhibit superlinear power-law dependences on the excitation level, with the exponent lying in the range 1.9–1.4 (larger values correspond to higher-energy lines), which is an indication of their excitonic origin [8]. Taking into account the temperature shift [11], we attribute the shortest wavelength line at 2.367 eV to free-exciton emission and other the lines to the emission of excitons bound to various types of impurities: an isolated neutral acceptor (apparently, typical of Cu_{Zn} and Li_{Zn} [4, 7]) for the 2.361-eV line; an isolated neutral double acceptor (probably, Si_{Te} or C_{Te} [12, 13]) for the 2.345-eV line; and a low-symmetry unidentified complex based on Cu [14] for the 2.322-eV line (which also has a phonon replica at 2.296 eV).

In the long-wavelength region of the spectra of all the samples under study, there is a band at ~1.88 eV, known to correspond to the emission of an O_{Te} isoelectronic center [15]. The low intensity of the oxygen-related band in the samples obtained by vacuum resublimation is due to the special purification of the source components. At the same time, the spectra of these samples contain a donor–acceptor band at ~1.68 eV, which is related to the background Cl impurity that forms deep-level impurity–defect complexes (in particular, acceptor $V_{Zn}Cl_{Te}$ A centers) [16]. Finally, the spectra of the samples grown under the conditions of an excess Zn content in the vapor phase (curve c) exhibit a previously unobserved weak band at ~1.43 eV (870 nm), which, most probably, originates from centers containing Te vacancies.

For comparison, in Fig. 1, we added the spectrum of an undoped single-crystal material produced under quasi-equilibrium conditions by free growth from a vapor phase at ~1100°C at a rate of ~50 µm/h [17] (curve d). The developed nonequilibrium techniques exhibit considerably (two orders of magnitude!) higher rates of structure formation; nevertheless, it can be seen that the material obtained compares well (in terms of the concentrations of different types of residual stoichiometric defects and background impurities) with high-quality single crystals grown under quasi-equilibrium conditions from the vapor phase at much higher temperatures.
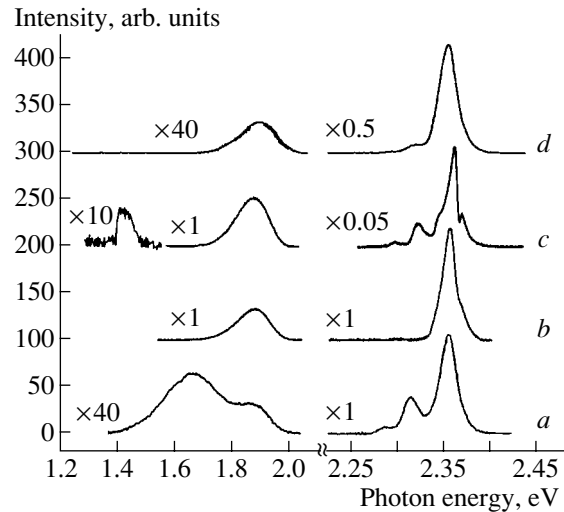

Fig. 1. Microphotoluminescence spectra of the materials under study at $T = 95$ K. Curves a, b, and c correspond to samples obtained by nonequilibrium vapor-phase techniques 1, 2, and 3, respectively; curve d corresponds to an undoped single crystal grown under quasi-equilibrium conditions from a vapor phase [17].

In order to study the behavior of the impurity–defect ensemble in the crystals under a heat treatment, the samples were annealed in the presence of an excess amount of cationic-component atoms. Such annealing of II–VI compounds (in the vapor phase or in the liquid metal) is used to clear the crystals of cationic vacancies and their associations with background impurities, which form deep-level compensating acceptor centers. An obvious consequence of such treatment is a reduction in the relative concentrations of cation-substitution impurities and, at the same time, an increase in the relative concentration of the impurities occupying anion sites in the lattice [5, 18]. In addition, such annealing results in the dissolution of inclusions and precipitates of Te present in the samples and extraction (segregation) of the impurities contained there [19, 20].

In this study, annealing of the samples for 72 h in an atmosphere of saturated Zn vapor at 840°C or in liquid zinc at 650°C did not lead to an enhancement of their luminescence (for the sample grown by method 1, there was even some decrease in the luminescence intensity). The spectra reveal only a partial redistribution between the emitting excitonic complexes (which manifests itself in the appearance of new bound-exciton lines at 2.333 and 2.316 eV, the latter with an LO-phonon replica at 2.288 eV) and disappearance of the $V_{Zn}Cl_{Te}$ impurity–defect A centers in the material grown by method 1 (see Fig. 2). Although a reduction in the intensity of the emission related to centers incorporating cation vacancies and cation-substitution impurities might be attributed, according to the common tendency, to a decrease in the concentration of such centers, a similar reduction in the intensities of the other spectral lines (including the free-exciton line) provides definite
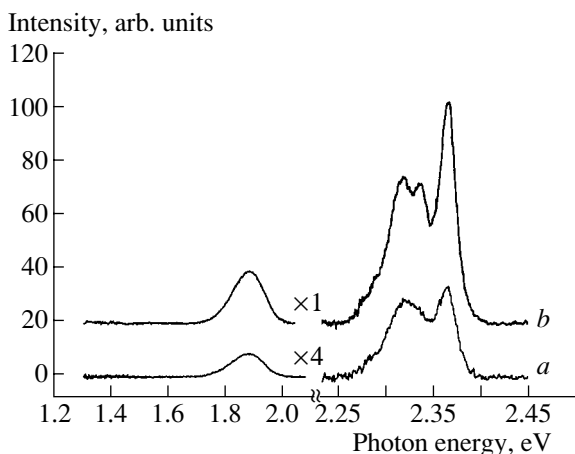
Intensity, arb. units

Fig. 2. Microphotoluminescence spectra of samples (*a*) 1 and (*b*) 2 (see curves *a* and *b* in Fig. 1) at $T = 95$ K recorded after annealing for 72 h in saturated Zn vapors at 840°C.

evidence of the low efficiency of the annealing. In general, reducing the concentration of growth defects in bulk undoped ZnTe remains a problem (cf, e.g., [20]).

In order to examine the uniformity of the grown material over the bulk of the ingots obtained, as well as to study the influence of the grain (subgrain) boundaries on the spatial distribution of point defects and impurities within single-crystal grains, we carried out microluminescence imaging measurements. In order to reveal the grain boundaries and crystal-structure defects within the grains, the sample surface was treated with a selective etchant (12.5N solution of NaOH, 80°C). The maximum grain size was as large as 1.5 mm in the samples grown by method 1 and up to 1 mm in other cases. The measurements were performed at wavelengths corresponding to the spectral peaks in Figs. 1 and 2. The general shape of the spectra did not change significantly across the grown ingots, excluding the local crystallization areas, whose position within the reactor suggested that the gas flows were highly turbulent in their vicinity. In Fig. 3, to demonstrate the imaging results, we show the data obtained for a sample grown under the conditions of congruent sublimation of the presynthesized binary compound and vapor flow in the reactor in the gas-dynamic regime. The spectrum of this sample is shown by curve *a* in Fig. 1. Figure 3a shows a photograph of a 2.45 × 2.45 mm² area whose luminescent image, recorded at the step of 35 μm and a wavelength of 525 nm (2.361 eV, exciton bound to a Cu_{Zn}/Li_{Zn} neutral acceptor), is shown in Fig. 3b. It can be seen from Fig. 3a that even neighboring single-crystal grains may have different orientations of the polar axis at the growth surface, which was revealed (upon selective etching) by the typical surface profile (on the black-and-white photograph, the bright (mirrorlike) regions correspond to the {111}A orientation and the dark regions correspond to the {111}B orientation). For ZnTe and CdTe, the simultaneous presence of grains with {111}A and {111}B orientations along the growth direction is indicative of nonequilibrium crystallization conditions [21] and is probably related to fluctuations in the composition of the vapor phase. Within the examined area of the sam-
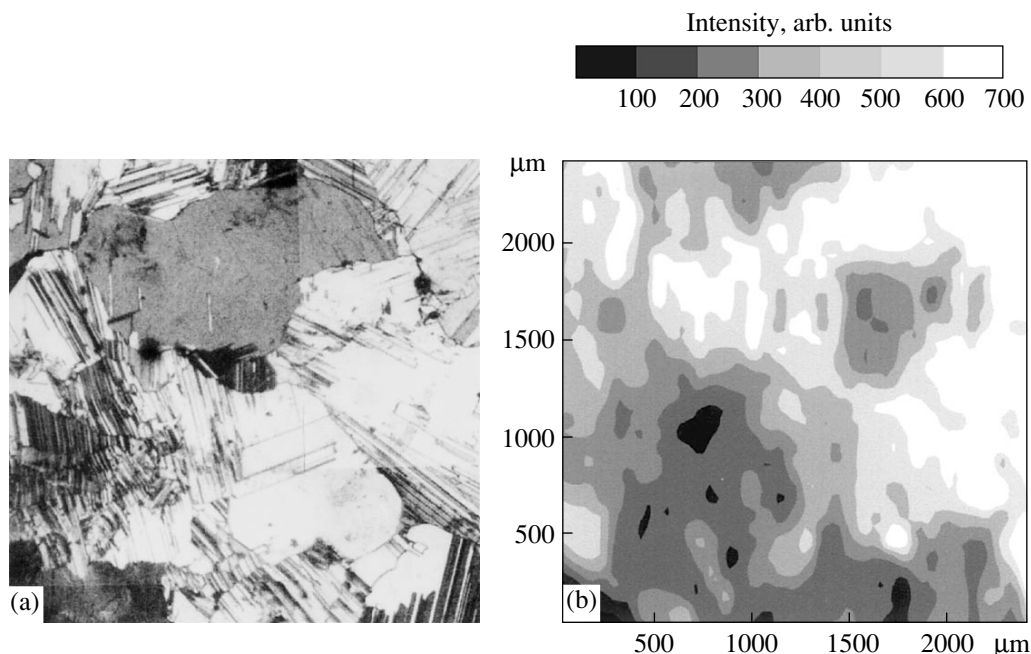

Fig. 3. Images of a sample grown under the conditions of congruent sublimation of a presynthesized binary compound and vapor flow in the reactor in a gas-dynamic regime (spectrum *a* in Fig. 1): (a) photograph of a 2.45 × 2.45 mm² area and (b) luminescent image of this area recorded at 525 nm (2.361 eV) with the step of 35 μm.

ple, the luminescence intensity varied by about a factor of 6; however, the variation was no more than twofold within individual single-crystal grains. It should be noted that higher intensities were observed in larger grains, while the orientation of the polar surfaces was of no importance. An identical "profile" of the luminescence intensity was obtained when scanning was carried out at wavelengths corresponding to the other peaks in curve *a* (Fig. 1): 534 nm (2.322 eV, an exciton bound at a low-symmetry Cu center) and 740 nm (1.68 eV, donor–acceptor transitions involving Cl centers). For each wavelength, the variations in the luminescence intensity within the grains was insignificant and there was no luminescent contrast in the vicinity of the grain and twin boundaries or the other extended structural defects (compare with the data from [9, 19, 20]). The absence of associations of residual defects is typical of nonequilibrium growth conditions with high crystallization rates and a vapor flow in the reactor in a gas-dynamic regime [22]. However, it should be noted that the shape of the luminescent images remained virtually unchanged even upon sample annealing. Apparently, this circumstance means that, in the materials investigated, the nonradiative centers responsible for the recombination processes are low-mobility thermally stable complexes formed during the growth due to the association of stoichiometry defects (and, probably, background impurities). These complexes are distributed relatively uniformly over the bulk of the crystal lattice.

4. CONCLUSIONS

Despite the fact that high-temperature (100-K) spectra of ZnTe are far less informative than low-temperature spectra, the results reported here indicate that materials obtained by nonequilibrium vapor-phase techniques compare well, in terms of the concentrations of different types of residual defects and background impurities, with high-quality single crystals grown from a vapor phase under quasi-equilibrium conditions at much higher temperatures. Except for the grain size in the texture, a considerable (by two orders of magnitude) increase in the crystallization rate did not lead to significant changes in the nature of the crystallization processes at the microscopic level. At the same time, the density of nonradiative centers remained fairly high, especially in the smaller grains. The low efficiency of thermal annealing and absence of a luminescent contrast at the single-crystal grain boundaries indicate that, in the materials investigated, the dominant nonradiative growth defects are low-mobility thermally stable complexes formed due to the association of stoichiometry defects and, probably, background impurities.

REFERENCES

1. J. Gu, K. Tonomura, N. Yoshikawa, and T. Sakaguchi, J. Appl. Phys. **44**, 4692 (1973).
2. V. V. Ushakov and Yu. V. Klevkov, Fiz. Tekh. Poluprovodn. (St. Petersburg) **37**, 1067 (2003) [Semiconductors **37**, 1042 (2003)].
3. V. V. Ushakov and Yu. V. Klevkov, Fiz. Tekh. Poluprovodn. (St. Petersburg) **37**, 1298 (2003) [Semiconductors **37**, 1259 (2003)].
4. N. Magnea, D. Bensahel, J. L. Pautrar, and J. C. Pfister, Phys. Status Solidi B **94**, 627 (1979).
5. P. J. Dean, H. Venghaus, J. C. Pfister, *et al.*, J. Lumin. **16**, 363 (1978).
6. D. C. Herbert, P. J. Dean, H. Venghaus, and J. C. Pfister, J. Phys. C **13**, 3641 (1978).
7. H. Venghaus and P. J. Dean, Phys. Rev. B **21**, 1596 (1980).
8. T. Schmidt, K. Lischka, and W. Zulehner, Phys. Rev. B **45**, 8989 (1992).
9. D. Bensahel, N. Magnea, and M. Dupuy, Solid State Commun. **30**, 467 (1979).
10. C. F. Klingshirn, W. Maier, B. Hönerlage, *et al.*, Solid-State Electron. **21**, 1357 (1978).
11. R. Pässler, E. Griebl, H. Riepl, *et al.*, J. Appl. Phys. **86**, 4403 (1999).
12. M. Magnea, J. L. Pautrar, L. S. Dang, *et al.*, Solid State Commun. **47**, 703 (1983).
13. P. J. Dean, M. J. Kane, N. Magnea, *et al.*, J. Phys. C **18**, 6185 (1985).
14. P. O. Holtz, B. Monemar, H. P. Gislason, and N. Magnea, J. Lumin. **34**, 245 (1986).
15. J. L. Merz, Phys. Rev. **176**, 961 (1968).
16. J. Bittebierre and R. T. Cox, Phys. Rev. B **34**, 2360 (1986).
17. Yu. V. Korostelin, V. I. Kozlovsky, and P. V. Shapkin, J. Cryst. Growth **214–215**, 870 (2000).
18. M. Magnea, J. L. Pautrar, L. S. Dang, *et al.*, Solid State Commun. **47**, 703 (1983).
19. D. Bensahel, M. Dupuy, and J. C. Pfister, Phys. Status Solidi A **55**, 211 (1979).
20. D. Bensahel and M. Dupuy, Phys. Status Solidi A **56**, 99 (1979).
21. Yu. V. Klevkov, V. P. Martovitskiĭ, and S. A. Medvedev, Fiz. Tekh. Poluprovodn. (St. Petersburg) **37**, 129 (2003) [Semiconductors **37**, 119 (2003)].
22. K. Durose and G. J. Russell, J. Cryst. Growth **86**, 471 (1988).

Exact Self-Compensation of Conduction in Cd$_{0.95}$Zn$_{0.05}$Te:Cl Crystals in a Wide Range of Cd Vapor Pressures

O. A. Matveev*^, A. I. Terent'ev*, N. K. Zelenina*, V. N. Gus'kov**, V. E. Sedov*, A. A. Tomasov*, and V. P. Karpenko*

Ioffe Physicotechnical Institute, Russian Academy of Sciences, St. Petersburg, 194021 Russia
^*e-mail: Oleg.Matveev@mail.ioffe.ru*
***Kurnakov Institute of General and Inorganic Chemistry, Russian Academy of Sciences, Moscow, 117907 Russia*
Submitted December 7, 2004; accepted for publication December 22, 2004

Abstract—The process of self-compensation in Cd$_{0.95}$Zn$_{0.05}$Te:Cl solid-solution crystals has been studied by annealing single crystals under a controlled Cd vapor pressure, with subsequent measurements of the Hall effect, photoluminescence, carrier lifetime and mobility, and photocurrent memory in the annealed crystals. By means of this annealing, conditions of thermal treatment that make it possible to fabricate low-conductivity samples with a low carrier density, 10^7–10^{11} cm^{-3}, are defined. In these samples, a $p \longrightarrow n$ conduction inversion is observed at a higher free-carrier density ($n, p \approx 10^9$ cm^{-3}) and the dependence of the electron density on the Cd vapor pressure exhibits a more gentle slope than in the case of CdTe:Cl crystals. The obtained data are discussed in terms of a self-compensation model in which intrinsic point defects act as acceptors with deep levels. This level is attributed to a Zn vacancy, which remains active at high Cd pressure. © 2005 Pleiades Publishing, Inc.

The synthesis of semi-insulating Cd$_{1-x}$Zn$_x$Te:Cl crystals is being widely studied at present [1, 2]. The low conductivity of these crystals is accounted for by self-compensation of charged point defects. The two mechanisms most frequently used to explain the self-compensation in a semiconductor doped with a donor impurity are the generation of oppositely charged intrinsic point defects [3–8] and the crystal lattice relaxation, which results in the formation of *DX* centers [9–11]. A high degree of self-compensation in a crystal is reached if it undergoes a slow post-growth cooling, when the interaction of charged point defects occurs [3, 4, 12].

We studied the self-compensation in CdTe:Cl by annealing single crystal samples under a controlled Cd vapor pressure P_{Cd}, with subsequent measurement of the Hall effect [13, 14]. The obtained data allowed us to determine the thermal conditions necessary for obtaining samples with low conductivity, ~10^{-10} Ω^{-1} cm^{-1}, and a low density of free carriers, 10^7–10^8 cm^{-3}. The nature of the p–n conduction inversion as a function of P_{Cd} at low carrier densities, 10^7–10^8 cm^{-3}, was established. On the Basis on these results, we determined the conditions necessary for controlling self-compensation during the post-growth annealing of a CdTe:Cl ingot.

Semi-insulating crystals with p-type conduction were reproducibly obtained via sample annealing and the growth of a CdTe:Cl ingot. Semi-insulating n-type crystals were obtained considerably less frequently, and, often, they exhibited inhomogeneous physical characteristics. However, even the earliest experiments on the growth of Cd$_{1-x}$Zn$_x$Te:Cl ($x = 0.0002$–0.1) demonstrated a reliable production of semi-insulating n-type crystals [15]. It is precisely this kind of n-type semi-insulating crystal that is demanded for the fabrication of *X*-ray detectors for computer tomography [15].

In this report, we present the results of investigation of single-crystal Cd$_{0.95}$Zn$_{0.05}$Te:Cl samples annealed under a controlled Cd vapor pressure.

In preparation for annealing, samples were cut from a Cd$_{0.95}$Zn$_{0.05}$Te:Cl ingot grown by horizontal unidirectional crystallization under controlled P_{Cd} [15]. The growth conditions (the melt overheating, the deviation from stoichiometry, and the growth rate) were the same as in the case of CdTe:Cl [16]. The Cl concentration in the ingot was defined by the CdCl$_2$ charge in the melt, 2×10^{-18} cm^{-3} (which was the same for CdTe:Cl). Before annealing, the as-grown Cd$_{0.95}$Zn$_{0.05}$Te:Cl samples demonstrated p-type conduction with a hole density $p = 10^8$–10^9 cm^{-3}. The method used for annealing was described in detail for CdTe:Cl [13]. The samples were annealed in a three-zone furnace in a quartz ampule. The annealing temperature was $t_{cr} = 900°C$, the temperature of the filling material was $t_p = 905°C$, and the temperature of metallic Cd t_{Cd} was defined in each experiment by the desired partial pressure of Cd. The filling material was prepared from the same crystal as the sample to be annealed, which meant that the sample composition remained unchanged during the annealing.

The density of carriers was determined from Hall measurements of $Cd_{0.95}Zn_{0.05}Te:Cl$ samples annealed under a selected partial pressure of Cd vapor. Figure 1a (points 2, 2') shows the dependence of the hole (p) and electron (n) density in these samples on P_{Cd}.

Points 1 and 1' in Fig. 1a show similar results for CdTe:Cl. At low P_{Cd}, both CdTe:Cl and $Cd_{0.95}Zn_{0.05}Te:Cl$ demonstrate p-type conduction. At intermediate P_{Cd}, a $p \longrightarrow n$ inversion of the conduction is observed.

At a high partial pressure of Cd, the crystals switch to n-type conduction. It is necessary to note that the conduction inversion for the CdTe:Cl crystals is observed within a very narrow range of P_{Cd} values and at low carrier densities, $p(n) = 10^7$–10^8 cm^{-3}.

In the $Cd_{0.95}Zn_{0.05}Te:Cl$ crystals, the conduction inversion $p \longrightarrow n$ is observed at higher carrier densities, $p(n) \gtrsim 10^9$ cm^{-3}. The curve describing the $n(P_{Cd})$ dependence for the CdTe:Cl crystals is very steep: n increases from 10^7 to 10^{15} cm^{-3} under only an approximately twofold increase in the partial pressure P_{Cd}. For the $Cd_{0.95}Zn_{0.05}Te:Cl$ crystals, the curve exhibits a more gentle slope: when P_{Cd} increases 10 times, the carrier density n increases from 10^7 to 10^{11} cm^{-3} (while the material remains virtually semi-insulating). In contrast to the case of CdTe:Cl, this behavior of the $n(P_{Cd})$ dependence in the $Cd_{0.95}Zn_{0.05}Te:Cl$ crystals creates considerably more favorable conditions for controlling the electrical properties of a crystal during its fabrication, specifically, by varying the partial pressure of the Cd vapor.

The low free-carrier density, $p(n) = 10^7$–10^8 cm^{-3}, in the $Cd_{1-x}Zn_xTe:Cl$ crystals is related to self-compensation of charged point defects. According to one of the models of self-compensation [9–11], a strong relaxation of the crystal lattice in the vicinity of Cl atoms leads to the formation of DX^- centers, which generates deep levels below the minimum of the conduction band. This circumstance accounts for the formation of semi-insulating n-$Cd_{1-x}Zn_xTe:Cl$ crystals. However, two points remain unaccounted for:

(i) The dependence of the electron density on P_{Cd}; indeed, in terms of this model, the lattice relaxation depends only on the composition of the solid solution (Zn content) and the nature of the dopant (Cl). (ii) The formation of DX^- centers in $Cd_{1-x}Zn_xTe:Cl$ becomes energetically favorable only at the Zn content $x \geq 0.2$ [10]. It is necessary to note that the formation of DX^- centers has been observed in $Cd_{1-x}Zn_xTe:Cl$ crystals with $x < 0.2$ [9, 11].

In terms of the other model [3–8], the self-compensation is accounted for by the formation of intrinsic point defects, i.e., metal vacancies (V_{Zn} and V_{Cd}), which act as acceptors, and by the association of charged donors and acceptors into centers that give rise to deep levels in the band gap. According to this model, the concentration of V_{Cd} acceptors in the crystal is high at low P_{Cd}. This circumstance leads to a high density of
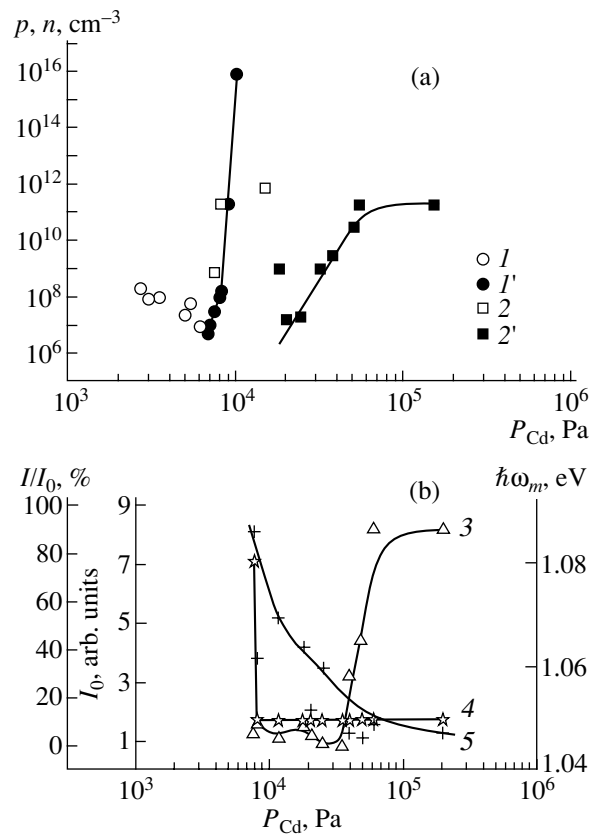

Fig. 1. (a) Carrier density and (b) PL characteristics as functions of the Cd vapor pressure during annealing of the samples. (a): (1) p-CdTe, (1') n-CdTe, (2) p-$Cd_{0.95}Zn_{0.05}Te$, and (2') n-$Cd_{0.95}Zn_{0.05}Te$. (b): (3) relative integral intensity I/I_0 of the luminescence band at 1 eV, (4) the position of peak of the 1-eV band $\hbar\omega_m$, and (5) total integral PL intensity I_0.

free holes, which can be seen in Fig. 1a for the CdTe:Cl and $Cd_{0.95}Zn_{0.05}Te:Cl$ crystals. As the pressure of the Cd vapor on the crystal increases, the concentration of V_{Cd} decreases. The dependence of p on P_{Cd} for the CdTe samples demonstrates a corresponding decrease in the hole density. For the $Cd_{0.95}Zn_{0.05}Te:Cl$ samples, we did not observe any clearly pronounced $p(P_{Cd})$ dependence. The high hole density and the lack of a clear $p(P_{Cd})$ dependence indicate that the V_{Cd} concentration remains high. The high value of $[V_{Cd}]$ is a consequence of insufficiently high P_{Cd} on the $Cd_{0.95}Zn_{0.05}Te:Cl$ crystal during the annealing. (Indeed, the partial pressure P_{Cd} for stoichiometric $Cd_{0.95}Zn_{0.05}Te:Cl$ must be higher than for CdTe at the same temperature [17].) At higher P_{Cd}, the concentration of donor centers, $[Cd_i] + [Cl_{Te}]$, exceeds the $[V_{Cd}]$ concentration. This behavior of the concentrations of charged defects correlates with the data in Fig. 1a, in which the conduction inversion $p \longrightarrow n$ is observed for CdTe:Cl and $Cd_{0.95}Zn_{0.05}Te:Cl$. For CdTe:Cl, the $p \longrightarrow n$ inversion is sharp (almost step-like). This variation in the carrier density is related to a
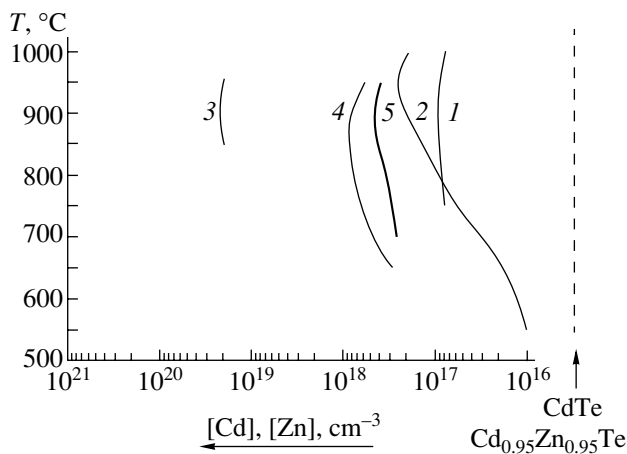
Fig. 2. Maximum solubility of Cd in CdTe: (*1*, [3]; *2*, [20]; *3*, [18]; and *4*, [19]) and of Cd and Zn in $Cd_{0.95}Zn_{0.05}Te$ (*5*, [17]) along the T–x section of the state diagram of the Cd–Zn–Te system.

"jump" in the Fermi level from a deep acceptor to a shallow donor (Cd_i and Cl_{Te}) level.

The rate at which the electron density n grows with P_{Cd} is considerably lower in the $Cd_{0.95}Zn_{0.05}Te$:Cl crystals than for CdTe:Cl. This fact may indicate that there is a weak dependence of the concentration of donor point defects $[Cd_i]$ and $[V_{Te}]$ on P_{Cd}. The limited solubility of these intrinsic point defects in $Cd_{1-x}Zn_xTe$:Cl can be seen in the state diagram of the Cd–Zn–Te system shown in Fig. 2. The limit of the maximum Cd concentration in a $Cd_{0.95}Zn_{0.05}Te$ crystal (curve *5*) indicates that the Cd_i and V_{Te} solubility is lower than that in CdTe (curves *3*, *4*). These curves reflect the total concentration of point defects. Furthermore, the limited V_{Te} solubility in the crystal results in limited solubility of the principal donor dopant substituting Te, i.e., Cl_{Te}. Therefore, from the data on the solubility of V_{Te} in $Cd_{0.95}Zn_{0.05}Te$ and CdTe, we may assume a lower solubility of Cl in the solid solution as compared to the binary compound. Prior to annealing, Cl in the $Cd_{0.95}Zn_{0.05}Te$:Cl samples exists in charged state at the concentration $[Cl_{Te}^+] \sim 10^{17}$ cm^{-3}, which is necessary to obtain a semi-insulating material with $p \sim 10^8$ cm^{-3}. During annealing at 900°C, the concentration of Cl_{Te}^+ defects can decrease due to egress of Cl to some inclusions in the crystal (or to a gaseous phase) or as a result of the retrograde character of the solubility of these defects in the crystal. As the content of Cl_{Te}^+ and Cd_i^+ decreases, the concentration of centers forming shallow levels in the band gap also decreases; therefore, the transition of the Fermi level from deep to shallow levels becomes more gradual. These considerations furnish a qualitative explanation of the difference between the

dependences of the electron density on P_{Cd} in $Cd_{0.95}Zn_{0.05}Te$ and CdTe (Fig. 1a).

The quantitative estimate is hindered by the following:

(i) The available experimental data on the solubility of point defects, which were obtained by different authors using different methods, strongly diverge from each other and from the results of calculations (see Fig. 2).

(ii) Until now, the concentration of charged point defects (V_{Zn} and Zn_i) in $Cd_{0.95}Zn_{0.05}Te$ has not been studied.

iii) The solubility of Cl in $Cd_{0.95}Zn_{0.05}Te$ has not yet been determined.

We have tried to estimate the maximum solubility of charged intrinsic donor defects using recent data on the total solubility of defects in $Cd_{0.95}Zn_{0.05}Te$ [17] and CdTe [19] and the data on charged intrinsic point defects in CdTe [3, 20] (the last data show only a slight scatter, see curves *1* and *2* in Fig. 2). We assume that the ratio between the total amounts of intrinsic point defects and charged defects in $Cd_{0.95}Zn_{0.05}Te$ is the same as in CdTe:

$$\left(\frac{[Cd_i^+] + [V_{Te}^+]}{[Cd_i] + [V_{Te}]}\right)_{CdTe}$$
$$= \left(\frac{[Cd_i^+] + [Zn_i^+] + [V_{Te}^+]}{[Cd_i] + [Zn_i] + [V_{Te}]}\right)_{Cd_{0.95}Zn_{0.05}Te}. \qquad (1)$$

This assumption is based on the fact that the crystal lattice energies in CdTe and $Cd_{0.95}Zn_{0.05}Te$ differ insignificantly [21] and the samples are annealed in similar P–T (pressure–temperature) conditions. We also assume that the Cd vapor pressure governs change in the concentration of charged defects (the Fermi level position and free-carrier density). The data on the concentration of defects at 900°C are taken from Fig. 2. For $Cd_{0.95}Zn_{0.05}Te$, we obtain $[Cd_i^+] + [Zn_i^+] + [V_{Te}^+] \approx 5 \times 10^{16}$ cm^{-3}. The electron density in the conduction band must be the same at high P_{Cd}; however, this is not the case (see Fig. 1a). Therefore, either assumption (1) is erroneous or the used concentration of point defects at 900°C does not correspond to the concentration of defects in the semi-insulating crystal at room temperature, at which the Hall effect was measured. If we assume that assumption (1) is correct and use it in the estimation of the concentration of defects at low temperatures (~500°C), when the equilibrium of the defects is "frozen" during the cooling of the crystal, we obtain an even higher value of $[Cd_i^+] + [Zn_i^+] + [V_{Te}^+]$, since the solubility of the metal in $Cd_{0.95}Zn_{0.05}Te$ at low temperatures is higher than in CdTe [17]. It is necessary to note, however, that, while discussing the dependence of the ratio

$$\left(\frac{[Cd_i^+] + [Zn_i^+] + [V_{Te}^+]}{[Cd_i] + [Zn_i] + [V_{Te}]}\right)_{Cd_{0.95}Zn_{0.05}Te}$$

Product of the carrier mobility by lifetime for electrons and holes and the photocurrent memory in samples annealed at different P_{Cd}

Before annealing			After annealing				
$(\mu\tau)_e$, cm^2 V^{-1}	$(\mu\tau)_h$, cm^2 V^{-1}	photocurrent memory, %	annealing no.	P_{Cd}, 10^4 Pa	$(\mu\tau)_e$, cm^2 V^{-1}	$(\mu\tau)_h$, cm^2 V^{-1}	photocurrent memory, %
~2 × 10^{-4}	~(1–3) × 10^{-5}	9–10	063	1.8	5 × 10^{-5}	4.5 × 10^{-5}	3.5
			064	0.8	4 × 10^{-5}	<2 × 10^{-7}	0.13
			067	2.5	5 × 10^{-5}	<8 × 10^{-7}	0.4
					3.5 × 10^{-5}	<2 × 10^{-6}	
					6 × 10^{-5}		
			070	5	~2.5 × 10^{-7}	<5 × 10^{-7}	0.17
					~2.5 × 10^{-6}	<2 × 10^{-7}	

on P_{Cd}, we have formally included $[Zn_i^+]$ in it, and we expect a conduction inversion through variation of the ratio $([V_{Cd}^-] + [V_{Cd}^{-2}])/[Cd_i^+]$ with P_{Cd}. The concentration of point defects involving Zn in a sample is controlled by the composition and temperature of the filling material in the ampule, and these parameters for the filling and the sample coincide. The hole density $p = 10^8$–10^9 cm^{-3}, which was measured in the samples before annealing, indicates that the intrinsic point defects with the greatest concentrations are $[V_{Cd}^-]$ and $[V_{Cd}^{-2}]$, and $[V_{Zn}^-]$ and $[V_{Zn}^{-2}]$. During annealing at high P_{Cd}, the concentration of $[V_{Cd}^-]$ and $[V_{Cd}^{-2}]$ in the metal sublattice decreases, whereas that of $[Cd_i^+]$ and $[V_{Te}^+]$ increases. In this situation, the concentrations of intrinsic point defects $[V_{Zn}^-]$ and $[V_{Zn}^{-2}]$, which are not directly related to P_{Cd}, may remain stable or change only slightly. The presence of a deep level in the band gap, associated with a center related to a Zn vacancy, can account for the slow increase in n with P_{Cd} occurring under a sharp increase in the concentration of shallow donors $[Cd_i^+]$ and $[Cl_{Te}^+]$.

Along with the Hall effect measurements, the photoluminescence (PL) spectra, carrier lifetime and mobility, and the photocurrent memory were measured in all the Cd$_{0.95}$Zn$_{0.05}$Te samples annealed at various pressures P_{Cd}.

PL was measured at 77 K in the range of photon energies $\hbar\omega = 0.8$–2.3 eV. The emission was excited by an Ar-ion laser (the photon energy was 2.43 eV and the flux density was ~10^{20} cm^{-2} s^{-1}) and detected by a cooled Ge photodiode. As is standard, the PL spectrum consisted of three bands peaked at about 1.6, 1.45, and 1 eV. We now restrict our consideration to the 1-eV band. Figure 1b shows the ratio of the integral intensity of this band I to the total intensity I_0 integrated over the whole spectrum (curve 3), the peak position $\hbar\omega_m$ of the

band (curve 4), and the total integral intensity I_0 (curve 5) as functions of P_{Cd}. The integral intensities were measured under the same excitation and detection conditions for different samples. It can be seen that I/I_0 remains virtually unchanged, at about 6%, up to $P_{Cd} = 3.5 \times 10^4$ Pa. It then increases to ~90% and tends to a constant value. It is noteworthy that the curves describing the electron density n and of the intensity I of the PL band level out in the same range of P_{Cd} (in Fig. 1a, curves 2'; Fig. 1b, curve 3). The fact that the spectral position of the band peak remains constant (at least for P_{Cd} corresponding to the n-type samples) indicates that the increase in the band intensity is related to an increase in the concentration of centers of the same kind rather than to the appearance of some other type of centers. The origin of the 1-eV band still remains unclear. Presumably, it has a complex nature [22, 23]. Several authors, including us, have attributed it to the capture of carriers by centers that are either isolated doubly negatively charged Cd vacancies, V_{Cd}^{-2} [3], or various complexes that include these vacancies [15, 24–27]. Under the conditions of our experiment, the concentration of Cd vacancies cannot increase with the pressure of the Cd vapor. However, it seems quite probable that the initial sample contains V_{Zn} vacancies, and, as was mentioned above, they are retained under annealing with a filling. This assumption is supported by the estimate of the energy position of the V_{Zn} level in ZnTe [23], which nearly coincides with the V_{Cd} level in CdTe. Under annealing at higher P_{Cd}, the concentration $[V_{Me}D]$ of acceptor complexes constituted by a metal vacancy and a donor, which are responsible for the PL band at 1.45 eV, decreases, with the result that the contribution of the 1-eV band increases.

As can be seen in Fig. 1b, an increase in the Cd vapor pressure during annealing reduces the integral PL intensity I_0. This observation indicates an increase in the concentration of nonradiative recombination centers (or emission outside the spectral range under study,

which seems unlikely). This dependence correlates with the data obtained for the product of the carrier mobility and lifetime and for the photocurrent memory in the samples annealed at high P_{Cd}. These data are presented below.

Using the time-of-flight method and irradiation with α particles (see, e.g., [28]), we measured the product of the carrier mobility and the lifetime for electrons $(\mu\tau)_e$ and holes $(\mu\tau)_h$ in the crystals under study before and after annealing (see table). It can be seen that the annealing changes $(\mu\tau)_e$ only slightly. At the same time, $(\mu\tau)_h$ in the annealed crystals is significantly reduced. This fact confirms the above-made assumption that the annealing of $Cd_{0.95}Zn_{0.05}Te$ crystals at high P_{Cd} leads to the formation of deep acceptor centers, which are possibly the intrinsic point defects V_{Zn}^- and V_{Zn}^{-2}. These centers are negatively charged, which results in an intense capture of holes.

The study of the same crystals before and after annealing by intense pulses of uniformly absorbed radiation (the computer tomography mode [29, 30]) has demonstrated the strong photocurrent memory present in the unannealed samples (see table). It can be seen that, after annealing at low P_{Cd} close to the pressure at which the $p \longrightarrow n$ inversion occurs (annealing no. 063), the photocurrent memory is slightly reduced. In annealing nos. 064, 067, and 070 at higher P_{Cd}, the photocurrent memory is strongly reduced: to (0.13–0.4)%. The magnitude of the photocurrent memory correlates with the dependence of $(\mu\tau)_h$ on P_{Cd} (see table). As is known [15, 29, 30], one of the origins of photocurrent memory is an incomplete collection of the hole component of the signal. In our case (annealing nos. 064, 067, 070), the hole component is virtually absent, which results in a strong decrease (by a factor of 10–20) in the photocurrent memory and indicates that there appears a large amount of deep acceptor levels responsible for the recombination of holes.

Thus, study of the self-compensation in single-crystal $Cd_{0.95}Zn_{0.05}Te$:Cl shows that the $p \longrightarrow n$ conduction inversion is observed at a higher free-carrier density $(n, p \sim 10^9 \text{ cm}^{-3})$ than in CdTe:Cl crystals. In addition it was found that the curve describing the dependence of the electron density on the Cd vapor pressure exhibits a more gentle slope.

Studies of photoluminescence, carrier lifetime and mobility, and photocurrent memory have confirmed the formation of a deep acceptor level in the band gap of the annealed crystals. This finding indicates that the low conductivity of annealed $Cd_{0.95}Zn_{0.05}Te$:Cl crystals can be explained in terms of a model of self-compensation via the formation of charged intrinsic point defects with a deep acceptor level. We assume that this level is related to Zn vacancies, which remain active at high P_{Cd}.

It is noteworthy that the revealed dependence of the electron density in $Cd_{0.95}Zn_{0.05}Te$:Cl on P_{Cd} creates considerably more favorable conditions for controlling the electrical properties of a crystal by varying the Cd vapor pressure during the fabrication of the material in comparison with CdTe:Cl.

REFERENCES

1. *Proceedings of 10th International Conference on II–VI Compounds* (Bremen, 2001); Phys. Status Solidi B **229**, 1 (2002).

2. *Proceedings of 11th International Conference on II–VI Compounds* (Niagara, 2003); Phys. Status Solidi C **1**, 621 (2004).

3. D. de Nobel, Philips Res. Rep. **14**, 361 (1959).

4. G. Mandel, F. F. Morehead, and P. R. Wagner, Phys. Rev. **136**, A826 (1964).

5. F. A. Kröger, *The Chemistry of Imperfect Crystals* (Wiley, New York, 1964; Mir, Moscow, 1969).

6. K. R. Zanio, in *Semiconductors and Semimetals*, Vol. 13: *Cadmium Telluride*, Ed. by R. K. Willardson and A. C. Beer (Academic, San Francisco, 1978), p. 230.

7. J. Marfaing, Thin Solid Films **387**, 123 (2001).

8. V. Babentsov, V. Corregider, K. Benz, *et al.*, Nucl. Instrum. Methods Phys. Res. A **458**, 85 (2001).

9. K. Khachaturyan, M. Kaminska, and E. R. Weber, Phys. Rev. B **40**, 6304 (1989).

10. D. J. Chadi, Phys. Rev. Lett. **72**, 534 (1994).

11. C. H. Park and D. J. Chadi, Phys. Rev. B **52**, 11884 (1995).

12. O. A. Matveev and A. I. Terent'ev, Fiz. Tekh. Poluprovodn. (St. Petersburg) **34**, 1316 (2000) [Semiconductors **34**, 1264 (2000)].

13. O. A. Matveev and A. I. Terent'ev, Fiz. Tekh. Poluprovodn. (St. Petersburg) **27**, 1894 (1993) [Semiconductors **27**, 1043 (1993)].

14. O. A. Matveev and A. I. Terent'ev, Fiz. Tekh. Poluprovodn. (St. Petersburg) **32**, 159 (1998) [Semiconductors **32**, 144 (1998)].

15. O. A. Matveev, A. I. Terent'ev, V. P. Karpenko, *et al.*, Phys. Status Solidi B **229**, 1073 (2002).

16. O. A. Matveev and A. I. Terent'ev, Fiz. Tekh. Poluprovodn. (St. Petersburg) **29**, 378 (1995) [Semiconductors **29**, 191 (1995)].

17. J. H. Greenberg, V. N. Guskov, M. Fiederle, and K. Benz, J. Cryst. Growth **270**, 69 (2004).

18. K. V. Kiseleva, U. V. Klevkov, S. N. Maksimovsky, *et al.*, in *Proceedings of International Symposium on Cadmium Telluride*, Ed. by P. Siffert and A. Cornet (Centre de Resich des Nucl., Strusburg, 1971), p. 12.

19. J. H. Greenberg, V. N. Guskov, V. B. Lazarev, and O. V. Shekershneva, J. Solid State Chem. **102**, 382 (1993).

20. F. T. Smith, Metall. Trans. **1**, 617 (1970).

21. N. N. Berchenko, V. E. Krevs, and V. G. Sredin, *Semiconductor Solid Solutions and Their Applications, II–VI: Reference Tables* (Min. Oborony, Moscow, 1982), p. 208 [in Russian].

22. C. B. Davis, D. D. Allred, A. Reyes-Mena, *et al.*, Phys. Rev. B **47**, 13363 (1993).

23. W. Stadler, D. M. Hofman, H. C. Alt, *et al.*, Phys. Rev. B **51**, 10619 (1995).

24. M. R. Lorenz, B. Segal, and H. H. Woodbury, Phys. Rev. **134**, 751 (1964).

25. G. Mandel, Phys. Rev. **134**, A1073 (1964).

26. N. V. Agrinskaya, E. N. Arkad'eva, and O. A. Matveev, Fiz. Tekh. Poluprovodn. (Leningrad) **4**, 370 (1970) [Sov. Phys. Semicond. **4**, 347 (1970)].

27. N. V. Agrinskaja and O. A. Matveev, Rev. Phys. Appl. **12**, 235 (1977).

28. N. K. Zelenina and A. A. Tomasov, Élektron. Tekh., Ser. Mater. **7**, 77 (1983).

29. N. K. Zelenina, S. N. Ignatov, V. P. Karpenko, *et al.*, Nucl. Instrum. Methods Phys. Res. A **283**, 274 (1989).

30. V. P. Karpenko, O. A. Matveev, and A. A. Tomasov, Élektron. Model. **11**, 92 (1989).

Translated by D. Mashovets